UNIVERSITY OF LIÈGE
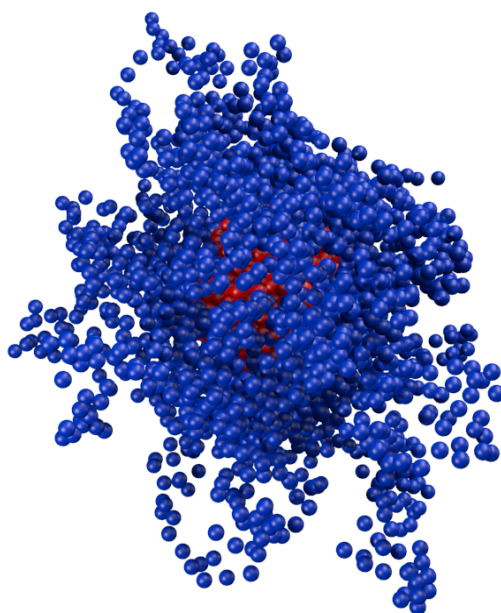**Faculty of Sciences**
Department of Chemistry

Molecular Dynamics Laboratory – Professor B. LEYH
Center for Education and Research on Macromolecules
CERM – Professor C. JEROME

Stimuli-responsive self-assembled macromolecular systems with potential drug delivery applications: structural characterization by Small-Angle Neutron Scattering

Academic year 2015-2016

Dissertation presented by
Arnaud Joset
To obtain the grade of
Doctor in Sciences

Systèmes macromoléculaires auto-assemblés sensibles à divers stimuli à applications biomédicales potentielles: caractérisation structurale par diffusion neutronique aux petits angles

Par Arnaud Joset

Résumé : Les colloïdes sont connus depuis le début du 19ème siècle mais ils ont suscité un regain d'intérêt durant les vingt dernières années, notamment grâce à leur utilisation dans des applications biomédicales ou la création de nouveaux matériaux.

L'objectif de cette thèse est l'étude d'échantillons colloïdaux sensibles à un ou plusieurs stimuli (pH, température, ligand, ions métalliques) par diffusion neutronique aux petits angles (SANS). Cette technique permet d'obtenir des informations sur la structure interne des objets mais aussi, dans certaines conditions, sur l'organisation des nano-objets en solution. À cette fin, plusieurs échantillons, formés par l'auto-assemblage de copolymères séquencés et de liposomes, ont été préparés. Une modélisation des sections efficaces a été menée afin de calculer l'évolution des principaux paramètres structuraux : taille, polydispersité, structure et volumes occupés par les différents composants hydrophiles et hydrophobes au sein des nano-objets. Les mesures SANS ont été réalisées en fonction de l'intensité du stimulus afin de quantifier l'évolution de ces paramètres.

La première partie expérimentale de ce travail porte sur l'analyse d'échantillons micellaires formés à partir de copolymères séquencés. Les séquences peuvent être biodégradables (ex. poly(ε-caprolactone)), biocompatibles (ex. poly(oxyde d'éthylène)), sensibles au pH (ex. poly(2-vinylpyridine), poly(acide acrylique)) ou à la température (ex. poly(N-isopropylacrylamide)). L'influence de la concentration et du pontage entre micelles a été étudiée via l'analyse de gels formés à partir de polystyrene-*b*-poly(tert-butylacrylate) PS-*b*-PtBA-tpy (-tpy: terpyridine) en présence d'ions métalliques.

La seconde partie expérimentale consiste en l'analyse de liposomes en présence d'une quantité croissante de β-cyclodextrine méthylée aléatoirement (RAMEB). Cette partie est divisée en deux chapitres. Le premier traite du cas de liposomes majoritairement composés de dimyristoylphosphatidylcholine (DMPC) et le deuxième traite de liposomes de DMPC dopés à l'aide de 30% de cholestérol.

Stimuli-responsive self-assembled macromolecular systems with potential drug delivery applications: structural characterization by Small-Angle Neutron Scattering

By Arnaud Joset

Abstract: Colloids are known since the early 19th century but they have mainly sparked interest since the last few decades thanks to their use in biomedical applications or in the design of new materials.

The aim of this thesis is the study of stimuli-responsive colloids by Small-Angle Neutron Scattering (SANS). The stimuli may be the pH, the temperature, the addition of a ligand or of metallic ions or a combination of them. SANS is a useful technique which provides information about the internal structure of nano-objects but also, if appropriate conditions are met, about the organization of the objects in solution. Several samples built from the auto-assembly of block copolymers and liposomes have been prepared. The macroscopic cross sections have been modeled with the aim to infer the main structural parameters of the samples: the global size, the polydispersity, the structure and volume occupied by the hydrophilic and hydrophobic components inside the nano-objects. The SANS measurements have been performed as a function of the intensity of the stimulus, in order to quantify the evolution of the structural parameters.

The first experimental part focuses on micellar samples built from sequenced block copolymers. The blocks may be biodegradable (e.g., poly(ε-caprolactone)), biocompatible (e.g., poly(ethylene oxide)), pH-sensitive (e.g., poly(2 vinylpyridine), poly(acrylic acid)) or temperature-sensitive (e.g., poly(N-isopropylacrylamide)). The influence of the concentration and the formation of bridges between micelles have been investigated through the analysis of metallo-supramolecular micellar gels resulting from the self-assembling of polystyrene-block-poly(tert-butylacrylate) PS-b-PtBA-tpy (tpy stands for terpyridine) block copolymers in the presence of transition metal ions.

The second part focuses on the analysis of liposomes interacting with an increasing concentration of Randomly Methylated β-cyclodextrins (RAMEB). This part is divided into two chapters. The first one deals with liposomes mainly composed of dimyristoylphosphatidylcholine (DMPC) and the second one investigates the effects of cholesterol doping on the same DMPC liposomes interacting with RAMEB.

Je tiens également à saluer Pierre Sibret avec qui nous avons passé beaucoup de temps à analyser les échantillons de triblocs. Les expériences de diffusion à Saclay ainsi que les réunions tardives dans les inondations resteront d'excellents souvenirs.

Cette thèse a été réalisée en coopération avec le CERM. Je tiens également à remercier les personnes qui font que ce service fonctionne aussi bien. Merci à Philippe, Christophe, Antoine, Valérie, Charlotte, Martine, Florence, Stéphanie, Bruno, Raphaël et à tous les autres pour leur bonne humeur, leur dynamisme et leur aide.

Je remercie également le Professeur Jean-François Focant ainsi que les assistants et préparateurs avec qui j'ai eu l'occasion de travailler dans le cadre du volet pédagogique de mon mandat : Grégory, Perrine, Armélinda, Thierry, Nicolas, Marie, Antoine Pierre-Hugues et Romain. Merci à vous pour les nombreux bons moments durant les réunions pour examens et les TP.

Toute ma sympathie va à Kathy et Véronique, mes chère voisines de bureau. Je suis très heureux que le hasard nous ai placé dans le même local.

Toute ma gratitude va à Enza, Stéphanie, Marie-Noëlle et Sophie pour leur disponibilité et de l'aide qu'elles m'ont apportée.

Je tiens également à remercier chaleureusement le professeur Robert Locht. Il est vrai que nos domaines de prédilection sont bien différents mais sa bonne humeur, ses conseils avisés et sa (longue rajouterait-il) expérience m'ont été utiles à plus d'une reprise. Nous nous soutenions dans les

moments incertains : la « lumière » versatile, des spectres énigmatiques et un spectromètre muet pour l'un et des ajustements numériques capricieux pour l'autre. Néanmoins, les difficultés ont passé. Il m'a également été d'un grand secours lors de la correction de mes soumissions en anglais. Son aimable contribution m'a grandement aidé à l'avancement et je ne saurais le remercier suffisamment.

Merci également à ma famille pour son soutien, ses marques d'attention et sa confiance qu'elle m'a manifesté tout au long de mes études et de ce travail. Je n'oublie pas non plus pas mes amis qui m'ont aidé à relativiser (en général autour d'un verre) lorsque les résultats n'étaient pas au rendez-vous.

Je remercie également Lalita pour ses encouragements, ses attentions, son optimisme à mon égard et son amour. Merci d'être là et de me renforcer par tes mots et tes attentions.

"The only real failure is the failure to try, and the measure of success is how we cope with disappointment."

— Deborah Moggach, The Best Exotic Marigold Hotel

Table of content

Abbreviations

A_c	Area per chain at the core-corona interface
b	Kuhn length of a polymer
$\tilde{b}_j$	Excess scattering length of the scatterer j
b_j	Scattering length of the scatterer j
CD	Cyclodextrin
CHOL	Cholesterol
D	Average thickness of the hydrophobic part of a liposome membrane
d	Average thickness of the hydrophilic part of a liposome membrane
DLS	Dynamic Light Scattering
DMF	Dimethylformamide
DMPC	Dimyristoylphosphatidylcholine
$d\Sigma(q)/d\Omega$	Macroscopic scattering cross section
$d\sigma(q)/d\Omega$	Differential scattering cross section
$\vec{k}$	Wave vector
L	Effective length of a chain considered as a rigid rod
LCST	Lower Critical Solution Temperature
m	Fraction of the phosphatidylcholine molecules included in liposomes.
N_{ch}	Number of chains
N_m	Aggregation number
P(q)	Form Factor
P2VP	poly(2-vinylpyridine)
PAA	Poly(acrylic acid)
PCL	poly(ε-caprolactone)
PEO	Poly(ethylene oxide)
PNIPAM	Poly(N-isopropylacrylamide)
PPO	Poly(propy1ene oxide)
PS	Polystyrene
PtBA	Poly(tert-butylacrylate)
$\vec{q}$	Scattering vector
RAMEB	Randomly Methylated β-Cyclodextrin
R_c	Radius of the core (micelles)
R_g	Radius of gyration
$\vec{r}_j$	Position vector of the scatterer j
S(q)	Inter-particle structure factor
SA	Stearylamine

SANS	Small-Angle Neutron Scattering
tpy	Terpyridine
V	Volume of the sample
v_j	Volume of the scatterer j
z	Degree of polymerization
Γ	Nano-object size distribution
κ_T	Isothermal compressibility
ρ_j	Scattering length density
$\tilde{\rho}_j$	Excess scattering length density

CHAPTER I

Introduction

Even if colloids have been used for many centuries, their scientific investigation started in the early 19th century. The word "colloid" is derived from the Greek word "*kolla*" which means glue with the suffix "*oid*" meaning "of similar form to". Before 1830, Brown [1] observed them using a microscope and described their random motion which was later named in his honor. Between 1850 and 1852, Sobrero [2] and Selmi [3,4] studied inorganic colloids made of silver chloride and Prussian blue, a pigment consisting of iron cyanide complexes. Later, Graham [5,6] managed to isolate some colloids with a dialysis system and published his results during the 1860s. He showed that colloid systems cannot diffuse through semi-permeable membranes. He discovered the ripening process which explains the growth of droplets through the continuous phase. In the beginning of the 20th century, the progress in chemistry and physics about atomic structure, diffusion processes, electrophoresis and light scattering favored the development of the colloid studies. Ostwald [7], Buzagh [8] and Hauser [9] worked for the promotion of colloid science while most of their colleagues still considered this field as a side branch of physical chemistry. In this context Ostwald wrote [10,9] in 1914 "Die Welt der vernachlässigten Dimensionen" (The world of neglected dimensions) and fought for the use of "colloid science" against "colloid chemistry". Today colloidal solutions are well known and extremely common in everyday life applications like paintings, inks, drugs, gelatin or food. Furthermore, many "smart" stimuli-responsive colloids have been developed during the last decades. The improvement of analysis and optical instruments has contributed to the development of this quite recent field. Colloidal dispersions are composed of nanoparticles and their building bricks have sizes of a few nanometers up to the micrometer range for the aggregates. Figure 1 shows three colloidal nanostructures architectures which will be considered in the present work i.e. polymeric micelles, nanogels and liposomes.

Micelles are spherical self-assemblies of amphiphilic molecules formed to decrease the surface tension. A common example is the self-assembly of fatty acids whose properties have been known for centuries. The first evidence of soap use is from Babylonian times and oil, soap and scrappers were commonly used in ancient Greek and Roman times. Surfactants have been used for ages to stabilize emulsions like Hollandaise Sauce for which the first references can be found already in 1593 and 1651 [11,12]. The cleaning properties of surfactants are also known for ages but the advent of nanotechnology has promoted them to the forefront during the two last decades. The understanding of the nature of micellar solutions has only started in the beginning of the 20th century. One of the precursors is McBain [13,14] who played a role in the study of surfactants, micellisation processes, their composition, charge and mobility.
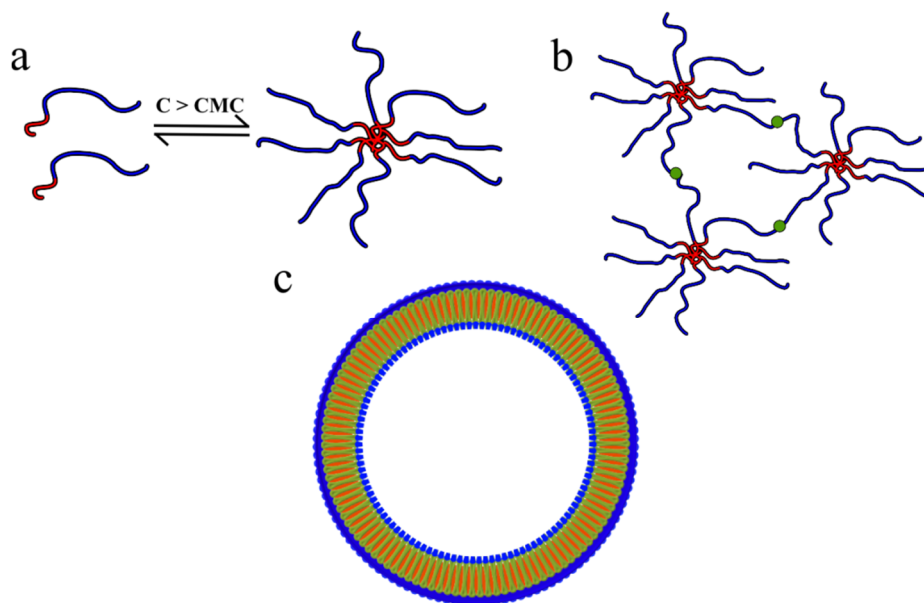
Figure 1 *a) micelle formation from block-copolymers b) micellar gel c) liposome*

When the surfactant concentration is higher than the critical micelle concentration (or CMC), the micellisation process takes place. In a polar solvent, the hydrophobic tails assemble to form the core and the hydrophilic tails form the corona toward the solvent. Nowadays micelles, liposomes and other soft matter material are extensively used in many fields [15] like thickening agents in water-based paints [16], cleaning agents in the restauration of art pieces [17] or to produce new mesoporous materials [18,19]. But the largest number of publications are devoted to possible nano-medicine applications. They are investigated to solubilize poorly soluble drugs in aqueous medium. [20-26]. The drug is encapsulated into the hydrophobic core of micelles which are designed to release it near the targeted sick tissues. The corona composition is designed to allow biocompatibility with plasma and to increase the selectivity while decreasing the drawback effects [27,28,20,29-34]. Such systems have complex structures in order to achieve their task e.g. access a tumor without being caught by the immune system [35-38,25,39-41,24,26].

Liposomes are spherical vesicles which have at least one lipid bilayer. They were discovered during the 1960's by Bangham et al [42]. When liposomes are made of several concentric lipid bilayers, they are called Multilamellar Large Vesicles (MLV). Their size may vary from 100 nm up to several micrometers. On the other side, the Small Unilamellar Vesicle (SUVs) are smaller than 100 nm.

Liposomes are used in a large variety of applications like drug delivering structure [43-45,38] and as models of biological membranes because of their similar composition but without organelles, which simplifies the data interpretation. [46].

In 2012, 53 systems based on liposomes were investigated as therapeutic treatment and 7 were already commercially available. Moreover, 8 systems based on micelles were investigated and 3 were commercially available [26]. Nowadays, the nano-objects are extensively studied but their size range and atomic content make it difficult to access their inner structure with the help of usual technique widely available like dynamic light scattering (DLS), atomic force microscopy or electron microscopy [28,35-37,39,47-49,25,50-52]. Nowadays the nano-object are expected to undergo structural changes under controlled stimuli i.e., modification of the temperature, pH change, or the presence of a triggering molecule. The stimuli-responsive behavior may allow the nano-object to target sick tissues. The structural change may result in the disruption of the objects, their aggregation or their reorganization. The study of the inner structure is challenging and the common techniques to study soft matter i.e. transmission microscopy or light scattering does not allow to isolate each component of the colloid. Small Angle Neutron Scattering is a helpful technique in this context because, coupled to a tailored modelling, it gives information on the organization of amphiphilic molecules inside the objects. Furthermore the measurements are performed in solution and dynamic processes can be studied over periods of several hours or days. The aim of this thesis is to study several stimuli-responsive colloids and the evolution of their internal structure when the intensity of the stimulus is tuned.

Context and aim

The synthesis of smart nanomaterials and their analysis with the help of SANS are tasks requiring distinctive but complementary skills. The birth of this project with the partnership of the Molecular Dynamics Laboratory and the Center for Education and Research on Macromolecules (CERM) was an excellent opportunity to study samples which have already potential use or which are good candidates in their area but lack some structural information.

This manuscript is divided into three parts. The first part (see Chapter 2) introduces SANS in order to (i) describe the general experimental and theoretical framework, (ii) enlighten the advantages of this technique in the study of soft matter samples and outline its peculiarities and (iii) introduce some models which are instrumental to our work.

In a second part (chapters 3 to 7) the experimental results are set out and discussed. In chapter 3, the effect of pH stimuli is assessed on polymeric micelles bearing polybase sequences. The studied objects are built from mixtures of two diblock copolymers, a polycaprolactone-*b*-poly(ethylene oxide) one and a polycaprolactone-*b*-poly(2-vinylpyridine) one. The hydrophobic core is built from polycaprolactone (PCL). The corona of hydrophilic poly(ethylene oxide) (PEO) stabilizes the nanocarriers. Thanks to a pH-sensitive sequence of poly(2-vinylpyridine) (P2VP), the micelles can adopt different structures in acidic and basic conditions. When the pH is acidic, the P2VP is protonated and the chains are repulsive. The diffusion of a hydrophobic drug would be facilitated in acidic conditions because the core is smaller than at basic pH when the P2VP collapses on the PCL core. SANS helped us to understand the behavior of the P2VP which is correlated with the micelle size evolution, a fact that DLS experiment could not explain.

In chapter 4, the stimuli are both the pH and the temperature. This section presents the investigation of micelles built from triblocks copolymers of polyacrylic acid (PAA), poly(N-isopropylacrylamide) (PNIPAM) and poly(ethylene oxide) in several conditions. At low pH, the PAA is protonated and expected to be hydrophobic, while at high pH, deprotonation leads to a hydrophilic polyelectrolyte. The PNIPAM is hydrophilic at temperatures below the transition temperature (32°C) and hydrophobic at higher temperature [53]. SANS measurements have been performed at pH equal to 2, 6 and 8 and at at 20, 30, 40 and 50°C. Dynamic light scattering and SANS revealed a bimodal distribution for micelles and aggregates. The presence of free chains at pH 6 and 8 that could not be detected by other common techniques is proved and quantitatively estimated by the analysis of the experimental data.

The three next chapters aim to study structural perturbation by addition of a triggering molecule.

The formation of metallo-supramolecular micellar gels is investigated by SANS in chapter 5. The micelles consist of polystyrene-*b*-poly(tert-butylacrylate), PS-*b*-PtBA-[, (-[represents terpyridine) block copolymers, dissolved in deuterared ethanol. The hydrophobic polystyrene core is stabilized by the poly(tert-butylacrylate) corona. The influence of the copolymer concentration on the micelle structure and on its space organization has been investigated, as well as the significant rheological impact of the subsequent addition of three metal ions (Fe(II), Ni(II) and Zn(II)) [54].

In chapters 6 and 7, the action of cyclodextrins (CDs) on liposomes (doped or not with cholesterol) is investigated. CDs are known to interact with the constituents of the membrane. The global size and the polydispersity of the liposomes, the thickness of both the hydrophilic and the hydrophobic parts of the membrane, and the coverage by the cyclodextrins of the liposome-water interface are inferred from the SANS data in the presence of an increasing concentration of CDs. The effect of CDs on the liposome structure was investigated at two temperatures bracketing the phospholipidic phase transition of the DMPC.

Finally, in a third part (Chapter 8) the general conclusions which summarize and encompass all our experimental and modelling results as well as possible perspectives for future work are presented.

References

1. Brown, R.: A brief account of microscopical observations made on the particles contained in the pollen of plants, and on the general existence of active molecules in organic bodies. 17 (1828).
2. Ieluzzi, G.: Ascanio Sobrero. Il contributo della Chimica per una strategia formativa e … **37**, 41-47 (2006).
3. Bary, P.-. Les origines de la chimie colloïdale : A. Baudrimont (1806-1880). In. L'Expansion scientifique française (Paris)
4. Guareschi, I.: Die Pseudosolutionen oder Scheinlösungen nach Francesco Selmi. Zeitschrift für Chemie und Industrie der Kolloide **8**, 113-123 (1911). doi:10.1007/BF01502930
5. Zsigmondy., R.: Colloids And The Ultramicroscope. 282 (1914).
6. Graham, T.: Liquid Diffusion Applied to Analysis. Philosophical Transactions of the Royal Society of London **151**, 183-224 (1861). doi:10.1098/rstl.1861.0011
7. Ostwald, W.: Ueber die Geschwindigkeitsfunktion der Viskosität disperser Systeme. I. Kolloid-Zeitschrift **36**, 99-117 (1925). doi:10.1007/BF01431449
8. Buzagh, A., Clayton, W., Darbishire, O.B.: Kolloidik. Colloid Systems. A Survey of the Phenomena of Modern Colloid Physics and Chemistry ... Translated by Otto B. Darbishire ... Edited by William Clayton, Etc. (1937).
9. Hauser, E.A.: The history of colloid science: In memory of Wolfgang Ostwald. Journal of Chemical Education **32**, 2 (1955). doi:10.1021/ed032p2
10. Deichmann, U.: "Molecular" versus "Colloidal": Controversies in Biology and Biochemistry, 1900–1940. Bulletin for the History of Chemistry **32**, 105-118 (2007).
11. Battus, C.: Eenen seer schoonen ende excellenten Cocboeck. (1593).
12. Varenne, F.d.L.: Le vrai cuisinier françois. 383 (1651).
13. Rideal, E.K.: Obituary Notices of Fellows of the Royal Society. The Royal Society **8**, 529-547 (1953).
14. McBain, J.W., Sierichs, W.C.: The solubility of sodium and potassium soaps and the phase diagrams of aqueous potassium soaps. Journal of the American Oil Chemists Society **25**, 221-225 (1948). doi:10.1007/BF02645899
15. Stuart, M.a.C., Huck, W.T.S., Genzer, J., Müller, M., Ober, C., Stamm, M., Sukhorukov, G.B., Szleifer, I., Tsukruk, V.V., Urban, M., Winnik, F., Zauscher, S., Luzinov, I., Minko, S.: Emerging applications of stimuli-responsive polymer materials. Nature materials **9**, 101-113 (2010). doi:10.1038/nmat2614
16. Maestro, A., González, C., Gutiérrez, J.M.: Interaction of surfactants with thickeners used in waterborne paints: a rheological study. Journal of colloid and interface science **288**, 597-605 (2005). doi:10.1016/j.jcis.2005.03.034
17. Grassi, S., Carretti, E., Pecorelli, P., Iacopini, F., Baglioni, P., Dei, L.: The conservation of the Vecchietta's wall paintings in the Old Sacristy of Santa Maria della Scala in Siena: The use of nanotechnological cleaning agents. Journal of Cultural Heritage **8**, 119-125 (2007). doi:10.1016/j.culher.2006.10.008
18. Caes, S., Malherbe, C., Krins, N., Arrebola, J.C., Henrist, C., Cloots, R., Vertruyen, B.: Lithium transition metal (Ti, Nb, V) oxide mesoporous thin films: Contrasting results when attempting direct synthesis by evaporation-induced self assembly. Microporous and Mesoporous Materials **172**, 87-94 (2013). doi:10.1016/j.micromeso.2013.01.015
19. Borlaf, M., Caes, S., Dewalque, J., Colomer, M.T., Moreno, R., Cloots, R., Boschini, F.: Effect of the RE (RE=Eu, Er) doping on the structural and textural properties of mesoporous TiO2 thin films obtained by evaporation induced self-assembly method. Thin Solid Films **558**, 140-148 (2014). doi:10.1016/j.tsf.2014.03.002
20. Danhier, F., Vroman, B., Lecouturier, N., Crokart, N., Pourcelle, V., Freichels, H., Jérôme, C., Marchand-Brynaert, J., Feron, O., Préat, V.: Targeting of tumor endothelium by RGD-grafted PLGA-nanoparticles loaded with paclitaxel. Journal of controlled release : official journal of the Controlled Release Society **140**, 166-173 (2009). doi:10.1016/j.jconrel.2009.08.011

21. Freichels, H., Alaimo, D., Auzély-Velty, R., Jérôme, C.: α-Acetal, ω-alkyne poly(ethylene oxide) as a versatile building block for the synthesis of glycoconjugated graft-copolymers suited for targeted drug delivery. Bioconjugate chemistry **23**, 1740-1752 (2012). doi:10.1021/bc200650n

22. Liu, J., Detrembleur, C., De Pauw-Gillet, M.-C., Mornet, S., Elst, L.V., Laurent, S., Jérôme, C., Duguet, E.: Heat-triggered drug release systems based on mesoporous silica nanoparticles filled with a maghemite core and phase-change molecules as gatekeepers. Journal of Materials Chemistry B **2**, 59 (2014). doi:10.1039/c3tb21229g

23. Liu, J., Detrembleur, C., Debuigne, A., De Pauw-Gillet, M.-C., Mornet, S., Vander Elst, L., Laurent, S., Duguet, E., Jérôme, C.: Glucose-, pH- and thermo-responsive nanogels crosslinked by functional superparamagnetic maghemite nanoparticles as innovative drug delivery systems. Journal of Materials Chemistry B **2**, 1009 (2014). doi:10.1039/c3tb21272f

24. Schleich, N., Sibret, P., Danhier, P., Ucakar, B., Laurent, S., Muller, R.N., Jérôme, C., Gallez, B., Préat, V., Danhier, F.: Dual anticancer drug/superparamagnetic iron oxide-loaded PLGA-based nanoparticles for cancer therapy and magnetic resonance imaging. International journal of pharmaceutics **447**, 94-101 (2013). doi:10.1016/j.ijpharm.2013.02.042

25. Gong, J., Chen, M., Zheng, Y., Wang, S., Wang, Y.: Polymeric micelles drug delivery system in oncology. Journal of controlled release : official journal of the Controlled Release Society **159**, 312-323 (2012). doi:10.1016/j.jconrel.2011.12.012

26. Etheridge, M.L., Campbell, S.a., Erdman, A.G., Haynes, C.L., Wolf, S.M., McCullough, J.: The big picture on nanomedicine: the state of investigational and approved nanomedicine products. Nanomedicine : nanotechnology, biology, and medicine **9**, 1-14 (2013). doi:10.1016/j.nano.2012.05.013

27. Cajot, S.: Tailor-made degradable copolymers for the design of advanced drug delivery systems. (2012).

28. Cajot, S., Van Butsele, K., Paillard, a., Passirani, C., Garcion, E., Benoit, J.P., Varshney, S.K., Jérôme, C.: Smart nanocarriers for pH-triggered targeting and release of hydrophobic drugs. Acta biomaterialia **8**, 4215-4223 (2012). doi:10.1016/j.actbio.2012.08.049

29. Kwon, G.S., Okano, T.: Polymeric micelles as new drug carriers. Advanced Drug Delivery Reviews **21**, 107-116 (1996). doi:http://dx.doi.org/10.1016/S0169-409X(96)00401-2

30. Lavasanifar, A., Samuel, J., Kwon, G.S.: Poly(ethylene oxide)-block-poly(L-amino acid) micelles for drug delivery. Advanced drug delivery reviews **54**, 169-190 (2002).

31. Hamaguchi, T., Matsumura, Y., Suzuki, M., Shimizu, K., Goda, R., Nakamura, I., Nakatomi, I., Yokoyama, M., Kataoka, K., Kakizoe, T.: NK105, a paclitaxel-incorporating micellar nanoparticle formulation, can extend in vivo antitumour activity and reduce the neurotoxicity of paclitaxel. British journal of cancer **92**, 1240-1246 (2005). doi:10.1038/sj.bjc.6602479

32. Kim, D.-W., Kim, S.-Y., Kim, H.-K., Kim, S.-W., Shin, S.W., Kim, J.S., Park, K., Lee, M.Y., Heo, D.S.: Multicenter phase II trial of Genexol-PM, a novel Cremophor-free, polymeric micelle formulation of paclitaxel, with cisplatin in patients with advanced non-small-cell lung cancer. Annals of oncology : official journal of the European Society for Medical Oncology / ESMO **18**, 2009-2014 (2007). doi:10.1093/annonc/mdm374

33. Matsumura, Y., Hamaguchi, T., Ura, T., Muro, K., Yamada, Y., Shimada, Y., Shirao, K., Okusaka, T., Ueno, H., Ikeda, M., Watanabe, N.: Phase I clinical trial and pharmacokinetic evaluation of NK911, a micelle-encapsulated doxorubicin. British journal of cancer **91**, 1775-1781 (2004). doi:10.1038/sj.bjc.6602204

34. Saif, M.W., Podoltsev, N.a., Rubin, M.S., Figueroa, J.a., Lee, M.Y., Kwon, J., Rowen, E., Yu, J., Kerr, R.O.: Phase II clinical trial of paclitaxel loaded polymeric micelle in patients with advanced pancreatic cancer. Cancer investigation **28**, 186-194 (2010). doi:10.3109/07357900903179591

35. Van Butsele, K., Cajot, S., Van Vlierberghe, S., Dubruel, P., Passirani, C., Benoit, J.-P., Jérôme, R., Jérôme, C.: pH-Responsive Flower-Type Micelles Formed by a Biotinylated Poly(2-vinylpyridine)- block -poly(ethylene oxide)- block -poly(ε - caprolactone) Triblock Copolymer. Advanced Functional Materials **19**, 1416-1425 (2009). doi:10.1002/adfm.200801117
36. Cajot, S., Riva, R., Billiet, L., Du Prez, F., Alexandre, M., Lecomte, P., Jérôme, C.: Novel Amphiphilic Mikto-Arm Star-Shaped Copolymers for the Preparation of PLA-Based Nanocarriers. Macromolecular Symposia **309-310**, 111-122 (2011). doi:10.1002/masy.201100044
37. Cajot, S., Lautram, N., Passirani, C., Jérôme, C.: Design of reversibly core cross-linked micelles sensitive to reductive environment. Journal of controlled release : official journal of the Controlled Release Society **152**, 30-36 (2011). doi:10.1016/j.jconrel.2011.03.026
38. Ganta, S., Devalapally, H., Shahiwala, A., Amiji, M.: A review of stimuli-responsive nanocarriers for drug and gene delivery. Journal of controlled release : official journal of the Controlled Release Society **126**, 187-204 (2008). doi:10.1016/j.jconrel.2007.12.017
39. Rapoport, N.: Physical stimuli-responsive polymeric micelles for anti-cancer drug delivery. Progress in Polymer Science **32**, 962-990 (2007). doi:10.1016/j.progpolymsci.2007.05.009
40. Gravel, E., Ogier, J., Arnauld, T., Mackiewicz, N., Ducongé, F., Doris, E.: Drug delivery and imaging with polydiacetylene micelles. Chemistry (Weinheim an der Bergstrasse, Germany) **18**, 400-408 (2012). doi:10.1002/chem.201102769
41. Gohy, J.-f., Willet, N., Varshney, S.K., Zhang, J.-x., Jérôme, R.: pH Dependence of the morphology of aqueous micelles poly (ethylene oxide) copolymers. e-Polymers(035), 1-10 (2002).
42. Bangham, A.D., Horne, R.W.: Negative staining of phospholipids and their structural modification by surface-active agents as observed in the electron microscope. Journal of Molecular Biology **8**, 660-IN610 (1964). doi:10.1016/S0022-2836(64)80115-7
43. Joset, A., Grammenos, A., Hoebeke, M., Leyh, B.: Investigation of the interaction between a β-cyclodextrin and DMPC liposomes: a small angle neutron scattering study. Journal of Inclusion Phenomena and Macrocyclic Chemistry **83**(3), 227-238 (2015). doi:10.1007/s10847-015-0558-z
44. Gharib, R., Greige-Gerges, H., Fourmentin, S., Charcosset, C., Auezova, L.: Liposomes incorporating cyclodextrin-drug inclusion complexes: current state of knowledge. Carbohydrate Polymers **129**, 175-186 (2015). doi:10.1016/j.carbpol.2015.04.048
45. Belička, M., Devínsky, F., Balgavý, P.: Neutrons in studies of phospholipid bilayers and bilayer–drug interaction. II. Small-angle scattering. Acta Facultatis Pharmaceuticae Universitatis Comenianae **61**, 12-20 (2014). doi:10.2478/afpuc-2014-0011
46. Oberholzer, T., Luisi, P.L.: The Use of Liposomes for Constructing Cell Models. Journal of Biological Physics **28**, 733-744 (2002). doi:10.1023/A:1021267512805
47. Hoo, C.M., Starostin, N., West, P., Mecartney, M.L.: A comparison of atomic force microscopy (AFM) and dynamic light scattering (DLS) methods to characterize nanoparticle size distributions. Journal of Nanoparticle Research **10**, 89-96 (2008). doi:10.1007/s11051-008-9435-7
48. Mata, J.P., Majhi, P.R., Kubota, O., Khanal, a., Nakashima, K., Bahadur, P.: Effect of phenol on the aggregation characteristics of an ethylene oxide-propylene oxide triblock copolymer P65 in aqueous solution. Journal of colloid and interface science **320**, 275-282 (2008). doi:10.1016/j.jcis.2007.12.033
49. Jensen, G.V., Shi, Q., Hernansanz, M.J., Oliveira, C.L.P., Deen, G.R., Almdal, K., Pedersen, J.S.: Structure of PEP–PEO block copolymer micelles: exploiting the complementarity of small-angle X-ray scattering and static light scattering. Journal of Applied Crystallography **44**, 473-482 (2011). doi:10.1107/S0021889811013343

50. Patterson, J.P., Kelley, E.G., Murphy, R.P., Moughton, A.O., Robin, M., Lu, A., Colombani, O., Chassenieux, C., Cheung, D., Sullivan, M.O., Epps, T.H., O'Reilly, R.K.: Structural characterization of amphiphilic homopolymer micelles using light scattering, SANS, and cryo-TEM. Macromolecules **46**, 6319-6325 (2013). doi:10.1021/ma4007544
51. Yu, Y., Wu, G., Liu, K., Zhang, X.: Force Required to Disassemble Block Copolymer Micelles in Water. Langmuir **26**, 9183-9186 (2010). doi:10.1021/la101235e
52. Duwez, A.S., Willet, N.: Molecular Manipulation with Atomic Force Microscopy. 287 (2011).
53. Hsu, S.-h., Yu, T.-L.: Dynamic viscoelasticity study of the phase transition of poly(N-isopropylacrylamide). Macromolecular Rapid Communications **21**, 476-480 (2000). doi:10.1002/(SICI)1521-3927(20000501)21:8<476::AID-MARC476>3.0.CO;2-O
54. Mugemana, C., Joset, A., Guillet, P., Appavou, M.-S., De Souza, N., Fustin, C.-A., Leyh, B., Gohy, J.-F.: Structure of Metallo-Supramolecular Micellar Gels. Macromolecular Chemistry and Physics **214**, 1699-1709 (2013). doi:10.1002/macp.201300288

12

CHAPTER II

Small-angle neutron scattering

The aim of this chapter is to introduce the small angle scattering (SAS) techniques, their advantages and limitations. The first section describes briefly some useful neutrons properties. The second section explains the reasons for choosing SANS to analyze our samples. The principles of SANS theory are presented in Sections 3 to 6. The production of neutrons and concerns about the experimental resolution are presented in Section 7. Sections 8 and 9 deal with examples of soft matter samples analyzed by SANS. Molecular Dynamics Simulations, a complementary theoretical method, is briefly discussed in Section 10.

1   Introduction to neutron properties

Neutrons show useful and amazing properties. This section will illustrate several of them. In order to simplify the account of these properties and the benefits of neutrons, a radiography experiment of an old camera is discussed. Figure 1 shows two radiographies of a usual camera. Figure 1a is a neutron radiography and Figure 1b shows an X-ray radiography. The camera is not digital as the photographic films holder is visible. The camera absorbing a few neutrons, the first image appears to be transparent: the inner parts are visible. The lenses, mirrors and film holder absorb more neutrons and the internal mechanism is clearly visible. At the time, camera housings were typically made of light metal (e.g. magnesium alloy) or thermosets. This part appears almost transparent on the X-ray radiography because the X-rays are weakly absorbed by light atoms which substantiates the hypothesis of a plastic housing frame. Furthermore the inner parts made of metal absorb the X-rays and appears black. The contrasts are strong and the inner structure of the camera is not as well defined on the X-ray radiography as on the neutron radiography and some parts are only visible with the help of neutrons.
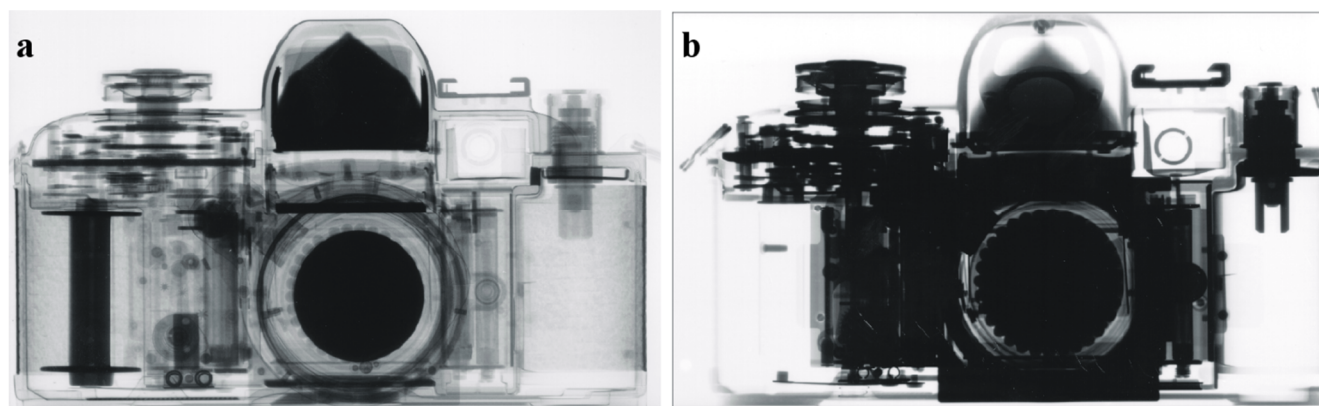
Figure 1 *Radiography of a camera. a) neutron b) X-rays. [1]*

The study of micelles with the help of neutron scattering is motivated by the above-explained advantages. While dynamic and static light scattering give information on the size of objects, both small angle scattering (using neutrons or X-rays) techniques allows determining the internal structure of self-assembled polymeric materials in solution, like the radiographies shown in Figure 1.

2   *Why using small angle scattering?*

Most micellar sample characterizations are performed using dynamic light scattering (DLS), static light scattering (SLS) and transmission electron microscopy (TEM). These techniques have their well-known advantages but they give only limited information about the inner structure of samples. Light scattering, for example, gives access to the size distribution and hydrodynamic radius but all the information on the size and composition of the core and corona is lost. Electronic microscopic pictures provide average radius of the core R_c and size distribution. Unfortunately, most block copolymers only contain light atoms like carbon and oxygen which give poor contrast with the background. Sometimes, information can however be obtained on the core or corona by using a contrast agent [2]. Moreover the measurements have to be made in dry conditions, leading to potential artefacts [3]. Contrarily, small angle neutron scattering (SANS) and X-ray small angle scattering (SAXS) do not suffer from this drawback because they can be directly performed on micellar solutions.

Small-angle scattering of neutrons (SANS) or X-rays (SAXS) techniques were originally developed by Guinier [4,5]. Both techniques are contemporary. The sources differ: a synchrotron or an X-Ray laboratory source for the SAXS and a nuclear reactor for SANS but these two techniques are based on common principles. In 1955 Guinier & Fournet [4] published "Small-Angle scattering of X-rays" to summarize the state of the art in the SAS field at the time. Since the first scattering experiments in the 1930's, numerous applications were found already in the 1950's in fields like chemistry, biology, and metallurgy.

In the following sections 3 to 6, we aim to give the necessary information to understand the main principles of SAS (Section 3 and 4) and the features of SAS study of soft matter samples (Section 5 and 6).

3   Scattering of X-rays or neutrons by a target

A neutron beam is focused on the sample and part of it is scattered by its atoms. The velocity of the neutrons and therefore the wavelength of the beam must be well-defined (see Section 7). The scattered neutrons undergo a change of direction which is characterized by the diffusion vector $\vec{q}$, which is also called scattering vector.

3.1   Incoming and outgoing wave functions

We shall focus here on elastic scattering and consider how the scattered wave can be written as a function of the scattering vector.
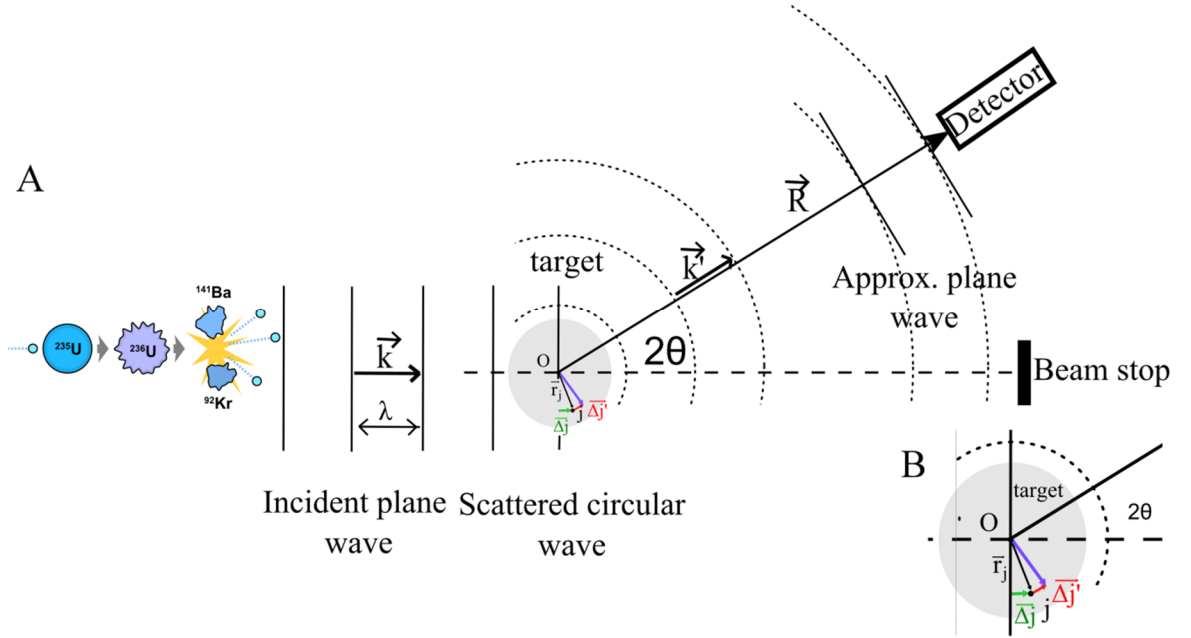
Figure 2 *A : Neutron scattering by an isotropic sample. The production of neutrons is described in section 7. B: enlargment of the neutron path difference between the scatterer at the origin of the target O and the scatterer j.*

The incoming plane wave of wavelength λ can be written as

$$\psi_{in}(\vec{r},t) = B\exp\left[i\left(\vec{k}\bullet\vec{r} - \omega t\right)\right] \tag{1}$$

where $\vec{k}$ is the wave vector whose modulus is equal to k = 2π/λ, B is a normalization factor and ω is the angular frequency. Some dephasing will appear between the waves

17

scattered by the various scatterers of the target. Let's consider two of them: one at the origin and one at the position $\vec{r}_j$. The wave scattered by j will be dephased with respect to that scattered by 0 by a quantity equal to the product of the wave vector and of the optical path difference.

$$\Delta\varphi = k\Delta_j - k'\Delta_{j'} = \vec{k}\bullet\vec{r}_j - \vec{k}'\vec{r}_j = -\left(\vec{k}'-\vec{k}\right)\bullet\vec{r}_j = -\vec{q}\bullet\vec{r}_j \tag{2}$$

where the scattering vector $\vec{q} = \vec{k}' - \vec{k}$ has been defined.
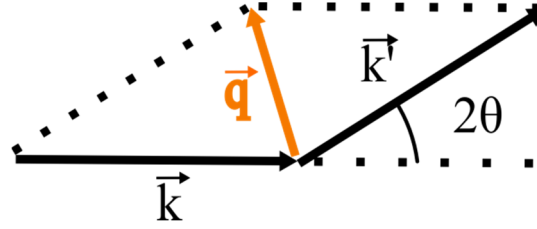
Figure 3 *Definition of the scattering vector* $\vec{q}$.

The modulus of $\vec{q}$ is given by the following formula:

$$|\vec{q}| = \frac{4\pi}{\lambda}\sin(\theta) \tag{3}$$

For N scatterers, the outgoing wave is therefore equal to

$$\psi_{out}(\vec{r},t) = B\sum_{j=1}^{N}b_j\exp\left(-i\vec{q}\bullet\vec{r}_j\right)\frac{\exp\left[-i\left(\vec{k}'\bullet\vec{r}-\omega t\right)\right]}{r} \tag{4}$$

if the sample-detector distance is much larger than the sample size. As the scatterers act as a source of scattered spherical waves, the last factor is divided by r. We can re-write (4) as

$$\psi_{out}(\vec{r},t) = B\,A(\vec{q})\frac{\exp\left[-i\left(\vec{k}'\bullet\vec{r}-\omega t\right)\right]}{r} \tag{5}$$

with the *scattering amplitude* defined as $A(\vec{q})$:

$$A(\vec{q}) = \sum_{j=1}^{N}b_j\exp\left(-i\vec{q}\bullet\vec{r}_j\right) \tag{6}$$

The coefficient b_j accounts for the particle-scatterer interactions and is called the **scattering length** because it has the dimension of a length. It can be shown that, within the so-called Born Approximation valid for weak target-particle interactions, b_j is given by the following equation

$$b_j = -\frac{m}{2\pi\hbar^2} \int_{space} V_j(\vec{r}) \exp(i\vec{q}\cdot\vec{r})d\vec{r} \qquad (7)$$

b_j is therefore proportional to the Fourier transform of the particle-scatterer interaction potential $V_j(\vec{r})$. For neutrons, the potential is short-range with respect to the usual q^{-1} domain ($\sim 1\text{Å}^{-1}$) so that $exp(-i\vec{q}\cdot\vec{r}) \simeq 1$ and

$$b_j = -\frac{m}{2\pi\hbar^2} \int_{space} V_j(\vec{r})d\vec{r} \qquad (8)$$

which does not depend on $\vec{q}$. b_j varies relatively randomly through the periodic table as displayed in Figure 4. For X-rays, the range of the electromagnetic interaction is close to q^{-1} so that b_j depends on $\vec{q}$. The Cromer-Mann formula reproduces empirically this dependency. In SAXS, for $q < 0.5\text{Å}^{-1}$, however, b_j can be considered as constant. It is given by the following formula at high X-ray energy:

$$b_j = \frac{e^2}{4\pi\varepsilon_0 m_e c^2} Z_j \qquad (9)$$

where Z_j is the atomic number of atom j and m_e is electron mass at rest. For X-rays, b_j increases therefore linearly with the atomic number.
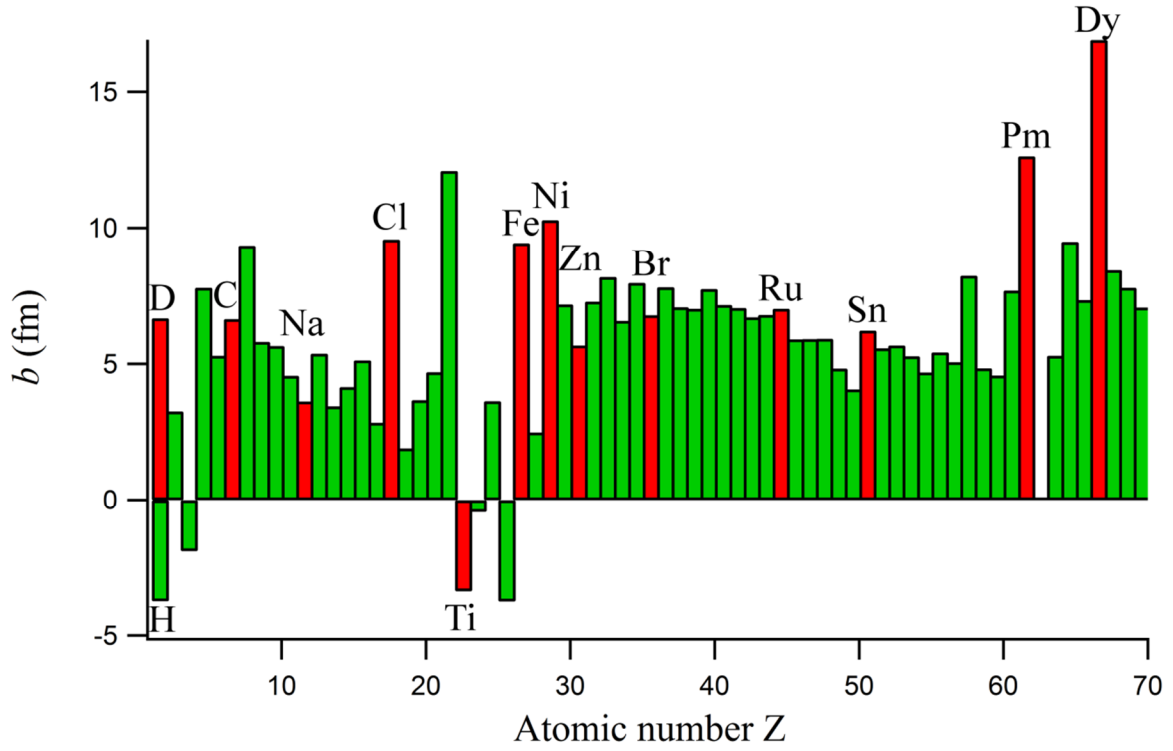
Figure 4 *Scattering lengths b of neutrons with respect to the atomic number Z. b varies relatively randomly through the periodic table.[6]*

3.2 Differential scattering cross section

If N is the *number of neutrons scattered per unit time into the solid angle dΩ around direction* $\vec{q}$, the differential scattering cross section (dσ(q)/dΩ) is defined as [7]

$$\frac{d\sigma}{d\Omega}(\vec{q}) = \frac{N}{d\Omega \times \text{density of flux of incoming neutrons}} \qquad (10)$$

where the density of flux is the number of incident neutrons per unit area per second. The measured intensity during SANS experiments is thus related to the cross section of the sample (see Section 7).
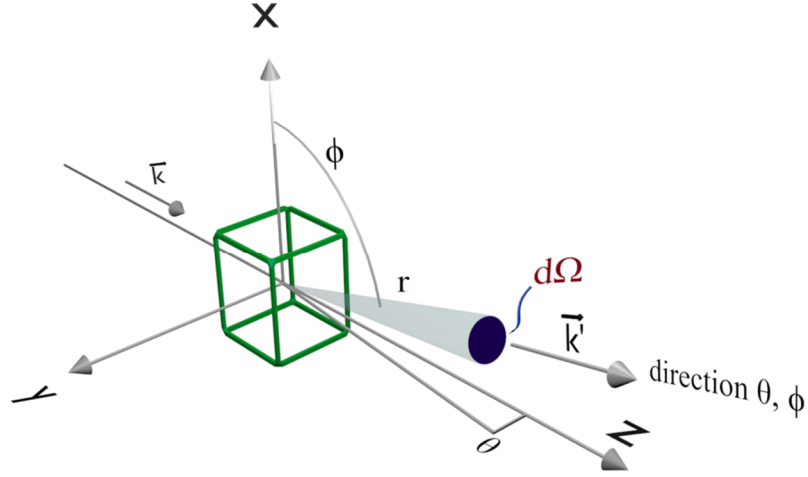
Figure 5 *Scattering geometry for an incident neutron beam* $(\vec{k})$ *scattered by a target (green cube).*

If we denote the incoming and outgoing densities of flux as J_{in} and J_{out}, we have

$$\frac{d\sigma}{d\Omega}(\vec{q}) = \frac{J_{out}(\vec{q})r^2 d\Omega}{J_{in}d\Omega} = \frac{J_{out}(\vec{q})r^2}{J_{in}} \tag{11}$$

In quantum mechanics, the density of flux is given by

$$\vec{J} = \frac{i\hbar}{2m}\left(\psi_i \vec{\nabla}\psi_i^* - \psi_i^* \vec{\nabla}\psi_i\right) \tag{12}$$

where $\vec{\nabla}$ is the gradient operator. Inserting (1) and (5) into (12) leads to

$$\vec{J}_{in} = B^2 \frac{\hbar\vec{k}}{m} \tag{13}$$

and

$$\vec{J}_{out} = B^2 \frac{\hbar\vec{k}\,'}{\hat{u}} \frac{\left|A(\vec{q})\right|^2}{r^2} \tag{14}$$

Inserting now (13) and (14) into (11), noting also that $\left|\vec{k}\right| = \left|\vec{k}\,'\right|$ for elastic scattering, we can write that

21

$$\frac{d\sigma}{d\Omega}(\vec{q}) = |A(\vec{q})|^2 = \sum_{j=1}^{N}\sum_{l=1}^{N} b_j b_l \exp\left[-i\,\vec{q}\bullet\left(\vec{r}_l - \vec{r}_j\right)\right] \tag{15}$$

This relationship is valid for both neutrons and X-Rays scattering. For neutron scattering an additional subtlety arises due to the fact that isotopes of the same element usually have quite different scattering lengths and that the different isotopes are distributed randomly in the sample. In addition, the neutron possesses a spin (*I=1/2*) which can interact with magnetic nuclei (that is, those that also have a non-zero spin). The resulting coupling can lead to different value of the total angular momentum, each situation being characterized by a different value of the associated scattering length. As a result, an ensemble average has to be performed so that (15) now becomes:

$$\frac{d\sigma}{d\Omega}(\vec{q}) = \sum_{j=1}^{N}\sum_{l=1}^{N} \langle b_j b_l \rangle \exp\left[-i\,\vec{q}\bullet\left(\vec{r}_l - \vec{r}_j\right)\right] \tag{16}$$

Separating the diagonal and the non-diagonal contributions

$$\frac{d\sigma}{d\Omega}(\vec{q}) = \sum_{j=1}^{N} \langle b_j^2 \rangle + \sum_{j=1}^{N}\sum_{l\neq j}^{N} \langle b_j b_l \rangle \exp\left[-i\,\vec{q}\bullet\left(\vec{r}_l - \vec{r}_j\right)\right] \tag{17}$$

If we consider that all nuclei of the sample correspond to the same element (but with a distribution of isotopes), we can write

- $\langle b_j^2 \rangle = \langle b^2 \rangle$ when l=j

- $\langle b_j b_l \rangle = \langle b \rangle\langle b \rangle = \langle b \rangle^2$ when $l \neq j$ because the isotopes are randomly distributed.

As the variance $(\Delta b)^2$ is equal to $(\Delta b)^2 = \langle b^2 \rangle - \langle b \rangle^2$, we can also write that $\langle b^2 \rangle = \langle b \rangle^2 + (\Delta b)^2$. So that (17) becomes

$$\frac{d\sigma}{d\Omega}(\vec{q}) = \langle b \rangle^2 \sum_{j}^{N}\sum_{l}^{N} \exp\left[-i\,\vec{q}\bullet\left(\vec{r}_l - \vec{r}_j\right)\right] + N(\Delta b)^2 \tag{18}$$

The cross section is now the sum of two terms called, respectively, the coherent $(d\sigma(\vec{q})/d\Omega)_{coh}$ and the incoherent $(d\sigma(\vec{q})/d\Omega)_{inc}$ cross sections.

$$\left(\frac{d\sigma}{d\Omega}\right)_{coh}(\vec{q}) = \langle b \rangle^2 \sum_{j}^{N}\sum_{l}^{N}\exp\left[-i\,\vec{q}\bullet\left(\vec{r_l}-\vec{r_j}\right)\right] \tag{19}$$

- This contribution depends on the spatial organization of the scatterers within the sample and, as a consequence, it is a function of $\vec{q}$. From this $\vec{q}$ variation, information can be inferred about the sample structure.

$$\left(\frac{d\sigma}{d\Omega}\right)_{inc}(\vec{q}) = N\left(\Delta b\right)^2 \tag{20}$$

- This contribution represents a constant background which provides no structural information. Incoherent scattering can represent a problem for polymer samples and for aqueous polymeric solutions because these samples contain a large fraction of H-scatterers, for which

$$\langle b_h \rangle = -3.74\,fm$$
$$\langle \Delta b_h \rangle = 25.27\,fm$$

As a consequence, coherent scattering by H nuclei represents only a small contribution on a large incoherent background. For ^{2}H (D) nuclei, however, the coherent contribution is larger than the incoherent one:

$$\langle b_d \rangle = 6.674\,fm$$
$$\langle \Delta b_d \rangle = 4.041\,fm$$

This is the reason why most of our experiments were performed in D$_2$O solutions.

In the following, we shall focus on the coherent scattering contribution. The incoherent background will always be subtracted during the experimental data handling procedure. For modelling purposes, we shall use, according to eq(19), the average $\langle b \rangle$ for each kind of nuclei of our polymer samples. In practice, only H, C, N and O need to be considered.

4   Small Angle Neutron Scattering (SANS)

Most of what will be presented in this section is valid for both X-Rays and Neutrons and for various kinds of samples. However, as we shall be interested mostly in polymer samples investigated by neutron scattering, we shall focus on self-assembled polymeric nano-objects like micelles or liposomes and neutron scattering.

Micelles of amphiphilic copolymers have usually a size of a few tens of nanometers. As a rule, they adopt a spherical shape so that we consider first the scattering cross section by a homogenous sphere. According to equations (15) or (19), and adopting the approximation of continuum, we can write that

$$\left(\frac{d\sigma}{d\Omega}\right)_{coh}(\vec{q}) = b^2 \left| \int\limits_{space} \rho(\vec{r}) \exp[-i\,\vec{q}\bullet\vec{r}]d\vec{r} \right|^2 \tag{21}$$

where

- $\langle b \rangle$ has been simply denoted as b.

- $\rho(\vec{r})$ is the constant particle density: $\rho(\vec{r}) = \dfrac{N}{\frac{4}{3}\pi R^3}$ where R is the radius of the

  sphere. It can be easily shown that

$$\left(\frac{d\sigma}{d\Omega}\right)_{coh}(q) = \frac{9N^2b^2}{(qR)^6}\left[\sin(qr) - qR\cos(qR)\right]^2 \tag{22}$$

Because of the isotropic nature of the problem, the cross section depends only on the modulus of the scattering vector.

This relationship is graphically displayed in Figure 6 which shows that that the cross section reaches the zero line for qR ~ 4.5 and remains small afterwards (although it continues to oscillate). The q-domain where relevant information can be obtained is thus defined by $q \times$ typical size ≈ 1. For polymer micelles, the typical size is located between:

- the monomer lengths:~3Å
- the global micellar radius:~a few hundred Å

so that the useful q-range is

$$10^{-3}\,\text{Å}^{-1}\langle q\langle 0.3\text{Å}^{-1} \tag{23}$$

For thermal neutrons, λ is in the Å range, i.e. 5Å. Converting the q range in a 2θ range using (3) leads to:

$$0.04°\langle 2\theta\langle 14° \tag{24}$$

This means that, only the small angle neutron scattering angle range needs to be sampled, hence the denomination "Small Angle Neutron Scattering" (SANS). The same is of course also valid for X-Rays (SAXS).
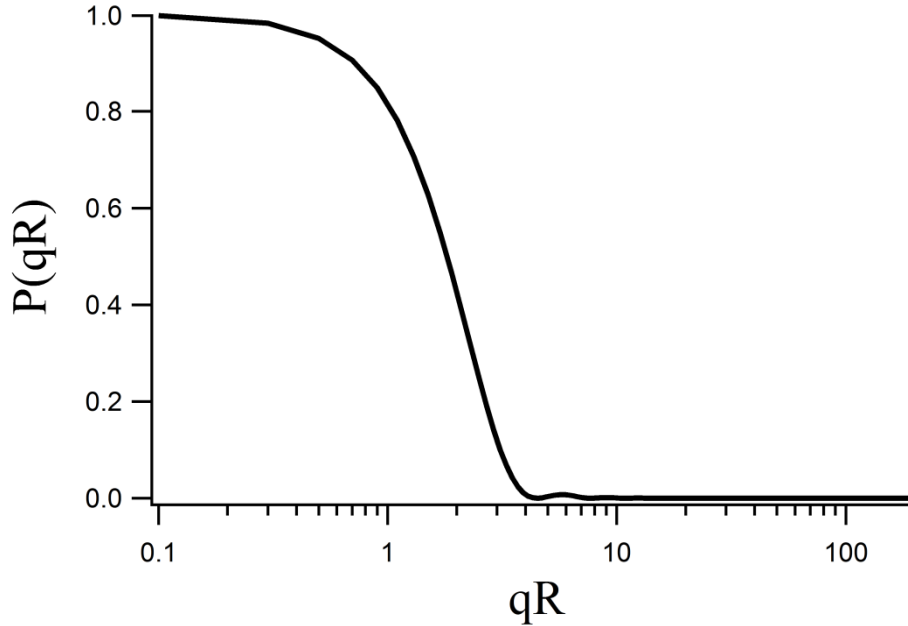
Figure 6 *Form factor of a sphere (Eq (22)) The cross section reaches the zero line for qR ~ 4.5 and remains small afterwards.*

5   *Form and Structure factors for micellar and liposomes solutions*

We shall focus here on what represents the nucleus of our research that is the investigation of aqueous solutions of self-organized copolymer micelles or phospholipid liposomes. We consider only the coherent scattering contribution. In this section we limit ourselves to monodisperse nanosized objects. The problems linked with the influence of polydispersity will be dealt with in the next section. The problem at hand is sketched in the figure below.
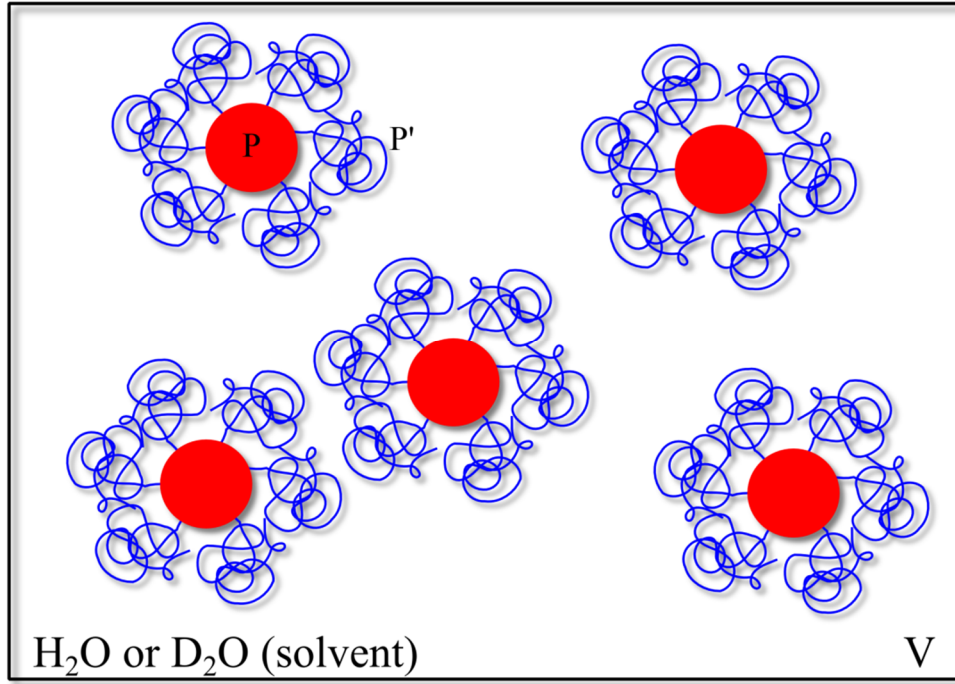
***Figure 7** Micellar solution. The micelles are built from a polymer block forming the core P (red), a polymer block forming the corona P' (blue) and solvent molecules S (not displayed).*

We are confronted to a multicomponent system:

- the polymer blocks forming the core (P)
- the polymer block forming the corona (P')
- the solvent molecules (S)

Because of the large density of particles in a liquid, we shall adopt a continuum formulation of eq(19). To simplify the notations, we replace $\langle b \rangle$ by b. We shall also use the so-called "macroscopic cross section" obtained by dividing the cross section by the sample volume, and denoted as $\frac{d\Sigma}{d\Omega}$ $d\Sigma/d\Omega$. Equation(19) becomes then, for a one-component system,

$$\frac{d\Sigma}{d\Omega} = \frac{b^2}{V} \left\langle \int_V \int_V \exp\left[-i\vec{q}\bullet(\vec{r}-\vec{r}')\right] \rho(\vec{r}) \rho(\vec{r}') d\vec{r}\, d\vec{r}' \right\rangle \tag{25}$$

where V is the volume of the entire sample. $\rho(\vec{r})$ is, as before (equation(21)) the particle (scatterer) density. Because of the fluctuating nature of polymer samples (and in general of

26

soft matter samples) and of liquid solvents, an ensemble average has to be performed, which is denoted by the $\langle \ \rangle$ brackets.

5.1 Scattering by one-component (quasi) continuous sample

Because of the already mentioned fluctuating nature of the systems considered in this work, when we focus on the situation at a given position $\vec{r}$, we observe density fluctuations, $\Delta\rho(\vec{r})$, so that we can write, in general,

$$\rho(\vec{r}) = \bar{\rho} + \Delta\rho(\vec{r}) \tag{26}$$

where $\bar{\rho}$ is the average density around which fluctuations take place. Eq (25) becomes now

$$\frac{d\Sigma}{d\Omega}(\vec{q}) = \frac{b^2}{V}\left\langle \int_V \int_V \exp\left[-i\,\vec{q}\bullet(\vec{r}-\vec{r}\,')\right]\left[\bar{\rho}+\Delta\rho(\vec{r})\right]\left[\bar{\rho}+\Delta\rho(\vec{r}\,')\right]d\vec{r}\,d\vec{r}\,'\right\rangle \tag{27}$$

Expanding the expression between brackets gives

$$\langle \ \rangle = \bar{\rho}^2 \int_V \exp\left[-i\,\vec{q}\bullet\vec{r}\right]d\vec{r} \int_V \exp\left[i\,\vec{q}\bullet\vec{r}\,'\right]d\vec{r}\,'$$

$$+ \bar{\rho}\int_V \exp\left[-i\,\vec{q}\bullet\vec{r}\right]d\vec{r}\left\langle \int_V \exp\left[i\,\vec{q}\bullet\vec{r}\,'\right]\Delta\rho(\vec{r}\,')d\vec{r}\,'\right\rangle + \bar{\rho}\left\langle \int_V \exp\left[-i\,\vec{q}\bullet\vec{r}\right]\Delta\rho(\vec{r})d\vec{r}\right\rangle\int_V \exp\left[i\,\vec{q}\bullet\vec{r}\,'\right]d\vec{r}$$

$$+\left\langle \int_V \exp\left[-i\,\vec{q}\bullet\vec{r}\right]\Delta\rho(\vec{r})d\vec{r}\int_V \exp\left[i\,\vec{q}\bullet\vec{r}\,'\right]\Delta\rho(\vec{r}\,')d\vec{r}\,'\right\rangle \tag{28}$$

An alternativeway of writing (28) is:

$$\langle \ \rangle = \overline{\rho^2} \int_V \exp\left[-i\,\vec{q}\bullet\vec{r}\right]d\vec{r} \int_V \exp\left[i\,\vec{q}\bullet\vec{r}\,'\right]d\vec{r}\,'$$

$$+ \bar{\rho}\int_V \exp\left[-i\,\vec{q}\bullet\vec{r}\right]d\vec{r} \int_V \exp\left[i\,\vec{q}\bullet\vec{r}\,'\right]\left\langle\Delta\rho(\vec{r}\,')\right\rangle d\vec{r}\,' + \bar{\rho}\int_V \exp\left[i\,\vec{q}\bullet\vec{r}\,'\right]\int_V \exp\left[-i\,\vec{q}\bullet\vec{r}\right]\left\langle\Delta\rho(\vec{r})\right\rangle d\vec{r}$$

$$+ \int_V \int_V \exp\left[-i\,\vec{q}\bullet(\vec{r}-\vec{r}\,')\right]\left\langle\Delta\rho(\vec{r})\Delta\rho(\vec{r}\,')\right\rangle d\vec{r}\,d\vec{r}\,'$$

$$\tag{28 bis}$$

The average of the fluctuations of the number of scatterers in volume V, ΔN, is equal to

$$\langle \Delta N \rangle = \langle N - \langle N \rangle \rangle = \left\langle \int_V \rho(\vec{r}) d\vec{r} - \bar{\rho} \int_V d\vec{r} \right\rangle$$

$$= \int_V \langle \Delta \rho(\vec{r}) \rangle d\vec{r}$$

It is clear that $\langle \Delta N \rangle = \langle N - \langle N \rangle \rangle = \langle N \rangle - \langle N \rangle = 0$. Taking into account that

$$\int_V \exp\left[-i\,\vec{q}\bullet\vec{r}\right] d\vec{r} = (2\pi)^3 \,\delta(\vec{q})$$

$$\delta(\vec{q}) = \delta(-\vec{q})$$

where δ is the Dirac distribution. Denoting $n(\vec{q})$ the Fourier transform of $\Delta\rho(\vec{r})$:

$$n(\vec{q}) = \int_V \exp\left[-i\,\vec{q}\bullet\vec{r}\right] \rho(\vec{r}) d\vec{r}$$

we can write (28) and (28 bis) as:

$$\langle \; \rangle = \overline{\rho^2}(2\pi)^6 \,\delta(\vec{q})\delta(-\vec{q}) + \langle n(\vec{q})n(-\vec{q}) \rangle \tag{29}$$

This is the sum of two contributions:

- an infinitely narrow contribution at $\vec{q} = 0$ which will be in any practical situation suppressed by the beam stop
- the $\quad \langle n(\vec{q})n(-\vec{q}) \rangle = \int_V \int_V \exp\left[-i\,\vec{q}\bullet(\vec{r} - \vec{r}')\right]\langle \Delta\rho(\vec{r})\Delta\rho(\vec{r}') \rangle d\vec{r}\,d\vec{r}' \quad$ contribution

  originating from the density fluctuations.

The final result for the cross section becomes:

$$\frac{d\Sigma}{d\Omega}(\vec{q}) = \frac{b^2}{V}\langle n(\vec{q})n(-\vec{q}) \rangle = \frac{b^2}{V}\int_V \int_V \exp\left[-i\,\vec{q}\bullet(\vec{r} - \vec{r}')\right]\langle \Delta\rho(\vec{r})\Delta\rho(\vec{r}') \rangle d\vec{r}\,d\vec{r}' \tag{30}$$

It is interesting to look at the situation when $\vec{q}$ approaches 0.

$$\frac{d\Sigma}{d\Omega}(0) = \frac{b^2}{V}\int_V \langle \Delta\rho(\vec{r})\Delta\rho(\vec{r}') \rangle d\vec{r}\,d\vec{r}' \tag{31}$$

Because the average of the square of the fluctuations of the number of scatterers in volume V, $\left\langle \left(\Delta N^2 \right) \right\rangle$ is equal to

$$\left\langle \left(\Delta N^2 \right) \right\rangle = \left\langle \left(\int_V \Delta\rho(\vec{r}) \, d\vec{r} \right)^2 \right\rangle = \int_V \int_V \left\langle \Delta\rho(\vec{r}) \Delta\rho(\vec{r}') \right\rangle d\vec{r} \, d\vec{r}' \qquad (32)$$

it follows that

$$\frac{d\Sigma}{d\Omega}(0) = \frac{b^2}{V} \left\langle \left(\Delta N \right)^2 \right\rangle \qquad (33)$$

A well-established relationship for the grand canonical ensemble which applies here for density fluctuating systems is

$$\left\langle \left(\Delta N \right)^2 \right\rangle = \frac{kT}{V} \kappa_T \left\langle N \right\rangle^2 \qquad (34)$$

where k is the Boltzmann constant, T is the temperature and

$$\kappa_T = -\frac{1}{V} \left(\frac{\partial V}{\partial P} \right)_T \qquad (35)$$

is the isothermal compressibility. As a result

$$\frac{d\Sigma}{d\Omega}(0) = \frac{\left\langle N \right\rangle^2}{V^2} b^2 kT \kappa_T = \frac{b^2 kT \kappa_T}{v^2} \qquad (36)$$

where v = V/<N> is the volume of the elementary scatterers.

Equations (30) and (36) are essential because they show that, for a one-component system, no scattering will be detected in the absence of any density fluctuation, that is, if $\Delta\rho(\vec{r}) = 0$. Fluctuations must be present for any scattering to be observed. For a one-component system, this requires density fluctuations. For a multi-component system, concentration fluctuations can take place as well, even if the system is incompressible.

5.2 Scattering from incompressible multi-component systems

Consider the system described in the Figure 7; if the scatterers are characterized by scattering lengths denoted as b_p, $b_{p'}$ and b_s[1] for respectively, the hydrophobic polymer block, the hydrophilic one and the solvent, we can write, just by generalizing equation (30)

$$
\begin{aligned}
\frac{d\Sigma}{d\Omega}(\vec{q}) = {} & \frac{b_p^2}{V}\left\langle n_p(\vec{q})n_p(-\vec{q})\right\rangle + \frac{b_{p'}^2}{V}\left\langle n_{p'}(\vec{q})n_{p'}(-\vec{q})\right\rangle \\
& + \frac{b_s^2}{V}\left\langle n_s(\vec{q})n_s(-\vec{q})\right\rangle + 2b_p b_{p'}\left\langle n_p(\vec{q})n_{p'}(-\vec{q})\right\rangle \\
& + 2b_p b_s\left\langle n_p(\vec{q})n_s(-\vec{q})\right\rangle + 2b_{p'}b_s\left\langle n_{p'}(\vec{q})n_s(-\vec{q})\right\rangle
\end{aligned}
\tag{37}
$$

The following partial scattering factor is now defined by

$$
S_{IJ}(\vec{q}) = \frac{v_I v_J}{V}\left\langle n_I(\vec{q})n_J(-\vec{q})\right\rangle
\tag{38}
$$

with $I, J \equiv p, p'$ or s. v_I is the molecular volume of the elementary scatterer of constituent I, that is, either a monomer or a solvent molecule. We also define the <u>scattering length density</u> for constituent I

$$
\rho_I = \frac{b_I}{v_I}
\tag{39}
$$

Inserting (38) into (37) leads to

$$
\begin{aligned}
\frac{d\Sigma}{d\Omega}(\vec{q}) = {} & \rho_p^2 S_{pp}(\vec{q}) + \rho_{p'}^2 S_{p'p'}(\vec{q}) + \rho_s^2 S_{ss}(\vec{q}) \\
& + 2\rho_p\rho_{p'}S_{pp'}(\vec{q}) + 2\rho_p\rho_s S_{ps}(\vec{q}) + 2\rho_{p'}\rho_s S_{p's}(\vec{q}) \\
= {} & \sum_I\sum_J \rho_I\rho_J S_{IJ}(\vec{q}) \qquad \text{with } I, J \equiv p, p', s
\end{aligned}
\tag{40}
$$

As, under normal working conditions, liquids can be considered as incompressible, we make the so-called incompressibility assumption:

---

[1] For polymer chains in the q-range investigated here, the monomer is considered as the elementary scatterer. For the solvent, the molecule is the elementary scatterer. The scattering length of a molecular scatterer is simply the sum of the scattering lengths of its individual atoms.

$$v_p \Delta \rho_p (\vec{r}) + v_{p'} \Delta \rho_{p'} (\vec{r}) + v_s \Delta \rho_s (\vec{r}) = 0 \qquad (41)$$

As $n_I (\vec{q}) = \int_V \exp[-i\vec{q} \cdot \vec{r}] \Delta \rho_I (\vec{r}) d\vec{r}$, it follows that

$$v_p n_p (\vec{q}) + v_{p'} n_{p'} (\vec{q}) + v_s n_s (\vec{q}) = 0 \qquad (42)$$

As a result:

$$v_s n_s (\vec{q}) = -v_p n_p (\vec{q}) - v_{p'} n_{p'} (\vec{q}) \qquad (43)$$

With this condition, we derive the expression for the scattering factors involving the solvent

$$S_{ss} (\vec{q}) = S_{pp} (\vec{q}) + S_{p'p'} (\vec{q}) + 2 S_{pp'} (\vec{q}) \qquad (44)$$

Similarly

$$S_{ps} (\vec{q}) = -S_{pp} (\vec{q}) - S_{pp'} (\vec{q}) \qquad (45)$$

Also

$$S_{p's} (\vec{q}) = -S_{p'p'} (\vec{q}) - S_{pp'} (\vec{q}) \qquad (46)$$

We now finally insert (44), (45) and (46) into (40)

$$\frac{d\Sigma}{d\Omega}(\vec{q}) = (\rho_p - \rho_s)^2 S_{pp} (\vec{q}) + (\rho_{p'} - \rho_s)^2 S_{p'p'} (\vec{q}) + 2(\rho_p - \rho_s)(\rho_{p'} - \rho_s) S_{pp'} (\vec{q}) \qquad (47)$$

This latter equation can be generalized to a larger multicomponent system, consisting of $I = 1, 2, \ldots n_I$ components in addition of the solvent:

$$\frac{d\Sigma}{d\Omega}(\vec{q}) = \sum_{I=1}^{n_I} \sum_{J=1}^{n_I} \underbrace{(\rho_I - \rho_s)}_{\Delta\rho_I} \underbrace{(\rho_J - \rho_s)}_{\Delta\rho_J} S_{IJ} (\vec{q}) \qquad (48)$$

This equation is of course valid only in the incompressibility regime. This approximation has allowed us to get rid of the solvent contribution and to obtain an equation for the cross section which emphasizes that what determines the magnitude of $d\Sigma/d\Omega$ is the contrast

(ρ_I-ρ_s) between the different components and the solvent. More precisely, (ρ_I-ρ_s) is called the "excess scattering length density", the word "excess" being in reference to the solvent.

For example, Figure 8 shows a micelle made of diblock copolymers in D_2O and H_2O. Figure 8a shows a large contrast between the solvent and the objects itself. The core and the corona show similar contrasts. Therefore the accuracy on the global radius of micelle is high. Information about the size of the core and the corona can be obtained if the contrast between the core and the corona is high enough. Figure 8b shows the same micelle in H_2O. The contrast between the micelle and the solvent is poor. Therefore the accuracies on the global radius, core and corona are poor. Figure 8c shows the same micelle in D_2O but the sequence in the corona is deuterated. The accuracy on the global radius is smaller than in Figure 8a but the accuracy on the size of the core is larger. The standard procedure consists in using a deuterated component with un-deuterated ones in order to increase the contrast of specific parts of the self-organized nano-object. The components can be the solvent [8,9], polymer [10], membrane constituents [11], etc.
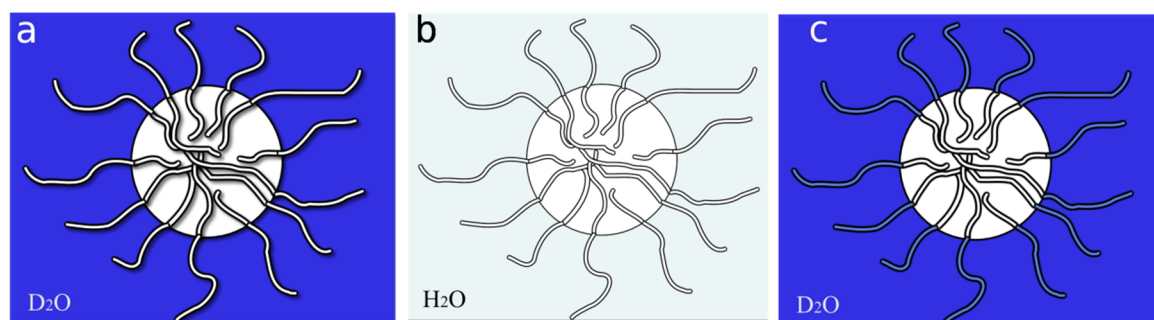
Figure 8 *Contrast of several polymers compositions in several solvents. a) un-deuterated polymers in D_2O, b) un-deuterated polymer in H_2O, c) un-deuterated core and deuterated corona in D_2O.*

In section 5.1, we emphasized that no scattering is observed at $\vec{q} \neq 0$ in the absence of density or concentration fluctuations. In a multicomponent system in the liquid state at atmospheric pressure, the concentration fluctuations are by far larger than the density fluctuations which can be neglected (incompressibility approximation). The detected scattering signal comes from the concentration fluctuations exclusively.

5.3 Contribution of the interactions between the nano-objects

We may also define the excess scattering length $\tilde{b}_i$ as follows

$$\Delta\rho_I = \rho_I - \rho_s = \frac{b_I}{v_I} - \frac{b_s}{v_s} = \frac{1}{v_I}\left(b_I - b_s\frac{v_I}{v_s}\right) = \frac{\tilde{b}_I}{v_I} \tag{49}$$

Then, using (48), (49) and (38), we obtain

$$\frac{d\Sigma}{d\Omega}(\vec{q}) = \frac{1}{V}\sum_I\sum_J \tilde{b}_I\tilde{b}_J \left\langle n_I(\vec{q})n_J(\vec{q})\right\rangle \tag{50}$$

Coming back from the continuous representation to the discrete one and remembering the developments leading to (28) and (29), it comes

$$\frac{d\Sigma}{d\Omega}(\vec{q}) = \frac{1}{V}\sum_I\sum_J \tilde{b}_I\tilde{b}_J \left\langle \sum_{j\in I}\sum_{l\in J}\exp\left[-i\vec{q}\bullet(\vec{r}_j - \vec{r}_l)\right]\right\rangle$$
$$= \frac{1}{V}\sum_I\sum_J\sum_{j\in I}\sum_{l\in J} \tilde{b}_I\tilde{b}_J \left\langle \exp\left[-i\vec{q}\bullet(\vec{r}_j - \vec{r}_l)\right]\right\rangle \tag{51}$$

In a sample like the one displayed on Figure 7, we have two components (and the solvent) which are distributed among different micelles, P forming the cores and P' the coronas. In equation (51), we favor a particular procedure to calculate the scattering cross section.

- We first calculate the contribution of the P blocks regardless which micelle they belong to;
- we then make the same for the P' blocks;
- and then we calculate the crossed PP' terms.

Another way to organize the terms appearing in (51) would be to calculate

- first the contributions of the individual micelles, that is, the $\left\langle \exp\left[-i\vec{q}\bullet(\vec{r}_j - \vec{r}_l)\right]\right\rangle$ terms where j and l belong to the same micelle but not necessarily to the same block.
- and then, the cross-terms between different micelles.

If we denote the micelles as α, β etc, we can then write the cross section as follows:

$$\frac{d\Sigma}{d\Omega}(\vec{q}) = \frac{1}{V}\left\{\sum_{\alpha=1}^{N_{mic}}\sum_{j=1}^{N}\sum_{l=1}^{N}\left\langle \tilde{b}_j\tilde{b}_l \exp\left[-i\,\vec{q}\bullet\left(\vec{r}_{\alpha j} - \vec{r}_{\alpha l}\right)\right]\right\rangle \right. $$
$$\left. + \sum_{\alpha=1}^{N_{mic}}\sum_{\beta\neq\alpha}^{N_{mic}}\sum_{j=1}^{N}\sum_{l=1}^{N}\left\langle \tilde{b}_j\tilde{b}_l \exp\left[-i\,\vec{q}\bullet\left(\vec{r}_{\alpha j} - \vec{r}_{\beta l}\right)\right]\right\rangle \right\}$$

(52)

We emphasize that (51) and (52) are completely equivalent. They correspond just to two different ways of grouping the terms. N_{mic} is the number of micelles present in the sample and N is the number of scatterers per micelle. Remember that we consider the micelles as monodisperse.

We refer to a common origin (the center of an arbitrarily chosen nano-object) to express all position vectors and we write:

$$\vec{r}_{\alpha j} = \vec{R}_\alpha + \vec{r}'_{\alpha j}$$

(53)

where:

- $\vec{R}_\alpha$ is the position vector of the center of micelle α
- $\vec{r}'_{\alpha j}$ is the position vector of the scatterer j of the micelle α with respect to the center of micelle α.

In the first term of (52), $\sum_{j=1}^{N}\sum_{l=1}^{N}\left\langle \tilde{b}_j\tilde{b}_l \exp\left[-i\,\vec{q}\bullet\left(\vec{r}'_{\alpha j} - \vec{r}'_{\alpha l}\right)\right]\right\rangle$ is clearly independent of α if all micelles are identical. This contribution is directly linked to the shape and internal structure of the individual micelles. The so-called form factor, $P(\vec{q})$, is defined by the following equation:

$$\sum_{j=1}^{N}\sum_{l=1}^{N}\left\langle \tilde{b}_j\tilde{b}_l \exp\left[-i\,\vec{q}\bullet\left(\vec{r}'_{\alpha j} - \vec{r}'_{\alpha l}\right)\right]\right\rangle = \left(\sum_{j=1}^{N}\tilde{b}_j\right)^2 P(\vec{q})$$

(54)

In equation (52), there are N_{mic} such terms. There are $N_{mic}(N_{mic}-1)$ terms of the form

$$\sum_{j=1}^{N}\sum_{l=1}^{N}\left\langle \tilde{b}_j\tilde{b}_l \exp\left[-i\,\vec{q}\bullet\left(\vec{r}_{\alpha j} - \vec{r}_{\beta l}\right)\right]\right\rangle \quad \text{with } \alpha \neq \beta$$

(55)

Inserting (53) into (55) leads to:

$$\sum_{j=1}^{N}\sum_{l=1}^{N}\left\langle \tilde{b}_{j}\tilde{b}_{l}\exp\left[-i\,\vec{q}\bullet\left(\vec{r}_{\alpha j}-\vec{r}_{\beta l}\right)\right]\right\rangle =$$
$$\sum_{j=1}^{N}\sum_{l=1}^{N}\left\langle \tilde{b}_{j}\tilde{b}_{l}\exp\left[-i\,\vec{q}\bullet\left(\vec{R}_{\alpha}-\vec{R}_{\beta}\right)\right]\exp\left[-i\vec{q}\bullet\vec{r}_{\alpha j}^{'}\right]\exp\left[+i\vec{q}\bullet\vec{r}_{\beta l}^{'}\right]\right\rangle \quad (56)$$

As the positions within one micelle are not correlated to those within another randomly chosen micelle, we can factorize the averages and write

$$\sum_{j=1}^{N}\sum_{l=1}^{N}\left\langle \tilde{b}_{j}\tilde{b}_{l}\exp\left[-i\,\vec{q}\bullet\left(\vec{r}_{\alpha j}-\vec{r}_{\beta l}\right)\right]\right\rangle =$$
$$\left\langle \exp\left[-i\,\vec{q}\bullet\left(\vec{R}_{\alpha}-\vec{R}_{\beta}\right)\right]\right\rangle \left(\sum_{j=1}^{N}\left\langle \tilde{b}_{j}\exp\left[-i\vec{q}\bullet\vec{r}_{\alpha j}^{'}\right]\right\rangle \right)\left(\sum_{l=1}^{N}\left\langle \tilde{b}_{l}\exp\left[+i\vec{q}\bullet\vec{r}_{\beta l}^{'}\right]\right\rangle \right) \quad (57)$$

We define the form factor amplitude, $F\left(\vec{q}\right)$, as follows

$$\sum_{j=1}^{N}\left\langle \tilde{b}_{j}\exp\left[-i\vec{q}\bullet\vec{r}_{\alpha j}^{'}\right]\right\rangle =\sum_{l=1}^{N}\left\langle \tilde{b}_{l}\exp\left[-i\vec{q}\bullet\vec{r}_{\beta l}^{'}\right]\right\rangle =\left(\sum_{j}^{N}\tilde{b}_{j}\right)F\left(\vec{q}\right) \quad (58)$$

It should be noted that, <u>because of the ensemble average, $P\left(\vec{q}\right)$ is</u>, as a rule, different from $\left|F\left(\vec{q}\right)\right|^{2}$. We also define $S\left(\vec{q}\right)$, <u>the interparticle structure factor</u>, as

$$S\left(\vec{q}\right)=\frac{1}{N_{mic}}\sum_{\alpha}\sum_{\beta}\left\langle \exp\left[-i\,\vec{q}\bullet\left(\vec{R}_{\alpha}-\vec{R}_{\beta}\right)\right]\right\rangle =1+\frac{1}{N_{mic}}\sum_{\alpha}\sum_{\beta\neq\alpha}\left\langle \exp\left[-i\,\vec{q}\bullet\left(\vec{R}_{\alpha}-\vec{R}_{\beta}\right)\right]\right\rangle \quad (59)$$

so that

$$\sum_{\alpha}\sum_{\beta\neq\alpha}\left\langle \exp\left[-i\,\vec{q}\bullet\left(\vec{R}_{\alpha}-\vec{R}_{\beta}\right)\right]\right\rangle =N_{mic}\left[S\left(\vec{q}\right)-1\right] \quad (60)$$

The second term of (52) becomes therefore:

$$\sum_{\alpha=1}^{N_{mic}}\sum_{\beta\neq\alpha}^{N_{mic}}\sum_{j=1}^{N}\sum_{l=1}^{N}\left\langle \tilde{b}_{j}\tilde{b}_{l}\exp\left[-i\,\vec{q}\bullet\left(\vec{r}_{\alpha j}-\vec{r}_{\beta l}\right)\right]\right\rangle =N_{mic}\left[S\left(\vec{q}\right)-1\right]\left(\sum_{j=1}^{N}\tilde{b}_{j}\right)^{2}\left|F\left(\vec{q}\right)\right|^{2} \quad (61)$$

Taking (54) and (61) into account and inserting them into (52) leads to

$$\frac{d\Sigma}{d\Omega}(\vec{q}) = \frac{1}{V}\left\{ N_{mic}\left(\sum_{j=1}^{N}\tilde{b}_j\right)^2 P(\vec{q}) + N_{mic}\left(\sum_{j=1}^{N}\tilde{b}_j\right)^2 |F(\vec{q})|^2 [S(\vec{q})-1]\right\}$$
$$= \frac{N_{mic}}{V}\left(\sum_{j=1}^{N}\tilde{b}_j\right)^2 P(\vec{q})\left\{1 + \frac{|F(\vec{q})|^2}{P(\vec{q})}[S(\vec{q})-1]\right\} \tag{62}$$

If the density within the nano-objects is relatively uniform, it can be assumed that $P(\vec{q}) \simeq |F(\vec{q})|^2$ so that

$$\frac{d\Sigma}{d\Omega}(\vec{q}) = \frac{N_{mic}}{V}\left(\sum_{j=1}^{N}\tilde{b}_j\right)^2 P(\vec{q})S(\vec{q}) \tag{63}$$

The cross section is then simply the product of four factors:

- a factor linked to the amount of material in the sample, N_{mic}/V
- a factor linked to the contrast, $\left(\sum_{j}^{N}\tilde{b}_j\right)^2$
- the form factor, $P(\vec{q})$, associated with the individual micelles
- the structure factor, $S(\vec{q})$, linked with the spatial organization of the micelles with respect to each other

Equation (59) shows that $S(\vec{q}) \to 1$ when $q \gg \dfrac{1}{\left|\vec{R}_\alpha - \vec{R}_\beta\right|}$ (see Figure 9). For dilute solutions, $\left|\vec{R}_\alpha - \vec{R}_\beta\right| \gg q^{-1}$ in the investigated q range. This means that in the q range outside the beam stop, $S(\vec{q})$ is equal to 1 and that

$$\frac{d\Sigma}{d\Omega}(\vec{q}) = \frac{N_{mic}}{V}\left(\sum_{j=1}^{N}\tilde{b}_j\right)^2 P(\vec{q}) \tag{64}$$

The analysis of the scattered intensity in the dilute regime gives therefore directly access to the form factor from which information on the structure of the individual nano-objects can be inferred provided an adequate model is compared to the experimental data.
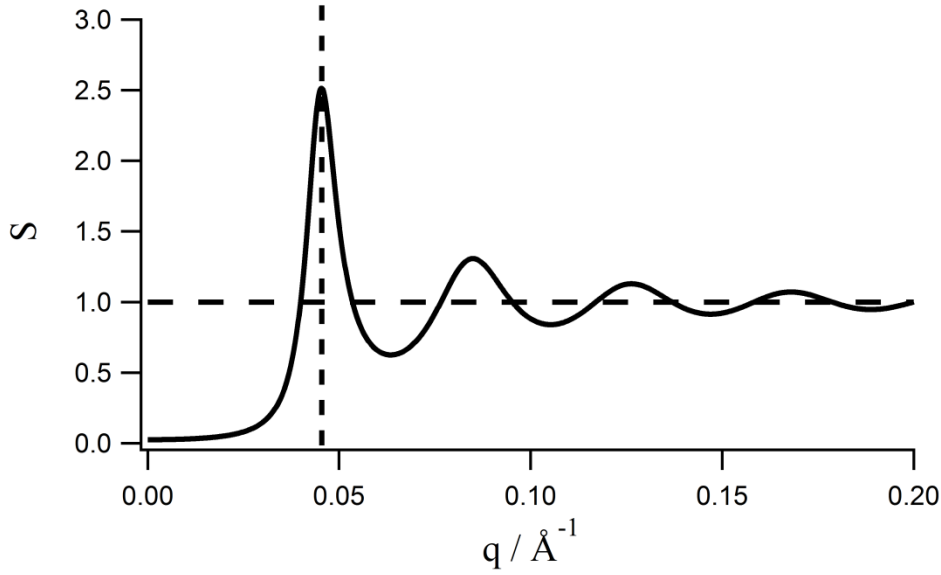
Figure 9 *Structure factor S(q). The curve depends on both the distance r at which the first neighbors of a micelle placed at the origin are found and the volume fraction of the solution φ. The values of r and φ are respectively equal to 150 Å and 0.45. The position of first maximum is equal to 2π/r = 0.041Å⁻¹.*

6   Influence of the polydispersity of the self-assembled objects

All the previous discussion was based on a collection of identical nano-objects. Reality is of course not so simple or ideal. The number of polymer chains inserted into a micelle varies within limits and, of course, this is reflected in the micellar size. The form factor will therefore be affected. The interactions between the micelles will also undergo such an influence so that the structure factor is expected to be modified.

In the so-called "decoupling approximation" [12], equation (62) is maintained but the form factor is averaged over the size distribution. As we mainly worked in the dilute regime, where equation (64) is valid, we shall focus here only on the effect of the polydispersity of the form factor.

We shall consider the aggregation number of the micelles[2], N_m, as the most relevant parameter. The other structural parameters, like the core radius, are function of N_m but the way they depend on N_m can change from one model to another.

Let us assume that dN_{mic} micelles have an aggregation number between N_m and $N_m + dN_m$. This number is related to a probability distribution:

$$\frac{dN_{mic}}{N_{mic}} = \Gamma(N_m) dN_m \tag{65}$$

In agreement with this definition, the distribution must be normalized

$$\int_1^{+\infty} \Gamma(N_m) dN_m = 1 \tag{66}$$

In equation (64), $\sum_j^N \tilde{b}_j$ is the sum over all scatterers of a micelle. It can be rewritten as

$$\sum_{j=1}^N \tilde{b}_j = N_m \tilde{b}_T \tag{67}$$

where $\tilde{b}_T$ is the sum of the excess scattering lengths of all atoms of one of the N_m polymer chains of the micelle. The polymer polydispersity is generally negligible, so that $\tilde{b}_T$ is the same for all chains. Taking (64)-(67) into account, we can write

$$\frac{d\Sigma}{d\Omega}(\vec{q}) = \frac{N_{mic}}{V} \int_1^{+\infty} N_m^2 (\tilde{b}_T)^2 P(\vec{q}; N_m) \Gamma(N_m) dN_m$$
$$= \frac{N_{mic}}{V} (\tilde{b}_T)^2 \int_1^{+\infty} N_m^2 P(\vec{q}; N_m) \Gamma(N_m) dN_m \tag{68}$$

where $P(\vec{q}; N_m)$ is the form factor for a particular N_m value. The total number of polymer chains in the sample, N_{ch}, is therefore given by

$$N_{ch} = N_{mic} \int_1^{+\infty} N_m \Gamma(N_m) dN_m \tag{69}$$

---

[2] The aggregation number is the number of polymer chains within a micelle.

Finally the scattering intensity of a polydisperse micellar population can be summarized as

$$\frac{d\Sigma}{d\Omega}(\vec{q}) = \frac{N_{ch}}{V}\tilde{b}_T^2 \frac{\displaystyle\int_1^{+\infty} N_m^2 P(\vec{q};N_m)\Gamma(N_m)\,dN_m}{\displaystyle\int_1^{+\infty} N_m \Gamma(N_m)\,dN_m} \tag{70}$$

$$= \frac{N_{ch}\tilde{b}_T^2}{V\langle N_m\rangle}\int_1^{+\infty} N_m^2 P(\vec{q};N_m)\Gamma(N_m)\,dN_m$$

The behavior of equation (70) at $\vec{q}=0$ can be calculated as $P(\vec{q}=0;N_m)=1$

$$\frac{d\Sigma}{d\Omega}(\vec{q}=0) = \frac{N_{ch}}{V}\tilde{b}_T^2 \frac{\langle N_m^2\rangle}{\langle N_m\rangle} \tag{71}$$

If we consider a dense homogenous core of radius R_c

$$N_m = \frac{4}{3}\pi\frac{R_c^3}{v_c} \tag{72}$$

where v_c is the volume of the hydrophobic block, Equation (71) then becomes

$$\frac{d\Sigma}{d\Omega}(\vec{q}=0) = \frac{N_{ch}}{V}\tilde{b}_T^2 \frac{\frac{4}{3}\pi\langle R_c^6\rangle}{\langle R_c^3\rangle}$$

7 Experiment

Neutrons are produced during nuclear reactions. There are two kinds of process able to deliver neutron fluxes usable for neutron scattering experiments: fission and spallation. [13]

During a fission reaction, a thermal neutron is absorbed by an uranium nucleus ^{235}U. The energy received by the nucleus is so high that it disintegrates into several fragments which correspond to moderately heavy atoms escorted by two to three neutrons. The amount of energy involved in this kind of reaction has a magnitude of several MeV. Some produced neutrons are involved in other fission reactions, leading to a chain reaction.

$$n + {}^{235}_{92}U \rightarrow {}^{236}_{92}U$$

$$\qquad (73)$$

$${}^{236}_{92}U \rightarrow {}^{144}_{56}Ba + {}^{89}_{36}Kr + 3n + 177 MeV$$
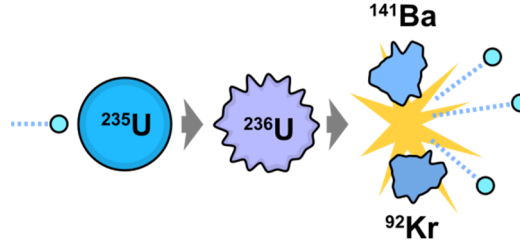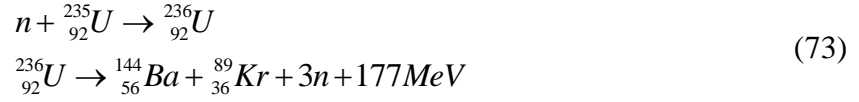
Figure 10 *Illustration of the fission process and production of neutrons. Neutrons are shown as light blue spheres[3].*

During the spallation process, high energy protons of the order of GeV energy hit a target composed of heavy atoms. After the impact, the target atoms are excited and spontaneously emit 20 to 25 neutrons. The energy of spallation neutrons varies from a few to hundreds of MeV. [13]

The neutrons produced by these techniques initially have a wide energy distribution. They are slowed down in a moderator containing D_2O. A velocity selector shown in Figure 11 is then used to obtain a neutron flux with a selected energy or wavelength. The velocity selector has the appearance of a many-bladed turbine. The blades are coated with a strongly neutron-absorbing material, such as Boron-10 (^{10}B)[4]. The resolution of the velocity selector is limited and it needs to be taken into account during the analysis of the data. The relative wavelength resolution $\Delta\lambda/\lambda$ is constant and close to 10% [13]. Because of equation (3), $\Delta\lambda/\lambda = \Delta q/q$. A triangular apparatus function is usually used to convolute the theoretical data in order to compare them to the experimental ones.

Neutrons are finally focused on the sample with the help of neutron guides (based on total reflection like in optical fibers). Typical neutron fluxes are of order 5×10^5 n cm^{-2} s^{-1} at the sample position [15] while SAXS flux are around 10^{15} photons cm^{-2} s^{-1} for third-generation synchrotron sources. [16]

---

[3] This illustration is in the public domain.

[4] A video describing the process can be seen in ref [14].
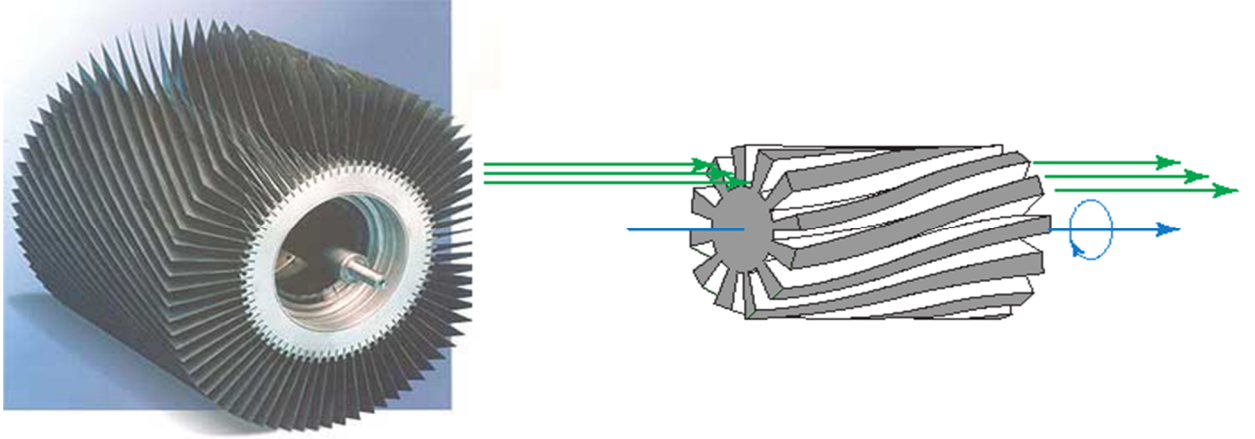
Figure 11 *Velocity selector. A cylinder of length L bears helical grooves of pitch P. The cylinder rotates about its axis at the angular momentum ω. Each groove allows the neutron*

with a velocity $V \approx \dfrac{P\omega}{2\pi}$ *[17]*

As neutrons possess no charge, they are more difficult to detect than charged particle. Their magnetic momentum, $-9.66 \ 10^{-27}$ J T^{-1}, is too low to be detected. However, neutron can be involved in reactions where ions are produced. During SANS experiments, gas detectors are commonly used. Nuclei with high cross-section react with thermal neutrons. The commonly used nuclides are ^{3}He, ^{6}Li and ^{10}B. Once the neutron is captured, the product releases charged particles or ions which are easily detected. The number of charged entities is proportional to the number of neutrons entering the chamber. The macroscopic cross section is related to the neutron flux through the following formula:

$$J_d = J_{in}\left(\frac{d\Sigma}{d\Omega}\right)\Delta\Omega\,A\,\varepsilon\,T\,/\,l \qquad (74)$$

where J_d is the scattered neutrons flux, J_{in} is the initial neutron flux, $\Delta\Omega$ is the solid angle, *A* is the sample area, ε is the detector response function, *T* is the transmission (attenuation coefficient of primary intensity) and */* is the distance covered by the neutrons in the sample. [18]

41

During this work a large amount of data were acquired in the *Laboratoire Leon Brillouin* at Saclay. The detector is based on the reaction of ^{10}B with neutron producing ^{7}Li and a α particle and γ radiation.

$$^{10}_{5}B + ^{1}_{0}n \rightarrow ^{7}_{3}Li + \underbrace{^{4}_{2}He}_{\alpha} + \gamma + 2.3 MeV$$
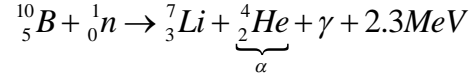
The detector is composed of multiple tubes containing BF$_3$. One of these tubes is shown in Figure 12a and they are disposed in a larger cylinder as show in Figure 12b. The position of the tube detecting the neutron is converted into an angle with respect to the incident direction. The intensity is proportional to the number of detected neutrons.

Another series of data was obtained at KWS-1 and KWS-2 diffractometer at the Jülich Centre for Neutron Science at the Forschungsneutronenquelle Heinz Maier-Leibnitz (FRMII) Outstation in Garching, Germany.

$$^{6}_{3}Li + ^{1}_{0}n \rightarrow ^{3}_{1}H + ^{4}_{2}He + 4.78 Mev$$
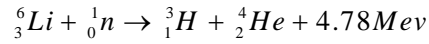
The neutron detectors installed on the instrument used are scintillation counters. They absorb the neutrons within a polymer or glass layer which is enriched by ^{6}Li and ZnS. Neutron absorption then leads to fluorescence radiation of ZnS by reaction with the alpha particle. The photons are detected by a photo multiplayer or directly on photographic film.
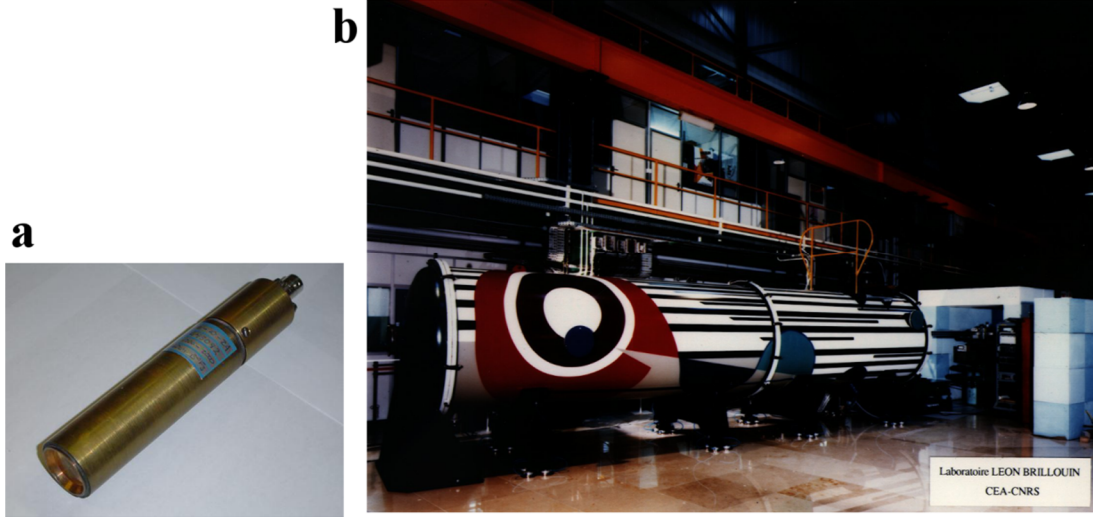
Figure 12 *a) BF3 detection tube. [19] b) Paxy's detector at Laboratoire Leon Brillouin, Saclay. Several BF3 tubes enriched to 96% ^{10}B are disposed in this chamber. Boron trifluoride is hightly toxic. Some samples discussed in this work were analyzed with the PACE diffractometer which uses a similar detector. [20,21]*

8   Form factors of common nano-objects

Equation (6) has been applied to various nano-object shapes. We already mentioned the form factor of a sphere P_s which is known since 1911 (see eq (22)) [22]. Among all available expressions for form factors, we may mention P_{ch}, the normalized form factor of a free Gaussian chain (Debye form factor) [23] and P_v, the normalized form factor of a vesicle [24]. $P_s(q)$, $P_{ch}(q)$, and $P_v(q)$ are displayed in Figure 13.

$$P_{ch}(q) = 2\frac{\exp\left(-q^2R_g^2\right)+q^2R_g^2-1}{\left(q^2R_g^2\right)^2} \tag{75}$$

where R_g is the radius of gyration of the chain.

$$P_v(\vec{q}) = \left[\frac{\sin(qR)}{qR}\frac{\sin\left(\frac{qd}{2}\right)}{\frac{qd}{2}}\right]^2 \tag{76}$$

where R is the radius of the vesicle and d is its thickness. $P_v(q)$ is called the separated form factor (SFF) and it is valid if R >> d.

To analyze SANS data from spherical objects like micelles, the first and simplest approach is to describe them as spheres. The major drawback is the q^{-4} power law followed by this expression at high q range ($qR > 20$). Mortensen [25] successfully applied this model on a pluronic sample in 1996. They are made of poly(ethylene oxide) (PEO) and poly(propylene oxide) (PPO) (PEO_{25}-b-PPO_{40}-b-PEO_{25}, PEO_{67}-b-PPO_{39}-b-PEO_{67}, PEO_{96}-b-PPO_{39}-b-PEO_{96}, and PEO_{99}-b-PPO_{65}-b-PEO_{99}). Mortensen [25] acknowledged that the behavior of the experimental form factor at large q-values does not follow the q^{-4} law but a q^{-2} behavior. In 1996, Pedersen [26] described its pluronic sample with an original model as summarized below.
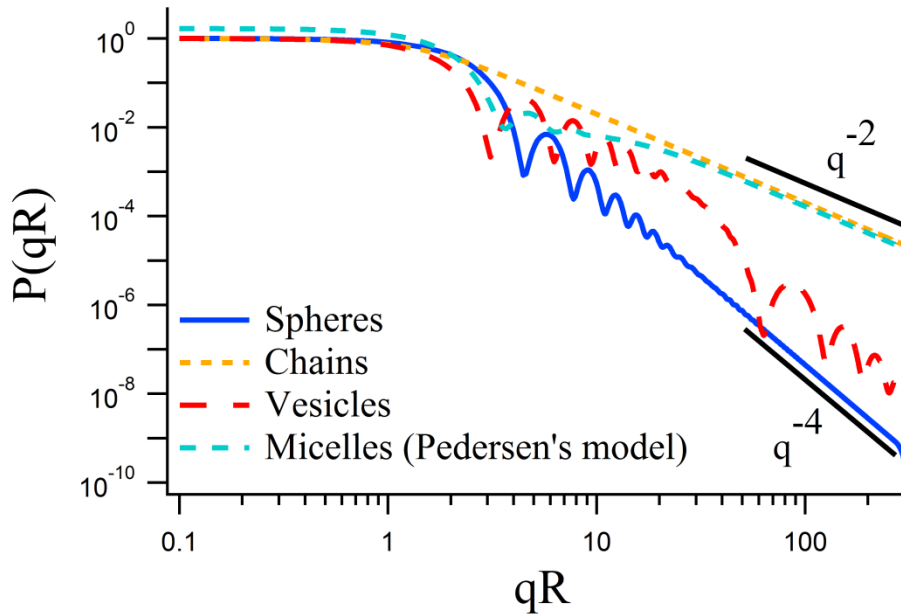
Figure 13 *Normalized form factor of several objects as a function of the product qR where R is the radius of the object (or its radius of gyration in the case of the chains). The thickness of the vesicle is equal to the radius of gyration of the corona divided by 10. The power law in the domain where qR >20 is equal to q^{-2} for the Gaussian chains and micelles while a power equal to q^{-4} is found for the spheres model. The models have been convoluted with an apparatus function in order to display realistic curves (see section 7). A triangular shape has been assumed for the scattering vector spread ($\Delta q/q = 10\%$).*

The power laws observed in scattering experiments in the $qR>20$ range are linked to the fractal dimension of the scattering objects. For the scattering by fractal masses of dimension D, the cross section is proportional to q^{-D}. For Gaussian chains in a θ-solvent, $D=2$ and a q^{-2}

behavior is observed. Taking the excluded volume into account (swollen chains in a good solvent) leads to $D=5/3$ and the cross section is proportional to $q^{-5/3}$. When the scattering object is delimited by a fractal surface of dimension D, the cross section becomes proportional to q^{D-6}. If the delimiting surface is a smooth one, $D=2$ and the Porod law obtains: $d\Sigma/d\Omega \propto q^{-4}$. This is the case of the scattering by a sphere.

The model described by Pedersen & Gerstenberg (P&G model) [26] provides the macroscopic cross section $d\Sigma/d\Omega(\vec{q})$ of a micelle made of diblock copolymer chains. It depends on the number of chains N_m, the radius of the core R_c and the radius of gyration of the corona R_g. The excess of scattering length of the blocks are noted $\tilde{b}_c$ and $\tilde{b}_{ch}$ for the core and the corona respectively. The excess scattering length of a sequence is defined as the product of its degree of polymerisation, z, by the excess scattering length of the repeating unit $\tilde{b}$. By applying the general relationship (64) to this particular situation, they obtained the following analytical expression for the cross section.

$$
\begin{aligned}
\left(\frac{d\Sigma}{d\Omega}\right)_{PQ}(\vec{q}) = {}& N_m^2 \tilde{b}_c^2 \left\{\frac{3}{(qR_c)^3}\left[\sin(qR_c) - qR\cos(qR_c)\right]\right\}^2 \\
& + N_m \tilde{b}_{ch}^2\, 2\, \frac{\exp(-q^2 R_g^2) + q^2 R_g^2 - 1}{(q^2 R_g^2)^2} \\
& + 2N_m^2 \tilde{b}_c\, \tilde{b}_{ch}\, \frac{3\left[\sin(qR_c) - qR_c\cos(qR_c)\right]}{(qR_c)^3}\, \frac{1-\exp(-q^2 R_g^2)}{q^2 R_g^2}\, \frac{\sin\left[q(R_c + R_g)\right]}{q(R_c + R_g)} \\
& + N_m(N_m - 1)\, \tilde{b}_{ch}^2 \left[\frac{1-\exp(-q^2 R_g^2)}{q^2 R_g^2}\right]\left[\frac{\sin\left[q(R_c + R_g)\right]}{q(R_c + R_g)}\right]^2
\end{aligned} \tag{77}
$$

The first term of this sum stands for the interference between the scatterers of the core (which is assumed to be spherical), the second stands for the scatterers within a given chain of the corona (which is assumed to be Gaussian). N_m takes into account all the chains of the corona. The third term stands for the interferences between scatterers in the core and corona and the latter stands for the interferences between scatterers of different chains in the corona. The Gaussian chains of the corona are prevented to penetrate the core. As it is not possible to take into account the non-penetration in the analytical formula, the chain origins are shifted at a distance $R_c + R_g$ from the micellar center. The outcome is the decrease of the penetration probability.

The first micellar samples which were analyzed with this model were composed of *[poly-(ethylene oxide)-poly(propylene oxide)-poly(ethylene oxide)]* PEO_{25}-*b*-PPO_{40}-*b*-PEO_{25} in D_2O at a temperature of 50 °C. At the specified experimental conditions, the copolymer forms micelles build from a PPO core and PEO corona [27-29,25]. The inter-micellar contribution was neglected because the solution was diluted enough in order to allow them to neglect the structure factor (see eq(64)). They took into account the polydispersity on the aggregation number through a Schultz distribution [26]. The core was assumed to be solvent free and the aggregation number is directly proportional to the volume of the core, see eq(72).
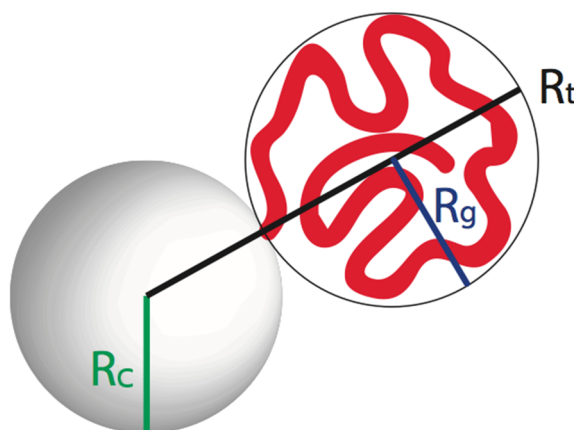
Figure 14 *Core-shell micelle with a core's radius equal to Rc and the gyration radius of the corona equal to R_g.*

9 A few examples from the literature

To determine inner structural properties and the stability of micelles, there are two possible approaches. The first one is to actually prepare the sample and then perform experiments like SANS or SAXS. An analytical theoretical model of the sample depending of the structural parameters has to be assumed and developed. The parameters may be the aggregation number, the polydispersity of the sample, and the size of the core and the corona in the case of micelles or the radius and the thickness of the membrane in the case of vesicle. The model is then fit by decreasing the χ^2 between the macroscopic cross section given by the model and the experimental data. This approach was used for a long time and was fully developed since the progress of informatics. The present work is based on this approach. The

second approach is called Molecular Dynamics (MD) Simulation and it will be described in Section 10.

Colloidal materials may display aggregation states and rheological behaviors which strongly depend on external stimuli like the pH, temperature, concentration… SANS can be used to study the transition between the different regimes. Hundreds of investigations can be found in the literature. The remaining of this section illustrates a few aspects, based on the analysis of some specific examples.

In 2007, Joseph et al. [30] studied the micelle formation of Pluronics® F127 triblocs copolymers (PEO_{100}-b-PPO_{65}-b-PEO_{100}) and their disruption in the presence of cyclodextrins. The PPO block becomes insoluble at temperatures higher than 18 to 23°C, depending on the concentration [31]. They first performed SANS experiments under several conditions of temperature and concentration and their model takes into account the formation of micelles at increasing temperature by introducing a balance between free chains and micelles in order to ensure mass conservation. They then characterized the structures resulting from the complexation with cyclodextrin and monitored the structural changes of the complexes over a wide range of temperatures (5 to 70 °C) and polymer/CD ratios. The scattering intensity, $I(q)$ was defined as

$$I(q) = \frac{c}{M} f\ P_{mic}S(q) + \frac{c}{M_{ni}}P_{uni}(q) \tag{78}$$

C is the polymer concentration (w/v), M is the mass of a micelle, M_{uni} is the mass of a chain. $P_{mic}(q)$ is the micellar form factor and $S(q)$ is the micellar structure factor. $P_{uni}(q)$ is the form factor of the free chains and f is the weight fraction of chains included in the micelles. $P_{uni}(q)$ is the Debye function [23].

The above example shows the great advantage of small angle scattering when information on micelles inner structure needs to be obtained. But SANS can also help to obtain structural information on the distribution of building molecules in other nano-objects i.e. vesicles. Liposomes are spherical vesicles with at least one lipid bilayer. They are widely studied as cell models. In addition to mimicking the membrane, liposomes can also be used as drug enhancers [32-37]. SANS gives access to the average radius, to the polydispersity, to the aggregation number, and to the thickness of the membrane. For example, Kučerka et al. [38] performed SAXS and SANS on liposomal solutions. The nature of the phosphatidylcholines

with fully saturated, mixed, and branched fatty acid chains, was studied at several temperatures. They showed that the bilayer thickness decreases as temperature increases because entropic driving force favors *gauche* conformations leading to a more compact molecular shape. Moreover, their study allowed them to show that longer saturated hydrocarbon chains have an increasingly larger chain to chain van der Waals attractive energy, resulting in smaller lateral areas. As expected, the unsaturated oleolyl fatty acid, whose unsaturated bond is *cis,* displays a larger area/lipid ratio. They also study the dependence between the double bond's position along the hydrocarbon chain and the chain disorder.

Another example of vesicle study is the work of Borchert et al. [39], who investigated the triggered release of a dye from vesicles built from poly(2-vinylpyridine) and poly(ethylene oxide) PEO-*b*-P2VP block copolymers. The PEO block is hydrophilic. At basic pH, the P2VP block is neutral and hydrophobic. When pH decreases below ~4, the P2VP chains become substantially protonated and hydrophilic. The degrees of polymerization of the blocks are chosen in order to prevent the formation of micelles. The model written by Borchert et al. [39] allows them to infer the average radius $\bar{R}$ of the vesicle, the standard deviation of R, the thickness of the membrane (which is assumed to be homogenous). The pH-dependent solubility of the block copolymers has been investigated by titration with dilute *HCl* while monitoring the pH and conductivity of the solution. When the P2VP blocks become charged, the vesicle slowly shrinks because of the loss of protonated copolymers. When their size has decreased by 40 to 50% of its initial size, the bilayer ruptures. The authors have studied the release of a dye upon increasing acetic acid concentration. Using a weak acid slows down the process.

Causse et al. [40] studied the solubilization behavior of tributylphosphate (TBP), a polar oil, in L64-pluronic micellar solutions by SANS and light scattering measurements. All measurements were performed at 308 K and the main varying parameter was the ratio c/c_{sat} where c is the TBP concentration and c_{sat} is its solubility in pure deionized water. While $c/c_{sat} < 70$, the system is monophasic: free chains are detected at low copolymer concentration (2%wt) and polydisperse core-shell micelles at larger ones (5%wt and 10%wt). At $70 < c/c_{sat} < 150$, a first phase separation occurs. When $c/c_{sat} > 150$, a second transition occurs and results in a new transparent phase. The authors detected the formation of larger objects and fitted the data with a model consisting of polydisperses spheres. Causse et al. [40]

observed the structure factor for most micellar samples and took it into account with the Percus and Yevick structure factor (PY), which accounts for the interactions between non charged homogenous spheres. The PY parameters are the interaction distance and the volume fraction of the spheres. Causse et al. [40] inferred the aggregation number of micelles, the thickness of the shell, the polydispersity of the core as well as the PY parameters. The parameters of the samples at $c/c_{sat} > 150$ are the aggregation number of the spheres, the number of TBP included, the radius of the spheres, and their polydispersity.

The following paragraph describes another example of a shape tuning under varying experimental parameters. Chécot et al. [41] studied the self-organization of poly(butadiene)-*b*-poly(L-glutamic acid) (PB-*b*-PGA) in aqueous or organic solutions. This diblock copolymer chains self-assemble either in micelles or in vesicles after direct dissolution in water, depending on the lengths of the blocks. The authors dissolved first the copolymer in water at pH 12 (PB$_{48}$-*b*-PGA$_{56}$, PB$_{48}$-*b*-PGA$_{114}$, PB$_{48}$-*b*-PGA$_{145}$) and in dichloromethane (PB$_{48}$-*b*-PGA$_{20}$). Static and dynamic light scattering and SANS experiments were performed on the samples and it was found that the more symmetric samples (PB$_{48}$-*b*-PGA$_{56}$) form vesicles and the asymmetric ones form micelles. When the hydrophilic block is short enough, inverse structures are able to be formed in organic solvents. The SANS measurements were performed in D$_2$O in order to increase the contrast between the copolymers and the solvent but Chécot et al. [41] found that the scattering of the PGA blocks is generally weak. The best fits of micelles and vesicles correspond to the form factors of spheres and of hollow spheres, respectively. The polydispersity of the sample was taken into account with a log-normal distribution of the radius.

SANS measurements are also performed on cylindrical or on worm-like micelles. For example, Madenci et al. [42] studied mixed lecithin–bile salt micelles. They created a model to quantitatively link the length of the micelle to both the total amphiphile concentration and and the molar ratios of bile salt to lecithin. The SANS macroscopic cross-sections were fitted with a model of polymer-like micelles, that is worm-like chains, including polydispersity and intermicellar interactions. The parameters of the model are: the minor radius r of the cylinder, the contour length L and the ellipticity of the cross section. The persistence length of the cylindrical micelles and the relative polydispersity in length were fixed. L was found to increase with dilution for all investigated dilution series. Furthermore, the authors inferred the internal composition of the micelles in regard to the length. Their assumption is that the

highly-curved end caps are mainly filled with bile salt molecule and therefore their abundance leads to the observed decrease of the length of the micelles.

The last example shows the effect of the excluded volume on the form factor of micelles. Most of the time, the corona contribution is taken into account with the help of the Debye formula (see section 8) which assumes a random walk pattern and a Gaussian distribution of the distances between the ends of the polymer chain. [23]. However, because of the constraints imposed by the valence bond angles and by the excluded volumes, not all configurations based on a random walk are allowed.

In 2003, Pedersen et al. [43] studied the effect of the excluded volume of the corona on the form factor of micelles built from poly(styrene)-*block*-poly(isoprene) (PS-*b*-PI) in decane which is a strongly selective solvent of the PI block. They performed contrast variation small-angle neutron scattering in combination with small-angle X-ray scattering measurements. SAXS provided scattering functions which were analyzed using Monte Carlo simulations for a model with a spherical core and a corona of semiflexible chains interacting with a hard-core potential [44]. They showed that two parameters affect mainly the shape of the corona: a reduced surface coverage of the corona chains (concentration relative to chain overlap concentration) and a curvature parameter, which is the width of the corona relative to the core radius. The fits of the experimental data provided the common parameters of micelles (aggregation number, polydispersity, core size, core solvation, and corona shape/size) but also some information on the interactions between the chains in the corona. Though the fits are good, this approach is quite time-consuming. Fortunately, many self-assembled systems do not require taking into account the excluded volume of the chains because the experimental data display a nearly q^{-2} behavior at $qR > 20$ (see Figure 13). [45,26,46]

The previous examples showed that it is possible to have access to structural information of various colloidal samples with SANS experiment. Nowadays, micelles are mainly studied as stimulus reactive nano-objects and their properties are monitored as a function of the experimental conditions (pH, temperature, concentration, etc) [47,48,2,45,49-51]. Small angle scattering experiments are then often used to complement other experimental techniques like light scattering or electron microscopy [8]. Theory can, however, also bring an essential contribution to the unravelling of the structures of nano-objects: we briefly discuss now molecular dynamics simulation.

10 Molecular Dynamics Simulation

A complementary approach to obtain structural information on micelles is to perform a molecular dynamics (MD) simulation [52-54]. This method is based on the study of the driving force for self-assembly [55]. Molecular dynamic simulations consist in the modelling of chemical systems in the context of N-body simulations. This method was initially developed to calculate the trajectory of stellar bodies in space. In molecular dynamics simulations, Newton's equations of motion are solved for atoms or molecules interacting in a virtual box, which allows visualizing the atomic motion over a given time period. The process is based on time step dynamics and the calculation processes are relatively slow because the number of atoms is quite large (10^4 to 10^6). When too many resources are needed to calculate the trajectory over a period of time larger than a microsecond, coarse graining (CG) methods are used. Coarse-graining relies on the assumption of a group of atoms as a larger entity. The MD simulations take into account the free energy difference between free surfactants and those located inside micelles at a given temperature. Let us denote the concentration of the free chains as C_1 and the concentration of micelles as C_n: if $C_1 \gg C_n$ and if the aggregation number n is $\gg 1$, it is possible to determine the critical micelle concentration (CMC), denoted as C.

$$\ln(Ca^3) = \frac{\Delta G}{kTn} \tag{79}$$

a represents the size of a surfactant tail bead [52]. kT is the thermal energy, ΔG is the difference between the free energy of micelles made of n chains and free chains. If f_n is the free energy of a micelle with an aggregation number n, and if f_1 is the free energy of a free chain:

$$\Delta G = f_n - nf_1 \tag{80}$$

The key step is the proper calculation of ΔG. Several models take into account different contributions to ΔG: electrostatic and hydrophobic [56-60,55,61-63]. Once equation (80) and the structural properties of surfactants are provided as an input to the program, iterations take place over a chosen time and length scale. The accuracy of the model depends on the expression of ΔG and on the size of the box where the surfactants evolve. The accuracy of the CMC and aggregation number estimations have been improved during the past decades

through the enhancement of computer capabilities [52,53]. But there remain relatively large differences between these simulations and SAXS or SANS experimental data. [52,64]

11 Summary

Small angle neutron scattering is a powerful technique to unravel the structure of micelles. The main advantages over usual techniques like TEM, DLS or even SAXS are:

1) The sensitivity to light atoms like hydrogen, carbon or oxygen.

2) The possibility to use deuterated molecules to tune the contrast of some parts of the micelles, like the core or the corona.

3) The possibility to obtain structural information on the inner structure of micelles and to infer information on the aggregation number, the size of the core, the size of the corona, and the polydispersity of the sample. If the core is swollen with solvent molecules, it is possible to take this into account through the volume fraction of polymer in the core.

The major drawbacks of the technique are the low neutron flux due to their production mode, the lower scattering cross sections for neutrons, and the fact that the analysis of the scattering cross sections requires some prior assumptions defining a reasonable model for the investigated systems. However, many research teams across the world successfully obtained information on various systems because the models are tailored and the data analysis workflow opens the door to self-made models.

12 References

1. Technology, V.U.o., Physics, I.o.A.a.S.: Neutron and X-rays radiography. http://www.ati.ac.at/~neutropt/experiments/Radiography/radiography.html (2001). Accessed 26/09 2014

2. Cajot, S., Riva, R., Billiet, L., Du Prez, F., Alexandre, M., Lecomte, P., Jérôme, C.: Novel Amphiphilic Mikto-Arm Star-Shaped Copolymers for the Preparation of PLA-Based Nanocarriers. Macromolecular Symposia **309-310**, 111-122 (2011). doi:10.1002/masy.201100044

3. Mittal, V., Matsko, N.B.: Analytical Imaging Techniques for Soft Matter Characterization. Springer, (2012)

4. André Guinier, G.F.: Small-angle scattering of X-rays. **18** (1955). doi:10.1016/0146-3535(89)90023-3

5. Guinier, A.: La diffusion des neutrons. Revue de physique appliquée, 1051 (1976).

6. Dianoux, A., Lander, G.: Neutron data booklet. (2003).

7. Jackson, A.J.: Introduction to Small-Angle Neutron Scattering and Neutron Reflectometry. (2008).

8. Mugemana, C., Joset, A., Guillet, P., Appavou, M.-S., De Souza, N., Fustin, C.-A., Leyh, B., Gohy, J.-F.: Structure of Metallo-Supramolecular Micellar Gels. Macromolecular Chemistry and Physics **214**, 1699-1709 (2013). doi:10.1002/macp.201300288

9. Filippov, S., Franklin, J., Konarev, P.: Hydrolytically degradable polymer micelles for drug delivery: A SAXS/SANS kinetic study. … (2013).

10. Wignall, G.D., Melnichenko, Y.B.: Recent applications of small-angle neutron scattering in strongly interacting soft condensed matter. Reports on Progress in Physics **68**, 1761-1810 (2005). doi:10.1088/0034-4885/68/8/R02

11. Hirai, M., Iwase, H., Hayakawa, T., Koizumi, M., Takahashi, H.: Determination of asymmetric structure of ganglioside-DPPC mixed vesicle using SANS, SAXS, and DLS. Biophysical journal **85**, 1600-1610 (2003). doi:10.1016/S0006-3495(03)74591-3

12. Kotlarchyk, M., Chen, S.H.: Analysis of small angle neutron scattering spectra from polydisperse interacting colloids. The Journal of Chemical Physics **79**, 2461 (1983). doi:10.1063/1.446055

13. Brückel, T., Heger, G., Richter, D.: Neutron Scattering. In, vol. 9. Jülich Forschungszentrum Jülich Edition, (2001)

14. Langevin, I.L.: SANS instrument D11. 1- Velocity selector 4.5 Å. http://youtu.be/q3QqHVchnW4 (2012). Accessed 08/10 2014

15. Schoenborn, B.P., Knott, R.B.: Neutrons in Biology. Springer US, (2012)

16. Seeck, O.H., Murphy, B.: X-Ray Diffraction: Modern Experimental Techniques. Pan Stanford, (2015)

17. CEA, L.L.B.-. La Source et les faisceaux sortis. http://iramis.cea.fr/llb/presllb/Part_2.pdf. Accessed 08/10 2014

18. Brûlet, A., Lairez, D., Lapp, A., Cotton, J.-P.: Improvement of data treatment in small-angle neutron scattering. J Appl crystallogr **40**, 165-177 (2007).

19. Seltzman, A.: IEC Fusion Reactor Mark 3 Neutron Detector. http://www.rtftechnologies.org/physics/fusor-mark3-neutron-detector.htm (2014). Accessed 17/10 2014

20. BRILLOUIN, L.L.: G2-3 Small Angle Neutron Scattering Facility PAXY. http://www-llb.cea.fr/spectros/spectro/paxy.html (1995). Accessed 17/10 2014

21. BRILLOUIN, L.L.: PACE LLB. http://www-llb.cea.fr/spectros/pdf/pace-llb.pdf (1995). Accessed 17/10 2014

22. Rayleigh, L.: On Dr. Johnstone Stoney's Logarithmic Law of Atomic Weights. Proceedings of the Royal Society A: Mathematical, Physical and Engineering Sciences **85**, 471-473 (1911). doi:10.1098/rspa.1911.0059

23. Debye, P.: Light Scattering in Solutions. Journal of Applied Physics **15**, 338 (1944).

24. Kiselev, M.a., Lesieur, P., Kisselev, a.M., Lombardo, D., Aksenov, V.L.: Model of separated form factors for unilamellar vesicles. Applied Physics A: Materials Science and Processing **74**, 1654-1656 (2002). doi:10.1007/s003390201837

25. Mortensen, K.: Structural studies of aqueous solutions of PEO - PPO - PEO triblock copolymers, their micellar aggregates and mesophases; a small-angle neutron scattering study. Journal of Physics: Condensed Matter **8**, A103 (1996).

26. Pedersen, J.S., Gerstenberg, M.C.: Scattering Form Factor of Block Copolymer Micelles. Macromolecules **29**, 1363-1365 (1996).

27. Zhang, Y., Lam, Y.M., Tan, W.S.: Poly(ethylene oxide)-poly(propylene oxide)-poly(ethylene oxide)-g-poly(vinylpyrrolidone): association behavior in aqueous solution and interaction with anionic surfactants. J Colloid Interface Sci **285**(1), 74-79 (2005). doi:10.1016/j.jcis.2004.12.033

28. Mata, J.P., Majhi, P.R., Guo, C., Liu, H.Z., Bahadur, P.: Concentration, temperature, and salt-induced micellization of a triblock copolymer Pluronic L64 in aqueous media. Journal of colloid and interface science **292**, 548-556 (2005). doi:10.1016/j.jcis.2005.06.013

29. Yang, L., Alexandridis, P., Steytler, D.C., Kositza, M.J., Holzwarth, J.F.: Small-Angle Neutron Scattering Investigation of the Temperature-Dependent Aggregation Behavior of the Block Copolymer Pluronic L64 in Aqueous Solution†. Langmuir **16**, 8555-8561 (2000). doi:10.1021/la000008m

30. Joseph, J., Dreiss, C.a., Cosgrove, T., Pedersen, J.S.: Rupturing polymeric micelles with cyclodextrins. Langmuir : the ACS journal of surfaces and colloids **23**, 460-466 (2007). doi:10.1021/la061850g

31. Alexandridis, P., Hatton, T.A.: DS thermodynamics , structure , dynamics , and modeling. **7757** (1995).

32. Guelluy, P.H., Fontaine-Aupart, M.P., Grammenos, A., Lecart, S., Piette, J., Hoebeke, M.: Optimizing photodynamic therapy by liposomal formulation of the photosensitizer pyropheophorbide-a methyl ester: in vitro and ex vivo comparative biophysical investigations in a colon carcinoma cell line. Photochem Photobiol Sci **9**(9), 1252-1260 (2010). doi:10.1039/c0pp00100g

33. Vrhovnik, K., Kristl, J., Sentjurc, M., Smid-Korbar, J.: Influence of liposome bilayer fluidity on the transport of encapsulated substance into the skin as evaluated by EPR. Pharm Res **15**(4), 525-530 (1998).

34. Battistini, L., Burreddu, P., Sartori, A., Arosio, D., Manzoni, L., Paduano, L., Derrico, G., Sala, R., Reia, L., Bonomini, S., Rassu, G., Zanardi, F.: Enhancement of the uptake and cytotoxic activity of doxorubicin in cancer cells by novel cRGD-semipeptide-anchoring liposomes. Molecular Pharmaceutics **11**, 2280-2293 (2014). doi:10.1021/mp400718j

35. Etheridge, M.L., Campbell, S.a., Erdman, A.G., Haynes, C.L., Wolf, S.M., McCullough, J.: The big picture on nanomedicine: the state of investigational and approved nanomedicine products. Nanomedicine : nanotechnology, biology, and medicine **9**, 1-14 (2013). doi:10.1016/j.nano.2012.05.013

36. Ntimenou, V., Fahr, A., Antimisiaris, S.G.: Elastic vesicles for transdermal drug delivery of hydrophilic drugs: a comparison of important physicochemical characteristics of different vesicle types. Journal of biomedical nanotechnology **8**(4), 613-623 (2012).

37. Mourtas, S., Mao, J., Parsy, C.C., Storer, R., Klepetsanis, P., Antimisiaris, S.G.: Liposomal gels for vaginal delivery of the microbicide MC-1220: preparation and in vivo vaginal toxicity and pharmacokinetics. Nano Life **1**(03n04), 195-205 (2010).

38. Kučerka, N., Nieh, M.P., Katsaras, J.: Fluid phase lipid areas and bilayer thicknesses of commonly used phosphatidylcholines as a function of temperature. Biochimica et Biophysica Acta - Biomembranes **1808**, 2761-2771 (2011). doi:10.1016/j.bbamem.2011.07.022

39. Borchert, U., Lipprandt, U., Bilang, M., Kimpfler, A., Rank, A., Peschka-Süss, R., Schubert, R., Lindner, P., Förster, S.: pH-induced release from P2VP-PEO block copolymer vesicles. Langmuir **22**, 5843-5847 (2006). doi:10.1021/la060227t

40. Causse, J., Oberdisse, J., Jestin, J., Lagerge, S.: Small-angle neutron scattering study of solubilization of tributyl phosphate in aqueous solutions of L64 Pluronic triblock copolymers. Langmuir : the ACS journal of surfaces and colloids **26**, 15745-15753 (2010). doi:10.1021/la1021164

41. Chécot, F., Brûlet, A., Oberdisse, J., Gnanou, Y., Mondain-Monval, O., Lecommandoux, S.: Structure of polypeptide-based diblock copolymers in solution: Stimuli-responsive vesicles and micelles. Langmuir **21**, 4308-4315 (2005). doi:10.1021/la0468500

42. Madenci, D., Salonen, A., Schurtenberger, P., Pedersen, J.S., Egelhaaf, S.U.: Simple model for the growth behaviour of mixed lecithin-bile salt micelles. Physical chemistry chemical physics : PCCP **13**, 3171-3178 (2011). doi:10.1039/c0cp01700k

43. Pedersen, J.S., Svaneborg, C., Almdal, K., Hamley, I.W., Young, R.N.: A Small-Angle Neutron and X-ray Contrast Variation Scattering Study of the Structure of Block Copolymer Micelles: Corona Shape and Excluded Volume Interactions. Macromolecules **36**, 416-433 (2003). doi:10.1021/ma0204913

44. Svaneborg, C., Pedersen, J.S.: Form Factors of Block Copolymer Micelles with Excluded-Volume Interactions of the Corona Chains Determined by Monte Carlo Simulations. Macromolecules **35**, 1028-1037 (2002). doi:10.1021/ma011046v

45. Willet, N., Gohy, J.-F., Auvray, L., Varshney, S., Jérôme, R., Leyh, B.: Core-shell-corona micelles by PS-b-P2VP-b-PEO copolymers: focus on the water-induced micellization process. Langmuir : the ACS journal of surfaces and colloids **24**, 3009-3015 (2008). doi:10.1021/la702180c

46. Hammouda, B., Ho, D.L., Kline, S.: Insight into Clustering in Poly (ethylene oxide) Solutions. Macromolecules, 6932-6937 (2004). doi:10.1021/ma049623d

47. Gohy, J.-f., Willet, N., Varshney, S.K., Zhang, J.-x., Jérôme, R.: pH Dependence of the morphology of aqueous micelles poly (ethylene oxide) copolymers. e-Polymers(035), 1-10 (2002).

48. Cajot, S., Lautram, N., Passirani, C., Jérôme, C.: Design of reversibly core cross-linked micelles sensitive to reductive environment. Journal of controlled release : official journal of the Controlled Release Society **152**, 30-36 (2011). doi:10.1016/j.jconrel.2011.03.026

49. Willet, N., Gohy, J.-F., Lei, L., Heinrich, M., Auvray, L., Varshney, S., Jérôme, R., Leyh, B.: Fast Multiresponsive Micellar Gels from a Smart ABC Triblock Copolymer. Angewandte Chemie **119**, 8134-8138 (2007). doi:10.1002/ange.200701757

50. Van Butsele, K., Cajot, S., Van Vlierberghe, S., Dubruel, P., Passirani, C., Benoit, J.-P., Jérôme, R., Jérôme, C.: pH-Responsive Flower-Type Micelles Formed by a Biotinylated Poly(2-vinylpyridine)- block -poly(ethylene oxide)- block -poly(ε -caprolactone) Triblock Copolymer. Advanced Functional Materials **19**, 1416-1425 (2009). doi:10.1002/adfm.200801117

51. Leyh, B., Creutz, S., Gaspard, J.-p., Bourgaux, C.: Shear-Induced Order in Aqueous Micellar Solutions of Amphiphilic Poly (tert- butylstyrene) - b -poly (Na methacrylate) Diblock. 9258-9264 (1998).

52. Jusufi, A.: Molecular simulations of self-assembly processes of amphiphiles in dilute solutions: the challenge for quantitative modelling. Molecular Physics **111**, 3182-3192 (2013). doi:10.1080/00268976.2013.826394

53. Marrink, S., Tieleman, D., Mark, A.: Molecular dynamics simulation of the kinetics of spontaneous micelle formation. The Journal of Physical …, 12165-12173 (2000).

54. Groot, R.: Mesoscopic simulation of polymer-surfactant aggregation. Langmuir **16**, 7493-7502 (2000).

55. Blankschtein, D., Shiloach, a., Zoeller, N.: Thermodynamic theories of micellar and vesicular systems. Current Opinion in Colloid & Interface Science **2**, 294-300 (1997). doi:10.1016/S1359-0294(97)80038-6

56. Maibaum, L., Dinner, A., Chandler, D.: Micelle formation and the hydrophobic effect. The Journal of Physical … **108**, 6778-6781 (2004). doi:10.1021/jp037487t

57. Puvvada, S., Blankschtein, D.: Molecular-thermodynamic approach to predict micellization, phase behavior and phase separation of micellar solutions. I.

Application to nonionic surfactants. The Journal of Chemical Physics **92**, 3710 (1990). doi:10.1063/1.457829

58. Nagarajan, R., Ganesh, K.: Comparison of Solubilization of Hydrocarbons in (PEO-PPO) Diblock versus (PEO-PPO-PEO) Triblock Copolymer Micelles. Journal of colloid and interface science **184**, 489-499 (1996).

59. Stephenson, B.C., Goldsipe, A., Beers, K.J., Blankschtein, D.: Quantifying the hydrophobic effect. 1. A computer simulation-molecular-thermodynamic model for the self-assembly of hydrophobic and amphiphilic solutes in aqueous solution. The journal of physical chemistry. B **111**, 1025-1044 (2007). doi:10.1021/jp065696i

60. Stephenson, B.C., Goldsipe, A., Blankschtein, D.: Molecular dynamics simulation and thermodynamic modeling of the self-assembly of the triterpenoids asiatic acid and madecassic acid in aqueous solution. The journal of physical chemistry. B **112**, 2357-2371 (2008). doi:10.1021/jp074310g

61. Srinivasan, V., Blankschtein, D.: Effect of counterion binding on micellar solution behavior: 1. Molecular-thermodynamic theory of micellization of ionic surfactants. Langmuir, 9932-9945 (2003).

62. Nagarajan, R., Wang, C.: Theory of surfactant aggregation in water/ethylene glycol mixed solvents. Langmuir, 5242-5251 (2000).

63. Goldsipe, A., Blankschtein, D.: Molecular-thermodynamic theory of micellization of pH-sensitive surfactants. Langmuir : the ACS journal of surfaces and colloids **22**, 3547-3559 (2006). doi:10.1021/la052896x

64. Jönsson, B., Edholm, O., Teleman, O.: Molecular dynamics simulations of a sodium octanoate micelle in aqueous solution. Journal of Chemical Physics **85**, 2259-2271 (1986). doi:10.1063/1.451122

CHAPTER III

Mixed block copolymers micelles

Arnaud Joset, Kathy Van Butsele, Annie Brûlet, Christine Jérôme, Bernard Leyh

Abstract

In this chapter, the preparation of micellar nanocarriers made of a mixture of diblock biocompatible copolymers, and their structural analysis by Small-Angle Neutron Scattering (SANS) are presented and discussed. These micelles have potential use in drug delivery applications against cancer. Their core is built from the hydrophobic polycaprolactone (PCL) block. The corona of hydrophilic polyethylene oxide (PEO) stabilizes the micelles by ensuring their solubility. A pH-sensitive sequence of poly(2-vinylpyridine) (P2VP) was also incorporated. When the pH is acidic, the P2VP is protonated and the chains are affected by repulsive interactions. In order to quantitatively measure the extension of the P2VP block at low pH and the resulting effect on the sizes of the core, corona and global radius of the micelles, we prepared PCL_{34}-b-$P2VP_{52}$ / PCL_{37}-b-$PEO_{(d4),104}$ and PCL_{64}-b-$P2VP_{31}$ / PCL_{65}-b-$PEO_{(d4)104}$ 50:50 mixtures of diblock copolymers. The SANS cross sections of the resulting mixed micelles have been recorded under different pH conditions. To analyze the data and infer the relevant structural parameters, we developed theoretical models consisting of a spherical water-free PCL core surrounded by a PEO corona of Gaussian chains with a thickness estimated as twice the chain gyration radius, Rg. Several alternatives for handling the P2VP zone have been proposed. The P2VP molecules are either treated as Gaussian chains, as rigid rods or as filling a homogeneous shell of thickness L with possible water penetration. The fitting of the models to the experimental scattering cross sections gives access to important structural parameters like the aggregation number, the core radius, the radius of gyration of the PEO corona chains and the thickness of the P2VP shell. Even though both samples display a decrease of the P2VP shell thickness upon pH increase, their response is nevertheless differentiated. Contrary to the sample with the shorter PCL block, the sample with the larger PCL block and the shorter P2VP block shows barely any micelle reorganization unless the temperature is increased to 70°C.

1 Introduction

Micelles built from mixed block-copolymers show many advantages for the development of colloid solutions with targeted compositions and properties. Such mixed copolymer micelles (MCM) result from the aggregation of chains of different compositions [1-8]. Their first obvious advantage is the easier synthesis of the building blocks. Generally, the preparation of multi-sequenced copolymers requires more steps, resulting in smaller yields compared to the preparation of several simpler copolymers [9]. The second advantage is the facility to study several micelles compositions by tuning one of the sequences (degree of polymerization, nature of the block, etc) without affecting the others. Finally, diblock copolymers are more easily available from commercial sources than triblock copolymers.

Li et al [10] prepared multi-functional hybrid micelles with magnetic nanoparticles embedded in the core. The micelles are made of pluronic F127 block copolymers, and peptide amphiphiles (PA). The purpose of such nano-objects is to promote theranostic applications, that is, the combination of drug release and diagnostic. The hydrophilic block of the PA is able to link to Fe^{3+} and Fe^{2+} ions to provide magnetic properties. Finally, the core is loaded with a drug which can be released at the location of sick tissues. The formation of micelles is quite easily achieved by mixing PA and F127 in water in the presence of the drug, $FeCl_2$ and $FeCl_3$.

Wu et *al* [11] described the formation of MCM in water from Poly(ethylene glycol)-*b*-poly(lactide) (PEG-b-PLA) and poly(lactide)-*b*-poly(N-isopropylacrylamide) PLA-*b*-PNIPAM. The core is built from the PLA sequence and the corona is composed of the PEG block. The PNIPAM is water-soluble at temperatures below the lower critical solution temperature (LCST=32°C) and is insoluble above. The LCST may be tuned by varying the copolymer composition and length. The micelles incorporated Ibuprofen, a well-known anti-fever drug. The goal of this study was to trigger the release of Ibuprofen through PEG channels as the PNIPAM chains collapse on the core at higher temperature. Wu *& al* [11] studied the drug release at 37 and 42 °C and observed higher rates at 42°C.

Kuo et *al* [6] prepared self-assembled hydrogen-bonded complexes that have vesicle and spherical structures from two block copolymers in non-selective solvents. First, they observed the formation of vesicles from the intermolecular complex formed after mixing

polystyrene-*b*-poly(4-vinylphenol) (PS-*b*-PVPh) with poly(methylmethacrylate)-*b*-poly(4-vinylpyridine)(PMMA-*b*-P4VP) in tetrahydrofuran (THF). Hydrogen bonding between the sites on the PVPh and P4VP blocks drives the process. In contrast, well-defined spherical structures form after blending PS-*b*-PVPh with PMMA-*b*-P4VP in N,N-dimethylformamide (DMF): the hydrogen bonds between the PVPh and P4VP blocks in DMF are weaker than those in THF. The resulting nano-objects are spherical inverse micelles which compartmented coronas made of the PS and PMMA blocks.

Halperin [8] demonstrated that a mixture of A-*b*-C and B-*b*-C diblock copolymers will only lead to co-micellization into mixed micelles if the two end blocks display low incompatibility. We may also mention the work of Koňák et al [7] who studied the comicellization of PS-*b*-PMMA diblock copolymers with different molecular weight.

Van Butsele & al [12] prepared micelle samples from a 50/50 mixture of diblock copolymers made of poly(ε-caprolactone) (PCL), poly(ethylene oxide) (PEO) and poly(2-vinylpyridine) (P2VP) (Figure 1). Such systems are expected to find applications in drug delivery against cancer [13,14,12]. The sample compositions were: PCL_{34}-*b*-PEO_{114} mixed with PCL_{32}-*b*-$P2VP_{52}$. The PCL is an aliphatic hydrophobic semi-crystalline polyester. Its melting point is relatively low (60°C). Its biocompatibility has been approved by the FDA in the USA [15-18]. It was chosen for its ability to be hydrolyzed in acidic conditions [19]. The PEO block is hydrophilic in the investigated temperature range (T< 60°C) [20]. It furthermore stabilizes the nanocarriers with respect to the plasma proteins in biological applications [21-23,14,13,24,25] and is also biologically safe [26-30].

At neutral pH, the hydrophobic zone consists of a core of PCL surrounded by a shell of neutral P2VP [12,31,32]. The hydrophilic corona is made of PEO chains. When pH decreases below ~4, the P2VP chains become substantially protonated and hydrophilic so that the hydrophobic zone is expected to have a reduced size, which facilitates the diffusion of the drug out of the core [33]. The pH in the neighborhood of tumor cells is lower than in healthy cells [13,14]. As a result, these micelles are expected to deliver their drug near the cancerous cells without affecting the healthy cells [13,14]. On the other hand, the extension of the repulsive P2VP charged chains might result in a global size increase of the micelles.

Van Butsele et al performed Dynamic light scattering (DLS) and Transmission Electron Microscopy (TEM) measurements as a function of the HCl concentration used for sample

preparation [12]. Both techniques led to the conclusion that the size of the micelles at neutral pH is larger than at acidic pH. Furthermore, the aggregation numbers (N_m) were inferred by Static Light Scattering (SLS) measurements and were found equal to 111 and 37 at neutral and acidic pH respectively. At this point, no information was available on the internal structure of the micelles, that is, the extension of the P2VP chains or the PEO radius of gyration.

The purpose of the present work is to obtain a more complete image of the micellization process of these mixed systems by performing Small-Angle Neutron Scattering (SANS) measurements, taking advantage of the H/D contrast variation. Two samples were prepared: [PCL$_{37}$-b-PEO$_{(d4)104}$ mixed with PCL$_{34}$-b-P2VP$_{52}$] and [PCL$_{65}$-b-PEO$_{(d4)104}$ mixed with PCL$_{64}$-b-P2VP$_{31}$]. The first sample is similar to those prepared by Van Butsele & *al* [12] but the PEO block of our version is fully deuterated in order to increase its contrast with PCL, P2VP and H$_2$O. We call it *sample I* in the following sections. The second sample shows longer PCL sequences and a shorter P2VP block. It is called *sample II* in the next sections. Several experiments were performed on *sample I* at concentration 0.1 and 0.4% w/w to evaluate the dilution effect on the structure. *Sample II* was investigated at two temperatures: 25°C and 70°C in order to observe any contraction of the PEO in the vicinity of its LCST [20,34]. The concentration of *Sample II* was equal to 0.4 % w/w.
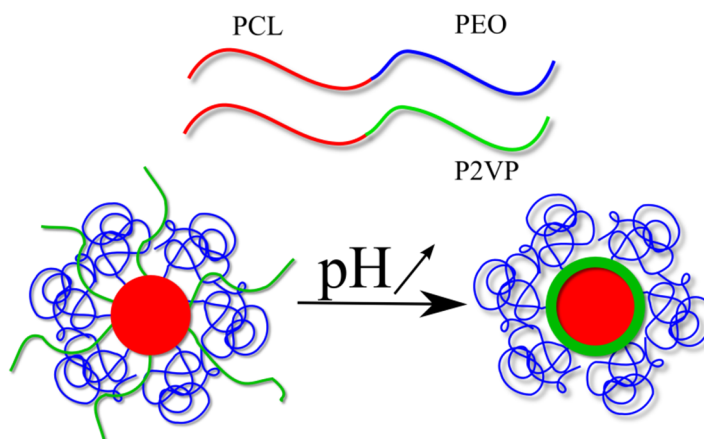
Figure 1 *Diblock copolymers and MCM made of PCL (red), PEO(blue) and P2VP (green). At acidic pH, the P2VP is positively charged and is hydrophilic. It precipitate on the core at basic pH.*

2   Materials and methods

2.1   Copolymer synthesis

The synthesis of the diblock copolymers was performed as previously reported [12,35]. The first diblock PCL_{37}-b-$PEO_{(d4),104}$ was prepared from PEO_{d4} of molecular weight (M_n) equal to 5000 g mol^{-1} which was purchased from Polymer Source™ . The size of the PCL block was reached by using the appropriate ratio of monomer to the PEO macro-initiator. The degree of polymerization was determined by ^{1}NMR by integration of characteristic ^{1}H NMR resonances for the initiator and for PCL or P2VP.

The second diblock PCL_{34}-*b*-$P2VP_{52}$ was prepared from a dual initiator bearing a primary alcohol and an alcoxyamine. The former allows polymerizing the ε-caprolactone (ε-CL) with a ring opening mechanism and the latter initiates the 2VP polymerization through a "controlled" nitroxide-mediated radical polymerization[12].. The composition of the blocks and their molecular weights are given in Table 1.

Table 1 *Composition of the block copolymers.* ^{a}*Polymer Source™ information determined by SEC measurements.* ^{b}*Calculated by integration of characteristic* ^{1}*H NMR resonances for the initiator and PCL or P2VP. The micellar solutions were prepared from mixture of samples A+B (sample I) and C+D (sample II).*

	Sample PCL_x-b-PEO_y ($P2VP_z$)	M_n PCl^b / g mol^{-1}	M_n PEO^a (or $P2VP^b$) / g mol^{-1}
A	PCL_{37}-*b*-$PEO_{(d4),104}$	4250	5000
B	PCL_{34}-*b*-$P2VP_{52}$	3900	5467
C	PCL_{65}-*b*-$PEO_{(d4),104}$	7470	5000
D	PCL_{64}-*b*-$P2VP_{31}$	7350	3259

2.2   Micellization of diblock micelles

Diblock copolymer solutions in D_2O and H_2O were investigated. The preparation of the aqueous micellar solutions was performed by adding 20 ml of water acidified with HCl to 5 ml of a copolymer mixture (50/50) solution in N,N-dimethylformamide (DMF) (1% w/w). The DMF is a good solvent for the three blocks. The solution was stirred for 2 hours and was then dialyzed against 800mL of milliQ water (or D_2O) acidified with HCl through cellulose

dialysis membranes (Spectrapor, cut off 3500Da). Because PCL is hydrophobic in these conditions, micellar solutions are obtained. Samples at higher pH conditions were basified with NaOH (0.1M). All samples were filtered through microfilters with an average pore size of 0.2 μm.

Sample I was analyzed under two pH conditions (acidic and basic). *Sample II* was analyzed under three pH conditions: acidic, intermediate and basic conditions. Table 2 displays the experimental pH and concentration conditions.

Table 2 *Experimental concentration and pH conditions at which the SANS measurements were performed.*

		Acidic pH	Intermediate pH	Basic pH
Sample I	0.1 % w/w	1.7 ± 0.50	/	10.8 ± 0.5
	0.4 % w/w	1.2 ± 0.50	/	8.8 ± 0.5
Sample II	0.4 % w/w	1.5 ± 0.50	4.5 ± 0.5	10.6 ± 0.5

2.3 Small-Angle Neutron Scattering

Small-angle neutron scattering (SANS) experiments were performed at the Laboratoire Léon Brillouin in Saclay, France, with the PACE instrument under the following conditions:

(i) wavelength = 5 Å, sample-to-detector distance = 1.5 m, (ii) wavelength = 12.0 Å, sample-to-detector distance = 4.7 m, so that a scattering vector (q) range from 0.00344 to 0.238Å^{-1} was available at a resolution ($\Delta q/q$) equal to 10%. The data were recorded with a two-dimensional detector consisting of 30 concentric rings of 1 cm thickness. Samples were contained in quartz cells with a 2 mm path length. Corrections for the electronic and ambient background noise and for sample holder contributions were carried out according to standard data handling procedures ([36]). The data corresponding to the copolymer solutions and to the pure solvent (D_2O or H_2O) were handled in an identical way, and the scattering intensities were converted to macroscopic scattering cross-sections per unit volume, $d\Sigma/d\Omega$ (cm^{-1}), by normalization with respect to the incoherent scattering of H_2O. The copolymer contribution was obtained by subtracting the cross section of the solvent, weighted by its volume fraction.

The concentrations mentioned in Table 2 correspond to the dilute regime where the structure factor can be assumed equal to 1 in the investigated q range, so that the macroscopic scattering cross section gives directly access to the form factor of the assembled nano-objects.

3   Models

In order to obtain information on the internal structure of the micelles, three models have been developed. They all derive from the Pedersen and Gerstenberg (PG) approach [37]. These authors assume that the core is spherical (radius denoted as R_c) and solvent free. The corona consists of Gaussian chains with a radius of gyration called R_g. The chains are anchored at $R_c + R_g$ in order to prevent the penetration of the chains in the core. In the models developed in the present work, the core is built from the PCL and the corona from the PEO chains. Depending on the pH, the P2VP block is part of the corona or of the core. Three models take into account this additional P2VP contribution in different ways. The first model assumes a homogeneous shell of P2VP around the PCL core. The second model assumes a corona built from two kinds of Gaussian chains: PEO and P2VP, each kind of chain having its own radius of gyration, $R_{g,PEO}$ and $R_{g,P2VP}$, respectively. These corona chains are assumed to be randomly distributed without any bias in favor of either kind of copolymer chain. The third model assumes that the ionized P2VP chains in acidic solution are extended because of the electrostatic repulsion and can accordingly be described as rigid rods with an effective length L. Finally, the polydispersity of the micelles due to a dispersion of the aggregation number, N_m, is taken into account through a Gaussian size distribution: $\Gamma(N_m)$. The aggregation number is defined as the number of PCL blocks in a micelle. The number of PEO or PCL chains is then equal to $N_m/2$.

The total excess scattering length $\tilde{b}$ of a block is calculated [38] from the atomic content of the monomer and from its degree of polymerization. For example, the excess scattering length of the PCL block, $\tilde{b}_{PCL}$ is calculated from the following expression:

$$\tilde{b}_{PCL} = z_{PCL}\left(b_{\varepsilon-CL} - \frac{v_{\varepsilon-CL}}{v_w} b_w \right) \tag{1}$$

where z_{PCL} is the degree of polymerisation of the PCL block, $b_{\varepsilon-CL}$ is the scattering length of the ε-CL monomer unit, and $v_{\varepsilon-CL}$ is its molecular volume. The volume and the scattering length of the solvent molecules, H_2O or D_2O are denoted as v_w and b_w respectively.

3.1   Model 1: PCL core, P2VP homogenous shell and PEO Gaussian chains

The first model involves a homogeneous P2VP shell surrounding the PCL core. The thickness of the shell is denoted as L and its outer radius is $R_e = R_c + L$. The PG model is

modified to take into account the contribution of the P2VP shell and the additional interference terms. The following equations summarize the different contributions to the scattering cross section per micelle. The first three contributions [equations (2), (3), and (4)] arise from the scattering of the individual subparts of the micelles: the PCL core [$F_c(q)$], the PEO corona [$F_{co}(q)$] and the P2VP shell [$F_s(q)$]:

$$F_c(q) = N_m^2 \tilde{b}_{PCL}^2 \left\{ \frac{3}{(qR_c)^3} \left[\sin(qR_c) - qR\cos(qR_c) \right] \right\}^2 \tag{2}$$

$$F_{co}(q) = N_m \tilde{b}_{PEO}^2 \frac{\exp(-q^2 R_{g,PEO}^2) + q^2 R_{g,PEO}^2 - 1}{(q^2 R_{g,PEO}^2)^2} \tag{3}$$

$$F_s(q) = \left[\frac{3N_m}{2} \frac{\tilde{b}_{P2VP}}{q^3(R_e^3 - R_c^3)} \right]^2 \left\{ \sin(qR_e) - qR_e\cos(qR_e) - \sin(qR_c) + qR_c\cos(qR_c) \right\}^2 \tag{4}$$

The other contributions are interference terms. The first one corresponds to the interference between the core and the corona $F_{c-co}(q)$:

$$F_{c-co}(q) = N_m^2 \tilde{b}_{PCL}\tilde{b}_{PEO} \frac{3\left[\sin(qR_c) - qR_c\cos(qR_c)\right]}{(qR_c)^3} \frac{1 - \exp(-q^2 R_{g,PEO}^2)}{q^2 R_{g,PEO}^2}$$
$$\times \frac{\sin\left[q(R_c + R_{g,PEO})\right]}{q(R_c + R_{g,PEO})} \tag{5}$$

The second one is the cross-term between the core and the shell:

$$F_{c-s}(q) = 9 \frac{N_m^2 \tilde{b}_{PCL}\tilde{b}_{P2VP}}{(qR_c)^3 q^3(R_e^3 - R_c^3)} \left[\sin(qR_c) - qR\cos(qR_c) \right]$$
$$\times \left[\sin(qR_e) - qR_e\cos(qR_e) - \sin(qR_c) + qR_c\cos(qR_c) \right] \tag{6}$$

The third one describes the interference between the corona and the shell:

$$F_{s-co}(q) = 2\left(\frac{N_m}{2}\right)^2 \tilde{b}_{PEO}\tilde{b}_{P2VP} 3\frac{\left[\sin(qR_e) - qR_e\cos(qR_e) - \sin(qR_c) + qR_c\cos(qR_c)\right]}{q^3\left(R_e^3 - R_c^3\right)}$$

$$\times \left[\frac{\sin\left[q\left(R_c + R_{g,PEO}\right)\right]}{q\left(R_c + R_{g,PEO}\right)}\right]\left[\frac{1-\exp\left(-q^2R_{g,PEO}^2\right)}{q^2R_{g,PEO}^2}\right] \tag{7}$$

The last interference term takes into account the interference between scatterers belonging to different corona chains:

$$F_{co-co}(q) = \frac{N_m}{2}\left(\frac{N_m}{2}-1\right)\tilde{b}_{PEO}^2\left[\frac{1-\exp\left(-q^2R_{g,PEO}^2\right)}{q^2R_{g,PEO}^2}\right]^2\left[\frac{\sin\left[q\left(R_c + R_{g,PEO}\right)\right]}{q\left(R_c + R_{g,PEO}\right)}\right]^2 \tag{8}$$

Finally, the cross section per micelle, $F_{shell}(q)$, can be written as the sum of the previously described contributions (2) to (8):

$$F_{shell}(q) = F_c(q) + F_s(q) + F_{co}(q) + F_{c-s}(q) + F_{c-co}(q) + F_{s-co}(q) + F_{co-co}(q) \tag{9}$$

3.2 Model 2: PCL core, mixed P2VP and PEO Gaussian chains

A second model has been developed in order to assess the robustness of the analysis procedure. It takes into account the contributions of P2VP as Gaussian chains with a radius of gyration equal to $R_{g,P2VP}$. Such contributions are similar to the ones presented for the PEO chains in section 3.1, provided $\tilde{b}_{PEO}$ is replaced by $\tilde{b}_{P2VP}$. To save space in the mathematical developments, these changes are implicitly done by adding a "prime" to the name of the corresponding PEO contribution: for example, $F_{co}(q)$ (equation (3)) applied to P2VP becomes $P'_{co}(q)$. The only additional cross-term takes into account the interferences between the scatterers of a chain of PEO and of a chain of P2VP, $P_{co-co'}(q)$.

$$F_{co-co'}(q) = \tilde{b}_{PEO}\tilde{b}_{P2VP}\left(\frac{N_m}{2}\right)^2\left[\frac{1-\exp\left(-q^2R_{g,P2VP}^2\right)}{q^2R_{g,P2VP}^2}\right]\left[\frac{1-\exp\left(-q^2R_{g,PEO}^2\right)}{q^2R_{g,PEO}^2}\right]$$

$$\times\left[\frac{\sin\left[q\left(R_c + R_{g,PEO}\right)\right]}{q\left(R_c + R_{g,PEO}\right)}\right]\left[\frac{\sin\left[q\left(R_c + R_{g,P2VP}\right)\right]}{q\left(R_c + R_{g,P2VP}\right)}\right] \tag{10}$$

The cross section per micelle of the model involving two kinds of Gaussian chains, $F_{chains(q)}$, is then equal to

$$F_{chains}(q) = F_c(q) + F_{co}(q) + F_{co}^{'}(q) + F_{c-co}(q) + F_{c-co}^{'}(q) + F_{co-co}(q) + F_{co'-co'}(q) + F_{co-co'}(q) \quad (11)$$

3.3 Model 3: PCL core, P2VP rods, and PEO Gaussian chains

A third model has been developed. It describes the P2VP blocks as rods with an effective length equal to L. Following the same logic as in 3.2, the different contributions are given below.

The self-contributions of the rods is given by the following equation [39]

$$F_r(q) = \frac{N_m}{2} \tilde{b}_{P2VP}^2 \left[\frac{2}{qL} Si(qL) - \frac{\sin^2\left(\frac{qL}{2}\right)}{\left(\frac{qL}{2}\right)^2} \right] \quad (12)$$

The interference term between the core and the rods $F_{c-r}(q)$ is equal to:

$$F_{c-r}(q) = N_m^2 \tilde{b}_{P2VP} \tilde{b}_{PCL} \left\{ \frac{3\left[\sin(qR_c) - qR_c \cos(qR_c)\right]}{(qR_c)^3} \right\} \left\{ \frac{Si\left[q(R_c + L)\right] - Si\left[qR_c\right]}{qL} \right\} \quad (13)$$

The interference term between the corona chains and the rods $F_{r-co}(q)$ is given by:

$$F_{r-co}(q) = \frac{N_m^2}{2} \tilde{b}_{PEO} \tilde{b}_{P2VP} \left\{ \frac{\sin\left[q(R_c + R_g)\right]}{q(R_c + R_g)} \right\} \left\{ \frac{Si\left[q(R_c + L)\right] - Si\left[qR_c\right]}{qL} \right\}$$
$$\times \left\{ \frac{1 - \exp\left(-q^2 R_g^2\right)}{q^2 R_g^2} \right\} \quad (14)$$

The last interference term takes into account the interference between scatterers belonging to different rod chains:

$$F_{r-r}(q) = \frac{N_m}{2}\left(\frac{N_m}{2} - 1\right) \tilde{b}_{P2VP}^2 \left\{ \frac{Si\left[q(R_c + L)\right] - Si\left[qR_c\right]}{qL} \right\}^2 \quad (15)$$

The cross section per micelle in this model $F_{rods\,(q)}$, is then equal to

$$F_{rods}(q) = F_c(q) + F_{co}(q) + F_r(q) + F_{c-co}(q) + F_{c-r}(q) + F_{co-co}(q) + F_{r-r}(q) + F_{co-r}(q) \quad (16)$$

3.4 Fitting procedures

The theoretical scattering cross section is finally convoluted with an apparatus function in order to take into account the experimental q-resolution. A triangular shape has been assumed for the scattering vector spread ($\Delta q/q = 10\%$). The resulting modelled SANS cross sections are then fitted to the experimental scattering curves and the quality of the fits has been monitored by calculating the χ^2 between the logarithm of the experimental and theoretical data, in order to weight similarly the whole q-range.

4 Comparison of SANS and DLS size distributions

To compare our SANS data with DLS data obtained by Van Butsele et al [12] in a previous work, we applied the following procedure. The analysis of the SANS data provides us with a number-weighted radius distribution, denoted Γ_n. The CONTIN algorithm used for the DLS data analysis leads to an intensity-weighted distribution, Γ_i, of the hydrodynamic radius. These two distributions are related but not equivalent and may be connected through the following equation [40,41]:

$$\Gamma_n = \frac{\Gamma_i}{\left[M\left(R\right)\right]^2 P(q;R)} \tag{17}$$

where $M(R)$ is the molecular weight of a micelle of global radius R. R is defined as $R_c + T$ where T is equal to $2\,R_{g,PEO}$ or to L depending which sequence is longer. $M(R)$ can be calculated based on the aggregation number N_m. $P(q;R)$ is the form factor of the micelle at the q value corresponding to the wavelength and detection angle of the DLS instrument. Because all the information required to calculate $P(q;R)$ is available from the analysis of our SANS data, we found more consistent and practical to convert the Γ_n SANS distributions into Γ_i distributions which are then comparable to the DLS distributions. This makes an easy and relevant comparison between hydrodynamic radii obtained by DLS, R_h, and average radii, R_i, obtained from SANS fits.

5   Results and discussion

DLS and SANS size distributions are observed to be monomodal. Figure 2 shows typical experimental cross sections in D_2O for *sample I* and *II*.
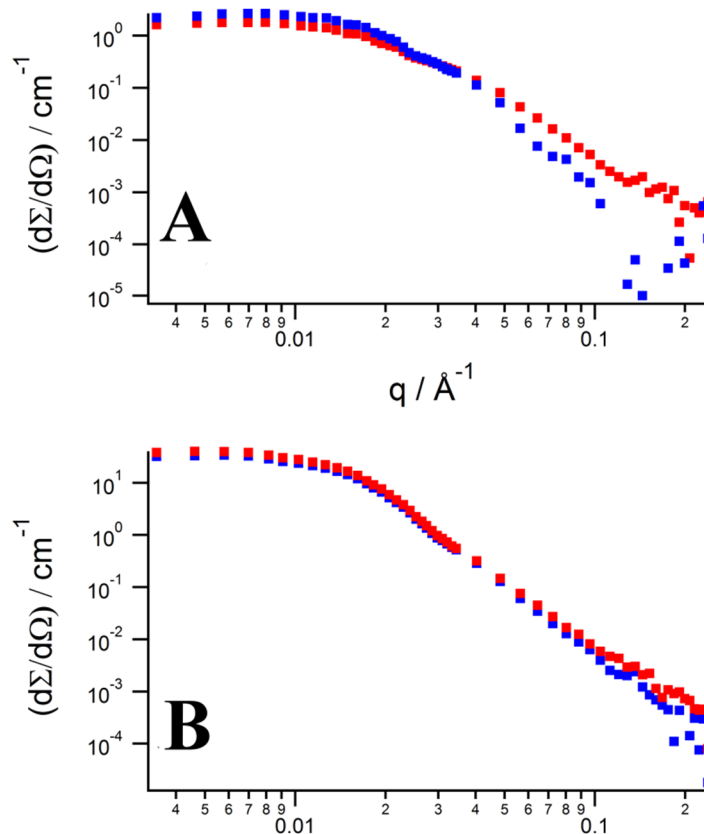
Figure 2 *Experimental cross sections of mixed micelles at acidic (red) and basic pH (blue). A: PCL_{37}-b-$PEO_{(d4),104}$ mixed with PCL_{34}-b-$P2VP_{52}$ (sample I) B: PCL_{65}-b-$_{PEO(d4),104}$ mixed with PCL_{64}-b-$P2VP_{31}$ (sample II). The intensity of B is larger than that of A, indicating larger and/or more numerous objects. The different behaviors observed at intermediate and large q values can be assigned to the structural response of the P2VP block upon pH variation.*

Figure 3 compares the fitting of the three models presented in Section 3 to an acidic mixed copolymer solution. The results show that the three models give very similar results. Slight discrepancies appear in the $0.1 – 0.2$ $Å^{-1}$ range, where the experimental uncertainties are larger anyway. Because of the similar results provided by the three models, it was decided to focus on the first two models, which describe the P2VP contribution either as a homogeneous shell or as a Gaussian chain collection.
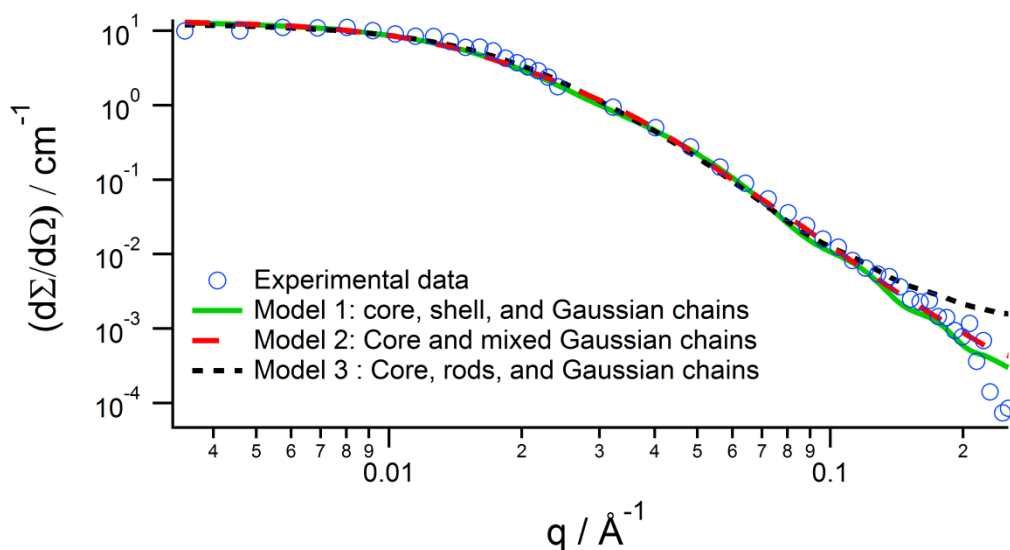
Figure 3 *SANS macroscopic cross section of sample I 0.4% w/w at pH = 1.2 (blue dots). Comparison of tree models accounting for the P2VP contribution as either a homogenous shell of thickness L (green solid line), a collection of Gaussian chains with a radius of gyration R_g (red dashed line), or rods of effective length L (black dotted line) [39](see appendix I). R_c= 39Å, L = 54Å and R_g = 18Å for the three curves.*

A representative series of experimental data and associated fits involving models 1 and 2are displayed in Figure 4.
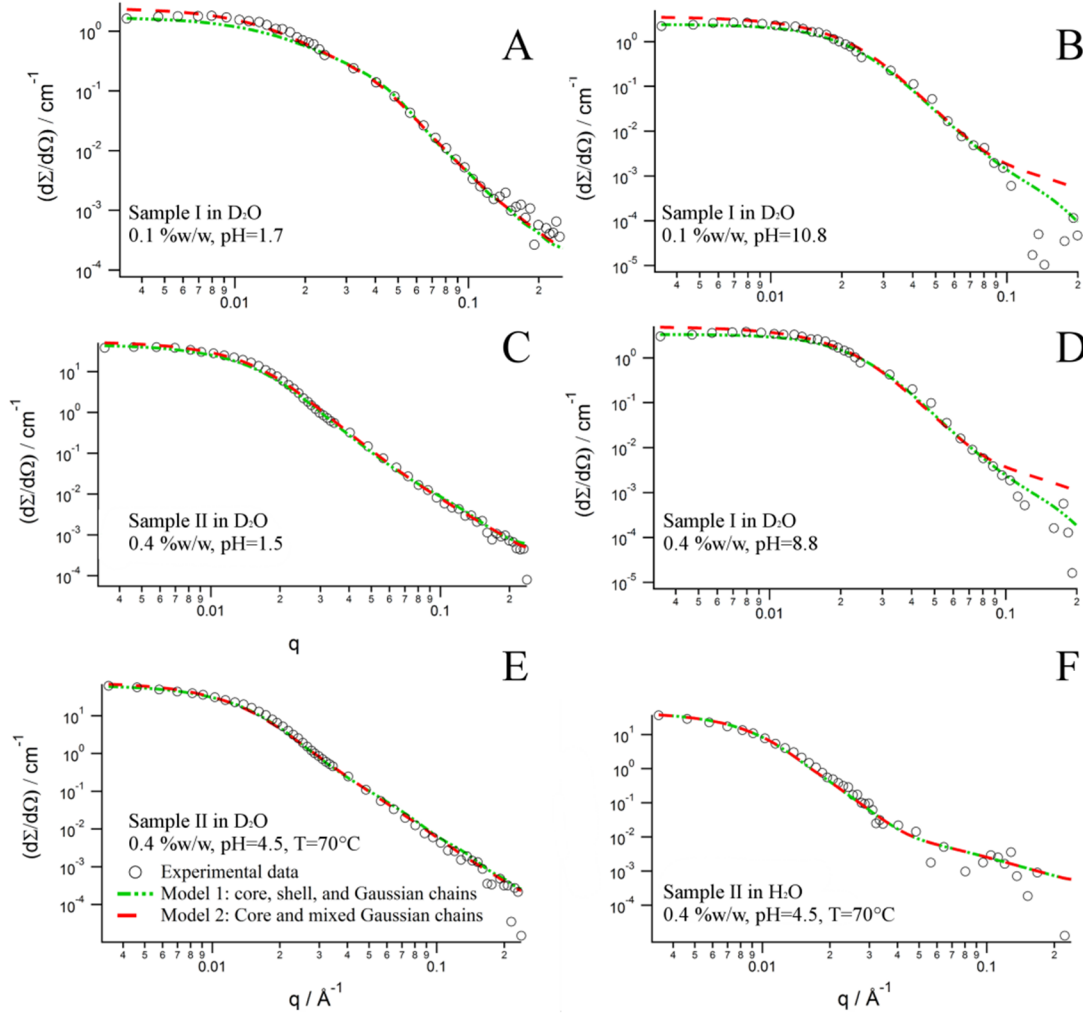
Figure 4 *Comparison of the two models considered in the fitting process for the SANS form factor. A: Sample I in D$_2$O, 0.1%w/w, pH=1.7. B: Sample I in D$_2$O, 0.1 % w/w, pH=10.8. C: Sample II in D$_2$O, 0.4 % w/w, pH= 1.5, T=25°C. D: Sample I in D$_2$O, 0.4 % w/w, pH=8.8. E: Sample II in D$_2$O, 0.4 % w/w, pH=4.5, T=70°C. F: Sample II in H$_2$O, 0.4 % w/w, pH = 4.5, T = 70°C. Divergences between the shell and the Gaussian chain models only occur at basic pH in D$_2$O for sample I: the experimental data follow a q^{-4} Porod law (see chapter 2) that the Gaussian chain model cannot reproduce [47].*

Figure 5 to 8 summarize the data inferred from the fits. The structural parameters obtained using either model and in both solvents, H$_2$O and D$_2$O, are compatible within experimental error and have been averaged in these figures.

As will be shown in the following discussion, the analysis of the SANS data for *sample I* leads to results compatible with, but more detailed than, the observations of Van Butsele *& al.*

[12]. The comparison with the data for *sample II* provides additional information on the influence of the chemical composition of the blocks on the micelle structure.

Linked to the respective polymerization degree of the P2VP block, the thickness of the P2VP zone is larger in the micelles of *sample I* than in *sample II*. The first noticeable result, valid for both samples, is the expected decrease of the thickness (*L)* of this shell as the pH increases (Figures 5 and 7). A decrease of 50 to 65% is observed. This suggests that P2VP is a good choice for pH responsive behavior, even with relatively short blocks (*Sample II,* DP = 31). The most noticeable collapse is logically observed for *sample I* with its longer P2VP sequence. . For *sample I*,the P2VP thickness at acidic pH is larger for the 0.4% w/w sample than for the 0.1 % w/w one. This difference may be related to the lowest pH value for the more concentrated sample (see Table 2): the additional positives charges may increase the electrostatic repulsions between the 2-VP monomer units, resulting in more extended P2VP chains.

Sample I exhibits results compatible with the original study of van Butsele et al. [12]: the total radius ($R_c + T$ see section 4) of the micelles increases with pH. The size increase of *sample I* was also confirmed by DLS measurement. The average hydrodynamic radius R_h increases by nearly 50% from 16.5 to 25 nm (C = 0.1 % w/w). This is compatible with our increase of R_i from 12.9 to 16.5 nm (+28%) and from 15.3 to 18.5 nm (21%) for the 0.1 and 0.4 % w/w samples respectively. The aggregation number (N_m) increases accordingly from 62 to 140 and from 90 to 150 respectively (Figure 5). Van Butsele measured an increase from 37 to 111 by static light scattering (SLS). The differences between both sets of data could be ascribed to the difference of experimental approach. SLS provides information on the average molar mass of the micelles, $M_{w,mic}$, but data extrapolation at infinite dilution and zero scattering angle need to be performed . When $M_{w,mic}$ is divided by the molar mass of a chain, the result is equal to the aggregation number [42-48]. The difference between SANS and SLS values are then probably linked to different hypotheses (i.e. the micelles are described as homogeneous spheres in SLS and the aggregation number is assumed invariant with concentration in our SANS data procedure) [49]. It has also to be kept in mind that N_m is proportional to the volume of the core and thus to R_c^3 so that an increase of 25% of the core radius leads to a factor 2 for the aggregation number.

Whatever its exact extent, the increase of N_m with pH is linked to the decrease of the zeta potential of the micelles. Van Butsele measured it previously [12] to be lower than 10 mV at

basic pH. The lack of electrostatic repulsion between the chains might favor micelle reorganization.

Furthermore, the average area per chain at the core-corona interface, $\langle A_c \rangle$, can be inferred from the aggregation number and from the core radius.

$$\langle A_c \rangle = 4\pi \left\langle \frac{R_c^2}{N_m} \right\rangle = 3\, z_{PCL}\, v_{\varepsilon-CL} \left\langle \frac{1}{R_c} \right\rangle \tag{18}$$

$\langle A_c \rangle$ is observed to decrease upon pH increase, from 600 Å^2 to 370Å^2 for the 0.1 %w/w sample and from 570Å^2 to 510Å^2 for the 0.4 %w/w sample (Figure 6). This could mean that when the P2VP collapses on the core, the surface of hydrophobic material exposed to water, before the micelles reorganize, becomes too large. The response of the system to this unfavorable lipophilic/hydrophilic balance is then the formation of larger micelles with a smaller interfacial area per chain.

This chain reorganization mechanism is compatible with the observed significant increase of the micelle polydispersity upon pH increase, from 26Å to 32Å and from 37 to 45Å for the 0.1% w/w and 0.4% w/w sample, respectively.
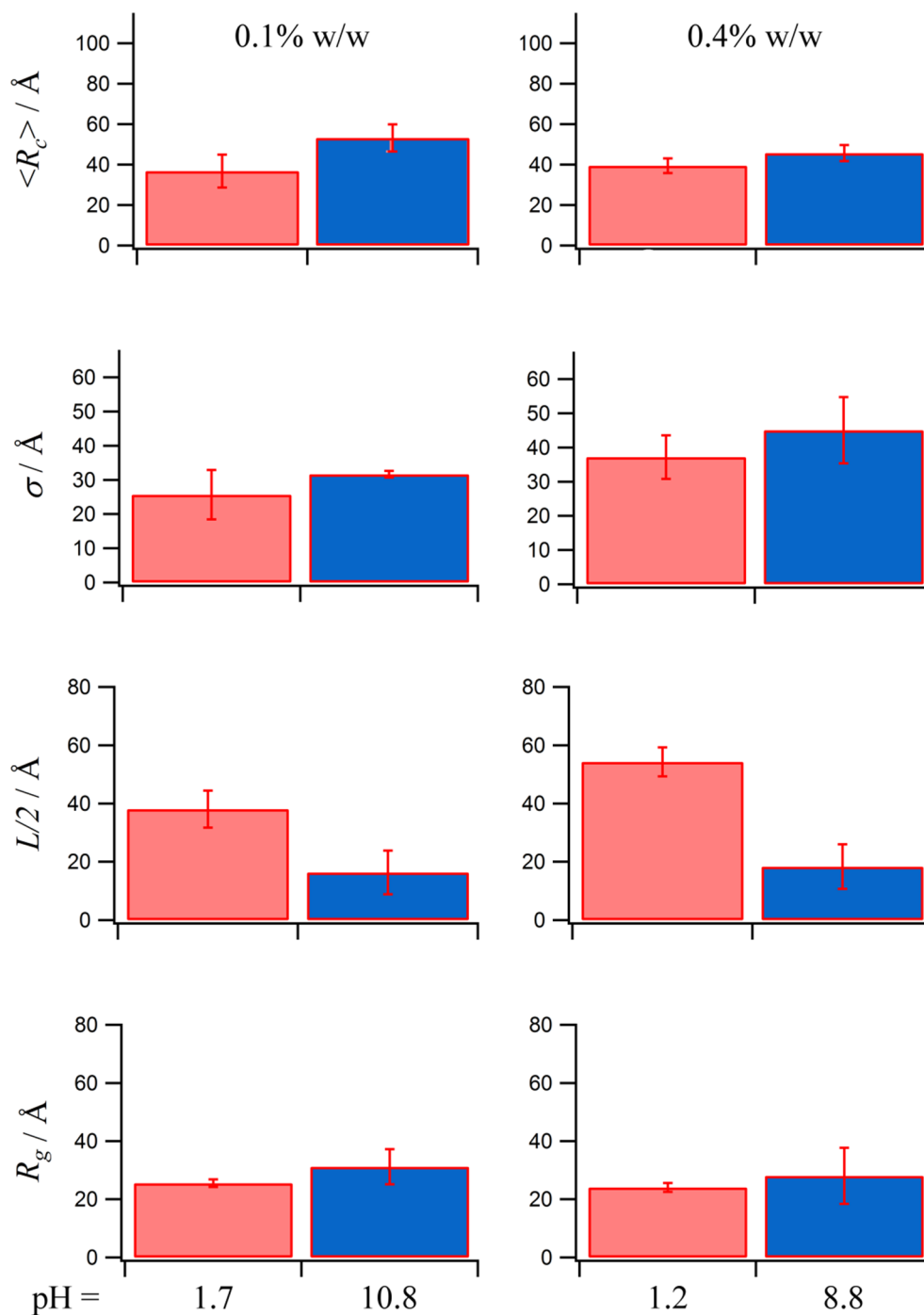
Figure 5 *Average structural parameters for sample I (PCL$_{37}$-b-PEO$_{(d4),104}$ mixed with PCL$_{34}$-b-P2VP$_{52}$) as a function of pH at concentrations equal to 0.1 and 0.4 % w/w. $<R_c>$: average PCL core radius; σ: standard deviation of the core size; L/2: half thickness of the P2VP shell; it is assumed to be equal to the radius of gyration of P2VP in the mixed Gaussian chain model (model 2); R$_g$: radius of gyration of the PEO chains.*
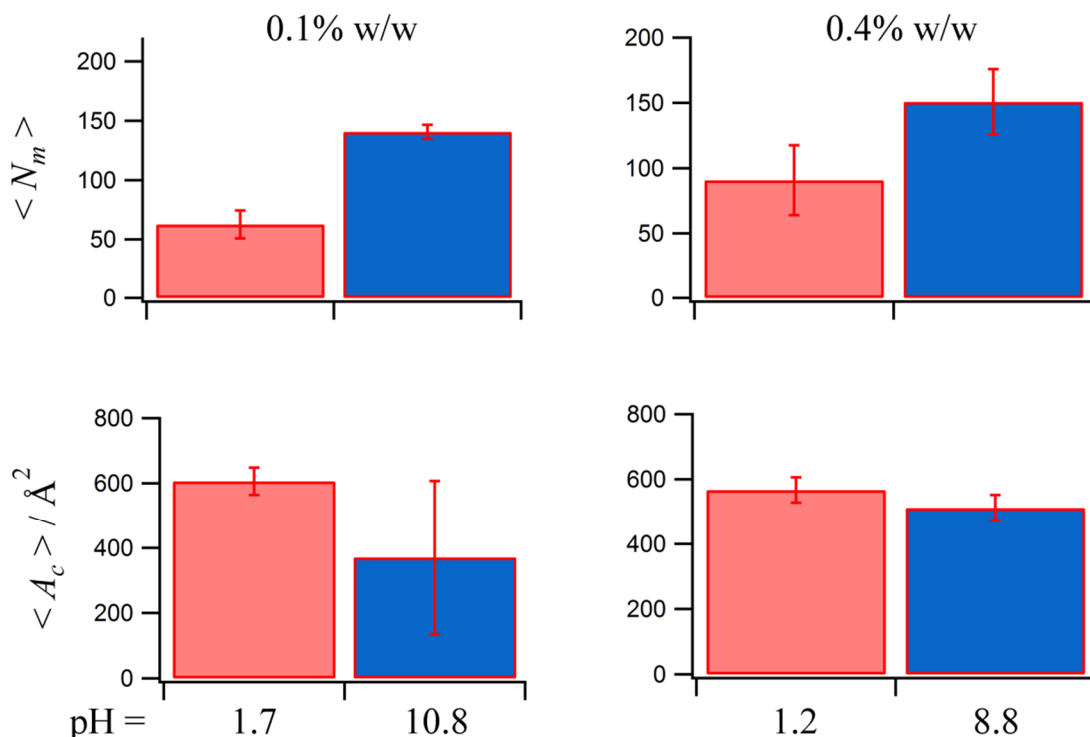
Figure 6 *Average aggregation number, N_m, and average surface per PEO chain, A_c, for sample I at concentrations equal to 0.1 and 0.4 % w/w.*

At 25°C, *Sample II* undergoes limited chain transfer between micelles upon pH increase. Comparing Figure 8 and figures 5 and 7 shows that the surface available per PEO chain at the core-corona interface is similar to that in *sample I*, at least at acidic pH, but that the P2VP thickness is, as already mentioned, 40% smaller. The fact that micelle reorganization is limited in *sample II* might be due to the small contribution of the short P2VP chains to the hydrophilic/lipophilic balance at this temperature, so that P2VP collapse on the core plays no significant role for the micelle stability. An additional reason to explain the absence of reorganization is the presence of a larger PCL block which increases the stability of the micelles [50]. At 70°C, however, the core size tends to slightly grow from acidic to basic pH, which is linked to an increase of the aggregation number (Figure 7 and 8). The lower hydrophilic character of the PEO block at higher temperature might be responsible for a less favorable hydrophilic/lipophilic balance and to a higher sensitivity to the P2VP collapse. The reorganization process leads then, as for *sample I*, to larger micelles whose interfacial area per

PEO chain slightly decreases. Furthermore, the radius of gyration of the PEO chains is slightly larger at 25°C than at 70°C.

Compared to *sample I*, the polydispersity of *sample II* seems to be less affected, at both temperatures, by the pH increase. The size distribution is not expected to change at 25°C but the stability of the standard deviation, σ, at 70°C is somewhat surprising since R_c and N_m increase with pH. It must be noticed that, already at low pH, σ for *sample II* is larger than for *sample I*, so that it might be less sensitive against any micellar reorganization.

For all experimental conditions adopted in this work, the volume fraction of PEO within the corona, ϕ, ranges between 0.05 and 0.2. This has to be compared to the critical volume fraction ϕ^*, which is calculated in the $0.03 < \phi^* < 0.1$ range. This means that the PEO corona corresponds to the dilute to semi-dilute regime. This will affect the extent of solvation of the PEO chains, which will in turn govern their radius of gyration. Based on a Kuhn segment length of 7Å, a radius of gyration of 21Å is estimated for ideal PEO chains [39], while a value of 29Å is obtained if the chains are assumed to be swollen by the water solvent [51]. A reasonable increase of the Kuhn length to 12Å leads to, respectively, 27Å and 36Å for the ideal and swollen chains. A comparison of figures 5 and 7 shows that we are clearly here in a transition situation between the dilute and semi-dilute regimes where variations of the core radius upon pH increase induce changes in the solvation degree of the corona which in turn affect the radius of gyration to an extent which is, however, difficult to predict.

Figure 7 *Average structural parameters of sample II (PCL$_{65}$-b-PEO$_{(d4),104}$ mixed with PCL$_{64}$-b-P2VP$_{31}$) as a function of pH at 25°C and 70°C. <R$_c$>: average PCL core radius; σ: standard deviation of the core size; L/2: half thickness of the P2VP shell; it is assumed to be equal to the radius of gyration of P2VP in the mixed Gaussian chain model (model 2); R$_g$: radius of gyration of the PEO chains.*
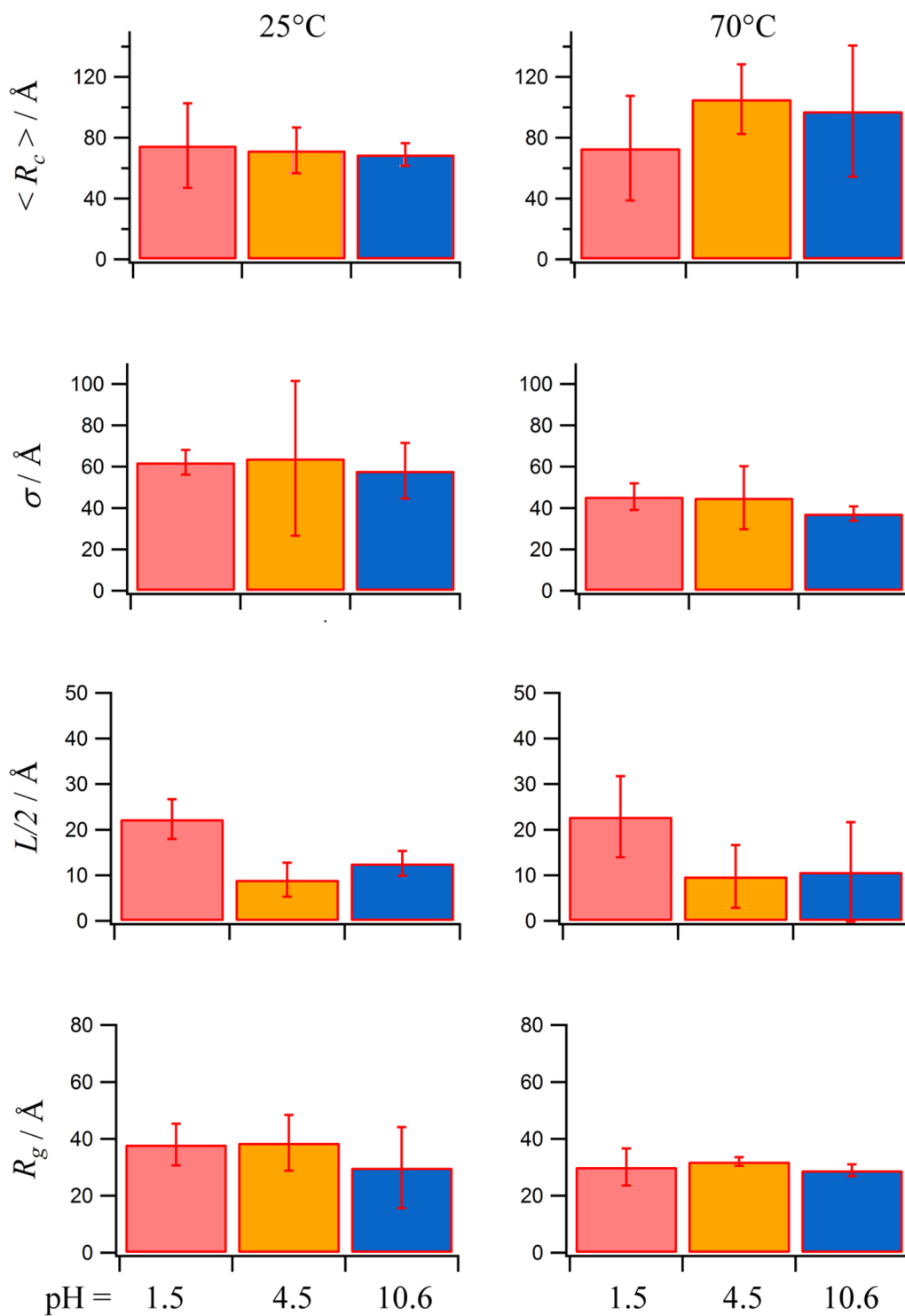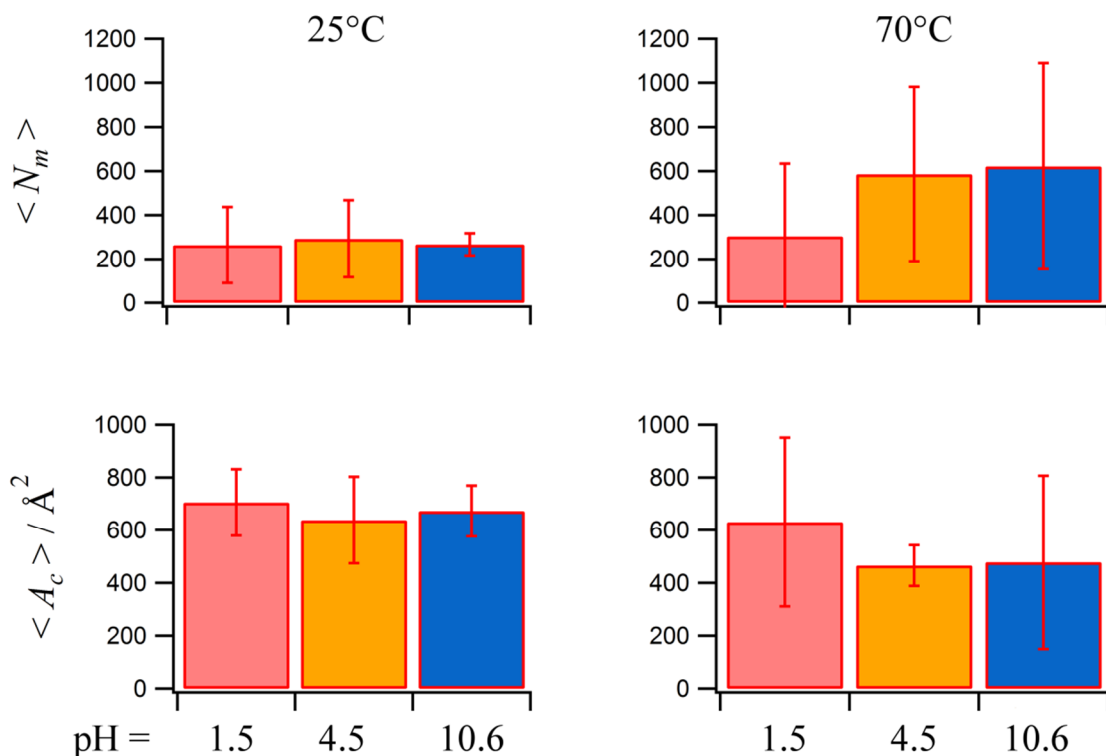
Figure 8 *Average aggregation number N_m and average surface per PEO chain at the core-corona interface, A_c, for sample II a function of the pH at 25 and 70°C.*

6   Conclusions

pH sensitive micellar solutions have been prepared by mixing two diblock copolymers. The micelles are built from a PCL hydrophobic core, a PEO corona which is hydrophilic below T = 70°C, and a P2VP, pH responsive sequence, which becomes substantially charged at pH < 4-5. Two samples have been investigated [PCL_{37}-*b*-$PEO_{(d4),104}$ mixed with PCL_{34}-*b*-$P2VP_{52}$] (*sample I*) and [PCL_{65}-*b*-$PEO_{(d4),104}$ mixed with PCL_{64}-*b*-$P2VP_{31}$] (*sample II*). SANS experiments were performed in the dilute regime in order to analyze the form factors. Three models were tested to ensure the robustness of the results. They are derived from the Pedersen and Gerstenberg model [37] and differ by the way the P2VP is described. The first model describes the P2VP zone as a homogenous shell at the surface of the PCL core, the second one describes it as a corona of Gaussian chains and the third one, limited to the acidic regime,

describes it as a collection of rigid rods. The analyses based on the three models are shown to lead to compatible structural parameters for the mixed micelles.

Both samples show a decrease of the P2VP thickness as the pH rises. This behavior is expected because the P2VP becomes hydrophobic at pH > 5 and collapses then on the core. *Sample I* shows an increase of the core radius and thus of the aggregation number as previously reported [12]. The reorganization of the micelles occurs in order to minimize the total size of the core-corona interface. The micellar size for *sample II* stays stable in all pH conditions at 25°C but tends to increase when pH increases at T = 70°C, as a result of a lower PEO water solubility. Two factors explain this behavior: the larger polymerization degree of the hydrophobic PCL block in *sample II* and the smaller polymerization degree of the P2VP chains.

This latter behavior of *sample II* is appealing because micelle reorganization at basic or neutral pH is an undesirable effect in therapeutic applications. Furthermore, a bigger core may encapsulate a larger quantity of drug. This will take place, however, at the cost of larger micelles [52], which are, of course, more easily detected and eliminated by the immune system. This is the reason why triblocks copolymers showing similar chemical compositions and sizes are now also the subject of detailed investigations [13,14,53].

7 *References*

1. Lazzari, M., Liu, G., Lecommandoux, S.: Block Copolymers in Nanoscience. Block Copolymers in Nanoscience, 1-428 (2008). doi:10.1002/9783527610570

2. Niu, D., Liu, X., Li, Y., Ma, Z., Dong, W., Chang, S., Zhao, W., Gu, J., Zhang, S., Shi, J.: Fabrication of uniform, biocompatible and multifunctional PCL-b-PAA copolymer-based hybrid micelles for magnetic resonance imaging. Journal of Materials Chemistry **21**, 13825 (2011). doi:10.1039/c1jm10929d

3. Borovinskii, A.L., Khokhlov, A.R.: Micelle Formation in the Dilute Solution Mixtures of Block-Copolymers. Macromolecules **31**, 7636-7640 (1998). doi:10.1021/ma980482n

4. Li, W., Wang, J., Liang, R., Deng, R., Zhu, J.: Co-assembly of Nanoparticles and Block Copolymers into Hybrid Micellar Aggregates. Recent Patents on Materials Science **6**, 40-58 (2013).

5. Yang, Z., Muller, A.H.E., Xu, C., Doyle, P.S., DeSimone, J.M., Lahann, J., Sciortino, F., Glotzer, S., Hong, L., Aarts, D.A.L., Chen, Y., Jiang, S., Hammond, P., Kretzschmar, I., Jiang, S., Granick, S., Schneider, H.-J., Shahinpoor, M.: Janus Particle Synthesis, Self-Assembly and Applications. FP001-279 (2012). doi:10.1039/9781849735100

6. Kuo, S.W., Tung, P.H., Lai, C.L., Jeong, K.U., Chang, F.C.: Supramolecular micellization of diblock copolymer mixtures mediated by hydrogen bonding for the observation of separated coil and chain aggregation in common solvents. Macromolecular Rapid Communications **29**, 229-233 (2008). doi:10.1002/marc.200700697

7. Koňák, Č., Helmstedt, M.: Comicellization of chemically identical diblock copolymers with different molecular parameters of the constituent blocks in a selective solvent. Macromolecules **34**, 6131-6133 (2001). doi:10.1021/ma010411f

8. Halperin, a.: Microphase separation in binary polymeric micelles. Journal de Physique **49**, 131-137 (1988). doi:10.1051/jphys:01988004901013100

9. Ebrahim Attia, A.B., Ong, Z.Y., Hedrick, J.L., Lee, P.P., Ee, P.L.R., Hammond, P.T., Yang, Y.Y.: Mixed micelles self-assembled from block copolymers for drug delivery. Current Opinion in Colloid and Interface Science **16**, 182-194 (2011). doi:10.1016/j.cocis.2010.10.003

10. Li, Y., Ma, J., Zhu, H., Gao, X., Dong, H., Shi, D.: Green synthetic, multifunctional hybrid micelles with shell embedded magnetic nanoparticles for theranostic applications. ACS Applied Materials and Interfaces **5**, 7227-7235 (2013). doi:10.1021/am401573b

11. Wu, C., Ma, R., He, H., Zhao, L., Gao, H., An, Y., Shi, L.: Fabrication of complex micelles with tunable shell for application in controlled drug release. Macromolecular Bioscience **9**, 1185-1193 (2009). doi:10.1002/mabi.200900232

12. Van Butsele, K., Sibret, P., Fustin, C.a., Gohy, J.F., Passirani, C., Benoit, J.P., Jérôme, R., Jérôme, C.: Synthesis and pH-dependent micellization of diblock copolymer mixtures. Journal of Colloid and Interface Science **329**, 235-243 (2009). doi:10.1016/j.jcis.2008.09.080

13. Cajot, S., Van Butsele, K., Paillard, a., Passirani, C., Garcion, E., Benoit, J.P., Varshney, S.K., Jérôme, C.: Smart nanocarriers for pH-triggered targeting and release of hydrophobic drugs. Acta biomaterialia **8**, 4215-4223 (2012). doi:10.1016/j.actbio.2012.08.049

14. Van Butsele, K., Cajot, S., Van Vlierberghe, S., Dubruel, P., Passirani, C., Benoit, J.-P., Jérôme, R., Jérôme, C.: pH-Responsive Flower-Type Micelles Formed by a Biotinylated Poly(2-vinylpyridine)- block -poly(ethylene oxide)- block -poly(ε -caprolactone) Triblock Copolymer. Advanced Functional Materials **19**, 1416-1425 (2009). doi:10.1002/adfm.200801117

15. Ulery, B., Nair, L., Laurencin, C.: Biomedical applications of biodegradable polymers. Journal of Polymer Science Part B: Polymer Physics **49**, 832-864 (2011). doi:10.1002/polb.22259.Biomedical

16. Gaucher, G., Dufresne, M.-H., Sant, V.P., Kang, N., Maysinger, D., Leroux, J.-C.: Block copolymer micelles: preparation, characterization and application in drug delivery. Journal of controlled release : official journal of the Controlled Release Society **109**, 169-188 (2005). doi:10.1016/j.jconrel.2005.09.034

17. Woodruff, M.A., Hutmacher, D.W.: The return of a forgotten polymer - Polycaprolactone in the 21st century. Progress in Polymer Science (Oxford) **35**, 1217-1256 (2010). doi:10.1016/j.progpolymsci.2010.04.002

18. Vangeyte, P., Leyh, B., Heinrich, M., Grandjean, J., Bourgaux, C., Je, R.: Self-Assembly of Poly(ethylene oxide)-b-poly(E-caprolactone) Copolymers in Aqueous Solution. Langmuir **20**, 8442-8451 (2004).

19. Cerrai, P., Cristallini, C., Chicca, M.D.: Hydrolysis of poly (ester-ether-ester) block copolymers in the presence of endothelial cells: in vitro modulation of endothelin release. Polymer bulletin **39**, 53-58 (1997).

20. Duval, M.: Monitoring of cluster formation and elimination in PEO solutions. Macromolecules **33**, 7862-7867 (2000). doi:10.1021/ma000423l

21. Chang, Y., Chu, W.L., Chen, W.Y., Zheng, J., Liu, L., Ruaan, R.C., Higuchi, A.: A systematic SPR study of human plasma protein adsorption behavior on the controlled surface packing of self-assembled poly(ethylene oxide) triblock copolymer surfaces. Journal of Biomedical Materials Research - Part A **93**, 400-408 (2010). doi:10.1002/jbm.a.32558

22. Hamaguchi, T., Matsumura, Y., Suzuki, M., Shimizu, K., Goda, R., Nakamura, I., Nakatomi, I., Yokoyama, M., Kataoka, K., Kakizoe, T.: NK105, a paclitaxel-incorporating micellar nanoparticle formulation, can extend in vivo antitumour activity and reduce the neurotoxicity of paclitaxel. British journal of cancer **92**, 1240-1246 (2005). doi:10.1038/sj.bjc.6602479

23. Xu, Z., Marchant, R.E.: Adsorption of plasma proteins on polyethylene oxide-modi " ed lipid bilayers studied by total internal re # ection # uorescence. **21**, 1075-1083 (2000).

24. Glavas, L., Olsén, P., Odelius, K., Albertsson, A.C.: Achieving micelle control through core crystallinity. Biomacromolecules **14**, 4150-4156 (2013). doi:10.1021/bm401312j

25. Lavasanifar, A., Samuel, J., Kwon, G.S.: Poly(ethylene oxide)-block-poly(L-amino acid) micelles for drug delivery. Advanced drug delivery reviews **54**, 169-190 (2002).

26. Aqil, a., Vasseur, S., Duguet, E., Passirani, C., Benoît, J.P., Roch, a., Müller, R., Jérôme, R., Jérôme, C.: PEO coated magnetic nanoparticles for biomedical application. European Polymer Journal **44**, 3191-3199 (2008). doi:10.1016/j.eurpolymj.2008.07.011

27. Saif, M.W., Podoltsev, N.a., Rubin, M.S., Figueroa, J.a., Lee, M.Y., Kwon, J., Rowen, E., Yu, J., Kerr, R.O.: Phase II clinical trial of paclitaxel loaded polymeric micelle in patients with advanced pancreatic cancer. Cancer investigation **28**, 186-194 (2010). doi:10.3109/07357900903179591

28. Etheridge, M.L., Campbell, S.a., Erdman, A.G., Haynes, C.L., Wolf, S.M., McCullough, J.: The big picture on nanomedicine: the state of investigational and approved nanomedicine products. Nanomedicine : nanotechnology, biology, and medicine **9**, 1-14 (2013). doi:10.1016/j.nano.2012.05.013

29. Stuart, M.a.C., Huck, W.T.S., Genzer, J., Müller, M., Ober, C., Stamm, M., Sukhorukov, G.B., Szleifer, I., Tsukruk, V.V., Urban, M., Winnik, F., Zauscher, S., Luzinov, I., Minko, S.: Emerging applications of stimuli-responsive polymer materials. Nature materials **9**, 101-113 (2010). doi:10.1038/nmat2614

30. Trivedi, R., Kompella, U.B.: Nanomicellar formulations for sustained drug delivery: strategies and underlying principles. Nanomedicine (London, England) **5**, 485-505 (2010). doi:10.2217/nnm.10.10

31. Lazzari, M., Liu, G., Lecommandoux, S.: Block Copolymers in Nanoscience. Wiley, (2007)

32. Borchert, U., Lipprandt, U., Bilang, M., Kimpfler, A., Rank, A., Peschka-Süss, R., Schubert, R., Lindner, P., Förster, S.: pH-induced release from P2VP-PEO block copolymer vesicles. Langmuir **22**, 5843-5847 (2006). doi:10.1021/la060227t

33. Torchilin, V., Amiji, M.M.: Handbook of Materials for Nanomedicine Pan Stanford Publishing, (2010)

34. Hammouda, B., Ho, D.L., Kline, S.: Insight into Clustering in Poly (ethylene oxide) Solutions. Macromolecules, 6932-6937 (2004). doi:10.1021/ma049623d

35. Vangeyte, P., Jérôme, R.: Amphiphilic Block Copolymers of High-Molecular-Weight Poly(ethylene oxide) and Either ε-Caprolactone or γ-Methyl-ε-Caprolactone: Synthesis and Characterization. Journal of Polymer Science Part A: Polymer Chemistry **42**, 1132-1142 (2004). doi:10.1002/pola.11072

36. Brûlet, A., Lairez, D., Lapp, A., Cotton, J.-P.: Improvement of data treatment in small-angle neutron scattering. J Appl crystallogr **40**, 165-177 (2007).

37. Pedersen, J.S., Gerstenberg, M.C.: Scattering Form Factor of Block Copolymer Micelles. Macromolecules **29**, 1363-1365 (1996).

38. Dianoux, A., Lander, G.: Neutron data booklet. (2003).

39. Higgins, J.S., Benoît, H.: Polymers and neutron scattering. Clarendon Press, (1994)

40. Hallett, A.F., Craig, T., Marsh, J., Nickel, B.: Number Distributions by Dynamic Light Scattering. Can. J. Spectr. **34**, 63-70 (1989).

41. Maulucci, G., De Spirito, M., Arcovito, G., Boffi, F., Castellano, A.C., Briganti, G.: Particle size distribution in DMPC vesicles solutions undergoing different sonication times. Biophys. J. **88**, 3545-3550 (2005).

42. Gracia, C.a., Gómez-Barreiro, S., González-Pérez, a., Nimo, J., Rodríguez, J.R.: Static and dynamic light-scattering studies on micellar solutions of alkyldimethylbenzylammonium chlorides. Journal of Colloid and Interface Science **276**, 408-413 (2004). doi:10.1016/j.jcis.2004.04.002

43. Jensen, G.V., Shi, Q., Hernansanz, M.J., Oliveira, C.L.P., Deen, G.R., Almdal, K., Pedersen, J.S.: Structure of PEP–PEO block copolymer micelles: exploiting the complementarity of small-angle X-ray scattering and static light scattering. Journal of Applied Crystallography **44**, 473-482 (2011). doi:10.1107/S0021889811013343

44. Li, X., Mya, K.Y., Ni, X., He, C., Leong, K.W., Li, J.: Dynamic and static light scattering studies on self-aggregation behavior of biodegradable amphiphilic poly(ethylene oxide)-poly[(R)-3-hydroxybutyrate]-poly(ethylene oxide) triblock copolymers in aqueous solution. The journal of physical chemistry. B **110**, 5920-5926 (2006). doi:10.1021/jp057004g

45. Thévenot, C., Grassl, B., Bastiat, G., Binana, W.: Aggregation number and critical micellar concentration of surfactant determined by time-dependent static light scattering (TDSLS) and conductivity. Colloids and Surfaces A: Physicochemical and Engineering Aspects **252**, 105-111 (2005). doi:10.1016/j.colsurfa.2004.10.062

46. Erhardt, R., Zhang, M., Böker, A., Zettl, H., Abetz, C., Frederik, P., Krausch, G., Abetz, V., Müller, A.H.E.: Amphiphilic Janus micelles with polystyrene and poly(methacrylic acid) hemispheres. Journal of the American Chemical Society **125**, 3260-3267 (2003). doi:10.1021/ja028982q

47. Nolan, S.L., Phillips, R.J., Cotts, P.M., Dungan, S.R.: Light Scattering Study on the Effect of Polymer Composition on the Structural Properties of PEO – PPO – PEO Micelles. **302**, 291-302 (1997).
48. Paillet, S., Grassl, B., Desbrières, J.: Rapid and quantitative determination of critical micelle concentration by automatic continuous mixing and static light scattering. Analytica Chimica Acta **636**, 236-241 (2009). doi:10.1016/j.aca.2009.02.011
49. Yang, L., Alexandridis, P., Steytler, D.C., Kositza, M.J., Holzwarth, J.F.: Small-Angle Neutron Scattering Investigation of the Temperature-Dependent Aggregation Behavior of the Block Copolymer Pluronic L64 in Aqueous Solution†. Langmuir **16**, 8555-8561 (2000). doi:10.1021/la000008m
50. Owen, S.C., Chan, D.P.Y., Shoichet, M.S.: Polymeric micelle stability. Nano Today **7**, 53-65 (2012). doi:10.1016/j.nantod.2012.01.002
51. Teraoka, I.: Polymer Solutions: An Introduction to Physical Properties. **3**, 360 (2002). doi:10.1002/0471224510
52. Kumar, V., Prud'homme, R.K.: Thermodynamic limits on drug loading in nanoparticle cores. Journal of pharmaceutical sciences **97**, 4904-4914 (2008). doi:10.1002/jps.21342
53. Cajot, S., Riva, R., Billiet, L., Du Prez, F., Alexandre, M., Lecomte, P., Jérôme, C.: Novel Amphiphilic Mikto-Arm Star-Shaped Copolymers for the Preparation of PLA-Based Nanocarriers. Macromolecular Symposia **309-310**, 111-122 (2011). doi:10.1002/masy.201100044

CHAPTER IV

SANS study of pH- and thermo-responsive micelles: from block-copolymers to aggregates

Arnaud Joset, Pierre Sibret Annie Brûlet, Christine Jérôme, Bernard Leyh

Abstract

This chapter sets out the investigation of the self-assembling of triblock copolymers consisting of polyacrylic acid (PAA), Poly(N-isopropylacrylamide) (PNIPAM) and poly (ethylene oxide) (PEO) in response to pH and temperature stimuli. At low pH, the PAA is protonated and expected to show a hydrophobic behavior, while at high pH, deprotonation leads to a hydrophilic polyelectrolyte. PNIPAM is hydrophilic at temperatures below the LCST (32°C) and hydrophobic at higher temperature. SANS measurements have been performed under several pH (2, 6 and 8) and temperature (20, 30, 40 and 50°C) conditions. Two samples were studied, PAA_{13}-*b*-$PNIPAM_{45}$-*b*-PEO_{45} and a PEO fully deuterated version, PAA_{11}-*b*-$PNIPAM_{46}$-*b*-$PEO_{d4;46}$, for which the PEO contribution to the SANS macroscopic scattering cross-section in heavy water is minimized. Several models have been developed to take into account the possible simultaneous presence, depending on the external stimuli, of free chains, micelles and aggregates, as well as the changes induced in the core and corona composition of the micelles. The fitting of these models to the experimental data leads to a detailed picture of the response of these colloidal systems when the external parameters are tuned.

1 *Introduction*

Among the various application fields of block-copolymers, the design of furtive nano-medicine treatments has been the subject of several investigations [1-8]. Some ongoing research projects aim at preparing stealthy and temperature-sensitive magnetic nanoparticles (MNPs) [9]. In order to prevent the coalescence of the particles, one particular promising approach is the preparation of "ferrofluid" dispersions of magnetics nanoparticles associated with short surfactants [10-12]. In this framework, Fe_3O_4 particles have been widely studied [13,14,11,15]. As this kind of particle is positively charged, poly(acrylic acid) (PAA) in basic conditions is often used to anchor a copolymer on the nanoparticle. In the perspective of preparing magnetic particles coated by temperature responsive copolymers, a specific triblock copolymer has been recently designed and synthesized in the Centre for Education and Research on Macromolecules (CERM) at the University of Liège (Belgium). This copolymer consists of a poly(acrylic acid) (PAA) block, a poly(N-isopropylacrylamide) (PNIPAM) central block, and a poly(ethylene oxide) (PEO) block. As the pKa of PAA is equal to 4.2 [16], this sequence is expected to be negatively charged at pH above 4.2 and neutral below [17]. The goal of designing such nano-objects is to use them as possible tumor-targeting treatments which release the drug close to sick tissues. The specific role of PNIPAM is to induce drug release upon temperature increase, because it displays a low critical solution temperature (LCST), which is equal to 32°C for pure PNIPAM and can be tuned in a limited range by copolymerization with acrylic acid. Below the LCST, PNIPAM is hydrophilic whereas it is hydrophobic at higher temperature. The PEO block is added to prevent the aggregation of the copolymer chains in conditions where PAA and PNIPAM are both hydrophobic, that is at acidic pH and temperature above the LCST. The second essential role of the highly flexible PEO chains is to make the nanoparticles stealthy with respect to the proteins of the immune system [2-5].

The aim of the present study is to reach a detailed picture of the structural response to temperature and pH of these self-assembled copolymers in a temperature and pH range bracketing respectively the LCST (20, 30, 40 and 50°C) and the pK_a of PAA (pH = 2.5 ±1 , 6.5±1, 7.5±1).

Based on the known behavior of the constitutive blocks of these copolymers, Figure 1 displays the prior expectations for the micellar structures as a function of temperature and pH.

At low temperature, in acidic conditions, the PAA chains are insoluble in water, whereas the PNIPAM and PEO blocks are hydrophilic. Micelles with a PAA core are thus expected to assemble. When the temperature crosses the LCST upwards, PNIPAM becomes hydrophobic and is expected to collapse on the core, leading to an increase of the core diameter. At basic pH and low temperature, the three blocks are soluble so that a free chain solution is likely to obtain. Above the LCST, a reorganization of the chains is predicted, leading to micelles with a hydrophobic PNIPAM core.

The samples were first analyzed by Sibret et *al* [18] and DLS experiments revealed bimodal size distributions for all pH and temperature conditions, as illustrated by Figure 2. The size of the smaller detected objects, with a hydrodynamic radius of about 200 Å, suggests that micelle self-assembling takes place. The second contribution has a maximum in the 600-800 Å range, that is, larger than the length of the completely extended copolymer chains. Concomitant aggregate formation is therefore the most reasonable hypothesis.
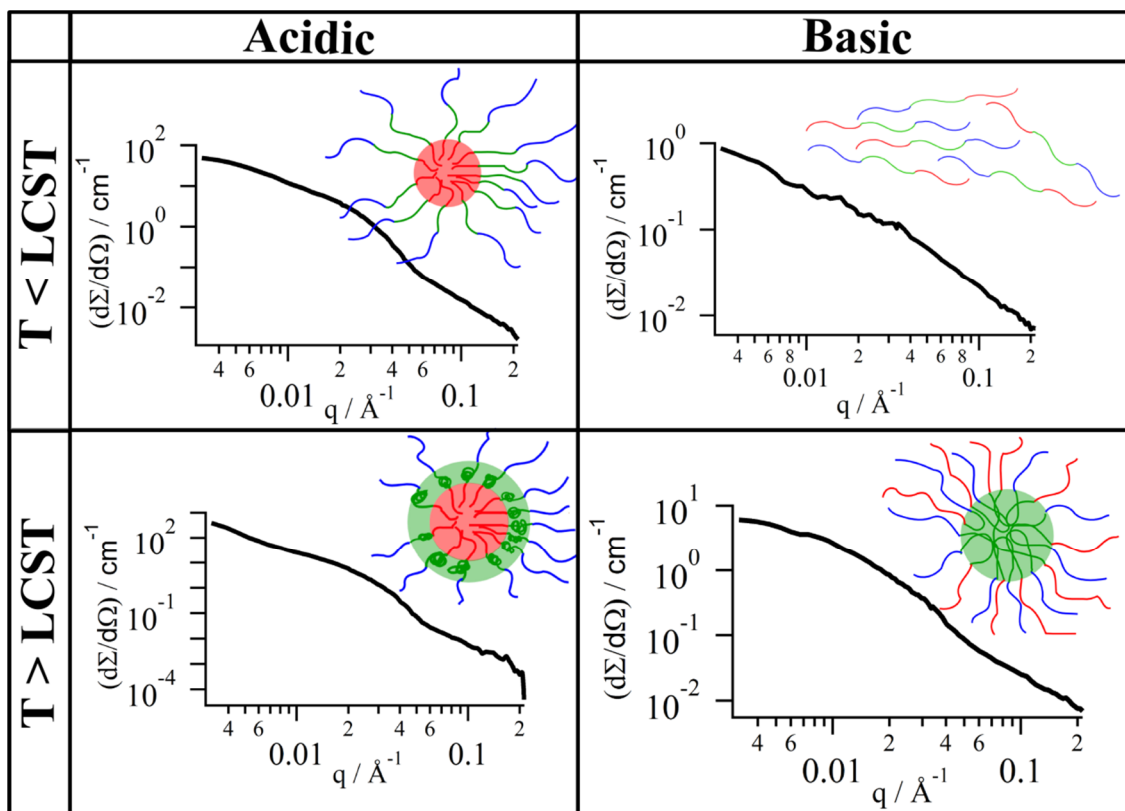
Figure 1 *SANS experimental data on the undeuterated polymer and prior expectations for the triblock copolymers self-assembled morphologies under typical (pH, T) experimental conditions. Color code: PEO (blue), PAA (red), PNIPAM (green).*
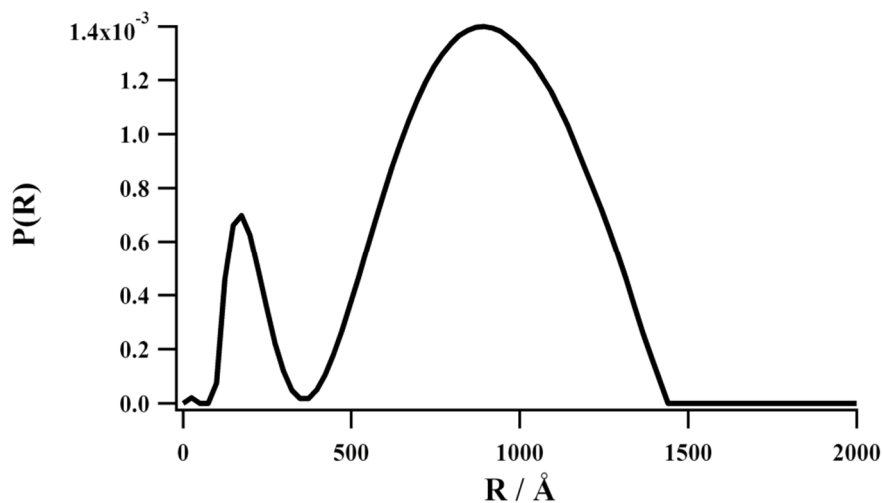
Figure 2 *Dynamic light scattering distribution of a PEO$_{45}$-b-PNIPAM$_{45}$-b-PAA$_{13}$ aqueous solution at pH=7.5±0.5 and 30°C. The average radii of the respective subpopulations (micelles and aggregates, respectively) are equal to 180 and 900 Å.*

To reach a deeper understanding of the complex behavior of such triblock copolymer self-assembled nano-objects when they are submitted to pH and temperature stimuli, we used a methodology based on small-angle neutron scattering (SANS). Two copolymers compositions were analysed: PEO_{45}-b-$PNIPAM_{45}$-b-PAA_{13} and $PEO_{(d4),46}$-b-$PNIPAM_{46}$-b-PAA_{11} where the PEO block of the latter is fully deuterated in order to increase its contrast with PNIPAM and PAA. The SANS technique, coupled with relevant modelling, is known to provide detailed information on the internal structure of self-organized nanosized objects [19-23].

2   Materials and methods

2.1   Materials

Acrylic acid (AA) was purified by distillation under reduced pressure. N-Isopropylacrylamide (Aldrich; 97%) was recrystallized twice from benzene–hexane 3 : 2 (v/v) and dried under vacuum prior to use. Hydrochloric acid (Aldrich) was used as a 25% v/v aqueous solution. 2-Dodecylsulfanylthiocarbonylsulfanyl-2-methylpropionic acid (DMP) 2,2′-azobis (isobutyronitrile) (AIBN), 2,2-azobis(4-methoxy-2,4-dimethylvaleronitrile) (V-70), N,N'-dicyclohexylcarbodiimide (DCC), 4-dimethylaminopyridine (DMAP), poly(ethylene oxide) methyl ether (CH$_3$-PEO-OH Mn ≈ 2000 g mol^{-1}), dimethylformamide (DMF), tetrahydrofuran (THF), (Trimethylsilyl)diazomethane were purchased from Sigma-Aldrich and were used without further purification. Deuterated poly(ethylene oxide) methyl ether (CD$_3$-PEO(d)-OD Mn ≈ 2200 g mol^{-1}) was purchased from Polymer Source.

2.2   Synthesis

The PEO-b-PNIPAM-b-PAA was synthetized using Reversible Addition-Fragmentation chain Transfer (RAFT) polymerization. The synthesis and characterization is described elsewhere [11,24]. The deuterated version was synthetized accordantly to the same protocol.

α-methoxy-ω-DMP-poly(ethylene oxide) (PEO-RAFT) macro-CTA was synthesized by esterification of the hydroxyl end-group of the mono-methoxy poly(ethylene oxide) by DMP accordantly to literature [12]. The PEO-b-PNIPAM was prepared in DMF, employing V-70 as the primary source of radicals. Typically 1 g of the macro-CTA PEO-DMP (Mn = 2400 g/mol, 0.4 mmol), 2.4 g of NIPAM (0.02 mol), 0.006 g of V-70 (0.02 mmol) and 10 ml of DMF were added into a reaction tube. The mixture was degassed by bubbling nitrogen during

5 minutes. This reaction mixture was heated in an oil bath at 30°C for 6 hours. The resulting polymer was precipitated twice in cold diethyl ether under vigorous stirring drying in vacuo for 24 hours.

2.2.1 Synthesis of PEO-b-PNIPAM-b-PAA block copolymer

The triblocks was synthesized using PEO-b-PNIPAM diblock as macro-CTA. Triblocks were prepared in DMF, employing AIBN as the primary source of radicals. Typically 1.5 g of PEO-b-PNIPAM (Mn = 6500 g/mol, 0.23 mmol), 0.3 g of AA (4 mmol), 0.0037 g of AIBN (0.02 mmol) and 4 ml of DMF were added into a reaction tube. The mixture was degassed by bubbling nitrogen during 5 minutes. This reaction mixture was heated in an oil bath at 80°C for 5 hours. The copolymer was precipitated into cold ether and dried in vacuo for 24 hours. Molecular weight composition and conversion rate were determined by ^{1}H NMR in DMSO-d_6. Molecular weight composition was determined by ^{1}H NMR in CDCl$_3$. Molar mass distributions ($M_w/M_{n)}$ were determined by size exclusion chromatography (SEC). The chemical composition of the copolymers is shown in Table 1.

2.2.2 Preparation of Triblock Copolymer solutions

A dialysis method was used to prepare aqueous copolymer solutions. The triblock copolymer was dissolved in DMF, a good solvent of the three blocks, at a 5 mg/mL concentration. After 5 hours of stirring, the solution was transferred into a dialysis bag (MWCO = 6000-8000 D) and dialyzed against a D$_2$O solution acidified with DCl (pH = 2.5 ± 1). Another batch of sample was dialyzed against pure D$_2$O. The resulting pH was then equal to 6.5±0.5. A basic solution was prepared by dissolving directly the copolymer (again at a 5 mg/mL concentration) in an NaOD solution in D$_2$O (pH~11). The resulting pH is equal to 7.5±0.5.

Table 1 *Degree of polymerization of the blocks determined by NMR, z. The monomeric segment lengths were determined based on equilibrium geometry data. The polydispersity index (Mn/Mw or PDI) obtained by size exclusion chromatography in N,N-dimethylformamide were equal to 1.24 and 1.21 for PEO$_{45}$-b-PNIPAM$_{45}$-b-PAA$_{13}$ and PEO$_{d4,46}$-b-PNIPAM$_{46}$-b-PAA$_{11}$ respectively.*

	z (Un-deuterated)	z (Deuterated)	Monomeric segment length	Kuhn segment length
PAA	13	11	2,51Å	15.7Å [25]
PNIP	45	46	2,51 Å	7Å [26]
PEO	45	46	3,58 Å	7.1Å [27]

Table 2 *Volume of the monomer units inferred from the respective densities: PAA [28]; PEO [29]; PNIPAM [30]; D$_2$O [31,32] and excess scattering lengths $\tilde{b}$ of the monomer unit (10^{-12} cm) [33].*

Monomer	Volume (Å^3)	$\tilde{b}$/ (10^{-12} cm)
AA	98	-4.62
NIPAM	171	-9.60
EO	65	-3.73
EO$_{d4}$	65	0.440
D$_2$O	30	0

2.3 Small-Angle Neutron Scattering (SANS)

Small-angle neutron scattering (SANS) experiments were performed at the Laboratoire Léon Brillouin in Saclay, France, with the PACE instrument under the following conditions: (i) wavelength = 5 Å, sample-to-detector distance = 2.0 m, (ii) wavelength = 13.0 Å, sample-to-detector distance = 4.7 m, such that a scattering vector (q) range from 0.00318 to 0.213Å^{-1} was available. The neutron wavelength resolution ($\Delta q/q$) was equal to 10%, and the beam diameter was set at 12 mm. The data were recorded with a two-dimensional detector consisting of 30 concentric rings of 1 cm width. Samples were contained in quartz cells with a 2 mm path length. Corrections for the electronic and ambient background noise and for sample holder contributions were carried out according to standard data handling procedures (see, e.g. [34]). The data corresponding to the copolymer solutions and to the pure solvent (D$_2$O) were treated in an identical way, and the scattering intensities were converted to macroscopic scattering cross-sections per unit volume, $d\Sigma/d\Omega$ (cm^{-1}), by normalization with

respect to the incoherent scattering of H_2O. The copolymer contribution was obtained by subtracting the cross section of the solvent, weighted by its volume fraction.

PEO_{45}-b-$PNIPAM_{45}$-b-PAA_{13} (0.40 % w/w) and $PEO_{(d4)46}$-b-$PNIPAM_{46}$-b-PAA_{11} (0.45% w/w) triblock copolymers solutions in D_2O were investigated. The above-mentioned concentrations were sufficiently low to reach the dilute regime where the structure factor can be assumed equal to 1 in the investigated q range. As a matter of fact, the first peak of the interparticle structure factor was not observed in the present SANS data, so that the macroscopic scattering cross section gives directly access to the form factor of the assembled nano-objects.

2.4 SANS Data handling

Based on the data of Table 1, the contour length, L, of the block copolymers is estimated to be 310 Å. For a homopolymer, the radius of gyration R_g is related to the contour length and to the Kuhn segment b by the following equation:

$$R_g^2 = \frac{Lb}{6} \tag{1}$$

For a multiblock copolymer, a generalization of this formula allows estimating the radius of gyration of the free chains:

$$R_g^2 = \frac{1}{6} \sum_{blocks} L_i b_i \tag{2}$$

A radius of gyration of 20 Å is then obtained for both the deuterated and the non-deuterated copolymer chains, which dismisses a free chain assignment to contribution with hydrodynamic radii larger than 100Å in the size distributions obtained by DLS (Figure 2) [18]. The sample must therefore also consist of micelles and aggregates whose internal structure have to be modelled in an appropriate way based on reasonable assumptions in both acidic or neutral/basic conditions.

The first qualitative conclusion which can be drawn from the general shape of the SANS cross sections inserted in Figure 1 is that they confirm the DLS-based conclusion that the size distributions are multimodal in all pH and temperature conditions. The scattering intensities measured by both techniques are strongly affected by the experimental pH and temperature conditions.

To analyze our SANS data, we adopted a similar approach to that of Joseph & al [35] who studied the structure of micelles made of PEO-*b*-PPO-*b*-PEO (pluronic) where PPO stands for poly(propylene oxide) with respect to the addition of cyclodextrin at several temperature. At 15°C, these copolymers are soluble and no micelles were identified but the formation of micelles was observed to take place upon temperature increase as PPO becomes more hydrophobic. This transition is extremely broad and micellization occurs on a large temperature scale. However, above 25°C, micellar structures are found. The cyclodextrins have the ability to disrupt the micelles, releasing free chains. These authors determined the molar fraction of copolymers involved either in free chains or in micelles or in aggregates, the total copolymer concentration being known.

Given a sample composed of three populations in the dilute regime, free chains (index ch), micelles (index m) and aggregates (index a), the resulting macroscopic scattering cross section can be written as the sum of three independent contributions:

$$\frac{d\Sigma}{d\Omega}(q) = \left[\frac{d\Sigma}{d\Omega}(q)\right]_{ch} + \left[\frac{d\Sigma}{d\Omega}(q)\right]_{m} + \left[\frac{d\Sigma}{d\Omega}(q)\right]_{a}$$

$$= \underbrace{I_{ch}(q=0)P_{ch}(q,R_{g,ch})}_{free\,chains} + \underbrace{I_m(q=0)\int_{0}^{+\infty} P_m(q,R)\,\Gamma_m(R)\,dR}_{micelles} \qquad (3)$$

$$+ \underbrace{I_a(q=0)\int_{0}^{+\infty} P_a(q,R)\,\Gamma_a(R)\,dR}_{aggregates}$$

Each contribution is the product of its normalized form factor *P(q,R)* weighted by the associated intensity at q=0, *I(q=0)*. Micelle and aggregate populations are characterized by their polydisperse size distribution *Γ(R)* where R is the radius of the nano-objects (micelles or aggregates). In the contribution of Sibret et al, refered to before [18], a simplified model has been developed in order to assess the relative contributions of micelles and aggregates to the scattering cross section. In the present paper, we propose more elaborate models for the different couples of temperature and pH conditions and we derive the corresponding analytical formulae for the scattering cross sections. By fitting these formulae to the experimental data, we shall then infer the parameters describing the inner structure of the objects for each set of experimental conditions.

Small objects scatter less than larger ones. Therefore any free chain contribution is too small to be detected by DLS. The simplified model used by Sibret et al [18] takes into account only two contributions of spherical objects, the micelles and the aggregates, each with its own Gaussian size distribution. To test the robustness of the procedure, two analytical form factors $P(q;R_g)$ have been tested: the Guinier law and the form factor of a homogeneous sphere. However, by doing so, no information about the internal structure of the micelles can be obtained. Furthermore, the quality of such simple model fits degrades as expected when $q > 1/R_g$. In the perspective of investigating the whole q range, more sophisticated approaches need to be considered.

Micelles are expected to contribute substantially in the whole investigated temperature and pH domain but for the low temperature, basic pH range, where all three block are water soluble. Their contribution to the scattered intensity depends on the composition of the core, of the corona and on the aggregation number. This section describes how the form factor has been modelled.

The intensity of the micelle contribution at $q=0$, $I_m(q=0)$, is related to the number of chains involved in micelles per unit volume, n. The polydispersity of the micelles due to a dispersion of the aggregation numbers, N_m, is taken into account through a size distribution: $\Gamma(N_m)$.

The following equation describes the micelle contribution.

$$\left[\frac{d\Sigma}{d\Omega}(q)\right]_m = \frac{n}{\langle N_m\rangle}\int_0^{+\infty}\tilde{b}_T^2(N_m)\Gamma(N_m)P_m(q;N_m)dN_m \tag{4}$$

where $\langle N_m\rangle$ is the average aggregation number per micelle, $\tilde{b}_T$ is the total excess scattering length of all scatterers within a micelle built from N_m chains and $P_m(q;N_m)$ is the corresponding normalized form factor. By convention, the indices *"c"* and *"co"* refer to the core and the corona, respectively. Based on the assumption of a dense hydrophobic core, the aggregation number of a micelle is related to its core radius R_c, to the volume of the monomer unit v_c (see Table 2) and to the degree of polymerization of the hydrophobic block z_c:

$$N_m = \frac{\frac{4}{3}\pi R_c^3}{z_c v_c} \tag{5}$$

The macroscopic cross-section of the micelles can be expressed as a function of the radius of the objects (eq(3)) or of the aggregation number (eq(4)). Depending on the problem, either approach may be more suitable. The conservation of matter implies that

$$\Gamma(N_m)dN_m = \Gamma(R_c)dR_c \tag{6}$$

In this work, a Gaussian size distribution $\Gamma(R_c)$ has been assumed.

The total excess scattering length of a micelle, $\tilde{b}_T$, is determined by the chemical content of the copolymer chains and by the micelle aggregation number. If $\tilde{b}_c$ and $\tilde{b}_{co}$ stay respectively for the excess scattering length of the individual polymer blocks in the core and in the shell, $\tilde{b}_T$ can be expressed by eq(7). Eq(5) and eq(7) lead then to eq(8) from which eq(9) follows for the micelle contribution to the scattering cross section at $q=0$.

$$\tilde{b}_T(N_m) = N_m\left(\tilde{b}_c + \tilde{b}_{co}\right) \tag{7}$$

$$\int_1^\infty \left[\tilde{b}_T(N_m)\right]^2 \Gamma(N_m)dN_m = \left(\tilde{b}_c + \tilde{b}_{co}\right)^2 \int_0^\infty N_m^2 \Gamma(N_m)dN_m$$
$$= \left(\tilde{b}_c + \tilde{b}_{co}\right)^2 \left(\frac{\frac{4}{3}\pi}{z_c v_c}\right)^2 \left\langle R_c^6\right\rangle \tag{8}$$

$$\left[\frac{d\Sigma}{d\Omega}(q=0)\right]_m = I_m(q=0) = n\left(\tilde{b}_c + \tilde{b}_{co}\right)^2 \left(\frac{\frac{4}{3}\pi}{z_c v_c}\right)\frac{\left\langle R_c^6\right\rangle}{\left\langle R_c^3\right\rangle} \tag{9}$$

Eq(9) allows us to determine n from the physical properties of the copolymers, $\tilde{b}_c$, $\tilde{b}_{co}$, z_c and v_c and from parameters related to the size distribution of the sample, that is $\left\langle R_c^3\right\rangle$ and $\left\langle R_c^6\right\rangle$, which will be inferred from the fits of the analytical cross sections to the experimental data.

The contribution of the aggregates is mainly detected at small q values. Because we have no prior expectation about their structure, which might also be ill-defined, we described them as homogenous spheres.

2.4.1.1 Acidic condition

At acidic pH, the free chain contribution can be neglected and the experimental scattering cross section is fitted by the following equation:

$$\frac{d\Sigma}{d\Omega}(q) = \frac{n}{\langle N_m \rangle} \int_0^{+\infty} \left[\tilde{b}_T(N_m) \right]^2 \Gamma(N_m) P_{P\&G}(q; N_m; R_g) dN_m$$
$$+ I_a(q=0) \int_0^{+\infty} P_a(q,R) \Gamma_a(R) dR$$

(10)

where the Pedersen & Gerstenberg model (P&G) [36] is selected for the micelle form factor. R_g is the radius of gyration of the corona chains. $\langle R_c^3 \rangle$ and $\langle R_c^6 \rangle$ are calculated during the procedure, allowing us to obtain n, as the value of $d\Sigma_m/d\Omega(q=0)$ is available from the simplified model [18] valid at low q. Several structural parameters can then be obtained through the fit of the modelled analytical scattering cross sections to the experimental data: the average radius of the micellar core, $<R_c>$, the standard deviation of the core radius distribution, σ_m, the radius of gyration of the corona chains, the average radius of the aggregates, $<R_a>$, and the associated standard deviation, σ_a. The Guinier Law and the sphere form factor were both used for the contribution of aggregates $P_a(q,R)$ and lead to similar results.

In the Pedersen-Gerstenberg model, the core is assumed to be dense and homogeneous whereas the corona consists in Gaussian hydrophilic chains. Prior to any fit, $\tilde{b}_c$ and $\tilde{b}_{co}$, which depend on the structure assumed for the micellar inner structure, have to be determined The copolymer consists of three blocks but, because of the temperature-dependent hydrophobicity of PNIPAM, and in order to simplify the problem, we assumed a mixed PEO-PNIPAM corona (below the LCST) or a mixed PAA-PNIPAM core (above the LCST). Average scattering lengths need then to be determined. At temperature lower than the LCST, the polymerization degree of the corona is equal to z_{co}:

$$z_{co} = z_{PEO} + z_{PNIPAM}$$

(11)

The averaged excess scattering length of a monomeric scatterer in the corona $\tilde{b}_{co}$ is therefore equal to:

$$\tilde{b}_{co} = \frac{z_{PEO}\, \tilde{b}_{EO} + z_{PNIPAM}\, \tilde{b}_{NIPAM}}{z_{PEO} + z_{PNIPAM}} \tag{12}$$

The volume of a monomeric scatterer is also weighted according to the polymerization degree in a similar way. At temperature larger than the LCST, the PNIPAM is expected to be hydrophobic and to be part of the core. The polymerization degree of the core, z_c, is equal to

$$z_c = z_{PAA} + z_{PNIPAM} \tag{13}$$

In a similar way to eq(12):

$$\tilde{b}_c = \frac{z_{PAA}\, \tilde{b}_{PAA} + z_{PNIPAM}\, \tilde{b}_{PNIPAM}}{z_{PAA} + z_{PNIPAM}} \tag{14}$$

2.4.1.2 Neutral and basic conditions

In neutral and basic conditions, the scattering intensity remains low (Figure 1), about one to two orders of magnitude smaller than in acidic conditions. Below the LCST, the copolymer chains are expected to be water soluble. However, the Debye model (Figure 3) for a pure free chain population fails to reproduce the observed cross sections. Scattering by free polymer chains remains a low intensity process. Micelles and aggregates have therefore also to be taken into account in order to account for the experimental data (see appendix I and II). The intensity at $q=0$ increases upon increasing temperature (Figure 3A). This suggests that the number of larger objects increases in parallel. Micelles most probably self-assemble from the free chains when PNIPAM becomes insoluble. The micelles are therefore assumed to consist of a PNIPAM core and of a corona made of PEO Gaussian chains, and negatively charged PAA extended chains (Figure 3B). Such extended chains may be modelled as rigid thin rods with an effective length L. To the best of our knowledge, the form factor of such complex objects has not been described in the literature. A more simple model involving only a dense core surrounded by rigid rods [37] has already been successfully used. For a core-Gaussian chains-rods situation, the following formula is obtained (the demonstration is given in Appendix I):

$$\frac{d\Sigma}{d\Omega}(\vec{q};R;Rg;L) = \frac{n}{N_m}\left[\left[N_m^2 \tilde{b}_{PNIPAM}^2 \frac{9}{(qR_c)^6}\left[\sin(qR_c)-qR_c\cos(qR_c)\right]^2\right.\right.$$

$$+ N_m \tilde{b}_{PEO}^2 \left[2\frac{\exp(-q^2R_g^2)+q^2R_g^2-1}{(q^2R_g^2)^2}\right]$$

$$+ N_m \tilde{b}_{PAA}^2 \left[\frac{2}{qL}Si(qL)-\frac{\sin^2\left(\frac{qL}{2}\right)}{\left(\frac{qL}{2}\right)^2}\right]$$

$$+ 2N_m^2 \tilde{b}_{PNIPAM}\,\tilde{b}_{PEO}\left\{\frac{3\left[\sin(qR_c)-qR_c\cos(qR_c)\right]}{(qR_c)^3}\right\}\left\{\frac{1-\exp(-q^2R_g^2)}{q^2R_g^2}\right\}\left\{\frac{\sin\left[q(R_c+R_g)\right]}{q(R_c+R_g)}\right\}$$

$$+ 2N_m^2 \tilde{b}_{PAA}\,\tilde{b}_{PNIPAM}\left\{\frac{3\left[\sin(qR_c)-qR_c\cos(qR_c)\right]}{(qR_c)^3}\right\}\left\{\frac{Si\left[q(R_c+L)\right]-Si\left[qR_c\right]}{qL}\right\}$$

$$+ N_m(N_m-1)\tilde{b}_{PEO}^2\left\{\frac{1-\exp(-q^2R_g^2)}{q^2R_g^2}\right\}^2\left\{\frac{\sin\left[q(R_c+R_g)\right]}{q(R_c+R_g)}\right\}^2$$

$$+ N_m(N_m-1)\tilde{b}_{PAA}^2\left\{\frac{Si\left[q(R_c+L)\right]-Si\left[qR_c\right]}{qL}\right\}^2 \tag{15}$$

$$+ 2N_m^2 \tilde{b}_{PAA}\,\tilde{b}_{PEO}\left\{\frac{\sin\left[q(R_c+R_g)\right]}{q(R_c+R_g)}\right\}\left\{\frac{Si\left[q(R_c+L)\right]-Si\left[qR_c\right]}{qL}\right\}\left\{\frac{1-\exp(-q^2R_g^2)}{q^2R_g^2}\right\}\right]$$

where

$$Si(x) = \int_0^x \frac{\sin(x')}{x'}dx' \tag{16}$$

The excess scattering length of a block i, $\tilde{b}_i$, is equal to product of the excess scattering length of the monomer unit by its degree of polymerization z_i. R_c is the radius of the PAA core, R_g is the radius of gyration of the PEO corona, and L is the effective length of the PAA rods.
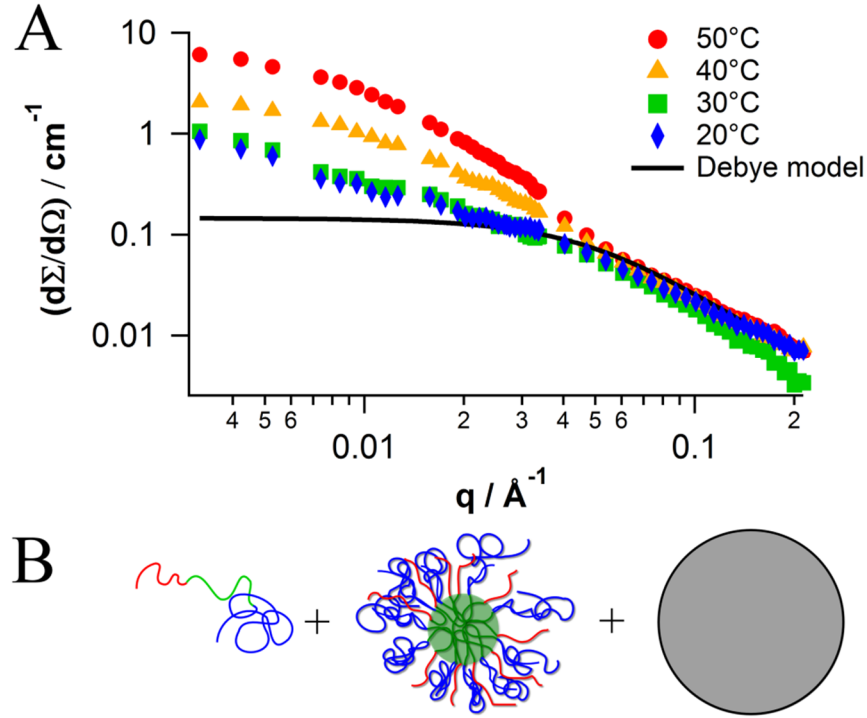
Figure 3 A: Experimental data (symbols) in basic conditions for non-deuterated polymers. The solid line displays the Debye model prediction for free chains with a 30 Å radius of gyration at 0.4% w/w concentration. The behavior is similar for the deuterated sample and in neutral condition. B: The fits which will be discussed in section 3 have been performed with a model involving a mixed population of free chains, of aggregates (grey) and of micelles with a core of PNIPAM (green), a corona of PEO and rods of PAA extending toward the solvent (eq(15)).

As in eq(4), this cross section has to be averaged over the aggregation number distribution. The structural parameters inferred from the model are then: the average radius of the micellar core $<R_c>$, the standard deviation of the core radius distribution, the radius of gyration of the PEO corona chains, the effective length of the PAA anionic chains, the average radius and the associated standard deviation for the aggregates.

2.5 Fitting procedures

Once the form factor of the micelles has been inserted into eq(3), the theoretical scattering cross section can be convoluted with an apparatus function which takes into account the experimental q-resolution. A triangular shape has been assumed for the scattering vector spread ($\Delta q/q = 10\%$). The resulting modelled cross sections are then fitted to the experimental scattering curves and the quality of the fit is monitored by calculating the χ^2

corresponding to the logarithm of the cross sections in order to weight similarly the whole sampled q-range.

3 *Results and discussion*

SANS cross-sections of micellar solution at pH = 2.5, 6.5 and 7.5 and at T = 20, 30, 40 and 50°C are displayed in Figure 4 together with fits based on the models described in section 2. A good agreement is observed between the experimental and fitted data. Figure 5 illustrates the relative contribution of micelles, aggregates and, when necessary, free chains under the three pH conditions.
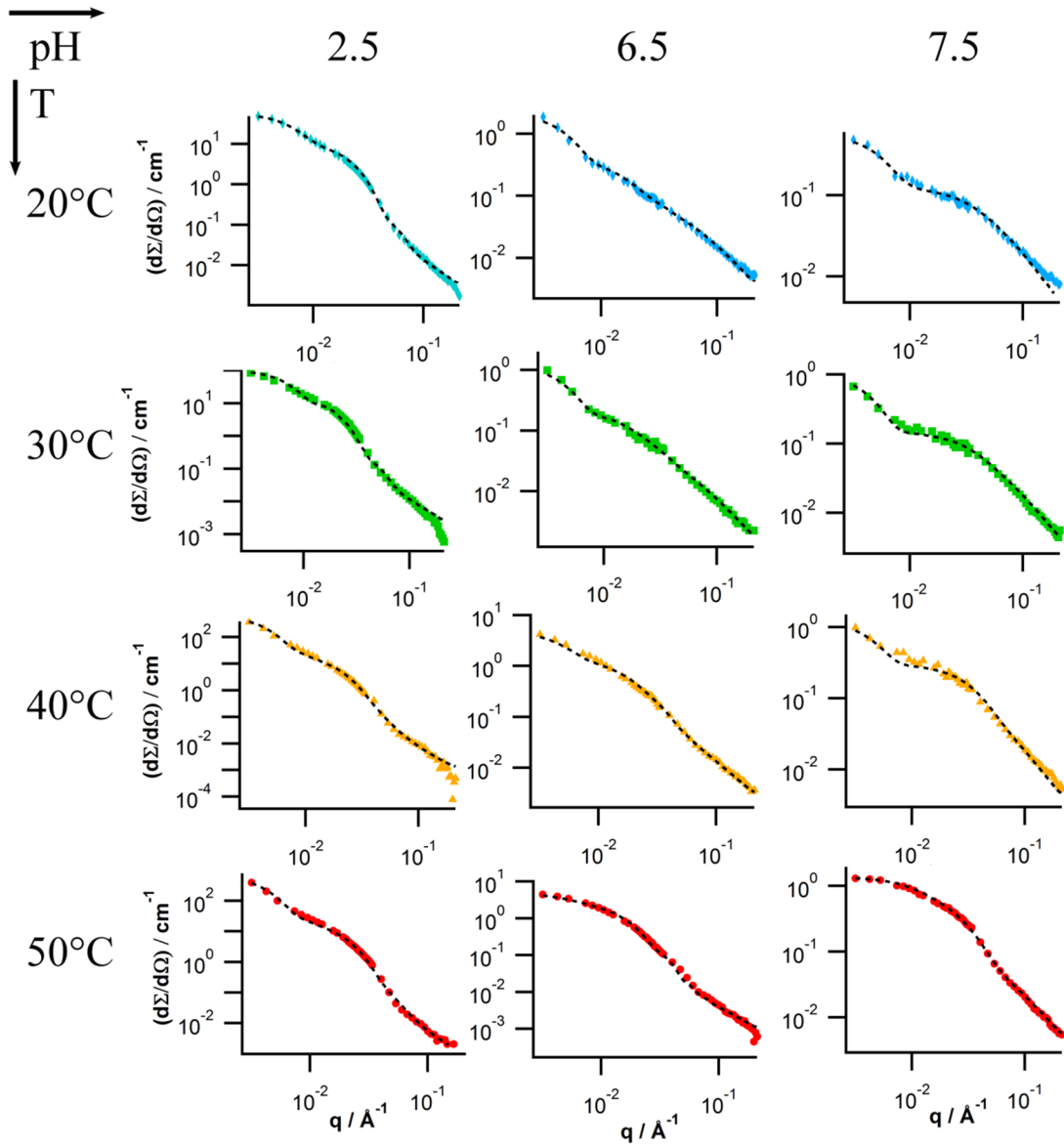
Figure 4 *SANS macroscopic cross sections of aqueous PEO-b-PNIPAM-b-PAA solutions in acidic (pH=2.5, non-deuterated PEO), neutral (pH=6.5, deuterated PEO) and basic (pH=7.5, deuterated PEO) conditions. Symbols: experimental data. Dotted lines: theoretical models (described in section 2).*
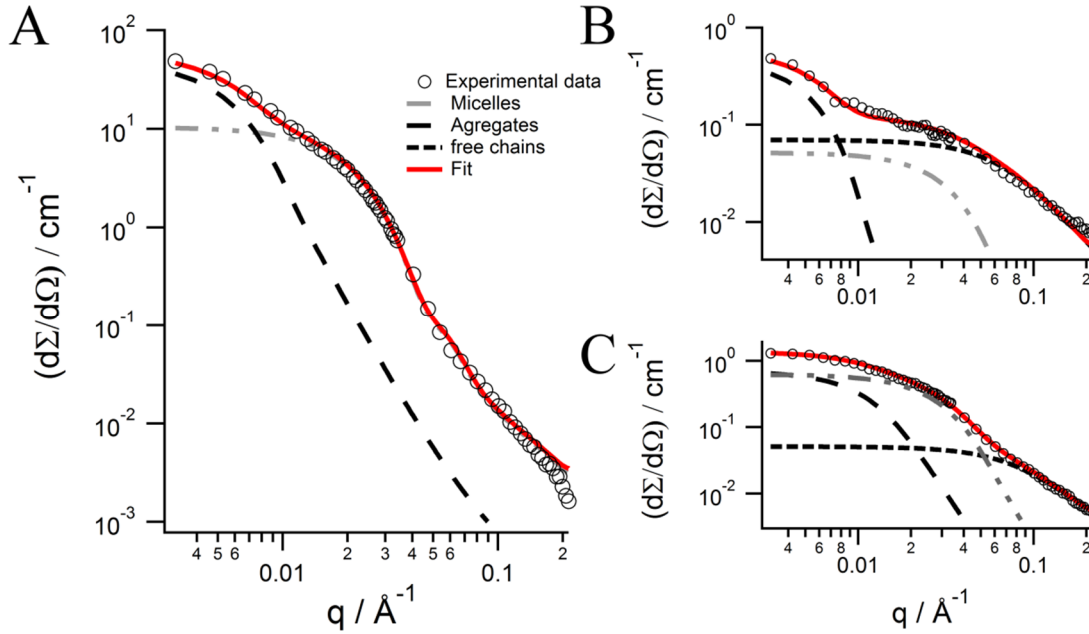
Figure 5 *SANS macroscopic scattering cross section of aqueous PEO-b-PNIPAM-b-PAA solutions. A: Non-deuterated copolymers at 20°C and pH=2.5; B: Deuterated copolymers at 20°C and pH=7.5; C: Deuterated copolymers at 50°C at pH=7.5. The contribution of micelles increases with temperature in basic condition. The contribution of free chains is neglected at acidic pH.*

3.1 Acidic conditions (pH < pKa,PAA)

Typical SANS curves displaying micelle and aggregate contributions in acidic conditions (pH=2.5) are presented in Figure 4. Deuterated and un-deuterated samples lead to similar results. The quality of the fits is not affected by the use of the Guinier law or of the homogeneous sphere form factor for the aggregate contribution. Figure 6 shows structural data obtained by averaging the results inferred from both undeuterated and deuterated polymers. A sigmoid behavior is observed for all parameters but for the corona chain radius of gyration, with an inflexion point located at 36±7.°C, which shows a good correlation with the PNIPAM LCST, which is known to vary within limits upon copolymerization [38]. The total micelle radius is estimated as $R_{tot} = R_c + 2R_g$. An increase of the average radius of the both the micelles (by about 50-60%) and the aggregates are observed upon crossing the LCST upwards. For the micelles, this increase results from an increase of the core radius whereas the radius of gyration of the corona chains remains nearly constant. This increase of the core radius has two origins: (i) because PNIPAM becomes hydrophobic above the LCST, the core is now composed of PAA and PNIPAM; (ii) the aggregation number is observed to roughly

double as the temperature crosses the LCST. We interpret this reorganization as resulting from chain exchange between micelles which is facilitated at higher temperature [39,40]. This chain reorganization is compatible with the observed significant increase of the micelle polydispersity through the LCST, measured as the standard deviation of the core size distribution, σ_m.

The size increase of the aggregate contribution is most probably linked to the fact that, above the LCST, the PEO block is the only water-soluble one, so that micelle aggregation becomes favored. This is also compatible with the increase of the aggregates polydispersity, as shown by the increase of the σ_a parameter. A corresponding increase of the fraction of chains included in the aggregates by 20 to 30% has also been noted.
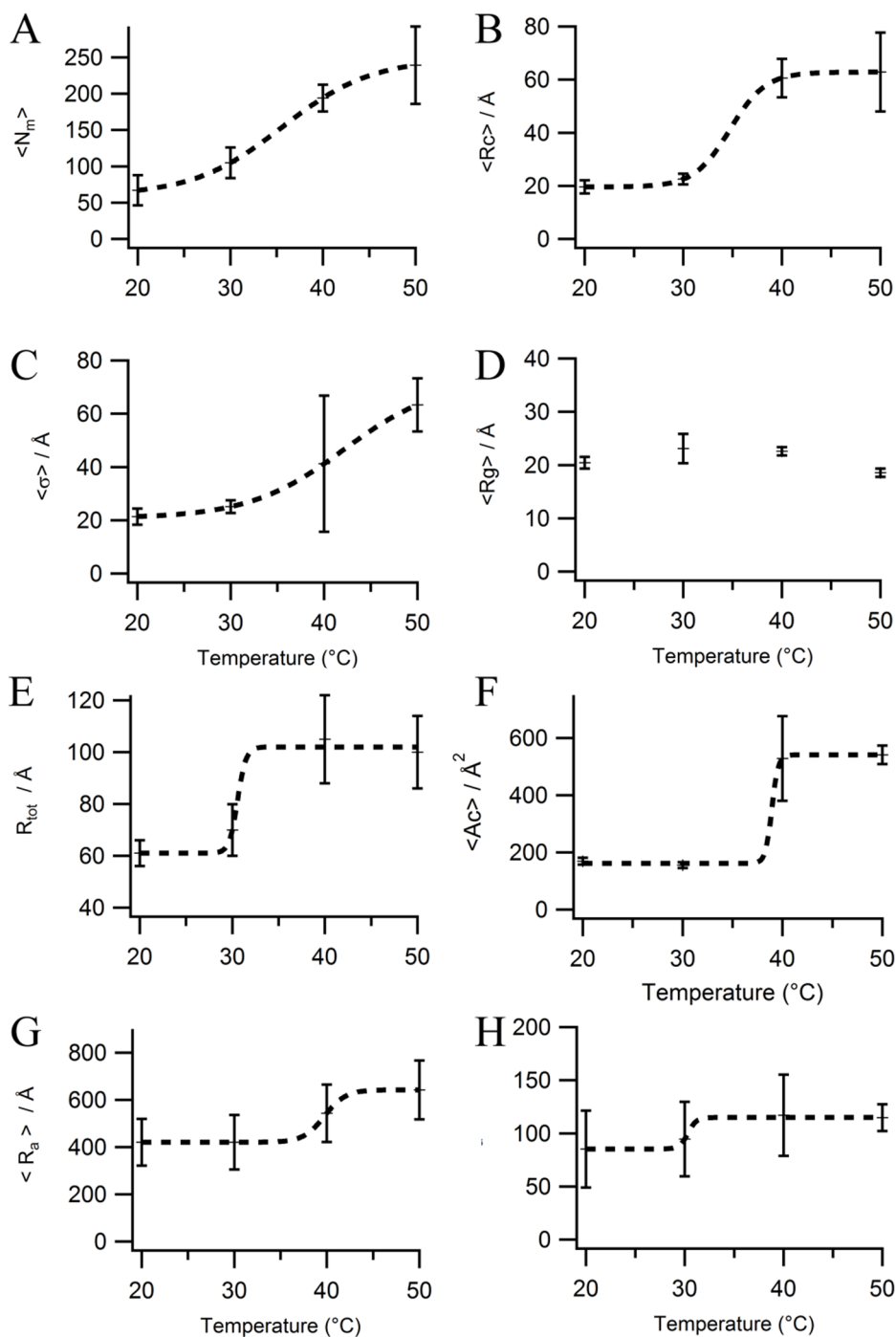
Figure 6 *Structural parameters obtained in acidic conditions (pH=2.5). Micelles: A: average aggregation number, B: average core radius; C: standard deviation of the radius size distribution; D: radius of gyration of the corona; E: total micelle radius; F: average surface per chain at the surface of the core; Aggregates: G: average radius; H: standard deviation of the radius size distribution. The dotted curves are intended to guide the eye. The position of the inflexion point is equal to T = 36±7°C.*

Contrarily to the others parameters, R_g, the radius of gyration of the corona chains remains unaffected when the temperature increases, even though the contour length of the chain is reduced because the PNIPAM$_{45}$ block has collapsed onto the core, so that the corona consists only of PEO$_{45}$ chains. In addition, the available area per PEO chain at the core-corona interface increases as the LCST is crossed (Figure 6F). We propose the following interpretation of this somewhat unexpected and paradoxical behavior. Below the LCST, the interfacial area per chain is relatively small (about 160 Å^2, see Figure 6F) and corresponds to a lateral extension of about 13 Å, much less than twice the radius of gyration of the corona chains, so that chain entanglement must take place. The volume fraction of the PNIPAM-*b*-PEO chains within the corona is then large: it can be estimated from the data of Tables 1 and Figure 6 to exceed 0.8. This corresponds to a situation similar to the bulk, from which most of the solvent molecules have been expelled. In such a quasi-bulk situation, the chains are expected to display an ideal behavior [41-43] with a radius of gyration related to the Kuhn segment length, *b*, and to the contour length of the PNIPAM-*b*-PEO chain, *L*, by eq(1). Based on the data of Table 1, in particular a Kuhn length of 7 Å, we then predict a radius of gyration for the corona chain of 18 Å. Above the LCST, only PEO belongs to the corona. Figure 6F shows that the interfacial area per chain is significantly larger (about 550 to 600 Å^2) so that a much smaller PEO volume fraction results. The latter can be estimated at 0.18, which corresponds to the semi-dilute regime with much less severe chain entanglement and with favored interactions with the solvent. In a good solvent, the radius of gyration is given by [43]

$$R_g^2 = \frac{25}{176} L^{6/5} b^{4/5} \tag{17}$$

Based again on the parameters of Table 1, we now predict a radius of gyration of 17 Å, close to the value below the LCST. It can be argued that the values found for R_g from the fits are larger, on average 21 Å. A moderate tuning of the Kuhn length can, however, account for this difference. Based on the fitted radius of gyration and on eq(1) (below the LCST) and eq(17) (above the LCST), we infer Kuhn segment lengths of 10 Å and 11 Å, respectively. These values remain reasonable. As a matter of fact, Vangeyte et al [37] found for PCL-*b*-PEO$_{114}$ copolymer micelles, Kuhn lengths of the PEO chains between 8 and 14 Å, depending on the aggregation number.

To summarize, the Kuhn segment length describing the chain stiffness does not vary much through the LCST. What significantly changes is the volume fraction of the hydrophilic

chains within the corona, from a bulk-like situation below the LCST, to a semi-dilute good solvent regime above the LCST, which leads to swollen PEO chains. Above the LCST, the hydrophilic chains have a smaller polymerization degree, but they are swollen, which leads to some compensation for the radius of gyration.

3.2 *Neutral and slightly basic conditions (pH > pKa$_{PAA}$)*

Samples at pH larger than the pK$_a$ of PAA display a very different behavior (Figures 1 and 4). The model based on a spherical PNIPAM core surrounded by negatively charged PAA rods and PEO Gaussian chains (eq(15)) has been used. Because of the small polymerization degree of the PAA block, the L parameter does not influence much the quality of the fits. We found an optimal value in all cases for L~25Å (80% extension). Figure 7 shows the evolution of several parameters with temperature.

A first result is that, even if they provide a small contribution to the scattering cross section, the free copolymer chains represent more than 90% of the samples below the LCST. When the LCST is crossed, the free chain fraction decreases with a concomitant self-assembling of micelles and also of aggregates. The percentage of chains inserted into micelles represents, however, barely more than 10% at 50°C, which means that micellization is not a favored process in conditions where the PAA is deprotonated and thus negatively charged. The average aggregation number of these micelles is of the same order of magnitude as under acidic conditions at low temperature.

These low micelle fractions explain the low scattered intensity at *q=0* at pH>6. The scattered intensity does not exceed a few tenth of cm^{-1} compared to a few hundred at acidic pH.

The amount of deprotonated acrylic repeat units is larger at pH=7.5 than at pH=6.5. The electrostatic repulsion is then expected to lead to smaller aggregates and micelles at the higher pH. Indeed the fraction of free chains remains always larger than 70% for the pH=7.5 sample, whereas it decreases to 23±7% at 50°C at pH=6.5. In a similar way, the fraction of chains in the aggregates increases as expected as the PNIPAM becomes insoluble. The negative charges of the PAA at pH = 7.5 keeps the fraction of chains in the aggregates lower than 24±7% whereas it reaches 65±7 % at pH 6.5±0.5.

The average radius of the aggregates under these pH conditions decreases upon crossing the LCST. Again, the aggregates are larger at pH=6.5 than 7.5 but their radius decreases by 40 % and 60% respectively from 20 to 50°C as seen in Figure 7F. As PNIPAM becomes more hydrophobic, the shift of the size distribution toward smaller radii might be linked to the decrease of water content of the aggregates.
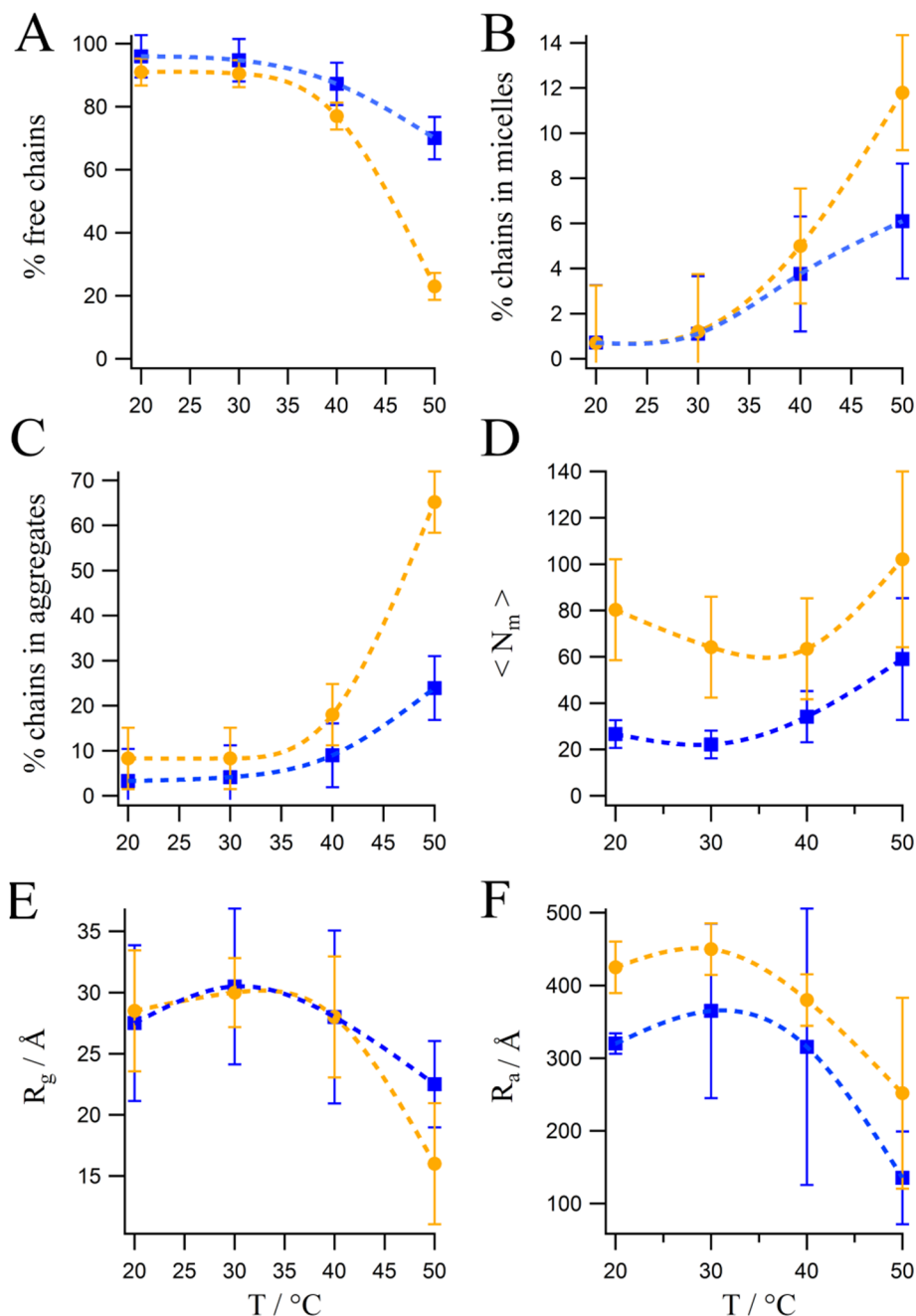
Figure 7 *Evolution of the structural parameters with respect to temperature. A-C: Fraction of free chains and of chains inserted in micelles and aggregates in the given nano-objects; D: Average aggregation number of the micelles; E: Radius of gyration of the corona*

chains or the free chains. F: average radius of the aggregates. Orange: pH=6.5; blue: pH=7.5.

4 Conclusions

Amphiphilic PEO$_{45}$-b-PNIPAM$_{45}$-b-PAA$_{13}$ and a PEO fully deuterated version, PEO$_{(d4)46}$-b-PNIPAM$_{46}$-b-PAA$_{11}$, were investigated by SANS. These samples are pH- and thermo-responsive. At low pH, the PAA is protonated and relatively hydrophobic, while at pH>5, the deprotonation leads to a hydrophilic polyelectrolyte. The PNIPAM is hydrophilic at temperature below the LCST (32°C) and hydrophobic at higher temperature. Somewhat surprisingly, DLS and SANS measurements reveal bimodal distribution at all pHs and temperatures investigated. To infer detailed information about the internal structure of the self-assembled nano-objects, the SANS cross sections have been fitted with analytical models involving a mixed population of core-corona micelles, spherical homogeneous aggregates and free chains. Polydispersity has been explicitly taken into account for the self-organized nanostructures through Gaussian distributions.

The scattering cross sections measured in acidic conditions are compatible with the presence of micelles built from a core of PAA and a corona of PNIPAM and PEO which we treated as undifferentiated to limit the number of fitting parameters. The Pedersen-Gerstenberg model (P&G) [36] successfully fits the micelle contribution. When temperature exceeds the LCST, the micelles reorganize through copolymer chain transfer and the aggregation number increases as well as the polydispersity. The PNIPAM collapses on the core and the only hydrophilic sequence is the PEO. The radius of gyration of the corona chains shows barely any change through the LCST as a result of some compensation between the chain length reduction and the swelling of the chains whose polymer volume fraction decreases leading to stronger interactions with the good solvent. The unfavorable hydrophilic/hydrophobic balance results in micelle aggregation leading to larger and more polydisperse aggregates.

The samples at pH= 6.5 and 7.5 show low intensities as the three sequences are soluble below the LCST. More than 90% of the chains are then freely dispersed in the solution. As the LCST is crossed, the free chain population decreases down to 70% at pH=7.5 while the micelle fraction increases. The majority of chains remain, however, unassembled, resulting in low scattering cross sections through the whole temperature range investigated. The strong

electrostatic repulsion induced by the negatively charged PAA blocks obviously hinders the self-assembling of the copolymer chains into micelles and this effect gets even more severe upon pH increase.

5 References

1. Tailor-made degradable copolymers for the design of advanced drug delivery systems. (2012).
2. Cajot, S., Lautram, N., Passirani, C., Jérôme, C.: Design of reversibly core cross-linked micelles sensitive to reductive environment. Journal of controlled release : official journal of the Controlled Release Society **152**, 30-36 (2011). doi:10.1016/j.jconrel.2011.03.026
3. Cajot, S., Riva, R., Billiet, L., Du Prez, F., Alexandre, M., Lecomte, P., Jérôme, C.: Novel Amphiphilic Mikto-Arm Star-Shaped Copolymers for the Preparation of PLA-Based Nanocarriers. Macromolecular Symposia **309-310**, 111-122 (2011). doi:10.1002/masy.201100044
4. Cajot, S., Van Butsele, K., Paillard, a., Passirani, C., Garcion, E., Benoit, J.P., Varshney, S.K., Jérôme, C.: Smart nanocarriers for pH-triggered targeting and release of hydrophobic drugs. Acta biomaterialia **8**, 4215-4223 (2012). doi:10.1016/j.actbio.2012.08.049
5. Van Butsele, K., Cajot, S., Van Vlierberghe, S., Dubruel, P., Passirani, C., Benoit, J.-P., Jérôme, R., Jérôme, C.: pH-Responsive Flower-Type Micelles Formed by a Biotinylated Poly(2-vinylpyridine)- block -poly(ethylene oxide)- block -poly(ε -caprolactone) Triblock Copolymer. Advanced Functional Materials **19**, 1416-1425 (2009). doi:10.1002/adfm.200801117
6. Kwon, G.S., Okano, T.: Polymeric micelles as new drug carriers. Advanced Drug Delivery Reviews **21**, 107-116 (1996). doi:http://dx.doi.org/10.1016/S0169-409X(96)00401-2
7. Lavasanifar, A., Samuel, J., Kwon, G.S.: Poly(ethylene oxide)-block-poly(L-amino acid) micelles for drug delivery. Advanced drug delivery reviews **54**, 169-190 (2002).
8. Huh, K.M., Lee, S.C., Cho, Y.W., Lee, J., Jeong, J.H., Park, K.: Hydrotropic polymer micelle system for delivery of paclitaxel. Journal of controlled release : official journal of the Controlled Release Society **101**, 59-68 (2005). doi:10.1016/j.jconrel.2004.07.003
9. Gould, P.: Nanoparticles probe biosystems. 36-43 (2004).
10. Aqil, A., Qiu, H., Greisch, J.-F., Jérôme, R., De Pauw, E., Jérôme, C.: Coating of gold nanoparticles by thermosensitive poly(N-isopropylacrylamide) end-capped by biotin. Polymer **49**, 1145-1153 (2008). doi:10.1016/j.polymer.2007.12.033
11. Aqil, a., Vasseur, S., Duguet, E., Passirani, C., Benoît, J.P., Jérôme, R., Jérôme, C.: Magnetic nanoparticles coated by temperature responsive copolymers for hyperthermia. Journal of Materials Chemistry **18**, 3352 (2008). doi:10.1039/b804003f
12. Aqil, a., Vasseur, S., Duguet, E., Passirani, C., Benoît, J.P., Roch, a., Müller, R., Jérôme, R., Jérôme, C.: PEO coated magnetic nanoparticles for biomedical application. European Polymer Journal **44**, 3191-3199 (2008). doi:10.1016/j.eurpolymj.2008.07.011
13. Lopez, J.A., González, F., Bonilla, F.A., Zambrano, G., Gómez, M.E.: Synthesis and characterization of fe 3o4 magnetic nanofluid. **30**, 60-66 (2010).
14. Pham Hoai Linh , P.V.T., Nguyen Anh Tuan , Nguyen Chi Thuan , Do Hung Manh, Nguyen Xuan Phuc Le Van Hong: Magnetic fluid based on Fe 3 O 4 nanoparticles: Preparation and hyperthermia application. Journal of Physics: Conference Series **187**, 012069 (2009). doi:10.1088/1742-6596/187/1/012069
15. Alili, L., Chapiro, S., Marten, G.U., Schmidt, A.M., Zanger, K., Brenneisen, P.: Effect of Fe3O4 Nanoparticles on Skin Tumor Cells and Dermal Fibroblasts. BioMed Research International **2015**, 11 (2015). doi:10.1155/2015/530957
16. Echeverria, C., Peppas, N.A., Mijangos, C.: Novel strategy for the determination of UCST-like microgels network structure: effect on swelling behavior and rheology. Soft Matter **8**, 337-346 (2012). doi:10.1039/C1SM06489D

17. Borukhov, I., Andelman, D., Borrega, R., Cloitre, M., Leibler, L., Orland, H.: Polyelectrolyte Titration: Theory and Experiment. The Journal of Physical Chemistry B **104**, 11027-11034 (2000). doi:10.1021/jp001892s

18. Sibret, P., Joset, A., Leyh, B., Jérôme, C. (to be published).

19. Kundu, S.K., Gupta, S., Stellbrink, J., Willner, L., Richter, D.: Relating structure and flow of soft colloids. European Physical Journal: Special Topics **222**, 2757-2772 (2013). doi:10.1140/epjst/e2013-02056-1

20. Hammouda, B.: SANS from Polymers—Review of the Recent Literature. Polymer Reviews **50**, 14-39 (2010). doi:10.1080/15583720903503460

21. Hammouda, B.: Probing Nanoscale Structures–the Sans Toolbox. NIST Center for Neutron Research, 224 (2010). doi:10.1016/j.nano.2007.10.035

22. Walker, L.M.: Scattering from polymer-like micelles. Current Opinion in Colloid and Interface Science **14**, 451-454 (2009). doi:10.1016/j.cocis.2009.08.001

23. Castelletto, V., Hamley, I.W.: Modelling small-angle scattering data from micelles. Current Opinion in Colloid and Interface Science **7**, 167-172 (2002). doi:10.1016/S1359-0294(02)00043-2

24. Alaimo, D., Beigbeder, A., Dubois, P., Broze, G., Jérôme, C., Grignard, B.: Block, random and palm-tree amphiphilic fluorinated copolymers: controlled synthesis, surface activity and use as dispersion polymerization stabilizers. Polym. Chem. **5**, 5273-5282 (2014). doi:10.1039/c4py00366g

25. Miquelard-Garnier, G., Creton, C., Hourdet, D.: Strain induced clustering in polyelectrolyte hydrogels. Soft Matter **4**, 1011-1023 (2008). doi:10.1039/B717460H

26. Zhang, W., Zou, S., Wang, C., Zhang, X.: Single Polymer Chain Elongation of Poly(N -isopropylacrylamide) and Poly(acrylamide) by Atomic Force Microscopy. 10258-10264 (2000).

27. Hill, R.: Hydrodynamics and electrokinetics of spherical liposomes with coatings of terminally anchored poly(ethylene glycol): Numerically exact electrokinetics with self-consistent mean-field polymer. Physical Review E **70**, 051406 (2004). doi:10.1103/PhysRevE.70.051406

28. Mark, J.: Polymer Data Handbook. New York, USA, 1274 (1999). doi:10.1021/ja907879q

29. Sigma-Aldrich: Poly(ethylene oxide) properties. http://www.sigmaaldrich.com/catalog/product/aldrich/181986 (2015). Accessed 30/01 2015

30. Shibayama, M., Karino, T., Miyazaki, S., Okabe, S., Takehisa, T., Haraguchi, K.: Small-Angle Neutron Scattering Study on Uniaxially Stretched Poly (N -isopropylacrylamide) - Clay Nanocomposite Gels. 10772-10781 (2005).

31. aussi, D.O.d.m.à.j. http://physchem.kfunigraz.ac.at/sm/Service/Water/D2Odens.htm.

32. Sigma-Aldrich: Deuterium oxide properties. http://www.sigmaaldrich.com/catalog/product/aldrich/151882 (2015). Accessed 15/06 2015

33. Dianoux, A., Lander, G.: Neutron data booklet. (2003).

34. Brûlet, A., Lairez, D., Lapp, A., Cotton, J.-P.: Improvement of data treatment in small-angle neutron scattering. J Appl crystallogr **40**, 165-177 (2007).

35. Joseph, J., Dreiss, C.a., Cosgrove, T., Pedersen, J.S.: Rupturing polymeric micelles with cyclodextrins. Langmuir : the ACS journal of surfaces and colloids **23**, 460-466 (2007). doi:10.1021/la061850g

36. Pedersen, J.S., Gerstenberg, M.C.: Scattering Form Factor of Block Copolymer Micelles. Macromolecules **29**, 1363-1365 (1996).

37. Vangeyte, P., Leyh, B., Heinrich, M., Grandjean, J., Bourgaux, C., Je, R.: Self-Assembly of Poly(ethylene oxide)-b-poly(E-caprolactone) Copolymers in Aqueous Solution. Langmuir **20**, 8442-8451 (2004).

38. Chen, Y., Sone, M., Fuchise, K., Sakai, R., Kakuchi, R., Duan, Q., Sun, J., Narumi, A., Satoh, T., Kakuchi, T.: Structural effect of a series of block copolymers consisting of poly(N-isopropylacrylamide) and poly(N-hydroxyethylacrylamide) on

thermoresponsive behavior. Reactive and Functional Polymers **69**, 463-469 (2009). doi:http://dx.doi.org/10.1016/j.reactfunctpolym.2008.12.016

39. Choi, S.H., Bates, F.S., Lodge, T.P.: Molecular exchange in ordered diblock copolymer micelles. Macromolecules **44**, 3594-3604 (2011). doi:10.1021/ma102788v
40. Choi, S.H., Lodge, T.P., Bates, F.S.: Mechanism of molecular exchange in diblock copolymer micelles: Hypersensitivity to core chain length. Physical Review Letters **104**, 1-4 (2010). doi:10.1103/PhysRevLett.104.047802
41. Wall, F.T., Seitz, W.a.: Simulation of polymers by self-avoiding, nonintersecting random chains at various concentrations. The Journal of Chemical Physics **67**, 3722 (1977). doi:10.1063/1.435311
42. Strobl, G.R.: The Physics of Polymers: Concepts for Understanding Their Structures and Behaviour. Springer, (1997)
43. Teraoka, I.: Polymer Solutions: An Introduction to Physical Properties. **3**, 360 (2002). doi:10.1002/0471224510

CHAPTER V

Structure of Metallo-Supramolecular Micellar Gels

C. Mugemana, A. Joset, P. Guillet, M.-S. Appavou, N. De Souza, C.-A. Fustin, B. Leyh,
J.-F. Gohy Macromolecular Chemistry and Physics 2013, 214, 1699.

Abstract

This chapter sets out a SANS investigation of metallo-supramolecular micellar gels built from polystyrene-block-poly(tert-butylacrylate) PS-b-PtBA-tpy (-tpy: terpyridine) block copolymers and transition metal ions is presented. The influence of the copolymer concentration on the structure and spatial organization of the micelles, as well as the impact of the subsequent addition of metal ions (Fe(II), Ni(II) and Zn(II)) on these characteristics were extensively studied. The experimental scattering cross sections were fitted with an analytical formula based on the Percus-Yevick hard sphere model and on the Pedersen-Gerstenberg model for the structure and the form factor, respectively. The resulting structural information was correlated with previously performed light scattering and rheology experiments.

1   Introduction

In the past decade, important efforts have been made toward novel and complex polymeric materials for applications in nanotechnology and other fields. A typical tool to produce well-defined nanostructures consists in using the self-assembly process of block copolymers either in bulk or in solution [1]. In solution, block copolymers are well known to undergo phase separation in a selective solvent of one of the blocks leading to micelles composed of a core formed by the insoluble blocks, which is surrounded by a corona formed by the soluble blocks [2,3]. One noteworthy feature of this self-assembly process is the accessibility of a wide range of distinct morphologies (*i.e.* spherical micelles, rod-like micelles, vesicles) depending on the characteristics of the block copolymers (composition, architecture, chemical structure of the monomers, etc). In addition, the combination of supramolecular interactions with block copolymer self-assembly has recently attracted a great attention in the field of polymer science, paving the way towards hybrid polymeric materials with unique properties [4-8] Indeed, the precision of modern polymer chemistry associated with the outstanding potential of supramolecular interactions has appeared to be an extremely promising area of research. Among the existing supramolecular interactions, metal-ligand interactions are of high interest: the coordination bond is highly directional, a wide range of easily functionalized ligands is available, and the characteristic stability and life-time of coordination bonds can be fine-tuned by selecting appropriate metal ions [8]. The incorporation of those metal-ligand complexes into polymeric architectures has led to the so-called metallo-supramolecular block copolymers showing magnetic [9,10], catalytic [11] or photo-physical [12-15] properties. Moreover, metallo-supramolecular block copolymers have recently proven to be extremely valuable precursors of advanced functional materials such as nanocages [16,17], stimuli-responsive micelles [18-20] and nanoporous membranes [21,22].

In this context, we have recently described an original method to trigger the hierarchical self-assembly of block copolymers using metal-ligand interactions [23-25]. Firstly, a polystyrene-*block*-poly(*tert*-butylacrylate) diblock copolymer bearing a terpyridine moiety at the chain end (PS-*b*-PtBA-tpy) was dissolved in ethanol, a selective solvent of the PtBA block, to yield micelles composed of a PS core and PtBA coronal chains bearing a terpyridine ligand at their extremity. The second level was then triggered by addition of metal ions to give flower-like micelles in dilute solutions [23], and micellar gels in the concentrated

regime [24,25]. Such attractive interactions are somewhat similar to those found in other associating systems such as telechelic polymers bearing hydrophobic stickers at the chain end [26]. Furthermore, the accordingly prepared micellar gels exhibited interesting viscoelastic properties, which could be easily fine-tuned as a function of the nature and concentration of the added metal ions. Besides the impact of metal ions, our group has recently demonstrated that the morphology of micelles also directs the mechanical properties of the micellar gels [25]. Interestingly, the possibility to break those metal-ligand complexes holding the micelles together was achieved either by addition of competing ligands or, in a reversible way, by mechanical stresses, leading to materials exhibiting self-healing properties [24]. Until now, light scattering was used to determine the typical sizes of those micelles in the dilute regime [23], while rheology enabled us to probe the mechanical properties of the micellar gels obtained in the concentrated regime [24,25]. However, no detail is yet available about either the inner structure of the micelles or about their organization in the gel state. Small angle neutron and X-ray scattering techniques provide ideal analysis tools to probe the morphology of ordered phases in block copolymer melts, solids and gels since the length-scale of these nanostructures ranges from 1 to 100 nm. While Small Angle X-ray Scattering (SAXS) is convenient to probe systems where the electron density contrast between polymer blocks is large enough, Small Angle Neutron Scattering (SANS) is more appropriate to investigate polymer structures in which the contrast is generated via isotopic labeling [27]. In case of SANS investigations of block copolymer micelles, two strategies have been described so far. The first one consists in selectively replacing hydrogen atoms by deuterium for one of the blocks in order to enhance the scattering contrast. The second more straightforward strategy consists in using a deuterated solvent to solubilize the corona of the micelles. In the dilute regime, the analysis of the SANS data highlights the form factor of the isolated micelles [28]. At higher concentrations, the contribution of the structure factor becomes significant, which is particularly interesting since the short-range organization of the micellar network or gel can then be monitored [29-34].

In the present contribution, a detailed SANS analysis of metallo-supramolecular micellar gels from polystyrene-*block*-poly(*tert*-butylacrylate) PS-*b*-PtBA-tpy diblock copolymers is presented and the results are correlated with previous rheology experiments [24,25]. To that end, a two-level hierarchical self-assembly is performed. The first level of organization is reached by solubilization of the PS-*b*-PtBA-tpy diblock copolymer in ethanol-d_6 to yield

micelles formed by a polystyrene core and surrounded by PtBA coronal chains bearing terpyridine at the chain end. A significant neutron scattering signal is thus generated due to the contrast between the non-deuterated copolymer micelles and deuterated ethanol. The second level is triggered upon addition of metal ions to generate a micellar network, which gives rise to a micellar gel whenever the metal-ligand complexes are stable enough to strengthen the network. This paper focuses on the SANS investigation of metallo-supramolecular gels and on the impact of metal ions on the micellar structure using appropriate models from the dilute to the concentrated regime.

2 Experimental Section

2.1 Instrumentation

^{1}H-NMR spectra were recorded on a 300 MHz Bruker spectrometer at 25°C. Chemical shifts are given in ppm downfield from tetramethylsilane (TMS). Size exclusion chromatography (SEC) was carried out on a system composed of two PSS Gram columns (100 Å and 1000 Å) connected to a Waters 410 differential refractometer and a Waters UV detector, with dimethylformamide containing 5 mM NH_4PF_6 as the carrier solvent (35 °C, 1 mL min^{-1}). Polystyrene standards were used for calibration. Dynamic light scattering (DLS) experiments were performed on a Malvern CGS-3 apparatus equipped with a He-Ne laser with a wavelength of 632.8 nm. The measurements were performed at 25 °C (90°) at 0.05 g L^{-1} concentration. The method of the cumulants was used to analyze DLS results, while the size distribution histograms were obtained by the CONTIN method. The polydispersity index (PDI) of the micelles was estimated from the Γ_2/Γ_1^2 ratio in which Γ_1 and Γ_2 represent the first and second order moments calculated from the cumulants method. Atomic force microscopy (AFM) analysis was performed on a Digital 50 Instruments Nanoscope V scanning force microscopy in tapping mode using NCL cantilevers (Si, 48 N m^{-1}, 300 kHz, Nanosensors). The silicon wafers were cleaned by immersion in a piranha solution (H_2SO_4 98% (70% v/v) and H_2O_2 35% (30% v/v)) for 15 minutes and thoroughly rinsed with ultrapure water. A few drops of the micellar solution (0.05 g L^{-1} concentration) were spin-coated onto a dried wafer at 2000 rpm for 40 s. Samples were then dried in vacuum at 35°C overnight, prior measurement.

SANS (Small Angle Neutron Scattering) experiments were performed on the KWS-2 diffractometer of the Jülich Centre for Neutron Science at the Forschungsneutronenquelle Heinz Maier-Leibnitz (FRMII) Outstation in Garching, Germany [35]. The solution samples were loaded in Hellma quartz cuvettes (404.000QX), while gels were sandwiched into quartz cells. The data were recorded at 20 °C and at a wavelength of $\lambda = 4.5$ Å (with a spread of $\Delta\lambda/\lambda = 20\%$) at 2 m and 8 m sample to detector distances, and a wavelength of $\lambda = 12$ Å at 8 m sample to detector distance to cover a wide range of scattering vectors, q, from 3×10^{-3} to 0.5 Å^{-1}. The dead time of the detector is 0.64 μs for the temporal convolution.

The scattered intensity was corrected for empty cell scattering and incoherent background by subtracting the ethanol-d$_6$ solvent. The 2D scattering patterns were radial averaged around the beam center and the macroscopic scattering cross sections, $d\Sigma/d\Omega$, were obtained in absolute scale by normalizing the data with respect to the flat incoherent scattering of a Plexiglas sample according to standard procedures developed at the Jülich Centre for Neutron Science at FRM(II) using the QtiKWS software.

2.2 Synthesis of terpyridine end-functionalized poly(tert-butylacrylate) macro-initiator PtBA$_{180}$-tpy

The 2,2,5-trimethyl-3-(1-(4'-(4"-terpyridinyloxy)methyl)phenylethoxy)-4-phenyl-3-azahexane (6.8×10^{-2} g, 1.2×10^{-4} mol) initiator was dissolved in purified *tert*-butylacrylate (6 g, 4.6×10^{-2} mol). For a degree of polymerization (DP) of 400 (at 100% conversion), 5% of free nitroxide with respect to the amount of initiator were added (12.8×10^{-4} g, 5.8×10^{-6} mol). Ten freeze-pump-thaw cycles were then applied to remove oxygen prior to polymerization in a carousel at 125 °C. A polymerization time of 1260 min was used in order to yield the PtBA$_{180}$-tpy block. After polymerization, the monomer was removed under low pressure in presence of acetone. The solid polymer was then dried overnight in a vacuum oven at room temperature. ^{1}H-NMR (CDCl$_3$; 300 MHz): δ = 8.66 (m, 2H; H$_{6,6"}$), 8.58 (m, 2H; H$_{3,3"}$), 8.08 (m, 2H; H$_{3',5'}$), 7.83 (m, 2H; H$_{4,4"}$), 7.57-7.18 (m, 22H; H$_{aromatics}$, H$_{5,5"}$), 5.35 (m, 2H; tpyOCH$_2$); 2.45-0.53 (m, 2160H; PtBA$_{backbone\ aliphatics}$), M$_n$ (^{1}H-NMR) = 23,600 g mol^{-1}, PDI (SEC) = 1.18, Yield: 62%.

Synthesis of terpyridine end-functionalized polystyrene-*block*-poly(*tert*-butylacrylate) block copolymers PS$_{70}$-*b*-PtBA$_{180}$-tpy

The terpyridine functionalized poly(*tert*-butylacrylate) macro-initiator PtBA$_{180}$-tpy (1 g, 4.1×10^{-5} mol), was dissolved in styrene (0.9 g, 9.3×10^{-3} mol). The degree of polymerization was set at 240 for a monomer conversion of 100%. Anisole (40% *w/t*) was added, and the reaction mixture underwent ten freeze-pump-thaw cycles to remove oxygen. The vessel was then transferred in an oil bath at 125°C. The polymerization was carried out during 510 minutes to reach a degree of conversion of 30%. After the polymerization reaction, the crude mixture was dissolved in acetone, and further dried under low pressure to remove the residual monomer. Finally, the block copolymer was dried overnight under vacuum at room temperature.

Analytical data for PS$_{70}$-*b*-PtBA$_{180}$-tpy: ^{1}H-NMR (CDCl$_3$): δ = 8.69 (m, 2H; H$_{6,6''}$), 8.62 (m, 2H; H$_{3,3''}$), 8.20 (m, 2H; H$_{3',5'}$), 7.93 (m, 2H; H$_{4,4''}$), 7.57-6.32 (m, 400H; PS$_{\text{backbone aromatics}}$), 5.35 (m, 2H; tpyOCH$_2$), 2.45-0.53 (m, 2520H; PS$_{\text{backbone aliphatic}}$ and PtBA$_{\text{backbone aliphatic}}$); M$_n$ (^{1}H-NMR) = 30,400 g mol^{-1}; PDI (SEC) = 1.26; Yield: 69%.

2.3 *Preparation of micellar gels*

The PS$_{70}$-*b*-PtBA$_{180}$-tpyblock copolymer was dissolved in deuterated ethanol (CD$_3$CD$_2$OD) at a concentration of 200 g L^{-1}, then stirred several days at room temperature and further diluted at concentrations of 20 g L^{-1}, 80 g L^{-1}, 120 g L^{-1}. A series of micellar gels of 80 g L^{-1}, 120 g L^{-1} and 160 g L^{-1} concentrations were respectively prepared from the 120 g L^{-1}, 160 g L^{-1} and 200 g L^{-1} micellar solutions upon addition of a determined volume of deuterated ethanol containing half an equivalent (with respect to the amount of terpyridine groups) of metal ions (NiCl$_2$.6H$_2$O; FeCl$_2$.4H$_2$O and ZnCl$_2$).

3 Results and Discussion

A PS$_{70}$-*b*-PtBA$_{180}$-tpy copolymer was synthesized by nitroxide-mediated radical polymerization (Scheme 1) as described elsewhere [23-25].
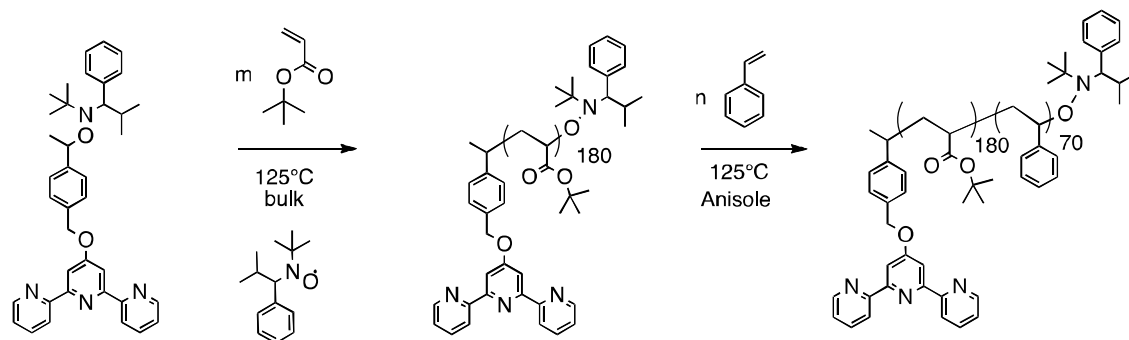
Scheme 1 *General synthetic strategy used to prepare the PS$_{70}$-b-PtBA$_{180}$-tpy copolymer (the numbers in subscript represent the average degrees of polymerization).*

This copolymer was dissolved in deuterated ethanol, a selective solvent for the PtBA block and a non-solvent of the PS block. The characteristic features of the resulting micellar solutions in the dilute regime were first investigated by DLS at a concentration of 0.05 g L^{-1}. The experimental autocorrelation function and the particle size distribution obtained by the CONTIN analysis of the DLS data revealed a unimodal distribution as shown in Figure 1. Cumulant analysis showed well-defined objects with a hydrodynamic radius of 25.8 nm (PDI as determined by DLS: 0.06). AFM analysis was used to determine the micellar morphology in the dry state, by analyzing the micelles spin-coated onto a silicon wafer. According to the AFM image (Figure 2), spherical micelles were obtained. The height of the objects measured by AFM corresponds essentially to the diameter of the micellar core with a small contribution from the collapsed coronal chains [36] and is equal to 18.0 ± 1.9 nm.
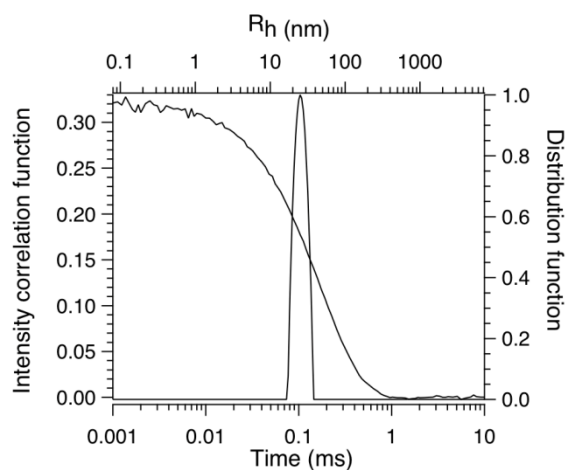
Figure 1 *Intensity autocorrelation function and the associated distribution function obtained by CONTIN analysis of the PS$_{70}$-b-PtBA$_{180}$-tpy micellar solution at a concentration of 0.05 g L^{-1}.*
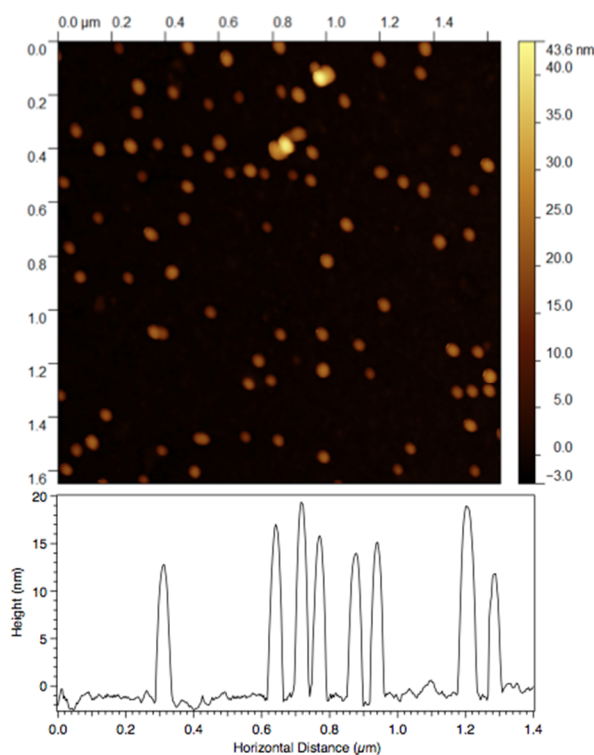
Figure 2 *AFM height image of micelles formed by the PS$_{70}$-b-PtBA$_{180}$-tpy copolymer at a concentration of 0.05 g L^{-1} and the plot of the height values obtained from a cross-section profile.*

123

Figure 3 shows the scattered intensities obtained by SANS on micellar solutions in deuterated ethanol at 2, 8, 12 and 20% *w/v* concentrations. At the lowest concentration investigated (2 % *w/v*), the macroscopic scattering cross section, $\frac{d\Sigma}{d\Omega}(q)$, decreases monotonically, suggesting that only isolated micelles are observed in this concentration regime, and giving thus access to the form factor of the micelles. In contrast, by increasing further the concentration to 8, 12 and 20% *w/v*, the scattering profiles revealed more and more clearly a structure factor peak arising from mutual interferences between the neutron waves scattered by different micelles.
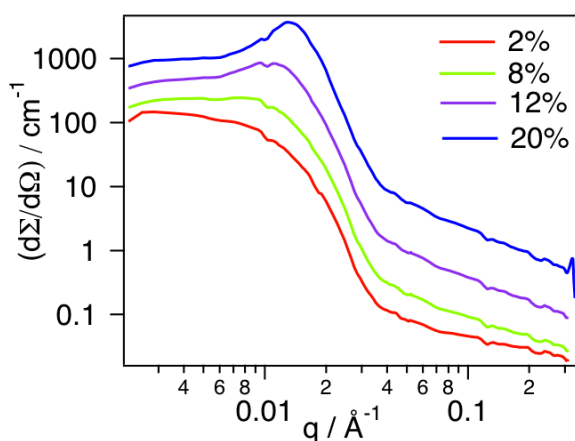
Figure 3 *SANS intensities $\frac{d\Sigma}{d\Omega}(q)$ versus* q *for the PS$_{70}$-*b*-PtBA$_{180}$-tpy block copolymer dissolved in deuterated ethanol for several copolymer concentrations. For clarity reasons the intensities of the concentrated solutions (8%; 12% and 20%* w/v*) were slightly shifted upward.*

The impact of the addition of metal ions on the structure and spatial organization of the micelles was further investigated upon addition of 0.5 eq. (with respect to the concentration of terpyridine ligands) of each metal ion (i.e. Fe(II), Ni(II) and Zn(II)) to the micellar solutions. The resulting scattering cross sections are plotted in Figure 4 for the micellar solutions at a concentration of 12% *w/v*. In the case of the micellar solutions dosed with Fe(II) and Ni(II) ions, an increase of the intensity of the structure factor peak in the low *q* regime was observed compared to the micellar solution with no metal ion. Such an increase results likely from the formation of a network of micelles connected via metal-terpyridine complexes, since Ni(II) and Fe(II) ions form preferentially *bis*-terpyridine complexes [37]. These complexes can be formed either in an intra-micellar way (thus leading to the formation of loops in the micellar corona) or in an inter-micellar way (thus leading to a network of connected micelles). In the

case of Zn(II), no structure factor peak was observed because Zn(II) rather forms *mono*-terpyridine complexes [37], which do not lead to a network of micelles. These observations are in agreement with previous results from rheology experiments, which revealed that upon addition of 0.5 eq. of Fe(II) and Ni(II) ions to the micellar solution at a concentration of 12% *w/v*, a hard gel exhibiting high moduli (both G' and G") was formed, while addition of Zn(II) ions only resulted in a viscous solution [24].
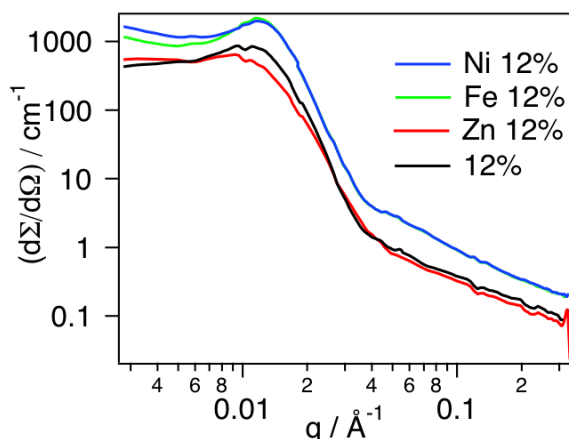
Figure 4 *SANS intensities $\frac{d\Sigma}{d\Omega}(q)$ versus q for the gels prepared from the PS$_{70}$-b-PtBA$_{180}$-tpy block copolymer in deuterated ethanol for different metal ions at a copolymer concentration of 12%* w/v.

To obtain quantitative information, the experimental scattering data have been fitted to an analytical model. In the framework of the so-called decoupling approximation [38], the macroscopic neutron scattering cross section of a system of polydisperse spherical micelles, $\frac{d\Sigma}{d\Omega}$, can be split into two factors. The first one is the form factor, *P(q)*, which describes the shape and internal structure of the micelles [39] and which must be averaged over the size distribution of the micelles. The interference effects arising from the spatial organization induced by the interactions between micelles is represented by a structure factor, *S(q)*. [29,39] The scattering intensity $\frac{d\Sigma}{d\Omega}$, can thus be written as (Equation 1).

$$I(q) = \frac{d\Sigma}{d\Omega} = \frac{N}{V}P(q) \times S(q) \quad (1)$$

where $\frac{N}{V}$ is the average number of micelles per unit volume. For dilute systems, where the scattering particles are separated by distances large enough so that no interference between neutrons scattered from different particles are detected, the structure factor *S(q)* is equal to 1 in the investigated *q* range. The intensity of the scattered neutrons is thus a function of the average form factor only. Since no structure factor peak was observed for the dilute solution at 2% *w/v* concentration, these data have been selected to choose an appropriate model for the form factor. The model of Pedersen and Gerstenberg was found to reproduce well the form factor of the micelles [28]. This model describes a block copolymer micelle as a desolvated dense spherical core formed by the insoluble blocks, surrounded by a corona of Gaussian chains dissolved in the selective solvent (*e.g* deuterated ethanol) (Scheme 2). Briefly, the form factor is the sum of four terms: the self-correlation of the spherical core, the self-correlation of the individual coronal chains, the cross term between the core and the chains, and the cross term between different coronal chains. It can be expressed as an analytical function of the core radius, R_i, of the radius of gyration of the individual coronal chains, R_g, of the degrees of polymerization of the two blocks, and of the excess scattering lengths of the elementary scatterers. As suggested by Pedersen and Gerstenberg, the coronal chains were anchored at a distance equal to R_g from the core-corona interface, in order to avoid any penetration of the PtBA coronal chains into the dense PS core. As we assume a dense PS core, its radius R_i is a single-valued function of the micelle aggregation number, N_m, the volume of the monomer and the degree of polymerization of the PS block being known. The average form factor *P(q)* can then be written as:

$$P(q) = \int_0^{+\infty} b_T^2(N_m) P_{PG}\big(q ; N_m , R_g\big)\, \Gamma(N_m)\, dN_m \quad (2)$$

$P_{PG}\big(q ; N_m , R_g\big)$ is the Pedersen-Gerstenberg form factor normalized to unity at *q* = 0. $\Gamma(N_m)$ is the probability density of the micelle size distribution, assumed to be a log normal one and expressed as a function of the aggregation number. $b_T(N_m)$ is the sum of the excess scattering lengths of all scatterers of a micelle whose aggregation number is equal to N_m. The monomers are assumed to be the elementary scatterers. Their scattering lengths are simply the sum of the scattering lengths of their constituent atoms and are given in Table 1 together with the corresponding molecular volumes, and scattering length densities. All required excess scattering lengths have been calculated based on these data. The contrast is seen to be optimal

between the corona and the solvent but a non-negligible contrast also appears between the hydrophobic core and the hydrophilic corona.

Table 1 *Scattering lengths b, molecular volumes V, and scattering length densities, b/V, determined for the monomers and the solvent used in this study.*

	Styrene	*tert*-**Butylacrylate**	**Ethanol-d$_6$**
b (cm)	2.325×10^{-12}	1.324×10^{-12}	5.914×10^{-12}
V (Å^3)	165	207	97
$\dfrac{\boldsymbol{b}}{\boldsymbol{V}}$ **(cm^{-2})**	1.409×10^{10}	6.396×10^{9}	6.097×10^{10}
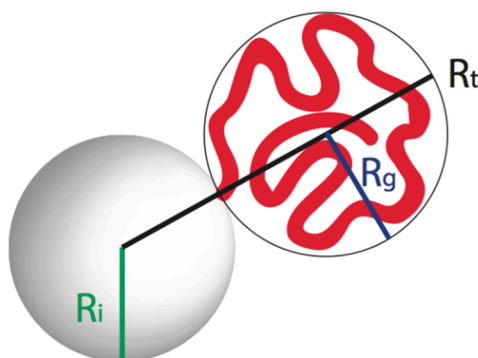
Scheme 2 *Schematic representation of the PS core (gray) with a radius R$_i$, surrounded by a PtBA coronal chain with a Gaussian conformation exhibiting a gyration R$_g$. R$_t$ = R$_i$ + 2R$_g$ is taken as an estimation of the total radius of the micelle.*

When the density of the scattering particles increases, the distance, *r*, between the particles decreases on average and interparticle interferences become significant, leading to a structure factor peak at increasing *q* values (Figure 3). Equation (3) relates the structure factor *S(q)* to the radial distribution function *g(r)*.

$$S(q) = 1 + 4\pi \frac{N}{V} \int_0^\infty [(g(r) - 1] \frac{\sin(qr)}{qr} r^2 \, dr \quad (3)$$

An analytical expression for $S(q)$ is available in the Percus-Yevick approximation applied to a solution containing a volume fraction ϕ of hard spheres with a diameter equal to σ [29]. The micelles are therefore modeled as effective hard spheres and σ represents the shortest possible distance between the centers of two neighboring micelles, that is, the intermicellar distance at which the potential energy becomes in theory infinite, in practice much larger than the thermal energy. The σ parameter also corresponds to the position of the first, most intense peak of $g(r)$, and will be called the "hard sphere interaction distance" in the following. Of course, as the micelles are in fact soft spheres, it is not unexpected that the value of σ might change depending on the packing conditions of the micelles.

The macroscopic scattering cross section corresponding to Equations (1)-(3) depends therefore on the following independent parameters: the average core radius ($\bar{R}_\iota$), the standard deviation of the core radius distribution (ΔR_i), the radius of gyration of the PtBA chains (R_g), the volume fraction of the micelles (ϕ) and the interaction distance between the micelles (σ). As already mentioned, the aggregation number and the core radius are linked by the assumption of a dense core. The cross section has been calculated using a homemade IGOR procedure and the parameters have been tuned using a non-linear least-square fitting procedure to optimize the agreement with the experimental data. It has to be mentioned that the theoretical cross sections have been convoluted by a triangular apparatus function to take the wavelength spread into account (see experimental section).

The experimental and calculated SANS intensities based on the Pedersen-Gerstenberg model are shown in Figure 5-a for the 2% *w/v* micellar solution. The average core radius was determined to be 99 ± 2 Å (note that this confidence interval takes only the precision of the numerical fitting procedure into account), in very good agreement with the AFM analysis (90 ± 10 Å). A radius of gyration of 46.0 ± 1 Å was obtained for P*t*BA coronal chains, leading to a total micellar radius of 191 ± 2 Å. These results are also compatible with the size of the micelles previously determined by DLS, that is, an average hydrodynamic radius R_h of 258 Å. In DLS, size averaging involves an intensity-weighted size distribution while the SANS data correspond to a simple number distribution. By converting the SANS number distribution to an intensity-weighted one [40,41], a value of 205 Å is calculated for the overall average radius.

The experimental and modeled scattering cross sections of the concentrated micellar solutions (concentrations ranging from 8 to 20 % *w/v*) are represented in Figures 5 (b-d). The model fits well the experimental curve in the low q regime, although at high q regime the model slightly peels off of the experimental curve and does not completely overlap. In the *q* range between 0.07 and 0.25 $Å^{-1}$, the experimental cross section scales as $q^{-1.7\pm0.1}$ for all four concentrations. This corresponds to the expected law for chains with excluded volume and results from the large aggregation number of the micelles and from the good solvent conditions of the coronal chains. The adopted Pedersen-Gerstenberg model, however, neglects excluded volume effects; this implies a q^{-2} dependence of the scattering cross section at high *q*. Additional interactions between terpyridine moieties, such as π-π interactions [42], which affect the conformation of the coronal chains, could also contribute to the observed deviations.
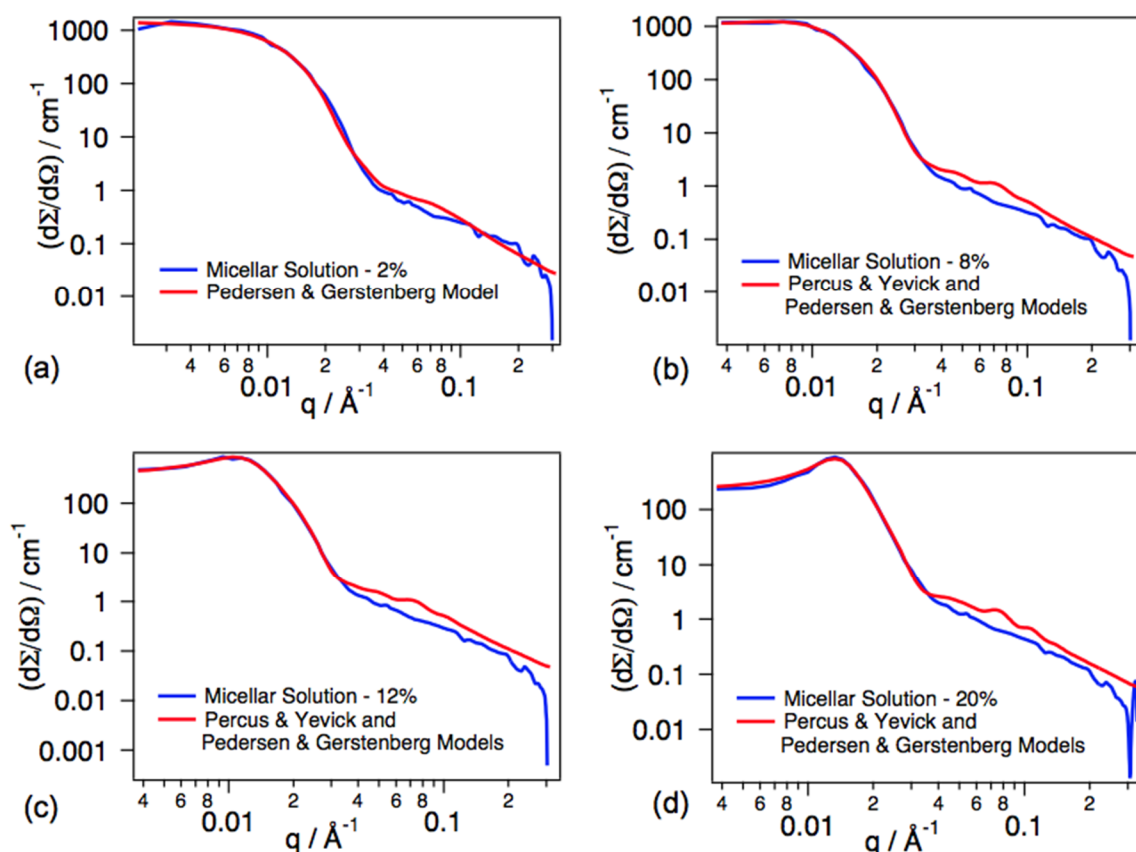
Figure 5 *Experimental and calculated SANS intensities of 2%* w/v *(a), 8%* w/v *(b), 12%* w/v *(c) and 20%* w/v *(d) micellar solution prepared from the PS$_{70}$-b-PtBA$_{180}$-tpy block copolymer in deuterated ethanol.*

The results obtained from the fits of the data are presented in Table 2. They include the core radius, the standard deviation of the core radius (ΔR_i), which gives an indication on the polydispersity of the micelle size, the radius of gyration of the PtBA chains, the total micellar radius (R_t), the hard sphere fraction volume, and the hard sphere interaction distance. Based on the large polydispersity ($\Delta R_i = 15$ Å corresponding to $\Delta N_{agg} = 180$) observed for the dilute solution, we consider that the decrease of the total micellar radius, that is, 20 Å from concentrations of 2 to 20 % *w/v*, is not significant. This is not surprising since the investigated micelles are formed of a glassy PS core which is not prone to reorganization and can therefore be considered as frozen.

Table 2 *Results obtained from the fits of SANS data for the PS$_{70}$-b-PtBA$_{180}$-tpy diblock copolymer micellar solutions at different concentrations in deuterated ethanol and upon addition of different metal ions at 8 and 12 %w/v concentration.*

%[a]	$\overline{R_i}$ / Å [b,c]	ΔR_i / Å [d]	R_g / Å [b,c]	R_t / Å [f]	ϕ [b,g]	σ / Å [b,h]	ϕ_{PG} [i]
2	99	14.7	46.0	191	-	-	0.03
8	92	9.2	45.3	182	0.08	553	0.14
12	91	9.5	42.6	176	0.19	470	0.20
20	87	2.9	42.0	171	0.27	420	0.35
Addition of metal ions at 8% w/v concentration							
Fe(II)	100	15.4	43.7	187	0.20	549	
Ni(II)	100	15.4	43.9	188	0.17	552	
Zn(II)	99	25.4	40.6	180	0.08	576	
Addition of metal ions at 12% w/v concentration							
Fe(II)	95	11.5	43.2	182	0.24	455	
Ni(II)	95	12.8	43.5	182	0.22	435	
Zn(II)	95	22.6	40.0	175	0.12	503	

(a) Concentration w/v
(b) The confidence intervals, resulting from the numerical fitting procedure, are estimated to about 2 Å for the core radius, to 1 Å for the coronal chain radius of gyration, to 0.01 for the hard sphere volume fraction, and to 2 Å for the hard sphere interaction distance.
(c) Average radius of the PS core, deduced from the average aggregation number $\overline{N_m}$
(d) Standard deviation on the PS core radius due to the polydispersity of N_m
(e) Radius of gyration of PtBA coronal chains

(f) Micellar total radius ($2R_g+\bar{R}_i$)

(g) Hard sphere volume fraction
(h) Hard sphere interaction distance
(i) Volume fraction estimated based on the Pedersen-Gerstenberg form factor analysis (Equation 4)

At concentrations larger than, or equal to, 8% *w/v*, a structure factor is visible and information on ϕ and σ can be inferred. As expected, ϕ increases steadily with increasing copolymer concentration reaching 0.27 at 20% *w/v*. The hard sphere interaction distance, σ, decreases when the concentration increases. No overlapping of the coronal chains takes place, however, since σ remains significantly larger than *$2R_t$*, even at 20% *w/v*. As mentioned previously, because the micelles are in fact soft spheres, it is not surprising that σ varies with the micelle concentration. At 20% *w/v*, micelles are thus more closely interacting but the coronal chains of neighboring micelles still do not overlap. The volume fraction can also be estimated independently based on the copolymer concentration ($\frac{m}{V}$) and on the parameters deduced from the Pedersen-Gerstenberg form factor analysis, that is the core radius and the total micellar radius ($R_t = R_i + 2R_g$), according to the following formula:

$$\phi_{PG} = \frac{N_A z_{core} V_{Styrene}}{M_n} \frac{m}{V} \left(\frac{R_t}{R_i}\right)^3 \quad (4)$$

where N_A is Avogadro's number, z_{core} is the degree of polymerization of the PS block, $V_{Styrene}$ is the volume of a styrene elementary scatterer, and M_n is the copolymer molar mass. The values of ϕ_{PG} are provided in the last column of the top part of Table 2. They are seen to correlate semi-quantitatively with the ϕ values deduced from the Percus-Yevick structure factor analysis. However, as the volume fraction depends on the third power of R_t, it is very sensitive to any variation on the total radius. This total radius is, in addition, a somewhat ill-

defined quantity because of the floppy nature of the Gaussian coronal chains, so that the definition of R_t as $R_i + 2R_g$ must be considered as only providing a reference value for comparison purposes.

After having inferred the internal structure of the micelles from diluted to concentrated solutions, we investigated the impact of the metal ions on the formation of a micellar network. To this end, the micellar solutions were exposed to three metal ions (*i.e.* Ni(II), Fe(II) and Zn(II)). These transition metals form complexes with terpyridine ligands exhibiting various binding strengths. As already reported, the addition of 0.5 eq. of Fe(II) and Ni(II), with respect to the terpyridine, to a PS-*b*-PtBA-tpy micellar solution in ethanol induces the formation of a micellar gel already at 8% *w/v* concentration, while only a viscous solution is obtained in presence of Zn(II) [24]. The neutron scattering data of the micellar gels were analyzed as described above using the models of Percus-Yevick for the structure factor and of Pedersen-Gerstenberg for the form factor. The experimental and the fitted neutron scattered intensities of the gels obtained upon addition of metal ions to the PS_{70}-*b*-$PtBA_{180}$-tpy micellar solutions are shown in Figure 6 while the structural parameters inferred from these fits are summarized in Table 2.
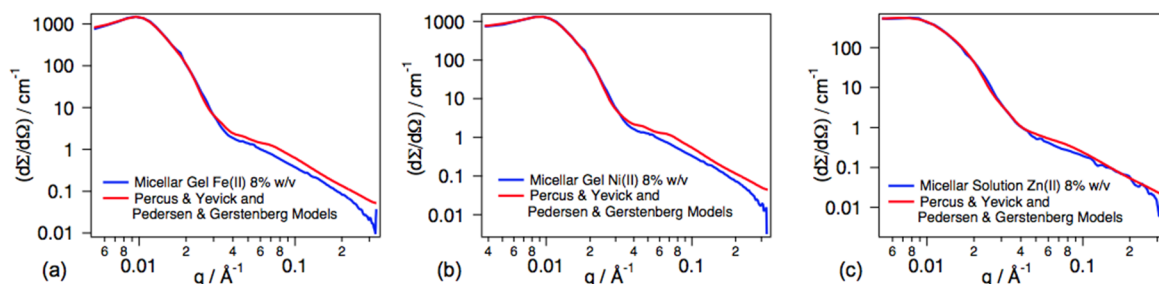
Figure 6 *Experimental and calculated SANS intensities of the micellar solutions, from the PS_{70}-*b*-$PtBA_{180}$-tpy block copolymer at a concentration of 8% w/v in deuterated ethanol, in the presence of Fe(II) (a), Ni(II) (b) and Zn(II) (c) ions.*

The addition of 0.5 eq. of Ni(II) or Fe(II) to the 8% *w/v* micellar solution leads to the formation of a network since these ions form stable complexes with terpyridine ligands. Table 2 shows that an increase of the copolymer volume fraction is observed, corresponding to a contraction of the system which becomes a gel. Volume fractions similar to those obtained for the 12% *w/v* micellar solution without metal ion (Table 2) are reached. Interestingly, the hard sphere interaction distance, σ, is not affected meaning that the network is consistent with micelles interconnected via metal-terpyridine complexes, without, however,

interpenetration of the coronal chains that may lead to coronal chain entanglements (Scheme 3).
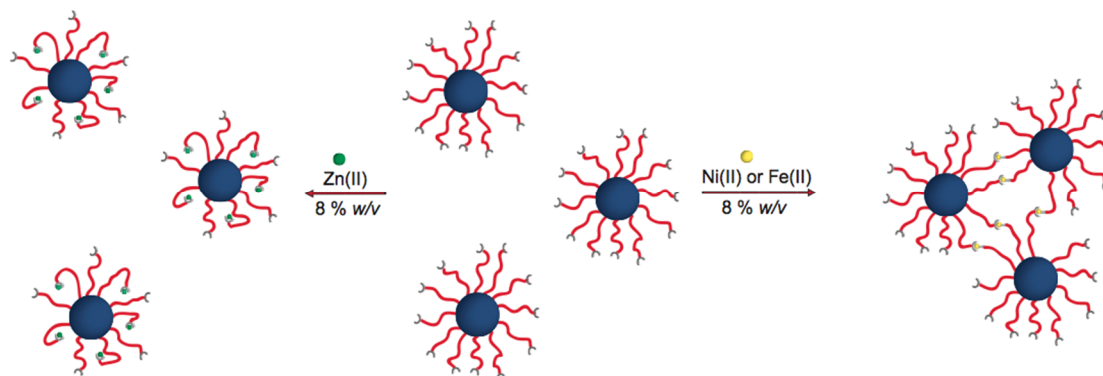
Scheme 3 *Schematic representation of the micellar network prepared by addition of Ni(II) or Fe(II) ions, and of the "flower like" micelles obtained in the case of Zn(II) ions at a concentration of 8%* w/v.

This interconnection process by chelation is responsible for the appearance of a hard gel. Two kinds of bridges between the PtBA chains are in fact expected: intramicellar and intermicellar. Most probably only a small fraction are intermicellar (the aggregation numbers are in the 350±200 range, taking the polydispersity into account) but these bridges are nevertheless responsible for the sol-to-gel transition. It must be noted here that the Percus-Yevick model of course does not take the intermicellar connectivity into account. As the number of connections must be small with respect to the aggregation number, their direct contribution to the cross section is not expected to be significant. Only their indirect contribution, *i.e.* the changes that they induce on the spatial ordering of the micelles, affects significantly the cross section.

Previous rheological measurements revealed that unlike Fe(II) or Ni(II), Zn(II) ions do not induce the formation of a network since Zn(II) ions form preferentially *mono*-complexes with terpyridine ligands [24]. Consistent with this hypothesis, SANS data for the micellar solution dosed with Zn(II) ions revealed a slight contraction of PtBA coronal chains of approximately 5 Å, which represents a decrease of 11% compared to the initial radius of gyration of P*t*BA coronal chains without metal ions. In this case, *mono*-complexes are formed, resulting likely in a partial collapse of the coronal chains bearing those *mono*-complexes due to the reduced solubility of the latter. Our group has previously reported a similar behavior on PS$_{47}$-*b*-PtBA$_{55}$-tpy block copolymer micelles in the dilute regime using DLS as characterization

tool [23] giving additional credit to the results obtained here by SANS. We also note that the hard sphere interaction distance increases by about 4% in the presence of Zn(II). This might result from the long-range electrostatic repulsion between the micelles, which now bear charges within the corona without being linked by intermicellar chelation.

At a micellar concentration of 12% *w/v*, the structure factor peak was observed prior addition of metal ions, meaning that micelles are initially already relatively closely packed. The addition of 0.5 eq. Fe(II) or Ni(II) ions resulted in an increase of the micellar volume fraction, as already described for the 8% *w/v* concentration, but also in a decrease of the interaction distance (Table 2, Figure A1, Appendix III). As already mentioned for the pure micellar solutions, this reflects the fact that the micelles cannot be rigorously described as hard spheres, so that some dependence of the interaction distance on the volume fraction occurs. For Zn(II), a slight decrease of the radius of gyration of the PtBA chains as well as an increase of the hard sphere interaction distance were evidenced, following the tendency already observed for the 8% *w/v* concentration. The global micellar radius remains, however, not affected within experimental uncertainties. As discussed above, this increase of σ might be due to the presence in the corona of charged terpyridine Zn(II) *mono*-complexes.

The most concentrated micellar gels were prepared at a concentration of 16% *w/v* (Figure A2, Appendix III). We should mention that the blank solution of the same concentration was not investigated. In order to be able to compare the micellar gels at 16% *w/v* with the situation without metal ions, a hard sphere interaction distance and a volume fraction obtained by linear interpolation between 12 and 20% *w/v* concentration are mentioned in Table A1, Appendix III. At a higher concentration, micelles are closely interacting as revealed by a higher volume fraction as well as a shorter interaction distance for the micellar solution with no metal ion (Table A1, Appendix III). The addition of 0.5 eq. Fe(II) and Ni(II) ions yields a hard gel in agreement with the inferred shorter intermicellar distances and higher volume fractions. The observed volume fractions remain, however, below the freezing transition ($\phi = 0.494$) for a hard sphere solution [43]. As mentioned above, the observed hard gel results from the reticulation process induced by intermicellar chelation between the terpyridine ligands and the metallic cations. Although Zn(II) ions do not induce the formation of a gel, a higher volume fraction as well as a shorter hard sphere interaction distance are evidenced compared to the previous lower concentrations. At such high concentration, the already dense packing of the

micelles is not expected to be much affected by the intermicellar chelation of the metal ions. The fact that the volume fraction for Fe(II) and Ni(II) ions remains close to 0.23 is thus not surprising. Taking into account a micellar radius in the dilute regime (2 % *w/v*) of 190 Å, the critical distance at which the overlap between coronal chains of neighboring micelles begins to occur is equal to 380 Å ($2R_t$). The addition of Fe(II) and Ni(II) ions therefore makes possible a slight interpenetration of the coronal chains of neighboring micelles, as evidenced by the decrease of σ to reach 365 Å and 357 Å, for Fe(II) and Ni(II) ions respectively. The larger decrease of σ, compared to the situation at 8 and 12 % *w/v*, might be interpreted as resulting from a larger number of intermicellar complexes due to the denser micelle packing. In the case of Zn(II) ions, σ decreases and becomes close to $2R_t$ because the formed *mono*-complexes do not induce a micellar network. At 8 and 12 % *w/v*, an increase of σ was observed upon addition of Zn(II) and was interpreted as resulting from long-range electrostatic repulsion by the charged terpyridine Zn(II) *mono*-complexes present in the corona. At higher concentration (both of the copolymer and of the ions), the larger ionic strength is expected to induce screening effects which, together with the already discussed decrease of the radius of gyration of the coronal chains, might account for the decrease of the interaction distance.

4 Conclusion

This contribution presents a detailed SANS investigation on metallo-supramolecular micellar gels based on PS-*b*-PtBA-tpy copolymers and transition metal ions. The influence of the concentration on the structure and spatial organization of the micelles was first studied without metal ions. At low concentration, the form factor prevails and may be described by the Pedersen-Gerstenberg model, from which the characteristic structural features of isolated micelles were determined. The inferred global sizes of these isolated micelles were found to be in agreement with dynamic light scattering results as well as with an AFM analysis. Upon increasing concentration, a structure factor peak arises from the interferences between the neutron waves scattered by more closely packed micelles. Fitting the experimental scattering cross section data with an analytical formula based on the Percus-Yevick hard sphere model for the structure factor and on the Pedersen-Gerstenberg model for the form factor allowed us

to determine the evolution of the volume fraction of the micelles and of the hard sphere interaction distance, as a function of the copolymer concentration. At a concentration of 20% *w/v*, micelles are closely interacting, but still without interpenetration of the coronal chains, a situation that would result in a hard sphere interaction distance shorter than twice the global micelle radius.

In a second step, the impact of the addition of three metal ions (Fe(II), Ni(II) and Zn(II)) on the micelle structure and the formation of a network was investigated. Ni(II) and Fe(II), which exhibit higher binding strengths, lead to a micellar gel where micelles are interconnected by metal-terpyridine complexes, as revealed by an increase of the micellar volume fraction. A decrease of the hard sphere interaction distance is observed only at concentrations larger than 12 % *w/v*. At the highest investigated concentration (16 % *w/v*), a slight interpenetration of the coronal chains of neighboring micelles is deduced but the volume fraction remains, however, below the value corresponding to the freezing transition for hard spheres. The large G moduli previously observed result therefore from the intermicellar reticulation induced by the terpyridine-metal ion complexation. On the other hand, Zn(II) forms intramicellar *mono*-complexes with terpyridine ligands. As a result, no micellar network is created, but rather a moderate collapse of the coronal chains was revealed by the decrease of the radius of gyration of PtBA coronal chains.

In conclusion, SANS appears to be a powerful tool to investigate such complex systems based on supramolecular micellar gels, by providing insight on the inner structure and on the spatial organization of the micelles, in correlation with previously performed light scattering and rheology experiments.

5 References

1. Hamley, I.W.: Ordering in thin films of block copolymers: Fundamentals to potential applications. Progress in Polymer Science (Oxford) **34**, 1161-1210 (2009). doi:10.1016/j.progpolymsci.2009.06.003
2. Riess, G.: Micellization of block copolymers. Progress in Polymer Science (Oxford) **28**, 1107-1170 (2003). doi:10.1016/S0079-6700(03)00015-7
3. Bates, F.S., Fredrickson, G.H.: Block copolymer thermodynamics: theory and experiment. Annual review of physical chemistry **41**, 525-557 (1990). doi:10.1146/annurev.physchem.41.1.525
4. Ligthart, G.B.W.L., Ohkawa, H., Sijbesma, R.P., Meijer, E.W.: Complementary quadruple hydrogen bonding in supramolecular copolymers. Journal of the American Chemical Society **127**, 810-811 (2005). doi:10.1021/ja043555t
5. Feldman, K.E., Kade, M.J., De Greef, T.F.a., Meijer, E.W., Kramer, E.J., Hawker, C.J.: Polymers with multiple hydrogen-bonded end groups and their blends. Macromolecules **41**, 4694-4700 (2008). doi:10.1021/ma800375r
6. Beck, J.B., Ineman, J.M., Rowan, S.J.: Metal / Ligand-Induced Formation of Metallo-Supramolecular Polymers. 5060-5068 (2005).
7. Fraser, C.L., Smith, A.P., Wu, X.: Metal Template-Assisted Block Copolymer Synthesis: Use of Solvent Polarity to Control Chain Conformation and Reactivity at the Metal Core. Journal of the American Chemical Society **122**, 9026-9027 (2000). doi:10.1021/ja001360p
8. Fustin, C.A., Guillet, P., Schubert, U.S., Gohy, J.F.: Metallo-supramolecular block copolymers. Advanced Materials **19**, 1665-1673 (2007). doi:10.1002/adma.200602170
9. Ruben, M., Ziener, U., Lehn, J.M., Ksenofontov, V., Gütlich, P., Vaughan, G.B.M.: Hierarchical self-assembly of supramolecular spintronic modules into 1D- and 2D-architectures with emergence of magnetic properties. Chemistry - A European Journal **11**, 94-100 (2005). doi:10.1002/chem.200400584
10. Schwarz, G., Bodenthin, Y., Tomkowicz, Z., Haase, W., Geue, T., Kohlbrecher, J., Pietsch, U., Kurth, D.G., Wu, J.-m.U.V., Wu, D.-. Tuning the Structure and the Magnetic Properties of Metallo-supramolecular Polyelectrolyte - Amphiphile. Journal of the American Chemical Society **133**(3), 547-558 (2011).
11. Leung, D.H., Fiedler, D., Bergman, R.G., Raymond, K.N.: Selective C-H bond activation by a supramolecular host-guest assembly. Angewandte Chemie - International Edition **43**, 963-966 (2004). doi:10.1002/anie.200352772
12. Winter, A., Ulbricht, C., Holder, E., Risch, N., Schubert, U.S.: Unusual Terpyridines as Ligands for Novel Light-Emitting Iridium(iii) Complexes: Synthesis and Characterization. In: Australian Journal of Chemistry, vol. 59 pp. 773-782. (2006)
13. Schulze, B., Friebe, C., Hager, M.D., Winter, A., Hoogenboom, R., Görls, H., Schubert, U.S.: 2,2':6',2''-Terpyridine meets 2,6-bis(1H-1,2,3-triazol-4-yl)pyridine: tuning the electro-optical properties of ruthenium(II) complexes. Dalton transactions (Cambridge, England : 2003), 787-794 (2009). doi:10.1039/b813925c
14. Burnworth, M., Tang, L., Kumpfer, J.R., Duncan, A.J., Beyer, F.L., Fiore, G.L., Rowan, S.J., Weder, C.: Optically healable supramolecular polymers. Nature **472**, 334-337 (2011). doi:10.1038/nature09963

15. dos Santos, C.M.G., Harte, A.J., Quinn, S.J., Gunnlaugsson, T.: Recent developments in the field of supramolecular lanthanide luminescent sensors and self-assemblies. Coordination Chemistry Reviews **252**, 2512-2527 (2008). doi:10.1016/j.ccr.2008.07.018

16. Moughton, A.O., Reilly, R.K.O.: Metal-Functionalized Nanocages Using Supramolecular Self-Assembly. Journal of the American Chemical Society **130**, 8714-8725 (2008).

17. Moughton, A.O., Stubenrauch, K., O'Reilly, R.K.: Hollow nanostructures from self-assembled supramolecular metallo-triblock copolymers. Soft Matter **5**, 2361-2370 (2009). doi:10.1039/B818955B

18. Mugemana, C., Guillet, P., Fustin, C.-A., Gohy, J.-F.: Metallo-supramolecular block copolymer micelles: recent achievements. Soft Matter **7**, 3673-3678 (2011). doi:10.1039/C0SM01274B

19. Yam, V.W.-W., Hu, Y., Chan, K.H.-Y., Chung, C.Y.-S.: Reversible pH- and solvent-responsive micelle-mediated self-assembly of platinum(II) terpyridyl-based metallo-supramolecular diblock copolymers. Chemical communications (Cambridge, England), 6216-6218 (2009). doi:10.1039/b911657e

20. Zhou, G., He, J., Harruna, I.I.: Self-assembly of amphiphilic tris(2,2′-bipyridine)ruthenium-cored star-shaped polymers. Journal of Polymer Science Part A: Polymer Chemistry **45**, 4204-4210 (2007). doi:10.1002/pola.22163

21. Fustin, C.A., Lohmeijer, B.G.G., Duwez, A.S., Jonas, A.M., Schubert, U.S., Gohy, J.F.: Nanoporous thin films from self-assembled metallo-supramolecular block copolymers. Advanced Materials **17**, 1162-1165 (2005). doi:10.1002/adma.200402073

22. Mugemana, C., Gohy, J.F., Fustin, C.A.: Functionalized nanoporous thin films from metallo-supramolecular diblock copolymers. Langmuir **28**, 3018-3023 (2012). doi:10.1021/la204920b

23. Guillet, P., Fustin, C.-A., Mugemana, C., Ott, C., Schubert, U.S., Gohy, J.-F.: Tuning block copolymer micelles by metal-ligand interactions. Soft Matter **4**, 2278-2282 (2008). doi:10.1039/B808280D

24. Guillet, P., Mugemana, C., Stadler, F.J., Schubert, U.S., Fustin, C.-A., Bailly, C., Gohy, J.-F.: Connecting micelles by metallo-supramolecular interactions: towards stimuli responsive hierarchical materials. Soft Matter **5**, 3409-3411 (2009). doi:10.1039/B910325B

25. Brassinne, J., Mugemana, C., Guillet, P., Bertrand, O., Auhl, D., Bailly, C., Fustin, C.-A., Gohy, J.-F.: Tuning micellar morphology and rheological behaviour of metallo-supramolecular micellar gels. In: Soft matter., vol. 8. p. 4499. Cambridge :, (2012)

26. Hamley, I.W.: The Physics of Block Copolymers. Oxford University Press, (1998)

27. Higgins, J.S., Benoît, H.: Polymers and neutron scattering. Clarendon Press, (1994)

28. Pedersen, J.S., Gerstenberg, M.C.: Scattering Form Factor of Block Copolymer Micelles. Macromolecules **29**, 1363-1365 (1996).

29. Percus, J.K., Yevick, G.J.: Analysis of Classical Statistical Mechanics by Means of Collective Coordinates. Physical Review **110**, 1-13 (1958).

30. Tang, T., Castelletto, V., Parras, P., Hamley, I.W., King, S.M., Roy, D., Perrier, S., Hoogenboom, R., Schubert, U.S.: Thermo-responsive poly(methyl methacrylate)-block-poly(N- isopropylacrylamide) block copolymers synthesized by RAFT polymerization: Micellization and gelation. Macromolecular Chemistry and Physics **207**, 1718-1726 (2006). doi:10.1002/macp.200600309

31. Wanka, G., Hoffmann, H., Ulbricht, W.: Phase Diagrams and Aggregation Behavior of Poly(oxyethylene)-Poly(oxypropylene)-Poly(oxyethylene) Triblock Copolymers in

Aqueous Solutions. Macromolecules **27**, 4145-4159 (1994). doi:10.1021/ma00093a016

32. Castelletto, V., Hamley, I.W., Yuan, X.F., Kelarakis, a., Booth, C.: Structure and rheology of aqueous micellar solutions and gels formed from an associative poly(oxybutylene)-poly(oxyethylene)-poly(oxybutylene) triblock copolymer. 138-145 (2005). doi:10.1039/b419103j

33. Gamys, C.G., Beyou, E., Bourgeat-Lami, E., David, L., Oberdisse, J.: SAXS and SANS characterization of gelable polystyrene-b-poly(acryloxy propyl triethoxysilane) (PS-b-PAPTES) diblock copolymer micelles before and after hydrolysis-condensation. Soft Matter **8**, 6564-6572 (2012). doi:10.1039/C2SM25412C

34. Willet, N., Gohy, J.-F., Lei, L., Heinrich, M., Auvray, L., Varshney, S., Jérôme, R., Leyh, B.: Fast Multiresponsive Micellar Gels from a Smart ABC Triblock Copolymer. Angewandte Chemie **119**, 8134-8138 (2007). doi:10.1002/ange.200701757

35. Radulescu, A., Ioffe, A.: Neutron guide system for small-angle neutron scattering instruments of the J??lich Centre for Neutron Science at the FRM-II. Nuclear Instruments and Methods in Physics Research, Section A: Accelerators, Spectrometers, Detectors and Associated Equipment **586**, 55-58 (2008). doi:10.1016/j.nima.2007.11.039

36. Guillet, P., Fustin, C.A., Lohmeijer, B.G.G., Schubert, U.S., Gohy, J.F.: Study of the influence of the metal - Ligand complex on the size of aqueous metallo-supramolecular micelles. Macromolecules **39**, 5484-5488 (2006). doi:10.1021/ma060929p

37. Holyer, R.H., Hubbard, C.D., Kettle, S.F.A., Wilkins, R.G.: The Kinetics of Replacement Reactions of Complexes of the Transition Metals with 2,2',2"-Terpyridine. Inorganic Chemistry **5**, 622-625 (1966). doi:10.1021/ic50038a027

38. Kotlarchyk, M., Chen, S.H.: Analysis of small angle neutron scattering spectra from polydisperse interacting colloids. The Journal of Chemical Physics **79**, 2461 (1983). doi:10.1063/1.446055

39. Pedersen, J.S.: Analysis of small-angle scattering data from colloids and polymer solutions: modeling and least-squares fitting. Advances in Colloid and Interface Science **70**, 171-210 (1997). doi:10.1016/S0001-8686(97)00312-6

40. Hallett, A.F., Craig, T., Marsh, J., Nickel, B.: Number Distributions by Dynamic Light Scattering. Can. J. Spectr. **34**, 63-70 (1989).

41. Maulucci, G., De Spirito, M., Arcovito, G., Boffi, F., Castellano, A.C., Briganti, G.: Particle size distribution in DMPC vesicles solutions undergoing different sonication times. Biophys. J. **88**, 3545-3550 (2005).

42. Long, X.-J., Dai, J.-W., Wu, J.-Z.: Synthesis and supramolecular networks of mono- and dinuclear manganese chloride complexes with 2-(2,2′ : 6′,2″-terpyridin-4′-yl)phenol. Journal of Coordination Chemistry **65**, 316-324 (2012). doi:10.1080/00958972.2011.652623

43. Rintoul, M.D., Torquato, S.: Metastability and Crystallization in Hard-Sphere Systems. Physical Review Letters **77**, 4198-4201 (1996). doi:10.1103/PhysRevLett.77.4198

CHAPTER VI

Investigation of the interaction between a β-cyclodextrin and DMPC liposomes: a small angle neutron scattering study

Abstract

In this chapter, the Small Angle Neutron Scattering technique (SANS) has been applied to investigate the interaction between a cyclodextrin (CD) and liposomes. From the modelling of the experimental neutron scattering cross sections, the detailed structure of dimyristoylphosphatidylcholine (DMPC) liposomes is assessed upon addition of increasing amounts of randomly methylated β-CD (RAMEB). This study has been performed at two temperatures bracketing the phase transition of the DMPC bilayers. The fraction of DMPC molecules incorporated into the vesicles is inferred. The dose-dependent phospholipidic extraction by RAMEB is quantified as well as the concomitant evolution of the liposome radius and of the thickness of the hydrophobic and hydrophilic parts of the membrane. The possible formation of CD-DMPC inclusion complexes is also assessed. The data suggest the dose-dependent coverage by RAMEB of the outer liposome interface. Our analysis highlights the important role of temperature on the mechanism of action of RAMEB. These results are discussed in the framework of the Area-Difference-Elasticity model.

1 Introduction

Cyclodextrins (CD) were first described by Villiers in 1891[1,2]. However, Schardinger and Cramer, at the beginning of the 20th century, really laid the foundations of cyclodextrin chemistry [3,4]. They discovered three types of natural cyclodextrins (CD), α-, β- and γ-CD, which consist respectively of six, seven and eight glucopyranose units linked head-to-tail to build a ring and which adopt each the shape of a truncated cone. CD present an hydrophilic surface and a lipophilic central cavity leading to inclusion and non-inclusion complexes for a variety of host molecules [5,6]. Intensively investigated due to their cavitant properties, CD are nowadays widely used in the food, cosmetic, textile or pharmaceutical industry [7-14].

β-CD are prone to include cholesterol because their cavity size is sufficiently large [15]. As a consequence, they are relevant tools to investigate the plasma cell membrane and particularly the lipid raft function [16-18]. Several studies showed that cholesterol-containing membranes are more sensitive to methylated CD than to natural CD [16,19,20]. Among the former, the randomly methylated β-CD (RAMEB) passed all toxicological tests [16,19-23].

Despite several studies [24], the mechanism of action of RAMEB on cell membranes remains poorly understood. Most measurements focused only on the cholesterol extraction and did not address the possible competitive phospholipid removal which might also be of major importance. β-CD are widely used indeed in the presence of phospholipids and some recent investigations have pointed out that lipid desorption induced by CD can lead to the formation of aggregates with solubilizing properties[25,26]. The understanding of CD action on phospholipid membranes is thus of the highest importance. In this paper, we investigate the interaction between a methylated β-CD and a model membrane using the Small-Angle Neutron Scattering technique (SANS), which is a powerful method to investigate model membranes [27-36]. This technique will first be applied to analyze the interaction between RAMEB and liposomes containing only phospholipids. In a second paper, the interaction between cyclodextrins (RAMEB) and cholesterol-doped liposomes will be addressed.

In a previous work, our group focused on the evaluation of the RAMEB action directly on cell membranes using electron spin resonance [37]. A more common way to evaluate the damage

caused by a CD on biomembranes is to use a lipid assay kit [16]. As the CD action on natural membranes is extremely complex, the use of models consisting of lipid bilayers is a relevant approach to reach a better understanding of the involved processes. Liposomes represent such an appropriate model. In addition to mimicking the membrane, liposomes can also be used as drug enhancers [38-43]. Another field also uses cyclodextrins as drug release modulators within liposomes [44-46].

Various techniques have been applied in order to understand the influence of CD on the stability as well as on the integrity of vesicle bilayers. Electron spin resonance highlighted the microviscosity changes induced by CD on liposome membranes [37]. The release of a fluorescent probe initially encapsulated in the liposomes has been used to evaluate the liposome integrity in contact with different amounts of CD [47]. Turbidity measurements have been performed to quantify the lipid leakage induced by CD on the liposome bilayer [19]. The structural changes were also assessed using differential scanning calorimetry [48], freeze-fracture electron microscopy [47], binding isotherms [49] or photon-correlation spectroscopy [19,23,49,50]. Despite all these studies, rare are those involving specifically the interaction between β-CD and phospholipids [19,49,51]. And, to the best of our knowledge, only information on the global liposome size and dispersity could be inferred from the previously mentioned techniques which do not give access to the internal structure of the bilayer.

The SANS technique is a powerful way to infer, from the modelling of the experimental neutron scattering cross sections, the detailed liposome structure which we define by the following parameters: average radius, thickness of both the hydrophobic and hydrophilic parts of the liposome bilayer, and liposome size polydispersity. In the present work, the evolution of these parameters has been monitored as a function of RAMEB concentration. The possible coverage by the RAMEB molecules at the liposome-water interface was also considered.

Because of the existence of a phase transition associated with a change in the conformational order of the phospholipid acyl chains influencing the membrane fluidity [52], the influence of RAMEB on the liposome structure was considered at two temperatures (above and below the bilayer phase transition). In this study, we selected liposomes resulting from the self-assembling

of dimyristoylphosphatidylcholine (DMPC) which have a phase transition temperature close to 23°C. Dynamic light scattering (DLS) and surface tension measurements were performed in parallel to the SANS investigation.

2 Materials and methods

2.1 Liposome preparation

Dimyristoylphosphatidylcholine (DMPC) and octadecylamine (also called stearylamine , SA) were purchased from Sigma (Aldrich, Belgium) and were used without further purification. Phospholipid vesicles were prepared by hydration of lipid films as described by Hope et al. [53]. DMPC was first dissolved in chloroform to a concentration of 7.4 mM. The liposomes contained a molar fraction of 90% of DMPC (4.5 mg/mL) and were doped with 10% of SA (0.2 mg/mL): SA was added to the vesicles in order to prevent their spontaneous fusion, which is known to appear above the DMPC bilayer phase transition temperature [54]. The chloroform/phospholipid mixture was then stirred for 5 min and the solvent was evaporated under vacuum. The resulting lipid film was suspended in deuterium oxide (Sigma Aldrich, Belgium), and stirred by a vortex mixer in order to obtain large multilamellar vesicles (MLV) [55]. After hydration, five freeze-thaw cycles using liquid nitrogen were carried out to allow a better incorporation of the SA into the liposome phospholipidic bilayers. The MLV suspension was then transferred into an extruder (Lipex Biomembrane, Canada) with two (stacked) polycarbonate filters (0.1 μm pore size, Nucleopore, CA), under a pressure gradient up to 6800Pa of nitrogen (Air Liquide, Belgium). The procedure was repeated ten times at 35°C and resulted in unilamellar liposomes, as demonstrated by Olson et al. [56]. Once prepared, the liposomes were incubated with RAMEB (degree of substitution equal to 12.6; purchased fromWacker Chemie GmbH, Germany) at selected concentrations. The RAMEB solution had been first filtered on a microfilter with a pore size of 0.2 μm.

2.2   Surface Tension Measurements

Aqueous RAMEB solutions were prepared at various concentrations in the 10^{-5} to 10^{-1} M range. Surface tension measurements were collected in multi-well plates supplied with a MicroTrough S (Kibron, Germany) apparatus. Each plate contained 15 wells with a volume of 500 µl each and the data collection was performed with the Film Ware software (version 3.4). Each measurement was repeated 15 times at room temperature.

2.3   Dynamic Light Scattering (DLS)

DLS measurements were carried out with a particle size analyzer (Delsa Nano C, Particle Analyzer, Beckman Coulter) at a fixed scattering angle of 165°. The light source is a diode laser operating at λ=658 nm and 30 mW power. Measurements on the DMPC-liposome solutions in contact with different amounts of RAMEB were performed at two different temperatures (14 and 34°C) in duplicate. Each measure lasted about 20 minutes. Initially the liposome and RAMEB solutions were both filtered on a microfilter with a pore size of 0.2 µm. Data were handled using the CONTIN algorithm using the Delsa Nano software. At least four individual histograms were averaged leading to smooth distributions.

2.4   Small-Angle Neutron Scattering (SANS)

The SANS cross-sections of unilamellar DMPC vesicles in D_2O in contact with different concentrations of RAMEB were collected at the Jülich Centre for Neutron Science (JCNS) at two temperatures: 14°C and 34°C. The KWS1 and KWS2 small-angle instruments were used to collect data at three sample-detector distances: 2, 8 and 20m. The neutron wavelength, λ, was equal to 6.00 Å ± 0.60 Å after mechanical velocity selection. These conditions correspond to a momentum transfer range, q, from 2.36 10^{-3} Å^{-1} to 1.96 10^{-1} Å^{-1} where $q = \frac{4\pi}{\lambda} \sin(\theta)$ and 2θ is the scattering angle.

The scattered neutrons were detected on a two-dimensional ^6Li scintillation counter. Radial averaging led to a one-dimensional scattering function $I(q)$. The incoherent background was removed using a blank sample. Corrections for the background and sample holder contributions were carried out according to standard data handling procedures (see, e.g. [57]. The data

corresponding to the liposome solutions and to the pure solvent (D_2O) were handled in an identical way, and the scattering intensities were converted to macroscopic scattering cross-sections per unit volume, $d\Sigma/d\Omega$ (cm^{-1}), using calibration with a Poly(methyl methacrylate) sample. The liposome contribution was obtained by subtracting the cross section of the solvent, weighted by its volume fraction.

2.5 SANS Data handling

The liposomes are assumed to be spherical, consisting of concentric shells of mean radius R. The inner hydrophilic shell, the hydrophobic shell and the outer hydrophilic shell thicknesses are respectively denoted as d_{in}, D, and d_{out}. (Fig. 1a) The macroscopic scattering cross-section for the liposomes is given by the following formula

$$\frac{d\Sigma}{d\Omega} = \frac{[DMPC]\, N_A 10^{-3}}{\langle N \rangle} \int_0^\infty |A(q)|^2 P_n(R)\, dR \quad (1)$$

with $\langle N \rangle = \int_0^\infty N(R) P_n(R)\, dR$

where [*DMPC*] is the total DMPC concentration in *mol/L*, $N(R)$ is the aggregation number of liposomes with radius R and $P_n(R)$ represents the liposome size distribution. Because the liposome solution was sufficiently diluted, the interferences between waves scattered by different liposomes may be ignored [58]. The scattering amplitude $A(q)$ is given by

$$A(q) = 4\pi \int_{liposome} \tilde{\rho}\ (r) \frac{\sin(qr)}{qr}\, r^2\, dr \quad (2)$$

where the excess scattering length density $\tilde{\rho}$ is a function of the distance r from the center of the liposome and is equal to

$$\tilde{\rho}(r) = \tilde{\rho}_{SA}\varphi_{SA}(r) + \tilde{\rho}_{DMPC}\varphi_{DMPC}(r) \quad (3)$$

Chapter VI – Investigation of the interaction between a β-cyclodextrin and DMPC liposomes

We define as elementary scatterers the respective hydrophobic tails and hydrophilic heads of SA and DMPC. Depending on the zone of the liposome considered, $\tilde{\rho}_{SA}$ and $\tilde{\rho}_{DMPC}$ correspond to the excess scattering length density of the head or tail of the molecules. φ_{SA} and φ_{DMPC} are their respective volume fractions. A linear water penetration profile is assumed in the polar parts of the DMPC/SA bilayer (Fig. 1b). When cyclodextrin was added, its possible presence at the liposome/water interface has been included in the model in the following way. An additional layer with a thickness equal to 7.8Å [59], that is the height of a β−CD molecule, is considered. The scattering length density for this layer is calculated assuming a variable volume fraction of cyclodextrin within this layer which is otherwise filled by the water solvent. This volume fraction is then an additional fitting parameter.
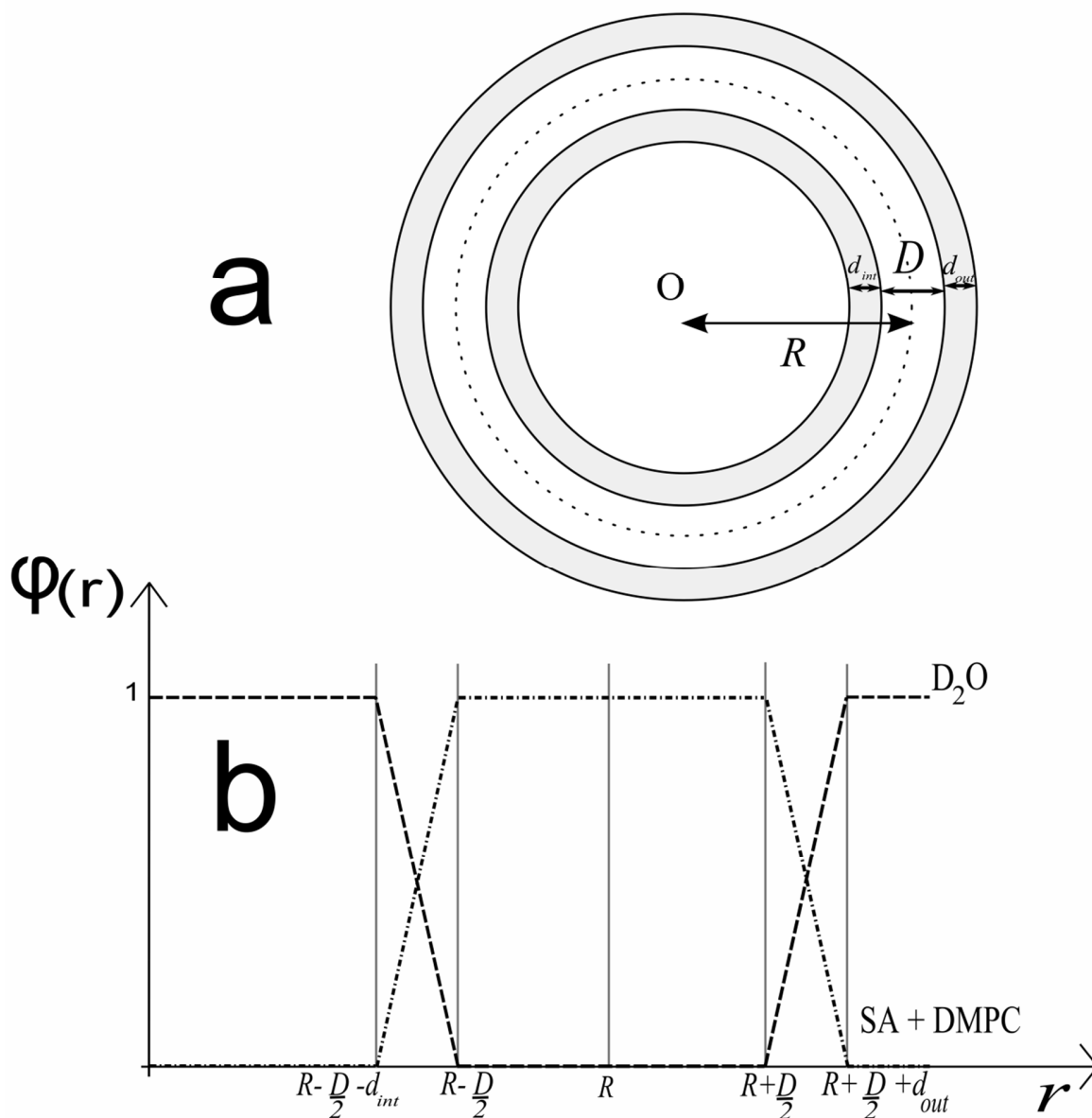
Fig. 1*(a) Structure of a modelled liposome (see text for details); (b) Volume fraction of the DMPC/SA constituents of the liposome as a function of the distance from the center of the liposome (dash-dotted line). The volume fraction of water is shown as a dashed line. The CD fraction is not shown.*

Chapter VI – Investigation of the interaction between a β-cyclodextrin and DMPC liposomes

The following size distribution, inspired from the analysis of the vesicle size obtained by Hope et al. (1985) [53], has been used

$$P_n(z) = C \exp(-e^{-z} - z + 1) \quad (3)$$

$$z = \frac{R - R_c}{\sigma} \quad (4)$$

where C is a normalization coefficient. The average radius is then given by $\langle R \rangle = R_c + 0.577\sigma$ and the standard deviation, δ, is proportional to σ: $\delta = 1.283\sigma$.

As will be discussed later, the addition of RAMEB leads to the partial disruption of the liposomes and to the possible formation of inclusion complexes between RAMEB molecules and extracted DMPC chains. The contribution of these complexes to the scattering cross section has to be also considered. Based on the work of Anderson et al. [60] who detected 4:1 RAMEB - 1-palmitoyl-2-oleoyl-sn-glycero-3-phosphocholine (POPC) CD-POPC complexes, we assumed that 4:1 RAMEB-DMPC might be present and we modelled them as homogeneous spheres with a volume equal to four times the volume of a RAMEB molecule and with a scattering length density estimated from the atomic composition of the RAMEB and DMPC molecules. As the contribution of these complexes is not expected to be large, it does not seem relevant to implement a most sophisticated model. This contribution is then simply weighted by an additional fitting parameter and added to the liposome cross section.

The model depends therefore on five independent parameters, that is: (i) the average radius of the liposome ($\langle R \rangle$), (ii) the standard deviation of the radius, (iii) the thickness of the hydrophobic part (D), (iv) the volume fraction of RAMEB covering the surface of the vesicles (φ), and (v) the weighting factor of the contribution of the RAMEB-DMPC inclusion complexes. The other parameters are not independent. The knowledge of R and D leads to the volume of the hydrophobic shell, from which the aggregation number (number of individual amphiphilic molecules that are self-assembled in the vesicle) can be calculated based on the individual molecular volumes of the hydrophobic scatterers. The knowledge of the aggregation number, of

the scatterer volumes, and of the volume fractions (see Fig. 1b) makes the calculation of d_{out} and d_{in}, possible.

Equation (1) involves the DMPC total concentration. However, due to the extrusion steps, the final total DMPC concentration is not precisely known. Part of the material must be retained by the polycarbonate filter during the repeated extrusion steps (see Material and methods). The actual final concentration of DMPC chains incorporated into the liposomes is related to the initial one (7.4 mM) via a correcting multiplying factor, denoted as m ($m \leq 1$). This factor, which results from the data fits, may also account for the possibility of (i) unassociated free DMPC chains which are too small to be seen in SANS and (ii) other types of self-assembled objects, like clusters of liposomes, whose size would be too large for them to be detected in our limited q range.

The total scattering cross section is then convoluted with an apparatus function in order to take into account the experimental resolution (see experimental part). A triangular shape has been assumed for the scattering vector spread ($\Delta q/q = 10\%$). The resulting model cross sections are then fitted to the experimental scattering curves and the quality of the fit has been monitored by calculating the χ^2 both in linear and in logarithmic mode.

2.6 Comparison of SANS and DLS size distributions

The analysis of the SANS data provides us with a number-weighted radius distribution, denoted P_n. The CONTIN algorithm used for the DLS data analysis leads to an intensity-weighted distribution, P_i, of the hydrodynamic radius. These two distributions are not equivalent but may be connected through the following equation [61,62]:

$$P_n = \frac{P_i}{[M(R)]^2 F(q;R)} \qquad (5)$$

where $M(R)$ is the molecular weight of a vesicle of radius R. $M(R)$ is proportional to the square of the vesicle radius:

$$M(R) = 4\pi R^2 \widetilde{D}\bar{\rho} \qquad (6)$$

where $\widetilde{D}$ represents the global thickness and $\bar{\rho}$ the average density of the bilayer. $F(q;R)$ is the form factor of the vesicle at the q value corresponding to the wavelength and detection angle of the DLS instrument. Because all the information required to calculate $F(q;R)$ is available from the analysis of our SANS data, we found more consistent and practical to convert the P_n SANS distributions to P_i distributions which are comparable to the DLS distributions. This makes an easy and relevant comparison between DLS and SANS data possible, as will be discussed in Section 3. It must be emphasized that the liposome radii obtained by averaging over P_i are as a rule larger than those obtained from P_n because of the R^2 weighting factor appearing in equation (6). This has to be kept in mind when comparing different figures of the discussion section.

3 Results and discussion

Typical SANS cross-sections of DMPC vesicles without and with added RAMEB (at a concentration of 20 mM) as well as fits using the model described in Section 2.5 are displayed in Fig. 2. A good agreement is observed between the experimental and fitted data.
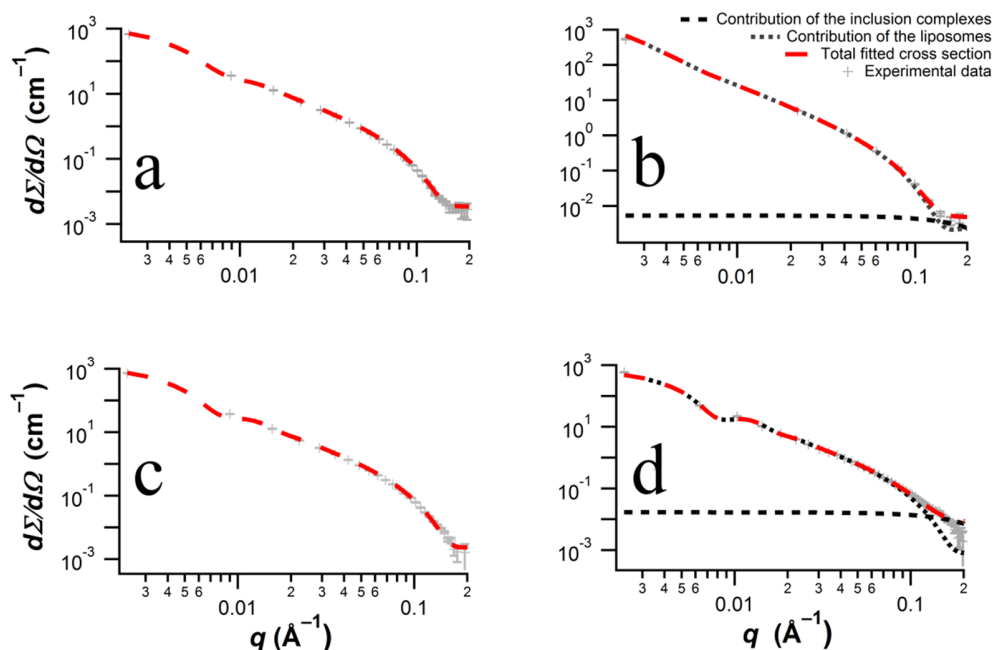
Fig. 2 *Experimental macroscopic cross-sections of the liposomes (+ gray symbols) and their fits to the analytical model described in section 2.5 (red dotted line). The individual contribution of RAMEB-DMPC inclusion complexes is displayed as a black dotted line. (a) Pure liposomes at 14°C; (b) Liposomes at 14°C in contact with RAMEB at a concentration of 20 mM; (c) Pure liposomes at 34°C; (d) Liposomes in contact with RAMEB at a concentration of 20 mM at 34°C.*

3.1 Fraction of DMPC molecules included in the unilamellar liposomes

The m parameter defined in Section 2.5 represents the fraction of the DMPC molecules which are actually included in liposomes. Three phenomena may be responsible for m values lower than unity: (i) the loss of DMPC material during the extrusion procedure, (ii) the presence of unassociated DMPC chains, and (iii) aggregation processes leading to structures which are too large to be detected in our q range. As RAMEB was added at the last step of the sample preparation procedure, the contribution of process (i) is the same for all samples. Relevant information may therefore be inferred about the possible additional influence of RAMEB on processes (ii) and (iii) globally, from the evolution of the m/m_0 parameter upon increasing

RAMEB concentration at 14°C and 34°C (Fig. 3). m_0 is the value of m in the absence of RAMEB.
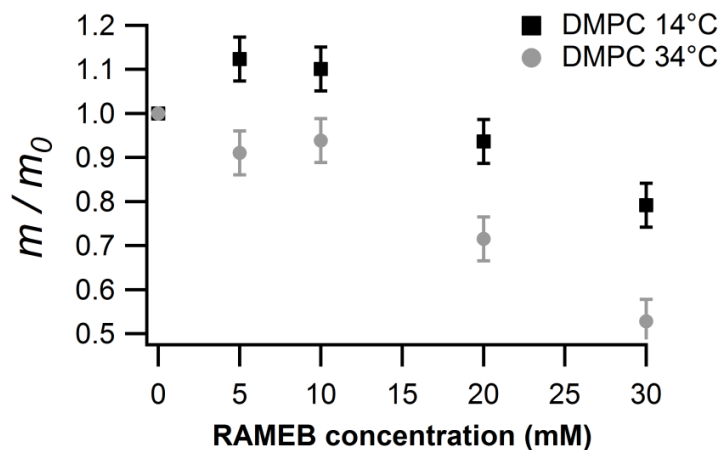
Fig. 3 *Influence of RAMEB on the fraction of DMPC molecules included in the liposomes (m/m$_0$ parameter) at 14°C (black squares) and 34°C (grey dots)*

Up to 10 mM of RAMEB, no significant variation of m/m_0 is detected within experimental limits. The slight increase from 1.0 to 1.12±0.05 in the [RAMEB] = 0 – 10 mM range at 14°C lies at the limit of experimental significance. It may be either assigned to experimental uncertainties or to a possible de-clustering of initially undetectable aggregated liposomes, leading to an increase of the cross section in the sampled q range. The most significant effect is, however, a regular linear decrease which takes place above 10 mM of CD for both temperatures. 21 ± 5 % of the initial liposomes are no longer detected at [RAMEB] = 30 mM at 14°C. At 34°C, this amount becomes even larger, 47 ± 5%. This effect is assigned to the solubilization of part of the liposomes resulting from the extraction of DMPC phospholipid chains by the β-CD, in agreement with the conclusions drawn by Hatzi and coworkers [19]. This extraction is made in a dose-dependent way and may lead either to aggregates composed of RAMEB and phospholipids that become larger with increasing RAMEB concentration [21,37] or to solubilized chains encapsulated by cyclodextrins [60] which provide a small contribution to the scattering cross section. As explained in section 2.5, we modelled this contribution by assuming, following Anderson et al [60] a 4:1 stoichiometry for the RAMEB-DMPC complexes and by describing

them as homogeneous spheres [63]. This contribution is displayed as black dotted lines in Fig. 2. It must be emphasized at this point that isolated DMPC or RAMEB molecules cannot be detected: they would lead to a scattering cross section in the 10^{-4} cm^{-1} range at $q = 0$, which corresponds to the noise level. Based on the cross section at $q = 0$ for this contribution and on the relevant scattering length values, the concentration of the inclusion complexes and therefore, the fraction of DMPC molecules included into these complexes can be inferred. The accuracy of these data is, however, limited, due to the small associated cross section. At [RAMEB] = 30 mM, the inclusion complex concentration is estimated to be 2.3±1.7 mM and 3.8±1.3mM at 14°C and 34°C, respectively. Compared to the total concentration of 7.4 mM, this corresponds to 31% and 51%. These values compare favorably with the above-cited values of 21% and 47% inferred above from the m/m_0 parameter, taking into account (i) the low accuracy of the determined inclusion complex cross section, and (ii) the fact that part of the DMPC molecules are lost during the extrusion process. Despite these caveats, these data suggest that DMPC extraction by RAMEB leading to inclusion complexes is probably one important mechanism operating under our experimental conditions.

Surface tension measurements were also performed, showing that RAMEB is able to weakly cluster above 15 ± 2 mM in agreement with Messner et al. [26]. These observations and the fact that no significant liposome solubilization is observed below 10 mM of RAMEB suggest that CD-clusters might also play a role in the liposome destruction.

The more efficient solubilization observed above the transition temperature is linked to the larger mobility of the DMPC chains in the fluid phase.

3.2 Liposome Radius, aggregation Number, and polydispersity

The evolution of the average radius of the surviving liposomes inferred from SANS upon addition of increasing amounts of RAMEB is shown in Fig. 4a. Without RAMEB addition, the average radius and aggregation number are identical below and above the transition temperature. This situation results directly from the extrusion procedure which governs the size distribution. These results are also in agreement with Kiselev et al. [64]. As soon as RAMEB is added, temperature is seen to influence the liposome size evolution: below the DMPC transition temperature, the average liposome radius increases upon addition of CD whereas it remains nearly constant at 34°C.
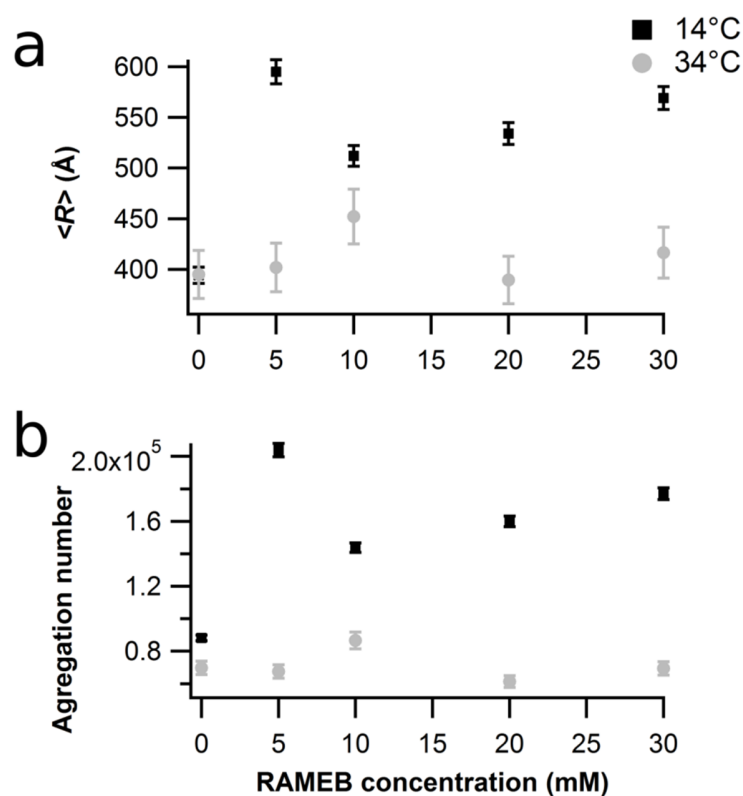
Fig. 4 *Average liposome radius (a) and aggregation number (b) at different RAMEB concentrations at 14°C (black squares) and 34°C (grey dots). Note that the displayed radii are obtained by averaging over a number-weighted size distribution.*

The evolution of the average size of the surviving liposomes is logically linked to that of the average aggregation number as shown in Fig. 4b.

Fig. 5a displays the influence of RAMEB on the liposome polydispersity. An increase is highlighted at 14°C but at 34°C the polydispersity is not significantly affected. This evolution is directly visible on the SANS cross sections displayed in Fig. 2.

This behavior as a function of the RAMEB concentration and of temperature is confirmed by DLS measurements (Fig. 5b and 5c). We recall here that the SANS size distributions have been converted into intensity-weighted distributions to make them comparable with the distributions inferred from DLS. As alluded to in Section 2.6, this is the reason why the maxima of the distributions in Figs. 5b and 5c correspond to larger radii than the average values of Fig. 4a, e.g. 395 Å (Fig. 4a) compared to 490 Å (Fig. 5b).
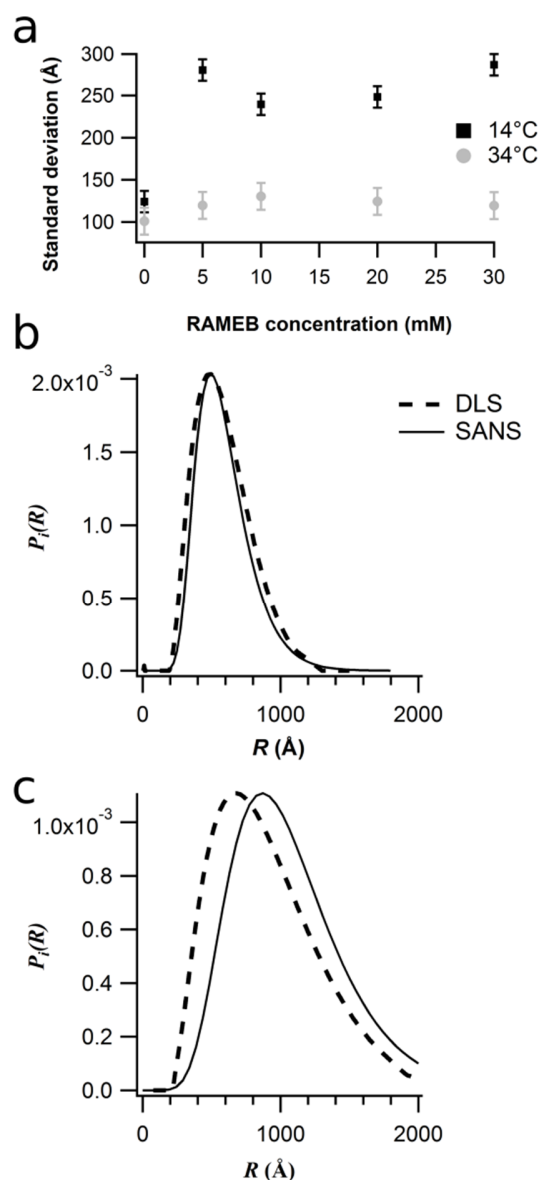
Fig. 5 *(a) Standard deviation of the radius of the DMPC liposomes at 14°C (black squares) and 34°C (grey dots), as inferred from SANS, as a function of RAMEB concentration. (b) Liposome radius distribution at 14°C determined by DLS (dotted line) and SANS (solid line) for pure liposomes and (c) for liposomes in contact with RAMEB at a concentration of 20 mM. The SANS size distributions have been converted into intensity-weighted distributions, $P_i(R)$, to make them comparable with the distributions inferred from DLS*

3.2.1 Below the DMPC transition temperature

Because it is well accepted that CD are not able to penetrate into phospholipid membranes [6,13,65], the increase in liposome size at 14°C could not be explained by a CD inclusion into the bilayer. We suggest that DMPC extraction by RAMEB leads to preferential destruction of the small vesicles so that the size distribution of the surviving liposomes is shifted towards larger R values. As will be discussed below (Section 3.2.3), small liposomes have a larger curvature and a higher elastic energy, so that phospholipid extraction by CD favors their solubilization compared to larger ones.

However, because an increase of the polydispersity is also observed, this mechanism cannot be the only one which operates. It might be suggested that the DMPC molecules from small disrupted liposomes partly become included into the RAMEB-DMPC inclusion complexes discussed above and partly contribute to the formation of larger, more stable liposomes which would be responsible for the increased polydispersity. It has been proposed by Puskas and Csempesz that cyclodextrins may induce aggregation/or fusion of the vesicles [66]. This hypothesis is also compatible with the shift in the size distribution towards larger R values as observed on Fig. 4a.

The comparison of Figs. 3 and 4a shows that the conclusions drawn from both the m/m_0 and R parameters are compatible. A RAMEB concentration of 7.5 ± 2.5 mM must be reached in order that a significant effect is observed.

3.2.2 Above the DMPC transition temperature

Figs. 3 and 4 lead us to the conclusion that, at 34°C, (i) the fraction of DMPC molecules within unilamellar liposomes decreases upon RAMEB addition but that (ii) the average vesicle size is not significantly affected by the interactions with the CD.

These observations lead us to the hypothesis that phospholipid extraction above the DMPC bilayer transition temperature disrupts the liposomes to about the same extent whatever their size, contrarily to the situation prevailing below the transition temperature. As a consequence, the size distribution remains more or less unaffected and the average radius change is negligible.

159

3.2.3 Comparison between the behaviors below and above the transition temperature

A double question arises. Why do small liposomes become more easily disrupted than bigger ones below the gel-fluid transition temperature? Why does this differentiated behavior vanish above the transition temperature?

Bending a bilayer has an energy cost. In the frame of the Area-Difference-Elasticity (ADE) model [67], the total elastic energy, E_B, of a bilayer of fixed mean area A is written as

$$E_B = \frac{1}{2}\kappa \int_A dA'(C_1 + C_2)^2 + \frac{\alpha\pi\kappa}{2D^2A}(\Delta A - \Delta A_0)^2 \qquad (7)$$

where κ is the bending modulus, C_1 and C_2 are the local curvatures along the two principal directions, D is the bilayer thickness, α is a constant which depends on the phospholipid and which is close to unity. ΔA_0 is the area difference between the outer and inner unstressed monolayers, due to the different numbers of phospholipid molecules they may contain, whereas ΔA is the actual area difference within the liposome. The first term of equation (7) is the Helfrich bending energy [68], at fixed bilayer area, whereas the second contribution takes into account the fact that bending a bilayer involves stretching the outer monolayer and compressing the inner one.

Equation (7) is strictly valid a 0 K. At finite temperatures, it becomes necessary to consider the membrane fluctuations through the renormalized bending energy [69,70]. The size distribution of a system of vesicles has been shown to depend exponentially on the renormalized bending energy, $E_B(R)$ divided by the thermal energy k_BT [69]. This renormalized bending energy takes into account the fact that membrane undulations at finite temperature lower the free energy uptake associated with the membrane bending required to build a vesicle. Vesicles of radius R close to the undulation wavelength will be formed preferentially. The effective, renormalized bending modulus decreases with the characteristic length scale of the vesicle, so that for

$$R \approx \tilde{D} \; exp\left(\frac{4\pi}{3}\frac{\kappa}{k_BT}\right) \qquad (8)$$

where κ is the not renormalized bending modulus, the renormalized bending modulus is close to zero [70]. κ has been observed to decrease by about two orders of magnitude at the transition temperature [70].

Equations (7) and (8) provide two possible, and not mutually exclusive, explanations for the observed temperature-dependent behavior. First, our liposome preparation procedure leads to unilamellar spherical liposomes with an average radius of 400 Å and a moderately narrow size distribution (Fig. 5). Despite their bending, they are kinetically stabilized, in particular through the insertion of stearylammonium chains. Below the transition temperature, due to the large κ value, the bending energy is expected to vary significantly through the sampled R range, so that the smaller vesicles are much less stable and more prone to disruption following RAMEB-induced phospholipid extraction. Bilayer reorganization and formation of larger vesicles are expected to take place as inferred from the increase of the liposome polydispersity. Above the transition temperature, the Helfrich energy is much smaller due to the above-mentioned decrease of the bending modulus, so that the stability differences for different radii are significantly attenuated. The extraction of DMPC chains by RAMEB is probably favored by the higher mobility of the phospholipid chains (as we already pointed out when analyzing the m/m_0 parameter) but all vesicle sizes tend to be affected in a similar way.

A second contribution may arise from the second term of equation (7). Extraction of DMPC molecules by RAMEB involves necessarily the outer monolayer so that ΔA_0 decreases leading to an increase of $\frac{\kappa}{A} (\Delta A - \Delta A_0)^2$. This effect will be particularly important for small liposomes (small mean area A) and in the gel phase (large κ). This is also compatible with the observed behavior.

3.2.4 *Coverage of the liposome external layer by RAMEB*

Another parameter derived from the data modelling is the volume fraction of RAMEB covering the liposome surface. Fig. 6 highlights the dose dependent covering of liposomes by RAMEB. The coverage levels off at a volume fraction of about 0.5 and the largest increase takes

place between [RAMEB] = 0 and 10 mM. This can be correlated to the threshold observed in Fig. 3 for efficient DMPC extraction. When 30 mM of RAMEB is reached, half of the vesicle surface is covered. An adsorption of native-CD on membranes has been previously reported [71] and explained by an hydrogen bond formation between the phospholipidic polar head group and one hydroxyl group of the CD. RAMEB, however, possesses less –OH groups, which are replaced by methyl groups, so that the interaction with DMPC is expected to be weaker. As a matter of fact, our data do not provide us with any information on the strength of the link between the RAMEB molecules and the liposome outer surface. The fact that a large molar excess of RAMEB with respect to DMPC is used and that evidence for inclusion complexes has been found, which pleads for reasonable interaction energies, may justify a relatively large volume fraction of RAMEB at the liposome-water interface.
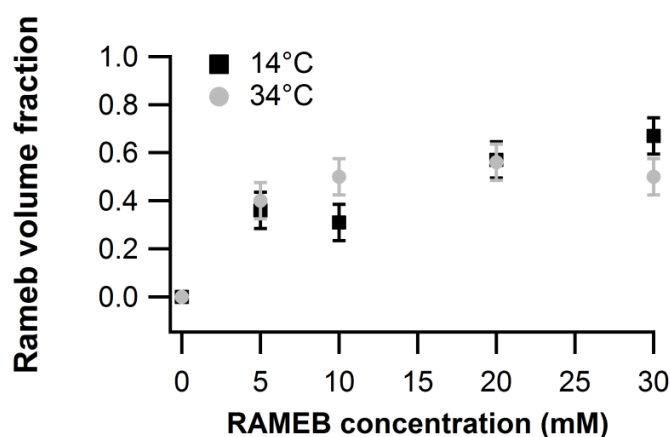
Fig. 6 *Volume fraction of RAMEB on the liposome surface at 14°C (black squares) and 34°C (grey dots)*

3.3 Bilayer thickness

The detailed liposome bilayer structure has also been assessed. Fig. 7 shows how the hydrophilic (Fig. 7a) and hydrophobic (Fig. 7b) sublayers of the membrane vary as a function of the RAMEB concentration. Note that *d* is the average thickness of the inner and outer hydrophilic sublayers.
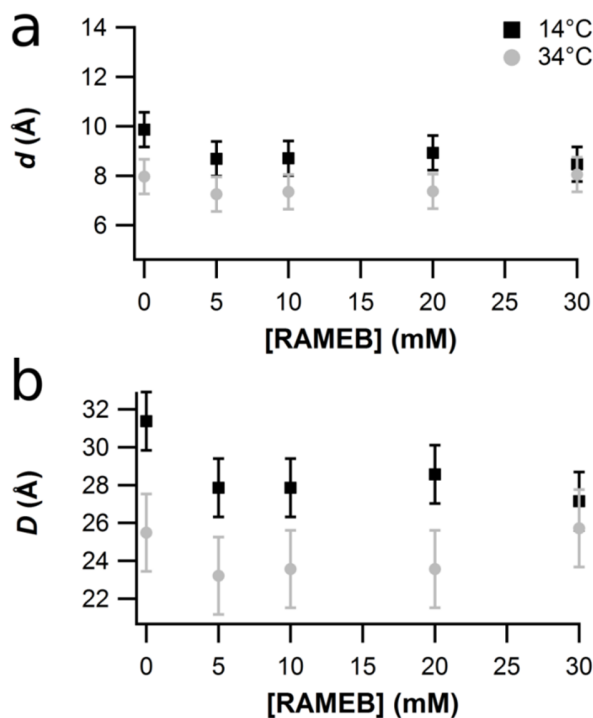
Fig. 7 *DMPC sublayer thickness as a function of RAMEB concentration at 14°C (black squares) and 34°C (grey dots). (a) Average hydrophilic sublayer thickness; (b) Hydrophobic sublayer thickness*

As inferred from the SANS data, the global thickness of the DMPC membranes in the absence of RAMEB is $41 \pm 4 \text{Å}$ at 34°C, with hydrophobic and hydrophilic contributions equal to respectively 25 ± 2 Å and $8,0 \pm 0,9$ Å. The membrane bilayer thickness of the same liposomes increases at 14°C and reaches 51 ± 3 Å with hydrophobic and hydrophilic contributions which are respectively $31,4 \pm 1,5$ Å and $9,9 \pm 0,7$ Å. These results are in agreement with Kiselev's [64,72-74] and Kučerka's works [33]. It has to be kept in mind that the Luzzati thickness displayed in the latter reference cannot be directly compared to our value [75,76]. The larger value of the DMPC membrane thickness at 14°C is associated with the DMPC phase transition. At 14°C, the DMPC molecules are in a rigid and structured phase: the hydrophobic chains adopt elongated *anti*-conformations which optimize their mutual non-covalent interactions. The maximum chain-length for the DMPC hydrophobic moiety in an all *anti*-configuration is equal to

$6 \times 2,5\text{Å}=15\text{Å}$, so that the hydrophobic sublayer is then expected to be 30Å thick which corresponds exactly to the observed hydrophobic thickness at 14°C. At 34°C, the phospholipid chains are in a fluid state leading to a thinner membrane because the entropic driving force favors *gauche* conformations leading to a more compact molecular shape. These results have been confirmed by several study [75,76].

DMPC extraction by RAMEB leads at 14°C to a decrease of the bilayer thickness of the surviving liposomes. On an absolute scale, the decrease is slightly more significant for the hydrophobic part than for the hydrophilic part. This decrease of the global bilayer thickness upon addition of RAMEB is compatible with the findings of our previous work [37]. At 34°C, no significant change could be inferred.

We suggest the following tentative mechanism, which is compatible with the results on the average radius presented in a Subsection 3.2. After phospholipid extraction by RAMEB, some liposomes are completely disrupted, some are not. Fig. 3 shows that, depending on the temperature, 25 to 45% of the liposomes are disrupted. They are either no longer detected in our SANS experiments or detected as RAMEB-DMPC inclusion complexes. In the surviving liposomes, the space made available by the extracted chains allows relaxation processes for the remaining ones. Intercalation of DMPC hydrophobic chains from the inner part of the liposome into the available free space of the outer part becomes possible. This space may also be used by their neighbor molecules which can now adopt a larger number of *gauche*-conformations and, as a consequence, a more compact shape leading to a thinner sublayer. From this point of view, it is logical that the long hydrophobic chains are more affected than the smaller polar heads, so that the hydrophobic sublayer thickness decreases more upon RAMEB addition than the hydrophilic ones. At 34°C, above the bilayer transition temperature, it can be argued that the larger proportion of *gauche*-conformations already present without RAMEB, as mentioned above, makes the bilayer less prone to an additional thickness reduction.

4   Conclusions

The small angle neutron scattering technique has been applied to characterize the influence of a methylated β-cyclodextrin (RAMEB) on the structural parameters of DMPC liposomes. The SANS data are corroborated by DLS experiments but provide us with a more detailed picture of the liposome – cyclodextrin interactions.

The evolution of the fraction of DMPC molecules inserted in the liposomes, and of the aggregation number, confirms that RAMEB at a concentration larger than 10 mM is able to significantly affect the vesicles by extracting phospholipids in a dose dependent way. Information about the coverage of the liposome outer interface by RAMEB was also accessed: at 30 mM of RAMEB, about half of the liposome is covered. Part of the extracted DMPC chains becomes inserted into RAMEB-DMPC inclusion complexes. Part of them participates in the reorganization of the vesicles, leading to larger, more stable liposomes. The fact that the RAMEB influence becomes significant only for [RAMEB] > 10 mM is compatible with the conclusions of Anderson et al [60], who conclude to minimal phospholipid membrane disruption below 15 mM.

The important influence of the temperature on the phospholipidic extraction has been highlighted. Below the bilayer transition temperature, the average liposome radius increases upon addition of RAMEB, an observation which we interpret as a preferential disruption of the small vesicles by the CD and which we correlate with the different contributions to the bilayer bending energy in the framework of the Area-Difference-Elasticity model [67]. The polydispersity increase is assigned to the reorganization process involving random insertion of extracted DMPC chains into larger liposomes. Above the transition temperature, due to a much smaller bilayer bending modulus, all vesicles are suggested to be affected to the same extent by the interaction with RAMEB, which leaves the size distribution nearly unaffected.

The modelled SANS data allowed us to evaluate the effect of the CD on the DMPC membrane thickness below and above the transition temperature. At 14°C, addition of RAMEB leads to a decrease of the bilayer thickness, which is interpreted as a relaxation of the remaining chains in the space made available by the loss of the extracted ones. No significant effect is observed at 34°C.

5   References

1. Ohvo-Rekilä, H., Slotte, J.P.: Cyclodextrin-Mediated Removal of Sterols from Monolayers: Effects of Sterol Structure and Phospholipids on Desorption Rate. Biochem **35**, 8018-8024 (1996).

2. Villiers, A.: Sur la transformation de la fécule en dextrine par le ferment butyrique. Compt. Rend. Fr. Acad. Sci. **112**, 536-538 (1891).

3. Cramer, F.: Einschlussverbindungen. Berlin (1954)

4. Schardinger, F.: kristallisierter Polysaccharide (Dextrine) aus Starkekleister durch Microben. Zentralbl. Bakteriol. Parasitenk. Abt. **29**, 188-197 (1911).

5. Gabelica, V., Galic, N., De Pauw, E.: On the specificity of cyclodextrin complexes detected by electrospray mass spectrometry. J. Am. Soc. Mass. Spectrom. **13**, 946-953 (2002).

6. Loftsson, T., Brewster, M.E.: Pharmaceutical applications of cyclodextrins. 1. Drug solubilization and stabilization. Journal of Pharmaceutical Sciences **85**(10), 1017-1025 (1996). doi:10.1021/js950534b

7. Hashimoto, H.: Present Status of Industrial Application of Cyclodextrins in Japan. J. Inclusion Phenom. Macrocyclic Chem. **44**, 57-62 (2002).

8. Buschmann, H.-J., Schollmeyer, E.: Applications of cyclodextrins in cosmetic products: A review. J. Cosmet. Sci. **53**, 185-191 (2002).

9. Hedges, A.R.: Industrial Applications of Cyclodextrins. Chem. Rev. **98**, 2035-2044 (1998).

10. Szejtli, J.: past, present and future of cyclodextrin research. Pure and Applied Chemistry **76**, 1825-1845 (2004).

11. Szejtli, J.: Cyclodextrins in the Textile Industry. Starch **55**, 191-196 (2003).

12. Loftsson, T., Brewster, M.E.: Pharmaceutical applications of cyclodextrins: basic science and product development. J Pharm Pharmacol **62**(11), 1607-1621 (2010). doi:10.1111/j.2042-7158.2010.01030.x

13. Loftsson, T., Duchene, D.: Cyclodextrins and their pharmaceutical applications. Int J Pharm **329**(1-2), 1-11 (2007). doi:10.1016/j.ijpharm.2006.10.044

14. Zarrabi, A., Vossoughi, M.: Paclitaxel/β-CD-g-PG inclusion complex: An insight into complexation thermodynamics and guest solubility. Journal of Molecular Liquids **208**, 145-150 (2015). doi:10.1016/j.molliq.2015.04.019

15. Brewster, M.E., Loftsson, T.: Cyclodextrins as pharmaceutical solubilizers. Adv Drug Deliv Rev **59**(7), 645-666 (2007). doi:DOI: 10.1016/j.addr.2007.05.012

16. Castagne, D., Fillet, M., Delattre, L., Evrard, B., Nusgens, B., Piel, G.: Study of the cholesterol extraction capacity of β-cyclodextrin and its derivatives, relationships with their effects on endothelial cell viability and on membrane models J Incl Phenom Macrocycl Chem **63**(225-231) (2008).

17. Graham, D.R.M., Chertova, E., Hilburn, J.M., Arthur, L.O., Hildreth, J.E.K.: Cholesterol Depletion of Human Immunodeficiency Virus Type 1 and Simian Immunodeficiency Virus with β-Cyclodextrin Inactivates and Permeabilizes the Virions: Evidence for Virion-Associated Lipid Rafts. J. Virology **77**, 8237-8248 (2003).

18. Zidovetzki, R., Levitan, I.: Use of cyclodextrins to manipulate plasma membrane cholesterol content: evidence, misconceptions and control strategies. Biochim Biophys Acta **1768**(6), 1311-1324 (2007). doi:10.1016/j.bbamem.2007.03.026

19. Hatzi, P., Mourtas, S., Klepetsanis, P.G., Antimisiaris, S.G.: Study of the interaction between cyclodextrins and liposome membranes: effect on the permeability of liposomes. International Journal of Pharmaceutics **225**, 15-30 (2007).

20. Loftsson, T., Masson, M.: Cyclodextrins in topical drug formulation: theory and pratice. International Journal of Pharmaceutics **225**, 15-30 (2001).

21. Grammenos, A., Mouithys-Mickalad, A., Guelluy, P.H., Lismont, M., Piel, G., Hoebeke, M.: ESR technique for noninvasive way to quantify cyclodextrins effect on cell membranes. Biochem Biophys Res Commun **398**(3), 350-354 (2010). doi:10.1016/j.bbrc.2010.06.050

22. Piel, G., Moutard, S., Uhoda, E., Pilard, F., Pierard, G.E., Perly, B., Delattre, L., Evrard, B.: Skin compatibility of cyclodextrins and their derivatives: a comparative assessment using a corneoxenometry bioassay. Eur J Pharm Biopharm **57**(3), 479-482 (2004). doi:10.1016/j.ejpb.2003.12.004

23. Piel, G., Piette, M., Barillaro, V., Castagne, D., Evrard, B., Delattre, L.: Study of the relationship between lipid binding properties of cyclodextrins and their effect on the integrity of liposomes. Int J Pharm **338**(1-2), 35-42 (2007). doi:10.1016/j.ijpharm.2007.01.015

24. Lê-Quôc, D.a.L.-Q.K.: http://www.espacesciences.com/index.html. (2000).

25. He, Y., Fu, P., Shen, X., Gao, H.: Cyclodextrin-based aggregates and characterization by microscopy. Micron **39**, 495-516 (2008).

26. Messner, M., Kurkov, S.V., Jansook, P., Loftsson, T.: Self-assembled cyclodextrin aggregates and nanoparticles. International Journal of Pharmaceutics **387**, 199-208. (2010).

27. Kučerka, N., Pencer, J., Sachs, J., Nagle, J., Katsaras, J.: Curvature effect on the structure of phospholipid bilayer. Langmuir **23**, 1292-1299. (2007).

28. Kučerka, N., Nieh, M., Pencer, J., Harroun, T., Katsaras, J.: The study of liposomes, Lamellae and Membranes Using Neutrons and X-rays. Curr Opin Colloid Int **12**, 17-22 (2007).

29. Pabst, G., Kučerka, N., Nieh, M., Rheinstädter, M., Katsaras, J.: Application of neutrons and X-ray scattering to the study of biologically relevant model membranes. Chem. Phys. Lipids **163**, 460-479 (2010).

30. Kučerka, N., Kiselev, M.a., Balgavý, P.: Determination of bilayer thickness and lipid surface area in unilamellar dimyristoylphosphatidylcholine vesicles from small-angle neutron scattering curves: a comparison of evaluation methods. European biophysics journal : EBJ **33**, 328-334 (2004). doi:10.1007/s00249-003-0349-0

31. Kučerka, N., Liu, Y., Chu, N., Petrache, H.I., Tristram-Nagle, S., Nagle, J.F.: Structure of fully hydrated fluid phase DMPC and DLPC lipid bilayers using X-ray scattering from oriented multilamellar arrays and from unilamellar vesicles. Biophysical journal **88**, 2626-2637 (2005). doi:10.1529/biophysj.104.056606

32. Kučerka, N., Nagle, J.F., Sachs, J.N., Feller, S.E., Pencer, J., Jackson, A., Katsaras, J.: Lipid bilayer structure determined by the simultaneous analysis of neutron and X-ray scattering data. Biophysical journal **95**, 2356-2367 (2008). doi:10.1529/biophysj.108.132662

33. Kučerka, N., Nieh, M.P., Katsaras, J.: Fluid phase lipid areas and bilayer thicknesses of commonly used phosphatidylcholines as a function of temperature. Biochimica et Biophysica Acta - Biomembranes **1808**, 2761-2771 (2011). doi:10.1016/j.bbamem.2011.07.022

34. Belička, M., Devínsky, F., Balgavý, P.: Neutrons in studies of phospholipid bilayers and bilayer–drug interaction. II. Small-angle scattering. Acta Facultatis Pharmaceuticae Universitatis Comenianae **61**, 12-20 (2014). doi:10.2478/afpuc-2014-0011

35. Belička, M., Devínsky, F., Balgavý, P.: Neutrons in studies of phospholipid bilayers and bilayer–drug interaction. I. Basic principles and neutron diffraction. Acta Facultatis Pharmaceuticae Universitatis Comenianae **61**, 1-11 (2014). doi:10.2478/afpuc-2014-0010

36. Uhríková, D., Kučerka, N., Teixeira, J., Gordeliy, V., Balgavý, P.: Structural changes in dipalmitoylphosphatidylcholine bilayer promoted by Ca2+ ions: a small-angle neutron scattering study. Chemistry and Physics of Lipids **155**, 80-89 (2008). doi:10.1016/j.chemphyslip.2008.07.010

37. Grammenos, A., Bahri, M.A., Guelluy, P.H., Piel, G., Hoebeke, M.: Quantification of Randomly-methylated-beta-cyclodextrin effect on liposome: an ESR study. Biochem Biophys Res Commun **390**(1), 5-9 (2009). doi:10.1016/j.bbrc.2009.08.172

38. Guelluy, P.H., Fontaine-Aupart, M.P., Grammenos, A., Lecart, S., Piette, J., Hoebeke, M.: Optimizing photodynamic therapy by liposomal formulation of the photosensitizer pyropheophorbide-a methyl ester: in vitro and ex vivo comparative biophysical investigations in a colon carcinoma cell line. Photochem Photobiol Sci **9**(9), 1252-1260 (2010). doi:10.1039/c0pp00100g

39. Vrhovnik, K., Kristl, J., Sentjurc, M., Smid-Korbar, J.: Influence of liposome bilayer fluidity on the transport of encapsulated substance into the skin as evaluated by EPR. Pharm Res **15**(4), 525-530 (1998).

40. Battistini, L., Burreddu, P., Sartori, A., Arosio, D., Manzoni, L., Paduano, L., Derrico, G., Sala, R., Reia, L., Bonomini, S., Rassu, G., Zanardi, F.: Enhancement of the uptake and cytotoxic activity of doxorubicin in cancer cells by novel cRGD-semipeptide-anchoring liposomes. Molecular Pharmaceutics **11**, 2280-2293 (2014). doi:10.1021/mp400718j

41. Etheridge, M.L., Campbell, S.a., Erdman, A.G., Haynes, C.L., Wolf, S.M., McCullough, J.: The big picture on nanomedicine: the state of investigational and approved nanomedicine products. Nanomedicine : nanotechnology, biology, and medicine **9**, 1-14 (2013). doi:10.1016/j.nano.2012.05.013

42. Ntimenou, V., Fahr, A., Antimisiaris, S.G.: Elastic vesicles for transdermal drug delivery of hydrophilic drugs: a comparison of important physicochemical characteristics of different vesicle types. Journal of biomedical nanotechnology **8**(4), 613-623 (2012).

43. Mourtas, S., Mao, J., Parsy, C.C., Storer, R., Klepetsanis, P., Antimisiaris, S.G.: Liposomal gels for vaginal delivery of the microbicide MC-1220: preparation and in vivo vaginal toxicity and pharmacokinetics. Nano Life **1**(03n04), 195-205 (2010).

44. Boulmedarat, L., Piel, G., Bochot, A., Lesieur, S., Delattre, L., Fattal, E.: Cyclodextrin-mediated drug release from liposomes dispersed within a bioadhesive gel. Pharm Res **22**(6), 962-971 (2005). doi:10.1007/s11095-005-4591-2

45. Gillet, A., Grammenos, A., Compere, P., Evrard, B., Piel, G.: Development of a new topical system: drug-in-cyclodextrin-in-deformable liposome. Int J Pharm **380**(1-2), 174-180 (2009). doi:10.1016/j.ijpharm.2009.06.027

46. Gharib, R., Greige-Gerges, H., Fourmentin, S., Charcosset, C., Auezova, L.: Liposomes incorporating cyclodextrin-drug inclusion complexes: current state of knowledge. Carbohydrate Polymers **129**, 175-186 (2015). doi:10.1016/j.carbpol.2015.04.048

47. Piel, G., Piette, M., Barillaro, V., Castagne, D., Evrard, B., Delattre, L.: Betamethasone-in-cyclodextrin-in-liposome: the effect of cyclodextrins on encapsulation efficiency and release kinetics. Int J Pharm **312**(1-2), 75-82 (2006). doi:10.1016/j.ijpharm.2005.12.044

48. Tsamaloukas, A., Szadkowska, H., Slotte, J.P., Heerklotz, H.: Interaction of cholesterol with lipid membranes and cyclodextrin charaterized by calorimetry. Biophys J **89**, 1109-1119 (2005).

49. Puskás, I., Barcza, L., Szente, L., Csempesz, F.: Features of the Interaction between Cyclodextrins and Colloidal Liposomes. Journal of Inclusion Phenomena and Macrocyclic Chemistry **54**(1-2), 89-93 (2006). doi:10.1007/s10847-005-4805-6

50. Piette, M., Evrard, B., Frankenne, F., Chiap, P., Bertholet, P., Castagne, D., Foidart, J.M., Delattre, L., Piel, G.: Pharmacokinetic study of a new synthetic MMP inhibitor (Ro 28-2653) after IV and oral administration of cyclodextrin solutions. Eur J Pharm Sci **28**(3), 189-195 (2006). doi:10.1016/j.ejps.2006.01.011

51. Hatzi, P., Mourtas, S., G. Klepetsanis, P., Antimisiaris, S.G.: Integrity of liposomes in presence of cyclodextrins: Effect of liposome type and lipid composition. International Journal of Pharmaceutics **333**, 167-176 (2007). doi:10.1016/j.ijpharm.2006.09.059

52. Caffrey, M., Hogan, J.: LIPIDAT: A database of lipid phase transition temperatures and enthalpy changes. DMPC data subset analysis. Lipids **61**, 1-109 (1992).

53. Hope, M., Bally, M., Webb, G., Cullis, P.: Production of large unilamellar vesicles by rapid extrusion procedure. Characterization of size distribution, trapped volume and ability to maintain a membrane potential. Biochem Biophys Acta **812**, 55-65 (1985).

54. Lentz, B., Carpenter, T., Alford, D.: Spontaneous fusion of phosphatidylcholine small unilamellar vesicles in the fluid phase. Biochem **26**, 5389-5397 (1987).

55. Coderch, L., Fonollosa, J., De Pera, M., Estelrich, J., De La Maza, A., Parra, J.L.: Influence of cholesterol on liposome fluidity by EPR. Relationship with percutaneous absorption. J Control Release **68**(1), 85-95 (2000). doi:10.1016/S0168-3659(00)00240-6

56. Olson, F., Hunt, C.A., Szoka, F.C., Vail, W.J., Papahadjopoulos, D.: Preparation of liposomes of defined size distribution by extrusion through polycarbonate membranes. Biochim Biophys Acta **557**(1), 9-23 (1979).

57. Brûlet, A., Lairez, D., Lapp, A., Cotton, J.-P.: Improvement of data treatment in small-angle neutron scattering. J Appl crystallogr **40**, 165-177 (2007).

58. Hammouda, B.: Probing nanoscale structures - The SANS tollbox. National Institute of Standards and Technology Center for Neutron Research Gaithersburg (2009)

59. Szejtli, J.: Introduction and General Overview of Cyclodextrin Chemistry. Chem. Rev. **98**, 1743-1753 (1998). doi:10.1021/CR970022C

60. Anderson, T.G., Tan, A., Ganz, P., Seelig, J.: Calorimetric Measurement of Phospholipid Interaction with Methyl-beta-Cyclodextrin. Biochemistry **43**, 2251-2261 (2004). doi:10.1021/bi0358869

61. Hallett, A.F., Craig, T., Marsh, J., Nickel, B.: Number Distributions by Dynamic Light Scattering. Can. J. Spectr. **34**, 63-70 (1989).

62. Maulucci, G., De Spirito, M., Arcovito, G., Boffi, F., Castellano, A.C., Briganti, G.: Particle size distribution in DMPC vesicles solutions undergoing different sonication times. Biophys. J. **88**, 3545-3550 (2005).

63. González-Gaitano, G., da Silva, M.a., Radulescu, A., Dreiss, C.a.: Selective Tuning of the Self-Assembly and Gelation of a Hydrophilic Poloxamine by Cyclodextrins. Langmuir **31**, 5645-5655 (2015). doi:10.1021/acs.langmuir.5b01081

64. Kiselev, M.A., Zemlyanaya, E.V., Aswal, V.K., Neubert, R.H.: What can we learn about the lipid vesicle structure from the small-angle neutron scattering experiment? Eur Biophys J **35**, 477-493 (2006).

65. Másson, M., Loftsson, T., Másson, G., Stefánsson, E.: Cyclodextrins as permeation enhancers: some theoretical evaluations and in vitro testing. Journal of Controlled Release **59**(1), 107-118 (1999). doi:Doi: 10.1016/s0168-3659(98)00182-5

66. Puskas, I., Csempesz, F.: Influence of cyclodextrins on the physical stability of DPPC-liposomes. Colloids and Surfaces B: Biointerfaces **58**(2), 218-224 (2007). doi:10.1016/j.colsurfb.2007.03.011

67. Miao, L., Seifert, U., Wortis, M., Döbereiner, H.-G.: Budding transitions of fluid-bilayer vesicles:The effect of area-difference elasticity. Phys. Rev. E **49**, 5389-5407 (1996).

68. Helfrich, W. Z. Naturforsch. C **28**, 693 (1973).

69. Morse, D.C., Milner, S.T.: Statistical mechanics of closed fluid membranes. Phys. Rev. E **52**, 5918-5945 (1995).

70. Charitat, T., Lecuyer, S., Fragneto, G.: Fluctuation and destabilization of single phospholipids bilayers. Biointerphases **3**, FB3-FB15 (2008).

71. Mascetti, J., Castano, S., Cavagnat, D., Desbat, B.: Organization of β-Cyclodextrin under Pure Cholesterol, DMPC, or DMPG and Mixed Cholesterol/Phospholipid Monolayers. Langmuir **24**(17), 9616-9622 (2008). doi:10.1021/la8004294

72. Kiselev, M.A., Zemlyanaya, E.V., Aswal, V.K.: Sans study of the unilamellar DMPC vesicles. The fluctuation model of lipid bilayer. Crystallography reports (2004).

73. Kiselev, M.A., Zbytovska, J., Matveev, D., Wartewig, S., Gapienko, I.V., Perez, J., Lesieur, P., Hoell, A., Neubert, R.: Influence of trehalose on the structure of unilamellar DMPC vesicles. Colloids and Surfaces A: Physicochemical and Engineering Aspects **256**(1), 1-7 (2005). doi:DOI: 10.1016/j.colsurfa.2004.09.017

74. Kucerka, N., Kiselev, M.A., Balgavy, P.: Determination of bilayer thickness and lipid surface area in unilamellar dimyristoylphosphatidylcholine vesicles from small-angle neutron scattering curves: a comparison of evaluation methods. Eur Biophys J **33**(4), 328-334 (2004). doi:10.1007/s00249-003-0349-0

75. Nagle, J.F., Tristram-Nagle, S.: Lipid Bilayer Structure. Current opinion in structural biology **10**, 474-480 (2000).

76. Nagle, J., Petrache, H., Gouliaev, N., Tristram-Nagle, S., Liu, Y., Suter, R., Gawrisch, K.: Multiple mechanisms for critical behavior in the biologically relevant phase of lecithin bilayers. Physical Review E **58**, 7769-7776 (1998). doi:10.1103/PhysRevE.58.7769

CHAPTER VII

Small-Angle Neutron Scattering investigation of cholesterol-doped DMPC liposomes interacting with β-cyclodextrin

Abstract

In this chapter, the Small-Angle Neutron Scattering technique (SANS) has been applied to characterize the influence of a randomly methylated β–cyclodextrin (CD), called RAMEB, on dimyristoylphosphatidylcholine (DMPC) liposomes doped with cholesterol. From the modelling of the experimental neutron scattering crosssections, the detailed response of the vesicle structure upon addition of increasing amounts of RAMEB up to 30 mM has been assessed. This study has been performed below and above the DMPC bilayer phase transition temperature and shows that cholesterol extraction by RAMEB is linked to a decrease of the average radius and of the aggregation number of the vesicles. This extraction takes place in a dose-dependent way until a more monodisperse population of cholesterol-free liposomes were obtained. In addition, the bilayer thickness evolution was inferred, as well as the liposome coverage by RAMEB.

1 Introduction

Cyclodextrins (CD) are cavitands with the shape of a truncated cone which consist of 6-8 D-glucopyranose units presenting a hydrophilic outer surface and a lipophilic central cavity. Due to their particular structure conferring them the ability to encapsulate a large number of organic molecules [1], CD have found a large field of applications including cosmetics, food and pharmaceutics [2-4]. It is well known that natural cyclodextrins have a limited aqueous solubility [5]. A random substitution of the hydrogen bond forming hydroxy groups might increase this solubility and these particular CD are identified as cyclodextrin derivatives (CDs). However, only a few of them passed through the toxicological evaluation: among them, the randomly-methylated β-cyclodextrin (RAMEB) [5].

Recently, CDs have been described as drug release modulators within liposomes [6,7]. Understanding the mechanism of action of CDs on liposomes is expected to improve the potentialities and the efficiency of CDs in this new field of interest. Moreover, liposomes are not only used as medical drug vectors [8-12] but they represent also a relevant cell membrane model [13]. Knowledge of CDs action on liposomes doped with cholesterol is of particular interest. As a matter of fact, cholesterol appears to be the major component of the so-called lipid rafts, which have been recognized as specialized cell-signaling micro-domains within the plasma membrane [14,15]. Cholesterol plays a key role in maintaining their structure and function [15,14,16]. As β-CDs like RAMEB have a significant cholesterol affinity [5,17,18], studying their interaction with membranes may contribute to a better understanding of the lipid raft functions.

Numerous works focused on the mechanism of action of CDs on liposomes and on the influence of CDs on the stability as well as on the integrity of the vesicle bilayer [17-26]. The liposome integrity has been explored in the presence of CD by measuring the release of a fluorescent probe initially encapsulated in the liposomes [19,21,22,24]. Differential scanning calorimetry has also been employed to investigate the structural changes induced by CDs on membranes [19,25], as well as freeze-fracture electron microscopy [21]. Researches also demonstrated the CDs affinities with phospholipids by using binding isotherms [19-21,23]. A new approach to measure the permeability and the liposome size using Surface Plasmon Resonance has been reported [27], and we proposed to use Electron Spin Resonance

spectroscopy to study cholesterol extraction by CDs [17,18]. However, the easiest and most commonly used method to characterize the interaction of CDs with liposomes remains Photon-Correlation Spectroscopy (PCS) [19-21,23], also called Dynamic Light Scattering (DLS), even though the information inferred remains limited.

Dynamic and static light scattering provide only information on the global liposome size and on the size dispersity. The internal structure of the bilayer cannot be assessed by such techniques [28]. The main purpose of the present investigation is to analyze the RAMEB action on liposome targets doped with cholesterol using Small-Angle Neutron Scattering (SANS). In a previous work [26], we have investigated the influence of RAMEB on vesicles made of dimyristiroylphosphatidylcholine (DMPC) only and demonstrated that SANS can significantly enhance our understanding about the influence of CDs on the liposome bilayer structure. We developed a tailored model of the liposome which includes its different substructures and which also allows for the possible coverage of the liposome outer interface by RAMEB molecules. By fitting this model to the experimental SANS cross sections, we could infer the average radius, the polydispersity, the thicknesses of the hydrophobic and hydrophilic parts of the bilayer and the volume fraction of RAMEB molecules at the surface of the vesicle, as a function of the RAMEB concentration and of the temperature which was chosen either below or above the transition from the rigid to the fluid membrane state (23.9°C for pure DMPC bilayers).

In the present paper, we investigate by SANS together with an adapted structural model, how cholesterol-doped liposomes are perturbed by increasing amounts of RAMEB. As in our previous study, the influence of the temperature will be examined. It has to be noted here that the presence of cholesterol abolishes the endothermic phase transition of the bilayer [17,29]. Indeed, above 25 mol% of cholesterol, the DMPC bilayer is in a liquid ordered phase (l_0), which is not significantly affected by a temperature change [30]. Cholesterol extraction by RAMEB is, however, expected to perturb this situation, which justifies the need to investigate both temperatures. Dynamic light scattering measurements will complement the SANS results.

2 Materials and methods

2.1 Liposome preparation

Dimyristoylphosphatidylcholine (DMPC), and octadecylamine, also called stearylamine (SA), were purchased from Sigma (Aldrich, Belgium). Cholesterol was obtained from Merck (Germany). All products were used without further purification. Lipid vesicles were prepared by hydration of lipid films as described by Hope et al [31]. Liposomes were doped with 10 mol% of SA, in order to prevent their spontaneous fusion, which is known to appear above the DMPC bilayer phase transition temperature [31]. In addition, the specificity of the present work is that the liposomes were doped with 30 mol% of cholesterol. Lipids were first dissolved in chloroform to a final concentration of 7.4 mM. The chloroform/lipid mixture was then stirred for 5 min and the solvent was evaporated under vacuum. The resulting lipid film was suspended in deuterium oxide (Sigma Aldrich, Belgium), and stirred by a vortex mixer in order to obtain large multilamellar vesicles (MLV) [32]. After hydration, five freeze-thaw cycles using liquid nitrogen were carried out to allow a better incorporation of the SA and cholesterol into the liposome phospholipidic bilayers. The MLV suspension was then transferred into an extruder (Lipex Biomembrane, Canada) with polycarbonate filters (0.1 μm pore size, Nucleopore, CA), under a pressure gradient of 6800 Pa of nitrogen (Air Liquid, Belgium). The procedure was repeated ten times at 35°C and resulted in unilamellar liposomes [33]. Once prepared, the liposomes were incubated with the selected concentrations of RAMEB (Wacker Chemie GmbH , Germany; degree of substitution equal to 12.6) which had been first filtered through a microfilter with a pore size of 0.2 μm.

2.2 SANS measurements

The SANS cross sections of unilamellar vesicles in D_2O in contact with different concentrations of RAMEB were recorded at two temperatures (14°C and 34°C). The experiments have been performed at the Jülich Centre for Neutron Science (JCNS). The KWS-1 and KWS-2 small-angle instruments have been used to collect data at three sample-detector distances: 2, 8 and 20m. The wavelength of the neutrons, λ, was equal to 6.00 ± 0.60 Å after mechanical velocity selection. These conditions gave access to a momentum transfer range, q, from $2.36 \ 10^{-3}$ Å^{-1} to $1.96 \ 10^{-1}$ Å^{-1} where $q = \frac{4\pi}{\lambda}\sin(\theta)$ and 2θ is the scattering angle. The scattered neutrons were detected on a two-dimensional ^{6}Li scintillation counter.

Radial averaging led to a one-dimensional scattering function *I(q)*. Corrections for the background and sample holder contributions were carried out according to standard data handling procedures [34]. The liposome dispersion and the pure D_2O sample were treated in the same way, and the scattering intensities were converted to macroscopic scattering cross sections per unit volume, $d\Sigma / d\Omega$ (cm^{-1}), by using calibration with Poly(methyl methacrylate). The liposome contribution was determined by subtracting the D_2O cross section weighted by its volume fraction.

2.3 SANS data analysis

The principle of the evaluation of the vesicle parameters from the SANS scattering cross section has been described in our previous work [26]. The model has been adapted to include the additional presence of cholesterol. The liposomes are described as a superposition of concentric homogeneous substructures. In our experiments, we select spherical unilamellar liposomes with a bilayer of average global radius *R* and this bilayer has been modelled by two peripheral hydrophilic parts (with thicknesses equal to d_{in} and d_{out}) and one intermediate hydrophobic part (thickness equal to *D*). As the peripheral parts of the bilayer are polar, a linear water penetration profile is assumed in these zones. Due to the curvature of the membrane, the aggregation number corresponding to the inner and outer sublayers, N_{in} and N_{out} are in principle different. Note also that the aggregation number includes all molecules present in the bilayer, that is, also cholesterol.

We now briefly recall the main points. The macroscopic scattering cross-section is written as:

$$\frac{d\Sigma}{d\Omega} = \frac{[DMPC]N_A 10^{-3}}{\langle N \rangle} \int_0^\infty |A(q)|^2 P_n(R)\, dR \qquad (1)$$

where [*DMPC*] is the total DMPC concentration in mol/L, *<N>* is the average aggregation number of the liposomes, *R* is the liposome radius and $P_n(R)$ represents the liposome size distribution. In the dilute regime, the interferences between waves scattered by different liposomes may be ignored [35] and the scattering amplitude *A(q)* is given by

$$A(q) = 4\pi \int_{liposome} \tilde{\rho}(r) \frac{\sin(qr)}{qr} r^2\, dr \qquad (2)$$

176

where the excess scattering length density $\tilde{\rho}$ is a function of the distance r from the center of the liposome and is equal to

$$\tilde{\rho}(r) = \tilde{\rho}_{SA}\varphi_{SA}(r) + \tilde{\rho}_{DMPC}\varphi_{DMPC}(r) + \tilde{\rho}_{CHOL}\varphi_{CHOL}(r) \qquad (3)$$

The respective hydrophobic tails and hydrophilic heads of SA and DMPC are taken as the elementary scatterers. $\varphi_{SA},\varphi_{DMPC}$ and φ_{CHOL} are the respective volume fractions of SA, DMPC and cholesterol. The distribution of the cholesterol molecules is considered to be uniform in the bilayer [17,30]. When cyclodextrin was added, its possible presence at the outer liposome interface has been included in the model by considering an additional layer with a thickness equal to the height of a RAMEB molecule (7.8Å).

As in our previous work [26], the presence of an additional small contribution to the cross section due to the possible formation of RAMEB-DMPC inclusion complexes [36] resulting from partial disruption of the membranes interacting with RAMEB has been checked . These complexes have been modelled as homogeneous spheres. However, the contribution of such complexes happened to be not significant in this case. When cholesterol-doped liposomes are investigated, additional complexes involving cholesterol and RAMEB must, however, also be considered. An upper limit for the possible contribution of 1:2 cholesterol-RAMEB complexes [37] was estimated to be 2.10^{-4} cm^{-1} at $q = 0$, by assuming a complete extraction of cholesterol: such a contribution corresponds to the background signal and was neglected. These complexes are too small indeed to give rise to a measurable SANS signal, so that we can draw no conclusion about their presence.

The scattering cross section has then been averaged over the size distribution of the liposomes and convoluted by a triangular apparatus function to take into account the scattering vector spread ($\Delta q/q$ = 10%). The fit quality has been assessed by monitoring the χ^2 in either linear or logarithmic mode [26].

2.4 *Dynamic Light Scattering Measurements (DLS)*

DLS measurements were carried out with a particle size analyzer (Delsa Nano C, Particle Analyzer, Beckman Coulter) at a fixed scattering angle of 165°. The light source was a diode

laser operating at λ=658 nm and 30 mW power. Measurements on the solutions composed of cholesterol-doped liposomes in contact with different amounts of RAMEB were performed at two different temperatures (14 and 34°C) in duplicate. Each measure lasted about 20 minutes. Initial liposome and RAMEB solutions were both filtered with a microfilter with a pore size of 0.2 µm. Data were handled using the CONTIN algorithm (Delsa Nano software). The average of several histograms leads to smooth distributions.

As explained in our previous paper [26], in order to compare the DLS intensity-weighted distributions and the SANS number distributions, the SANS size distributions must be multiplied by R^4 and by the form factor, $F(q;R)$, of the vesicle at the q value corresponding to the wavelength and detection angle of the DLS instrument. Because all the information required to calculate $F(q;R)$ is available from the analysis of our SANS data, we converted the SANS number distributions to equivalent DLS intensity distributions.

3   *Results and discussion*

SANS macroscopic cross-sections of cholesterol-doped liposomes with or without added RAMEB, as well as fits using the model described in the "SANS data analysis" Section are displayed in Fig. 1. A good agreement, monitored by the χ^2 values, is observed between the experimental and modelled data.
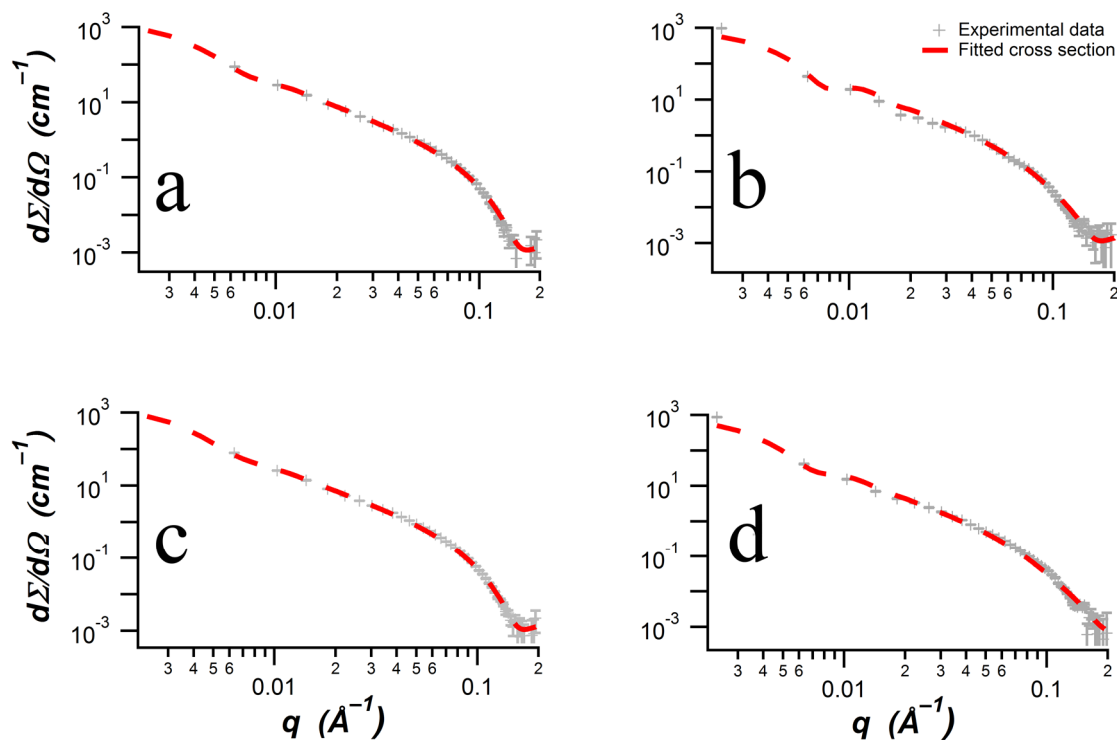
Fig. 1 *Experimental macroscopic cross-sections of the liposomes (+ gray symbols) and their fits to the analytical model (see "SANS Data Handling Section") (red dotted line). (a) Pure cholesterol-doped liposomes at 14°C; (b) Liposomes at 14°C in contact with RAMEB at a concentration of 20 mM; (c) Pure cholesterol-doped liposomes at 34°C; (d) Liposomes in contact with RAMEB at a concentration of 20 mM at 34°C.*

3.1 *Fraction of molecules included into unilamellar liposomes*

In the investigated q range, liposomes and DMPC-RAMEB inclusion complexes [26,36] can in principle be observed. Free DMPC chains as well as 1:2 cholesterol-RAMEB complexes provide a negligible cross section and large clusters of liposomes would only be detected at lower q values. It turns out that for cholesterol-doped liposomes, no significant contribution of the DMPC-RAMEB inclusion complexes could be detected. Based on the known total DMPC concentration and on the experimental scattering cross section, the fraction of lipid and cholesterol molecules contained in the vesicles can be inferred. In our previous paper [26], we denoted as m the fraction of chains included in the unilamellar liposomes and we normalized it with respect to its value in the absence of RAMEB, m_0. Fig. 2

shows the evolution of m/m_0 upon increasing RAMEB concentration below (14°C) and above (34°C), the rigid-fluid transition temperature of the pure DMPC bilayer (23.9 °C).

The extracting role of RAMEB as well as its solubilization ability for pure DMPC liposomes has already been demonstrated [6,26]. For cholesterol-free DMPC liposomes, we observed that extraction by RAMEB started at [RAMEB] $\approx$ 10 mM. For cholesterol-doped liposomes, the effect seems more progressive, with no clear concentration threshold. At the largest RAMEB concentration investigated (30mM), 27 ± 6 % of liposomes happen to be affected by liposome solubilization at 14°C, whereas this ratio reaches 54 ± 6 % at 34°C. In comparison with our previous study [26], it can thus be inferred that RAMEB damages 5 to 10 % more liposomes when they are doped with cholesterol.
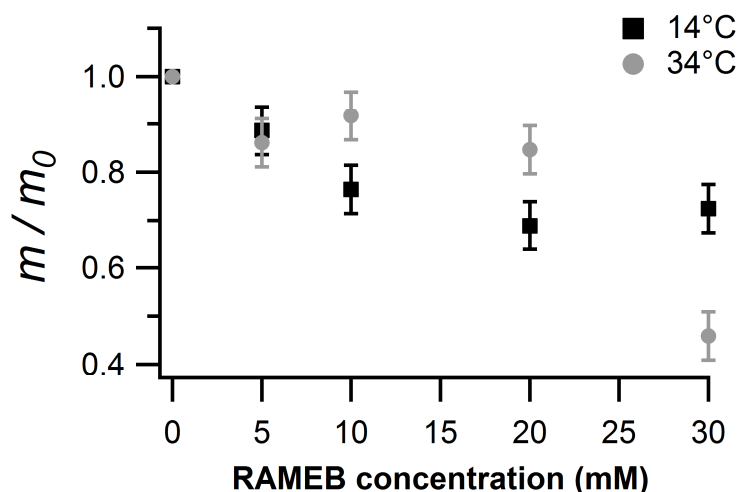
Fig. 2 *Influence of RAMEB on the fraction of molecules included in the cholesterol-doped liposomes (m/m_0 parameter) at 14°C (black squares) and 34°C (grey dots)*

3.2 *Liposome Radius and Aggregation Number*

Fig. 3 shows the evolution of the average liposome radius inferred from SANS upon addition of increasing concentrations of RAMEB at 14°C and 34°C. A monotonous linear decrease of about 10% is observed over the RAMEB concentration range. No significant temperature effect could be detected. This size decrease has been confirmed by DLS measurements (Figs. 4b and 4c).

Liposomes doped with 30 % of cholesterol display a mean radius of 458 ± 18 Å (average between the values at 14 and 34°C) without RAMEB. When 30 mM of RAMEB is added, the average radius of the surviving liposomes reaches 424 ± 17 Å, which becomes closer to the size of cholesterol-free liposomes without RAMEB [26]. Therefore, even if RAMEB is able to extract DMPC phospholipids from membranes [26], the present data and the fact that no DMPC-RAMEB complexes could be evidenced here suggest that the high affinity of β-CD for cholesterol [5,17,18] favours the competitive cholesterol extraction, also in agreement with our previous Electron Spin Resonance study [17]. However, as already emphasized, we have no direct possibility to detect the very small cholesterol-RAMEB complexes.

The decrease of the liposome size is directly linked to a decrease of the average aggregation number (which also includes the cholesterol molecules), as shown in Fig. 3b. At [RAMEB] = 30 mM, the relative decrease reaches 19 ± 8%. Invoking again the known affinity of RAMEB for cholesterol, this indicates that about two-third of the cholesterol molecules are extracted from the surviving liposomes at [RAMEB] = 30 mM. The m/m_0 data discussed above show also that part of the liposomes are disrupted and may form clusters which are no longer detected in the investigated q range.
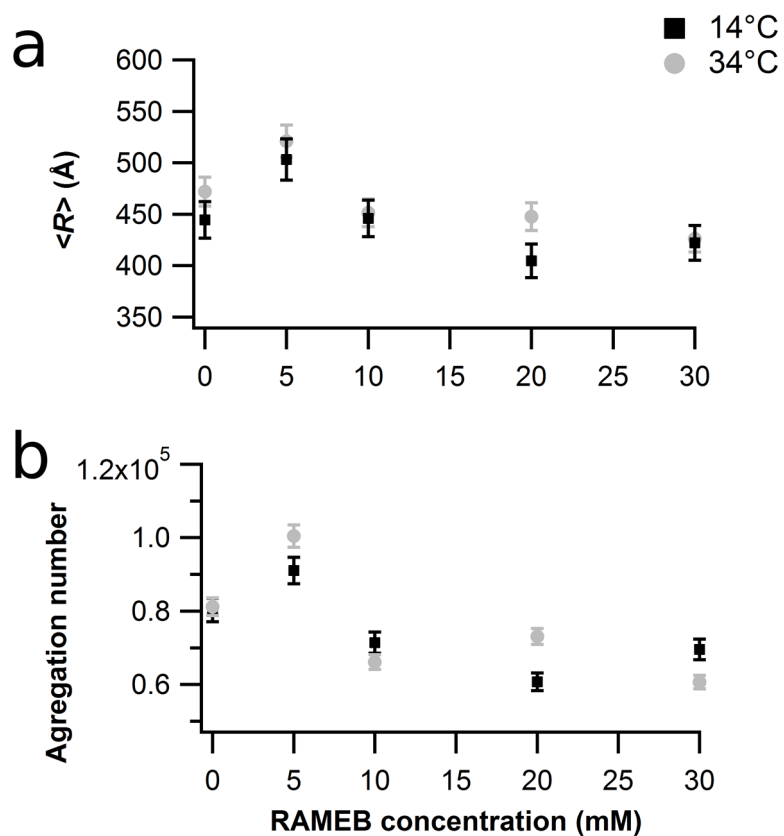
***Fig. 3*** *Average liposome radius (a) and aggregation number (b) for increasing RAMEB concentrations at 14°C (black squares) and 34°C (grey dots). Note that the displayed radii are obtained by averaging over a number-weighted size distribution.*

3.3 Polydispersity of the liposomes

Fig. 4a shows the influence of RAMEB on the polydispersity measured as the standard deviation of the size distribution (Å). A decrease of $33 \pm 5\%$ is observed for both temperatures. These results were confirmed by DLS experiments (Figs. 4b and 4c).

The polydispersity data suggest a lipidic reorganization of the vesicles to reach a more homogeneous population. Such a behavior have been previously reported on large liposomes [38]. The standard deviation reached at [RAMEB] = 30 mM is compatible with the 100-110 (Å) range observed for cholesterol-free liposomes without RAMEB. We emphasized in the previous parts of the discussion that, in liposomes surviving the RAMEB treatment, cholesterol extraction had been favoured compared to DMPC extraction. We repeatedly observed that the structure found for initially cholesterol-doped liposomes interacting with RAMEB (at 30 mM) tends to become closer to that of pure cholesterol-free liposomes without RAMEB. We may therefore conclude that the decrease of the size dispersion is also a signature of the cholesterol extraction.
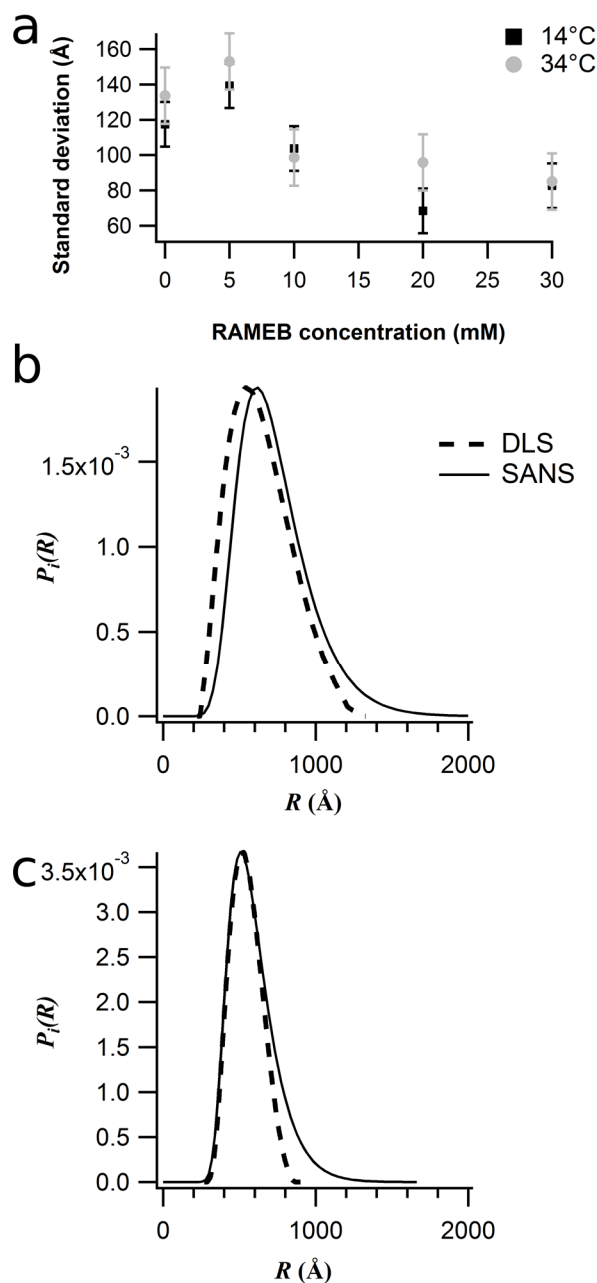
Fig. 4 (a) *Standard deviation of the radius of cholesterol-doped DMPC liposomes at 14°C (black squares) and 34°C (grey dots), as inferred from SANS, as a function of RAMEB concentration. (b) Liposome radius distribution at 14°C determined by DLS (dotted line) and SANS (solid line) for cholesterol-doped liposomes without RAMEB and (c) in contact with RAMEB at a concentration of 30 mM. The SANS size distributions have been converted into intensity-weighted distributions, $P_i(R)$, to make them comparable with the distributions inferred from DLS. This has the effect of shifting the distribution towards larger R values.*

3.4   Coverage of the outer liposome interface by RAMEB

Analyzing the SANS data gives us also access to the volume fraction of RAMEB which covers the vesicle outer interface. The presence of RAMEB molecules on membranes has been previously reported with DMPC-liposomes [26] in agreement with a study of Mascetti et al. [39]. It has been rationalized by invoking the formation of a hydrogen bond between the phospholipidic polar head group and one hydroxyl group of CD, even though this interaction should be somewhat less favoured for methylated CDs like RAMEB. The results obtained with cholesterol-doped DMPC liposomes are quite similar to those for pure DMPC liposomes with a coverage of about half of the vesicle outer surface at [RAMEB] = 30 mM and 14°C (Fig. 5).
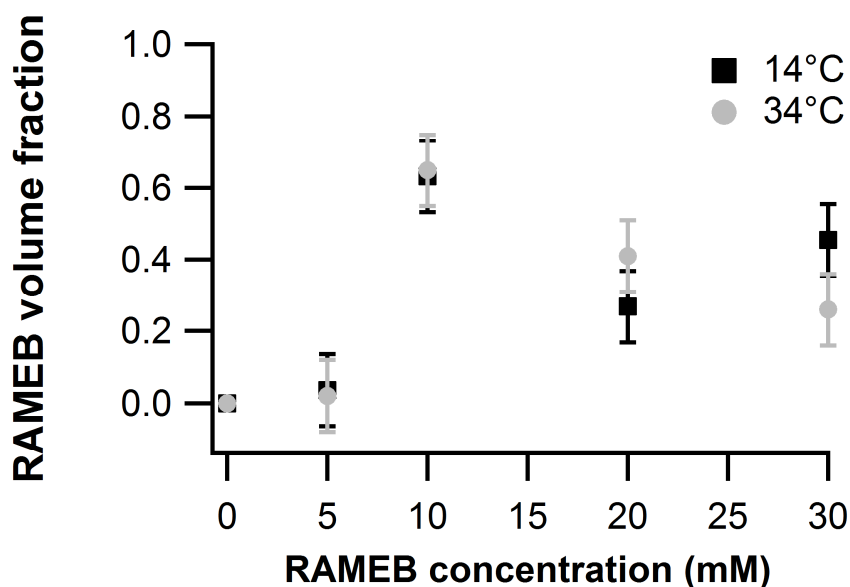
Fig. 5 *Volume fraction of RAMEB on the liposome surface at 14°C (black squares) and 34°C (grey dots)*

3.5 Bilayer thickness

Fig. 6 highlights how the hydrophilic (Fig. 6a) and hydrophobic (Fig. 6b) sublayers of the membrane respond to an increasing RAMEB concentration. The total bilayer thickness is equal to $D+2d$. Note that the hydrophilic layer thickness has been averaged: $d = 1/2\,(d_{in} + d_{out})$.
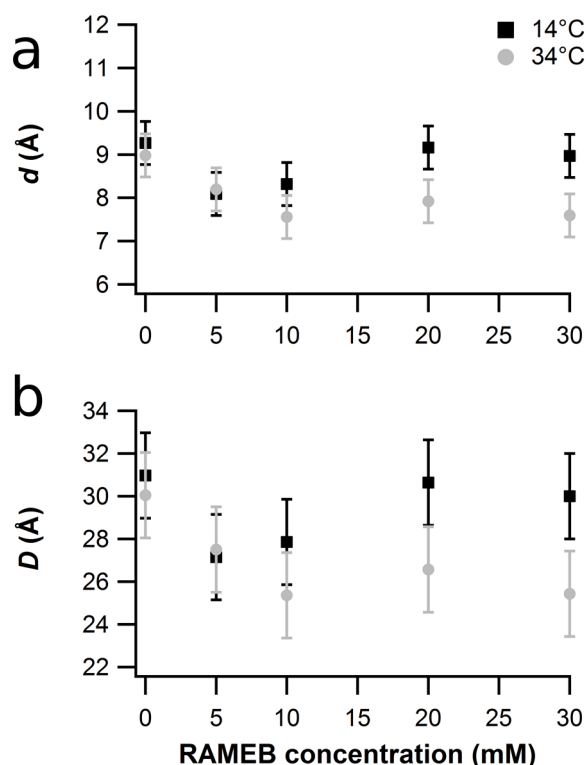
Fig. 6 *Liposome sublayer thickness for increasing RAMEB concentrations at 14°C (black squares) and 34°C (grey dots). (a) Average hydrophilic sublayer thickness; (b) Hydrophobic sublayer thickness*

As inferred from the data modelling, the cholesterol-doped liposomes at 14°C and 34°C have the same total bilayer thickness (48.5 ± 3Å) in the absence of RAMEB, with hydrophilic (*d*) and hydrophobic (*D*) contributions equal to respectively 9.0 ± 0.5 Å and 30.5 ± 2 Å. Temperature has no influence on the membrane thickness under such conditions because, as already mentioned, the endothermic phase transition of the bilayer is not observed in the presence of cholesterol [17,29]: the DMPC bilayer is then in a liquid ordered phase (l_O), which is not significantly affected by a temperature change [30]. The data obtained in the

present work are indeed very similar to those obtained below the transition temperature for cholesterol-free DMPC liposomes: $D = 31.4 \pm 1.5$ Å and $d = 9.9 \pm 0.7$ Å [26].

Progressive addition of RAMEB keeps the membrane thickness nearly unaffected at 14°C. It leads to a thinning of the bilayer at 34°C. At [RAMEB] = 30 mM, the bilayer thickness reaches 41 ± 3 Å with a hydrophilic contribution equal to 8.0 ± 0.5 Å and a hydrophobic contribution equal to 25 ± 2 Å. These values correspond to those found in our previous article [26] for cholesterol-free liposomes at 34°C without RAMEB ($D = 25 \pm 2$ Å and $d = 8 \pm 1$ Å) , suggesting that the thickness decrease is directly linked to cholesterol extraction, and that cholesterol extraction is significant enough to reactivate the membrane phase transition which is inhibited in the presence of cholesterol. This result supports the conclusions drawn in the previous subsections from the analysis of the aggregation number. If about two-third of the initial 30 mol% cholesterol doping is removed by RAMEB, the remaining cholesterol amount (10%) is below 25% and thus insufficient to inhibit the membrane phase transition [30].

4   Conclusions

The small-angle neutron scattering technique was applied to characterize the influence of a methylated β-cyclodextrin (RAMEB) on the structural parameters of liposomes doped with 30 mol% cholesterol. The SANS data are corroborated by DLS experiments but provide us with a more detailed picture of the liposome – cyclodextrin interactions.

The evolution of the fraction of lipid molecules inserted in the liposomes (m/m_0 parameter), of the aggregation number, of the average radius as well as of the bilayer thickness confirms that RAMEB is able to significantly affect the vesicles and to extract cholesterol in a dose dependent-way. At a RAMEB concentration of 30mM, about two-third of the added cholesterol has been removed. At this CD concentration, the observed structure for the surviving liposomes tends to become close to that observed in our previous work for cholesterol-free DMPC liposomes without RAMEB. The membrane phase transition which was inhibited by the presence of the cholesterol molecules reappears.It is also concluded that RAMEB-induced extraction leads to a less polydisperse vesicle population

The combination of our various results strongly suggests that RAMEB extract preferentially cholesterol rather than DMPC chains when vesicle membranes are doped with 30 mol% cholesterol.

In the absence of RAMEB, the global thickness of the cholesterol-doped bilayer, as well as the respective thicknesses of the sublayers, are similar at 14°C and 34°C because cholesterol erases the rigid-fluid transition. After substantial cholesterol extraction by RAMEB, the membrane thickness is reduced at 34°C but remains nearly unchanged at 14°C. The decrease at 34°C can be explained by a relaxation of the chains due to the free space left by the extracted cholesterol molecules and by the recovered fluidity of the membrane.

In conclusion, the model proposed in this paper leads to a consistent analysis of most of the data inferred from our SANS measurements and allows us to draw conclusions on the mechanisms of interaction between cyclodextrins and liposomes. The methods used in this work can be applied to the characterization of any kind of vesicles doped with cholesterol and incubated with different types of cyclodextrins.

5 *References*

1. Loftsson, T., Brewster, M.E.: Pharmaceutical applications of cyclodextrins. 1. Drug solubilization and stabilization. Journal of Pharmaceutical Sciences **85**(10), 1017-1025 (1996). doi:10.1021/js950534b
2. Loftsson, T.: Cyclodextrin in skin delivery. Cosmet **115**(10), 59-66 (2000).
3. Loftsson, T., Duchene, D.: Cyclodextrins and their pharmaceutical applications. Int J Pharm **329**(1-2), 1-11 (2007). doi:10.1016/j.ijpharm.2006.10.044
4. Hedges, A.R.: Industrial Applications of Cyclodextrins. Chem. Rev. **98**, 2035-2044 (1998).
5. Loftsson, T., Masson, M.: Cyclodextrins in topical drug formulation: theory and pratice. International Journal of Pharmaceutics **225**, 15-30 (2001).
6. Boulmedarat, L., Piel, G., Bochot, A., Lesieur, S., Delattre, L., Fattal, E.: Cyclodextrin-mediated drug release from liposomes dispersed within a bioadhesive gel. Pharm Res **22**(6), 962-971 (2005). doi:10.1007/s11095-005-4591-2
7. Gillet, A., Grammenos, A., Compere, P., Evrard, B., Piel, G.: Development of a new topical system: drug-in-cyclodextrin-in-deformable liposome. Int J Pharm **380**(1-2), 174-180 (2009). doi:10.1016/j.ijpharm.2009.06.027
8. Vrhovnik, K., Kristl, J., Sentjurc, M., Smid-Korbar, J.: Influence of liposome bilayer fluidity on the transport of encapsulated substance into the skin as evaluated by EPR. Pharm Res **15**(4), 525-530 (1998).
9. Guelluy, P.H., Fontaine-Aupart, M.P., Grammenos, A., Lecart, S., Piette, J., Hoebeke, M.: Optimizing photodynamic therapy by liposomal formulation of the photosensitizer pyropheophorbide-a methyl ester: in vitro and ex vivo comparative biophysical investigations in a colon carcinoma cell line. Photochem Photobiol Sci **9**(9), 1252-1260 (2010). doi:10.1039/c0pp00100g
10. Battistini, L., Burreddu, P., Sartori, A., Arosio, D., Manzoni, L., Paduano, L., Derrico, G., Sala, R., Reia, L., Bonomini, S., Rassu, G., Zanardi, F.: Enhancement of the uptake and cytotoxic activity of doxorubicin in cancer cells by novel cRGD-semipeptide-anchoring liposomes. Molecular Pharmaceutics **11**, 2280-2293 (2014). doi:10.1021/mp400718j
11. Etheridge, M.L., Campbell, S.a., Erdman, A.G., Haynes, C.L., Wolf, S.M., McCullough, J.: The big picture on nanomedicine: the state of investigational and approved nanomedicine products. Nanomedicine : nanotechnology, biology, and medicine **9**, 1-14 (2013). doi:10.1016/j.nano.2012.05.013
12. Ntimenou, V., Fahr, A., Antimisiaris, S.G.: Elastic vesicles for transdermal drug delivery of hydrophilic drugs: a comparison of important physicochemical characteristics of different vesicle types. Journal of biomedical nanotechnology **8**(4), 613-623 (2012).
13. Allan, D.: Mapping the lipid distribution in the membranes of BHK cells (mini-review). Molecular membrane biology **13**(2), 81-84 (1996).
14. Simons, K., Ikonen, E.: Functional rafts in cell membranes. Nature **387**(6633), 569-572 (1997). doi:10.1038/42408
15. Zajchowski, L.D., Robbins, S.M.: Lipid rafts and little caves. European Journal of Biochemistry **269**(3), 737-752 (2002). doi:10.1046/j.0014-2956.2001.02715.x
16. Han, S., Chiang, J.Y.L.: Mechanism of Vitamin D Receptor Inhibition of Cholesterol 7α-Hydroxylase Gene Transcription in Human Hepatocytes. Drug Metabolism and Disposition **37**(3), 469-478 (2009). doi:10.1124/dmd.108.025155

17. Grammenos, A., Bahri, M.A., Guelluy, P.H., Piel, G., Hoebeke, M.: Quantification of Randomly-methylated-beta-cyclodextrin effect on liposome: an ESR study. Biochem Biophys Res Commun **390**(1), 5-9 (2009). doi:10.1016/j.bbrc.2009.08.172

18. Grammenos, A., Mouithys-Mickalad, A., Guelluy, P.H., Lismont, M., Piel, G., Hoebeke, M.: ESR technique for noninvasive way to quantify cyclodextrins effect on cell membranes. Biochem Biophys Res Commun **398**(3), 350-354 (2010). doi:10.1016/j.bbrc.2010.06.050

19. Piel, G., Piette, M., Barillaro, V., Castagne, D., Evrard, B., Delattre, L.: Study of the relationship between lipid binding properties of cyclodextrins and their effect on the integrity of liposomes. Int J Pharm **338**(1-2), 35-42 (2007). doi:10.1016/j.ijpharm.2007.01.015

20. Puskas, I., Csempesz, F.: Influence of cyclodextrins on the physical stability of DPPC-liposomes. Colloids Surf B Biointerfaces **58**(2), 218-224 (2007). doi:10.1016/j.colsurfb.2007.03.011

21. Piel, G., Piette, M., Barillaro, V., Castagne, D., Evrard, B., Delattre, L.: Betamethasone-in-cyclodextrin-in-liposome: the effect of cyclodextrins on encapsulation efficiency and release kinetics. Int J Pharm **312**(1-2), 75-82 (2006). doi:10.1016/j.ijpharm.2005.12.044

22. Hatzi, P., Mourtas, S., Klepetsanis, P.G., Antimisiaris, S.G.: Study of the interaction between cyclodextrins and liposome membranes: effect on the permeability of liposomes. International Journal of Pharmaceutics **225**, 15-30 (2007).

23. Puskás, I., Barcza, L., Szente, L., Csempesz, F.: Features of the Interaction between Cyclodextrins and Colloidal Liposomes. Journal of Inclusion Phenomena and Macrocyclic Chemistry **54**(1-2), 89-93 (2006). doi:10.1007/s10847-005-4805-6

24. Goldstein, D.B.: The Effects of Drugs on Membrane Fluidity. Annual Review of Pharmacology and Toxicology **24**(1), 43-64 (1984). doi:doi:10.1146/annurev.pa.24.040184.000355

25. Tsamaloukas, A., Szadkowska, H., Slotte, J.P., Heerklotz, H.: Interaction of cholesterol with lipid membranes and cyclodextrin charaterized by calorimetry. Biophys J **89**, 1109-1119 (2005).

26. Joset, A., Grammenos, A., Hoebeke, M., Leyh, B.: Investigation of the interaction between a β-cyclodextrin and DMPC liposomes: a small angle neutron scattering study. Journal of Inclusion Phenomena and Macrocyclic Chemistry **In press** (2015). doi:10.1007/s10847-015-0558-z

27. Grammenos, A.: Effets d'une cyclodextrine au sein de systèmes membranaires: Une étude multispectroscopique. 88 (2011).

28. Arriaga, L.R., López-Montero, I., Monroy, F., Orts-Gil, G., Farago, B., Hellweg, T.: Stiffening Effect of Cholesterol on Disordered Lipid Phases: A Combined Neutron Spin Echo + Dynamic Light Scattering Analysis of the Bending Elasticity of Large Unilamellar Vesicles. Biophysical Journal **96**, 3629-3637 (2009). doi:10.1016/j.bpj.2009.01.045

29. Bieri, V.G., Wallach, D.F.: Fluorescence quenching in lecithin and lecithin/cholesterol liposomes by parmagenetic lipid analogues. Introduction of a new probe approach. Biochim Biophys Acta **389**(3), 413-427 (1975).

30. Almeida, P.F.F., Vaz, W.L.C., Thompson, T.E.: Lateral diffusion in the liquid phases of dimyristoylphosphatidylcholine/cholesterol lipid bilayers: a free volume analysis. Biochem **31**(29), 6739-6747 (1992). doi:10.1021/bi00144a013

31. Hope, M., Bally, M., Webb, G., Cullis, P.: Production of large unilamellar vesicles by rapid extrusion procedure. Characterization of size distribution, trapped volume and ability to maintain a membrane potential. Biochem Biophys Acta **812**, 55-65 (1985).
32. Coderch, L., Fonollosa, J., De Pera, M., Estelrich, J., De La Maza, A., Parra, J.L.: Influence of cholesterol on liposome fluidity by EPR. Relationship with percutaneous absorption. J Control Release **68**(1), 85-95 (2000). doi:S0168-3659(00)00240-6 [pii]
33. Olson, F., Hunt, C.A., Szoka, F.C., Vail, W.J., Papahadjopoulos, D.: Preparation of liposomes of defined size distribution by extrusion through polycarbonate membranes. Biochim Biophys Acta **557**(1), 9-23 (1979).
34. Brûlet, A., Lairez, D., Lapp, A., Cotton, J.-P.: Improvement of data treatment in small-angle neutron scattering. J Appl crystallogr **40**, 165-177 (2007).
35. Hammouda, B.: Probing Nanoscale Structures–the Sans Toolbox. NIST Center for Neutron Research, 224 (2010). doi:10.1016/j.nano.2007.10.035
36. Anderson, T.G., Tan, A., Ganz, P., Seelig, J.: Calorimetric Measurement of Phospholipid Interaction with Methyl-beta-Cyclodextrin. Biochemistry **43**, 2251-2261 (2004). doi:10.1021/bi0358869
37. Castagne, D., Dive, G., Evrard, B., Frédérich, M., Piel, G.: Spectroscopic studies and molecular modeling for understanding the interactions between cholesterol and cyclodextrins. J. Pharm. Pharm. Sci. **13**(3), 362-377 (2010).
38. Leventis, R., Silvius, J.R.: Use of Cyclodextrins to Monitor Transbilayer Movement and Differential Lipid Affinities of Cholesterol. Biophys J **81**(4), 2257-2267 (2001). doi:Doi: 10.1016/s0006-3495(01)75873-0
39. Mascetti, J., Castano, S., Cavagnat, D., Desbat, B.: Organization of β-Cyclodextrin under Pure Cholesterol, DMPC, or DMPG and Mixed Cholesterol/Phospholipid Monolayers. Langmuir **24**(17), 9616-9622 (2008). doi:10.1021/la8004294

CHAPTER VIII

General conclusions and perspectives

The number of commercial products which include nanoparticles increases every year (i.e. [1] for nanomedicine applications). They are designed to display specific characteristics (i.e. highly soluble, non-toxic) and a controlled behavior, (i.e. stimuli responsive...). When the complexity of such systems increases, the chemical behavior of the samples (size distribution, aggregates formation, nano-object reorganization...) does not always fit the expected properties (see chapters 3 and 4). In these cases, Small-Angle Neutron Scattering (SANS) is extremely useful to unravel a complex behavior. Unfortunately, SANS is not a turnkey technique. However, by developing tailored models and fitting them to the experimental data, the structural parameters of the colloids can be inferred. Furthermore, this technique gives precious structural information in solution, a direct advantage compared to microscopy techniques on dried samples.

In the present work, various stimuli-responsive self-assembled nano-objects have been investigated by SANS analysis as a function of the intensity of the selected external stimulus. The nano-objects discussed in this thesis are micelles built from amphiphilic block copolymers and liposomes composed of a phospholipidic membrane. The present section summarizes the results obtained in chapters 3 to 7. The composition of the samples is briefly reviewed and the models which were used to analyze the macroscopic SANS cross section versus scattering vector q are discussed.

Chapters 3 to 5 present our investigations of different micellar solutions using and extending form factors inspired by the work of Pedersen and Gerstenberg (P&G) [2]. The micelles result from the self-assembling of either a mixture of diblock copolymers (PCL-*b*-P2VP and PCL-*b*-PEO), or of triblock copolymers (PAA-*b*-PNIPAM-*b*-PEO) or of a diblock copolymer bearing a terpyridine end to chelate transition metal ions. The stimuli were either the pH, the temperature, or the nature and the concentration of divalent ions. The structural parameters of the micelles inferred from these models are: the radius R_c of the spherical core, its standard deviation and the radius of gyration R_g of the corona whose chains are considered as being Gaussian. The aggregation number is inferred from the values of R_c. Table 1 gives a synopsis of the models used to fit the form factor of the micelles for each investigated sample.

Table 1 Summary of the micellar solution studies: block copolymer compositions; pH and temperature conditions, and form factor models used to account for the micelle contribution to the scattering cross section.

Samples	Core	Corona (GC[a])	3rd sequence	Conditions
PCL$_{37}$-b-PEO$_{(d4)104}$ mixed with PCL$_{34}$-b-P2VP$_{52}$	PCL	PEO	P2VP (GC[a])	pH = 1.5 ; 4.5 and 9
and	PCL	PEO	P2VP (S[b])	pH = 1.5 ; 4.5 and 9
PCL$_{65}$-b-PEO$_{(d4)104}$ mixed with PCL$_{64}$-b-P2VP$_{31}$	PCL	PEO	P2VP (RR[c])	pH = 1.5
PEO$_{45}$-b-PNIPAM$_{45}$-b-PAA$_{13}$	PAA	mixed PNIPAM-PEO	/	pH = 2.5; T = 20 and 30°C[1]
and	mixed PAA-PNIPAM	PEO	/	pH = 2.5; T = 40 and 50°C
PEO(d4)$_{46}$-b-PNIPAM$_{46}$-b-PAA$_{11}$	PNIPAM	PEO	PAA (RR[c])	pH = 6,5 and 7,5, T= 20 and 30°C
	PNIPAM	PEO	PAA (RR[c])	pH = 6,5 and 7,5, T = 40 and 50°C
PS-b-PtBA-tpy	PS	PtBA	/	2%; 8%;12% and 20% w/w 8%; 12%; 16% w/w and addition of 0.5 eq Fe(II), NI(II) or Zn(II)

(a) Gaussian chains
(b) Homogeneous shell
(c) Rigid rods

---

[1] less than 1% of the chains are involved in the micelles

In chapter 3, micelles built from mixed block copolymers were prepared. Two compositions have been investigated: [PCL$_{37}$-*b*-PEO$_{(d4)104}$ mixed with PCL$_{34}$-*b*-P2VP$_{52}$] (*Sample I*) and [PCL$_{65}$-*b*-PEO$_{(d4)104}$ mixed with PCL$_{64}$-*b*-P2VP$_{31}$] (*Sample II*). The micelles have been prepared under acidic pH conditions and the SANS measurements have been performed in order to assess the structural reorganization of the micelles upon increasing pH. The P2VP is pH responsive and its contribution has been accounted for by three models to ensure the robustness of the results. They are derived from the Pedersen and Gerstenberg model [2] and differ by the way the P2VP is described. The first model describes the P2VP zone as a homogenous shell at the surface of the PCL core, the second one describes it as a corona of Gaussian chains and the third one, limited to the acidic regime, describes it as a collection of rigid rods. As expected, the P2VP sequence collapses on the PCL core as the pH increases. The size of the micelles as well as the aggregation number increase with pH for *Sample I*. This is a strong proof of a reorganization of the chains. This kind of sample was previously investigated by DLS and TEM but unambiguous evidence of the P2VP chain collapse on the core at high pH was lacking. The information inferred from the SANS experiments enlighten the role of the length of the copolymer blocks on the structural behavior of the micelles as a function of pH.

In chapter 4, amphiphilic PEO$_{45}$-*b*-PNIPAM$_{45}$-*b*-PAA$_{13}$ and a version with fully deuterated PEO, PEO$_{(d4)46}$-*b*-PNIPAM$_{46}$-*b*-PAA$_{11}$, were investigated by SANS. These samples are both pH- and thermo-responsive. At low pH, the PAA is protonated and relatively hydrophobic, while at pH>5, deprotonation leads to a hydrophilic polyelectrolyte. The PNIPAM is hydrophilic at temperature below the LCST (32°C) and hydrophobic at higher temperature. Because the presence of a bimodal size distribution has been observed at all pH's and temperatures investigated, the SANS cross sections have been fitted with analytical models involving a mixed population of core-corona micelles, spherical homogeneous aggregates and free chains. A similar model has been previously developed by Joseph & al [3] and Willet & al [4] but it was limited to free chains and micelles. These samples were challenging because of the multi stimuli-responsive behaviour as well as the short lengths of the sequences. Indeed, the degrees of polymerisation of the sequences are quite small giving rise to several difficulties. First, the free chains are small and hardly detected by SANS. Secondly, the PEO failed to fully solubilize the micelles and the presence of aggregates has been detected at all temperature and pH investigated. Their presence complicates the analysis because the macroscopic cross section is affected in the low *q* domain investigated. Finally,

not only the size of the core and the corona but even the organization of the copolymer blocks within the micelles is stimuli-dependent. The micelles were modelled as a PAA core and a mixed PEO-PNIPAM corona (below the LCST) or a mixed PAA-PNIPAM core (above the LCST) and a PEO corona as described in Table 1.At pH > pKa$_{PAA}$, the free chain contribution had to be taken into account in addition to the aggregates and the micelles. The micelles were then assumed to consist of a PNIPAM core and of a corona made of PEO Gaussian chains and negatively charged PAA extended chains modelled as rigid thin rods.

In Chapter 5, we describe the investigation of metallo-supramolecular micellar gels based on PS-*b*-PtBA-tpy copolymers and transition metal ions. The micellar solutions have been studied in the presence or not of transition metal ions (Fe(II), Ni(II) and Zn(II)). The form factors have been fitted by the P&G model [2]. At low concentration, the structure factor can be assumed equal to 1. As the copolymer concentration increases, a structure factor peak arises and the data were interpreted by combining the P&G model and the Percus-Yevick hard sphere model [5]. As the information about the internal structure of the micelles are given by the P&G model, the Percus-Yevick hard sphere model allowed us to determine the evolution of the volume fraction of the micelles and of the hard sphere interaction distance, as a function of the copolymer concentration. The resulting structural information was correlated with previously performed light scattering and rheology experiments. Indeed, the gel formation as well as the an increase of the intensity of the structure factor peak in the low *q* regime has been observed in the presence of Fe(II) and Ni(II) since these ions form stable *bis*-terpyridine complexes [6]. These complexes can be formed either in an intra-micellar way (thus leading to the formation of loops in the micellar corona) or in an inter-micellar way (thus leading to a network of connected micelles). The structure factor peak was not observed in presence of Zn(II) as it rather forms *mono*-terpyridine complexes [6].

Chapters 6 and 7 cover the action of cyclodextrins (CD) on liposomes (doped or not with cholesterol). The form factor of undoped unilamellar liposomes has been widely studied in the literature [7-12]. The aim of these chapters is rather to get a deeper understanding of the interactions taking place between a cyclodextrin (CD) and liposomes. The structure of DMPC liposomes was assessed upon addition of increasing amounts of RAMEB. These studies have been performed at two temperatures bracketing the phase transition of the DMPC bilayers. We were able to determine the fraction of DMPC molecules included in the vesicles as well as the possible formation of CD-DMPC inclusion complexes. Moreover, several structural parameters have been inferred as a function of the CD concentration: the radius, the

polydispersity, the thickness of both the hydrophobic and the hydrophilic parts of the membrane as well as the aggregation number and the RAMEB coverage at the liposome-water interface.

In the absence of cholesterol at 14°C, a fraction of the extracted DMPC chains becomes inserted into RAMEB-DMPC inclusion complexes. Another fraction of them participates in the reorganization of the vesicles, leading to larger, more stable liposomes. This conclusion is also compatible with the increase of the polydispersity upon increasing RAMEB concentration. This observation was interpreted as a preferential disruption of the small vesicles by the CD. At 34°C, the average vesicle size is not significantly affected by the interactions with the RAMEB. We suggest that all vesicles are then affected to the same extent by the interaction with RAMEB.

By using the same model for liposomes doped or not with cholesterol, we were able to enlighten his role in the membrane in accordance with the available literature [13-15]. Moreover, at 30 mM RAMEB, we showed that the observed structure for the surviving liposomes (chapter 7) tends to become close to that observed for liposomes without RAMEB (chapter 6). This is consistent with a favored cholesterol extraction by RAMEB.

Perspectives

Perspectives for a further development of this or related works could be envisaged in three directions: (i) sample preparation; (ii) data analysis, and (iii) extension to other colloidal systems.

During this work, the solvent and the composition of the sample varied widely from one situation to another and this resulted in a large scattering of the difficulties associated with the analysis of the SANS macroscopic cross sections. Some options to facilitate the future exploitation of experimental data emerge from our work. From a chronological point of view, the first samples studied in this thesis were the micelles built from a mixture of diblock copolymers (chapter 3). The PEO sequence was deuterated and the data acquisition was performed in H_2O and D_2O. Unfortunately, the data obtained in H_2O display a large incoherent contribution[2]. This led to an unfavorable signal-to-noise ratio after subtraction of the incoherent background, making a reliable data analysis very difficult. On the other hand,

---

[2] The origins of the incoherent scattering cross section are discussed in Chapter 2.

the most recently investigated samples are the triblock copolymers (chapter 4), for which two versions of the samples have been synthesized, with a deuterated and with a non-deuterated PEO block. The two samples displayed very close degrees of polymerization for each sequence. Such samples can be prepared if the synthesis procedure is well controlled. The availability of such "twin samples" helped a lot the analysis of the data. They made the comparison of the experimental data to several models possible with the strong constraint of the compatibility of the inferred structural data for the two samples. In our case, the deuterated PEO was chosen because of his commercial availability. Here also, some data have been recorded in H_2O but the signal-to-noise ratio was unfortunately again unfavorable.

A modelling procedure based on realistic hypotheses is essential to infer as much information as possible from the small-angle scattering cross sections. Different improvements could be proposed. As previously mentioned, the corona chains have been described in the majority of our models as Gaussian chains, according to the P&G methodology. This is often reasonable because most of our samples exhibit a q^{-2} behavior at large q-values. Some of them, however, display a $q^{-1.7}$ behavior (chapters 3 and 5). This result indicates that the excluded volume of the corona chains has to be taken into account. In these cases, it should be possible to analyze the experimental data using a better suited model. For example, Perdersen & al [16] already investigated the effect of the excluded volume on the form factor through another approach: the attachment of a hard sphere potential to Kuhn segments in order to prevent them to merge. They managed to test several chain models using Monte Carlo simulations and compared the results by fitting the corresponding form factors to their experimental data. This approach is more time consuming but it has proven its reliability.

Our methodology was based on the development of analytical models leading to closed-form formulas for the scattering cross section with parameters which could be fitted to mimic the experimental data. Alternative approaches based on molecular dynamics simulations could bring a complementary view on the problem, allowing to handle in a more realistic way questions like the excluded volume or interactions between scatterers.

Finally, most of the approaches which we have developed are not specific to the copolymers investigated in this thesis and their application field is quite large. Situations where free chains, micelles and aggregates coexist may frequently arise, especially when various stimuli induce the reorganization of nano-objects. Even if it is desired that the

copolymer size and composition be designed to avoid, e.g., aggregate formation, such a procedure will always require some trial-and-error steps for which an information-rich structural analysis method like SANS is an essential tool. The methods developed here can be very helpful in such a context. Furthermore, specific models like the core-rod model can also find applications for the study of colloid systems involving polyelectrolyte, multi-charged, chains.

References

1. Etheridge, M.L., Campbell, S.a., Erdman, A.G., Haynes, C.L., Wolf, S.M., McCullough, J.: The big picture on nanomedicine: the state of investigational and approved nanomedicine products. Nanomedicine : nanotechnology, biology, and medicine **9**, 1-14 (2013). doi:10.1016/j.nano.2012.05.013

2. Pedersen, J.S., Gerstenberg, M.C.: Scattering Form Factor of Block Copolymer Micelles. Macromolecules **29**, 1363-1365 (1996).

3. Joseph, J., Dreiss, C.a., Cosgrove, T., Pedersen, J.S.: Rupturing polymeric micelles with cyclodextrins. Langmuir : the ACS journal of surfaces and colloids **23**, 460-466 (2007). doi:10.1021/la061850g

4. Willet, N., Gohy, J.-F., Auvray, L., Varshney, S., Jérôme, R., Leyh, B.: Core-shell-corona micelles by PS-b-P2VP-b-PEO copolymers: focus on the water-induced micellization process. Langmuir : the ACS journal of surfaces and colloids **24**, 3009-3015 (2008). doi:10.1021/la702180c

5. Percus, J.K., Yevick, G.J.: Analysis of Classical Statistical Mechanics by Means of Collective Coordinates. Physical Review **110**, 1-13 (1958).

6. Holyer, R.H., Hubbard, C.D., Kettle, S.F.A., Wilkins, R.G.: The Kinetics of Replacement Reactions of Complexes of the Transition Metals with 2,2',2"-Terpyridine. Inorganic Chemistry **5**, 622-625 (1966). doi:10.1021/ic50038a027

7. Kucerka, N., Kiselev, M.A., Balgavy, P.: Determination of bilayer thickness and lipid surface area in unilamellar dimyristoylphosphatidylcholine vesicles from small-angle neutron scattering curves: a comparison of evaluation methods. Eur Biophys J **33**(4), 328-334 (2004). doi:10.1007/s00249-003-0349-0

8. Kiselev, M.A., Zbytovska, J., Matveev, D., Wartewig, S., Gapienko, I.V., Perez, J., Lesieur, P., Hoell, A., Neubert, R.: Influence of trehalose on the structure of unilamellar DMPC vesicles. Colloids and Surfaces A: Physicochemical and Engineering Aspects **256**(1), 1-7 (2005). doi:DOI: 10.1016/j.colsurfa.2004.09.017

9. Kiselev, M.a., Zbytovska, J., Matveev, D., Wartewig, S., Gapienko, I.V., Perez, J., Lesieur, P., Hoell, a., Neubert, R.: Influence of trehalose on the structure of unilamellar DMPC vesicles. Colloids and Surfaces A: Physicochemical and Engineering Aspects **256**, 1-7 (2005). doi:10.1016/j.colsurfa.2004.09.017

10. Zemlyanaya, E.V., Kiselev, M.a., Zbytovska, J., Almasy, L., Aswal, V.K., Strunz, P., Wartewig, S., Neubert, R.: Structure of unilamellar vesicles: Numerical analysis based on small-angle neutron scattering data. Crystallography Reports **51**, S22-S26 (2006). doi:10.1134/S1063774506070054

11. Pabst, G., Kučerka, N., Nieh, M., Rheinstädter, M., Katsaras, J.: Application of neutrons and X-ray scattering to the study of biologically relevant model membranes. Chem. Phys. Lipids **163**, 460-479 (2010).

12. Boggara, M.B., Krishnamoorti, R.: Small-Angle Neutron Scattering Studies of Phospholipid-NSAID Adducts, vol. 26. vol. 8. American Chemical Society, Washington, DC, ETATS-UNIS (2010)

13. Zajchowski, L.D., Robbins, S.M.: Lipid rafts and little caves. European Journal of Biochemistry **269**(3), 737-752 (2002). doi:10.1046/j.0014-2956.2001.02715.x

14. Grammenos, A., Bahri, M.A., Guelluy, P.H., Piel, G., Hoebeke, M.: Quantification of Randomly-methylated-beta-cyclodextrin effect on liposome: an ESR study. Biochem Biophys Res Commun **390**(1), 5-9 (2009). doi:10.1016/j.bbrc.2009.08.172

15. Bieri, V.G., Wallach, D.F.: Fluorescence quenching in lecithin and lecithin/cholesterol liposomes by parmagenetic lipid analogues. Introduction of a new probe approach. Biochim Biophys Acta **389**(3), 413-427 (1975).

16. Pedersen, J.S., Svaneborg, C., Almdal, K., Hamley, I.W., Young, R.N.: A Small-Angle Neutron and X-ray Contrast Variation Scattering Study of the Structure of Block Copolymer Micelles: Corona Shape and Excluded Volume Interactions. Macromolecules **36**, 416-433 (2003). doi:10.1021/ma0204913

CHAPTER IX

Appendices

Appendix I

Supporting Information of chapter IV

SANS cross section of the polymeric micelles in at pH > 4.2

The present section provides the demonstration of the SANS cross section of a polymeric micelle which consists of a PNIPAM core and a corona made of PEO Gaussian chains and negatively charged PAA extended chains described as rigid rods.

A, B, and C denote blocks of PAA, PNIPAM or PEO, respectively. To denote two chains of the same sequence, we use a "prime", i.e. B and B'.
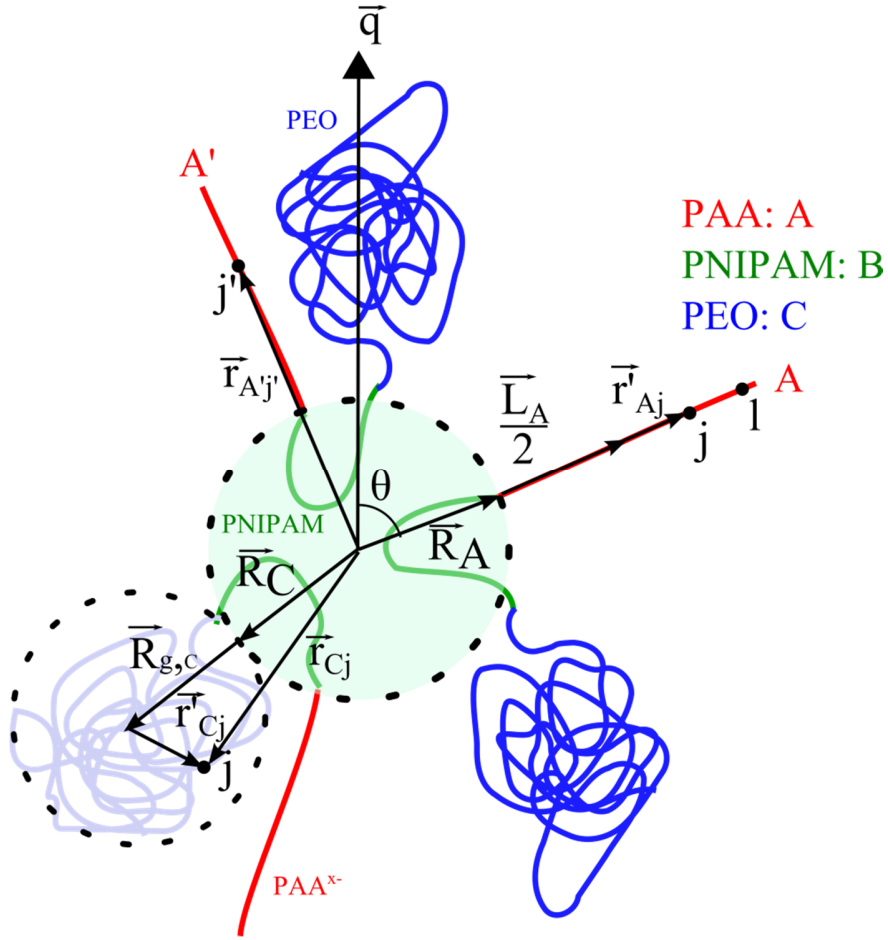
Figure A1*: Micelle made of negatively charged PAA extended chains (A), a PNIPAM spherical core (B), and a corona of PEO Gaussian chains (C). The position of the scatterers is defined from the center of the micelle which* $\left|\vec{R}_A\right| = \left|\vec{R}_C\right| = R$*, the radius of the core. R_g is the radius of gyration of the PEO chains and L is the effective length of the PAA rods. $\vec{R}_A$ is the position vector of the anchoring point of the rod A at the surface of the core. $\vec{L}_A/2$ is the vector from this anchoring point to the middle of the rod A. $\vec{r}'_{Aj}$ is the position vector of the jth scatterer of rod A with respect to the middle of the rod. Θ is the angle between the scattering vector $\vec{q}$ and the direction of rod A.*

The differential scattering cross section of such a micelle is equal to:

$$\frac{d\sigma}{d\Omega}(\vec{q}) = \sum_{j=1}^{N}\sum_{l=1}^{N} b_j b_l \left\langle \exp\left[-i\,\vec{q}\bullet\left(\vec{r}_l - \vec{r}_j\right)\right]\right\rangle \qquad (A1)$$

where *b* is the excess–scattering length of an elementary scatterer. In the present section, a monomer unit is considered as the elementary scatterer, whose scattering length is defined as the sum of the scattering lengths of its atoms. The degree of polymerization of a chain is z and the indices "A", "B" and "C" refer to the PAA, PNIPAM and PEO block, respectively, and N_m is the aggregation number of a micelle. For example, b_A is the scattering length of the acrylic acid unit, $C_3H_4O_2$ and z_A is the degree of polymerization of the PAA chains. To simplify, we shall denote the cross section for an individual micelle as $F(\vec{q})$.

$$
\begin{aligned}
F(\vec{q}) = & \, b_B^2 \sum_{B=1}^{N_m} \sum_{B'=1}^{N_m} \sum_{l \in B}^{z_B} \sum_{j \in B'}^{z_B} \left\langle \exp\left[-i\,\vec{q}\bullet\left(\vec{r}_{Bl} - \vec{r}_{B'j}\right)\right]\right\rangle \text{ contribution of the core} \\
& + b_A^2 \, N_m \sum_{l \in A}^{z_A} \sum_{j \in A}^{z_A} \left\langle \exp\left[-i\,\vec{q}\bullet\left(\vec{r}_{Al} - \vec{r}_{Aj}\right)\right]\right\rangle \text{ contribution of the rods} \\
& + b_C^2 \, N_m \sum_{l \in C}^{z_C} \sum_{j \in C}^{z_C} \left\langle \exp\left[-i\,\vec{q}\bullet\left(\vec{r}_{Cl} - \vec{r}_{Cj}\right)\right]\right\rangle \text{ contribution of the Gaussian chains} \\
& + \text{ interference terms}
\end{aligned}
\tag{A2}
$$

The following interference terms need to be taken into account:

- core - Gaussian chains (c-co)
- Gaussian chains – Gaussian chains (co-co)
- core – rods (c-r)
- rods – rods (r-r)
- Gaussian chains – rods (co-r)

1.1 Contribution of the core

The contribution of the core is given by the first term of eq(A2). It is not needed to individualize the chains. We consider $N_m \times z_B$ scatterers homogenously distributed in the core. The scattering amplitude is given by $A(\vec{q})$

$$
A(\vec{q}) = N_m \, b_B \, z_B \frac{3}{(qR)^3}\left[\sin(qR) - qR\cos(qR)\right]
\tag{A3}
$$

The contribution of the core to the scattering cross section is equal to $\left|A(\vec{q})\right|^2$, that is,

$$F_c(\vec{q}) = N_m^2 (b_B \, z_B)^2 \frac{9}{(qR)^6} [\sin(qR) - qR\cos(qR)]^2 \qquad (A4)$$

where R is the radius of the core.

1.2 Contribution of the Gaussian chains of the corona

The following well-known result is the Debye equation which also appears in the Pedersen-Gerstenberg model.[1] R_g is the radius of gyration of a single chain of the corona.

$$F_{co}(\vec{q}) = N_m (b_C \, v_C)^2 \left[2\frac{\exp(-q^2 R_g^2) + q^2 R_g^2 - 1}{(q^2 R_g^2)^2} \right] \qquad (A5)$$

1.3 Contribution of the rods

This section intends to demonstrate the contribution of the rods. The effective length of the rods is L (**Figure A1**). The contribution of the rods is equal to

$$F(\vec{q}) = N_m b_A^2 \sum_{l \in A}^{z_A} \sum_{j \in A}^{z_A} \left\langle \exp\left[-i\vec{q} \bullet (\vec{r}_{Al} - \vec{r}_{Aj}) \right] \right\rangle \qquad (A6)$$

If we assume that the rod is a continuum, we can write

$$\sum_{i=1}^{z_A} \exp(-i\,\vec{q} \bullet \vec{r}_{Al}) \cong \int_0^{z_A} \exp(-i\,q\,j\,\Delta\cos\theta)dj$$

$$= \frac{1 - \exp(-i\,q\,z_A\Delta\cos\theta)}{iq\Delta\cos\theta} \qquad (A7)$$

where Δ is the length of a segment of the polymer block: $L = z_A \times \Delta$. θ is the angle between the scattering vector $\vec{q}$ and the direction of the rod.

Therefore

$$\sum_{l\in A}^{z_A}\sum_{j\in A}^{z_A}\exp\left[-i\vec{q}\bullet\left(\vec{r}_{Al}-\vec{r}_{Aj}\right)\right]=\frac{\left[1-\exp\left(iqL\cos\theta\right)\right]\left[1-\exp\left(-iqL\cos\theta\right)\right]}{-iq\Delta\cos\theta}$$

$$=4\frac{\sin^2\left(\dfrac{qL\cos\theta}{2}\right)}{q^2\Delta^2\cos^2\theta}$$

(A8)

Eq(A8) needs to be averaged over all orientations with respect to the scattering vector.

$$\left\langle 4\frac{\sin^2\left(\dfrac{qL\cos\theta}{2}\right)}{q^2\Delta^2\cos^2\theta}\right\rangle=\frac{1}{4\pi}\int_0^{2\pi}d\phi\int_0^{\pi}\sin\left(\theta\right)\,4\frac{\sin^2\left(\dfrac{qL\cos\theta}{2}\right)}{q^2\Delta^2\cos^2\theta}\,d\theta$$

(A9)

$$=\frac{2}{q^2\Delta^2}\int_0^{\pi}\frac{\sin^2\left(\dfrac{qL\cos\theta}{2}\right)}{\cos^2\theta}\sin\theta d\theta$$

By substituting $x=\dfrac{qL\cos\theta}{2}$ and solving by parts, we obtain the contribution of the rods [2]:

$$F_r\left(\vec{q}\right)=N_m b_A^2 z_A\left\{\frac{2}{qL}Si\left(L\right)-\frac{\sin^2\left(\dfrac{qL}{2}\right)}{\left(\dfrac{qL}{2}\right)^2}\right\}$$

(A10)

where $Si\left(x\right)=\displaystyle\int_0^x\frac{\sin\left(x'\right)}{x'}dx'$

1.4 *Interference term between the core and the Gaussian chains*

This term accounts for the interference terms between the PNIPAM core (B) and the PEO Gaussian chains (C). The Gaussian chains are anchored at a distance R' = R$_c$+R$_g$ from the center of the micelles in order to avoid the penetration of the chains inside the core. The following equation is provided by the Pedersen- Gerstenberg Model:[1]

$$F_{c-co}\left(\vec{q}\right) = 2\, N_m^2 b_C z_C b_B z_B \left\{ \frac{3\left[\sin\left(qR\right) - qR\cos\left(qR\right)\right]}{\left(qR\right)^3} \right\} \left\{ \frac{1 - \exp\left(-q^2 R_g^2\right)}{q^2 R_g^2} \right\} \left\{ \frac{\sin\left[q\left(R + R_g\right)\right]}{q\left(R + R_g\right)} \right\}$$

(A11)

1.5 Interference terms between two Gaussian chains

Each chain interferes with $N_m - 1$ similar chains. The number of interference terms is therefore equal to $N_m(N_m - 1)$.

$$F_{co-co}\left(\vec{q}\right) = b_c^2 N_m\left(N_m - 1\right)\left\langle \sum_{l \in C}^{z_C} \sum_{j \in C'}^{z_C} \exp\left[-i\vec{q}\bullet\left(\vec{r}_{Cl} - \vec{r}_{C'j}\right)\right]\right\rangle$$

(A12)

where l and j are two scatterers which belong to two different PEO chains C and C' respectively. The contribution given by (A12) was already proven by Pedersen and Gerstenberg.[1]

$$F_{co-co}\left(\vec{q}\right) = b_c^2 z_c^2 N_m\left(N_m - 1\right)\left[\frac{1 - \exp\left(-q^2 R_g^2\right)}{q^2 R_g^2}\right]^2 \left\{\frac{\sin\left[q\left(R + R_g\right)\right]}{q\left(R + R_g\right)}\right\}^2$$

(A13)

1.6 Interference term between the core and the rods

The interference term between the core (B) and the rods (A) is equal to

$$F_{c-r}\left(\vec{q}\right) = 2 b_A b_B N_m \left\langle \sum_{\substack{l=1 \\ \forall B}}^{N_m z_B} \sum_{j \in A}^{z_A} \exp\left(-i\vec{q}\bullet\left(\vec{r}_{Bl} - \vec{r}_{Aj}\right)\right)\right\rangle$$

(A14)

The position vector of j, $\vec{r}_{Aj}$, can be written as a sum (see **Figure A1**):

$$\vec{r}_{Aj} = \vec{R}_A + \frac{\vec{L}_A}{2} + \vec{r}_{Aj}'$$

(A15)

where $\vec{R}_A$ is the position vector of the origin of rod A at the surface of the core. $\vec{L}_A/2$ is the vector from this origin to the middle of the rod. $\vec{r}_{Aj}'$ is the diffusion vector of the jth scatterer of the rod A measured from the middle of the rod. The PAA chains are assumed to be radially oriented

with respect to the center of the core to minimize the electrostatic repulsions between the charged rods. Therefore

$$\vec{R}_A \parallel \vec{L}_A \parallel \vec{r}_{Aj}'$$

$$F_{c-r}(\vec{q}) = 2b_A b_B N_m \left\langle \sum_{\substack{l=1 \\ \forall B}}^{N_m z_B} \exp\left[-i\vec{q}\bullet\vec{r}_{Bl}\right] \right\rangle \left\langle \exp\left[i\vec{q}\bullet\left(\vec{R}_A + \frac{\vec{L}_A}{2}\right)\right] \sum_{j=-z_A/2}^{z_A/2} \exp\left[i\vec{q}\bullet\vec{r}_{Aj}'\right] \right\rangle \quad (A16)$$

As in eq(A3), we can write

$$b_B \sum_{\substack{l=1 \\ \forall B}}^{N_m z_B} \exp\left[-i\vec{q}\bullet\vec{r}_{Bl}\right] = N_m b_B z_B \frac{3\left[\sin(qR) - qR\cos(qR)\right]}{(qR)^3} \quad (A17)$$

Making the assumption of a continuum,

$$\sum_{j=-\frac{3A}{2}}^{z_A/2} \exp\left[i\vec{q}\bullet\vec{r}_{Aj}'\right] \simeq \int_{-\frac{z_A}{2}}^{\frac{z_A}{2}} \exp\left[iqj\Delta\cos\theta\right]dj$$

$$= \frac{2\sin\left(\dfrac{qL\cos\theta}{2}\right)}{q\Delta\cos\theta} \quad (A18)$$

Averaging over all all orientations with respect to the diffusion vector $\vec{q}$, multiplying by (A18) and inserting into (A16) leads to:

$$F_{c-r}(\vec{q}) = 2b_A z_A b_B z_B N_m^2 \left\{ \frac{3\left[\sin(qR) - qR\cos(qR)\right]}{(qR)^3} \right\} \left\{ \frac{Si\left[q(R+L)\right] - Si(qR)}{qL} \right\} \quad (A19)$$

1.7 Interference terms between the rods

To obtain the interference terms between the rods $F_{r-r}(\vec{q})$ we proceed like in section 1.6. There are $N_m(N_m-1)$ interference terms:

$$F_{r-r}(\vec{q}) = b_A N_m (N_m - 1) \left\langle \sum_{l \in A}^{z_A} \sum_{j \in A'}^{z_A} \exp\left[-i\vec{q} \bullet \left(\vec{r}_{Al} - \vec{r}_{A'j}\right)\right] \right\rangle \tag{A20}$$

The scatterers l and j belong to two different rods A and A' respectively. $\vec{r}_{Al}$ and $\vec{r}_{A'j}$ can be decomposed as follows (see **Figure A1**):

$$\begin{aligned}\vec{r}_{Al} &= \vec{R}_A + \frac{\vec{L}_A}{2} + \vec{r}'_{Al} \\ \vec{r}_{A'j} &= \vec{R}_{A'} + \frac{L_{A'}}{2} + \vec{r}'_{A'j}\end{aligned} \tag{A21}$$

Therefore

$$\begin{aligned}F_{r-r}(\vec{q}) = b_A^2 N_m (N_m - 1) &\left\langle \exp\left[-i\vec{q} \bullet \left(\vec{R}_A + \frac{\vec{L}_A}{2}\right)\right] \sum_{l=-z_a/2}^{z_A/2} \exp\left[-i\vec{q} \bullet \vec{r}'_{Al}\right] \right\rangle \\ &\times \left\langle \exp\left[i\vec{q} \bullet \left(\vec{R}_{A'} + \frac{\vec{L}_{A'}}{2}\right)\right] \sum_{j=-z_A/2}^{z_A/2} \exp\left[i\vec{q} \bullet \vec{r}'_{A'j}\right] \right\rangle\end{aligned} \tag{A22}$$

The rods are randomly chosen, so both averages between brackets can be performed separately. The same line of reasoning as in the previous section leads to:

$$F_{r-r}(\vec{q}) = b_A^2 z_A^2 N_m (N_m - 1) \left\{ \frac{Si\left[q(R+L) - Si(qR)\right]}{qL} \right\}^2 \tag{A23}$$

1.8 Interference terms between a Gaussian chains and a rod

The interference term between the Gaussian chains and the rods $F_{co-r}(\vec{q})$ is obtained in a similar way as in the previous section. Each chain can interfere with each rod and vice versa. There are therefore $2 \times N_m^2$ interference terms.

$$F_{co-r}(\vec{q}) = b_A b_C N_m^2 \left\langle \sum_{l\in A}^{z_A} \sum_{j\in C}^{z_C} \exp\left[-i\vec{q}\bullet\left(\vec{r}_{Al} - \vec{r}_{Cj}\right)\right] \right\rangle$$

$$+ b_A b_C N_m^2 \left\langle \sum_{l\in C}^{z_C} \sum_{j\in A}^{z_A} \exp\left[-i\vec{q}\bullet\left(\vec{r}_{Cj} - \vec{r}_{Al}\right)\right] \right\rangle \qquad \text{(A24)}$$

$$= 2 b_A b_C N_m^2 \left\langle \sum_{l\in A}^{z_A} \sum_{j\in C}^{z_C} \exp\left[-i\vec{q}\bullet\left(\vec{r}_{Al} - \vec{r}_{Cj}\right)\right] \right\rangle$$

As previously mentioned, we can decompose the position vector of each scatterer as follows (see **Figure A1**)

- for the rods: $\vec{r}_{Al} = \vec{R}_A + \dfrac{\vec{L}_A}{2} + \vec{r}_{Ai}'$

- for the Gaussian chains: $\vec{r}_{Cj} = \vec{R}_C + \vec{R}_{g,c} + \vec{r}_{Cj}'$

The Gaussian chains are anchored at a distance $\vec{R}_C + \vec{R}_{g,C}$ from the center of the micelle in order to prevent the penetration of the corona chains into the core. Because the orientations of the Gaussian chains and the rods are random, the average on the orientation can be performed separately:

$$F_{co-r}(\vec{q}) = 2 N_m^2 b_A b_C \left\langle \exp\left[-i\vec{q}\bullet\left(\vec{R}_A + \dfrac{\vec{L}_A}{2}\right)\right] \sum_{l=-z_A/2}^{z_A/2} \exp\left[-i\vec{q}\bullet\vec{r}_{Al}'\right] \right\rangle$$

$$\times \left\langle \exp\left[i\vec{q}\bullet\left(\vec{R}_c + \vec{R}_{g,C}\right)\right] \right\rangle \left\langle \sum_{j\in C}^{z_C} \exp\left[i\vec{q}\bullet\vec{r}_{Cj}'\right] \right\rangle \qquad \text{(A25)}$$

$$F_{co-r}(\vec{q}) = 2 N_m^2 b_A z_A b_C z_C \left\{ \dfrac{\sin\left[q\left(R+R_g\right)\right]}{q\left(R+R_g\right)} \right\} \left\{ \dfrac{1-\exp\left[-q^2 R_g^2\right]}{q^2 R_g^2} \right\} \left\{ \dfrac{Si\left[q\left(R+L\right)\right] - Si\left[qR\right]}{qL} \right\}$$

$$\text{(A26)}$$

1.9   *Scattering cross section of a micelle population*

If the number of chains per unit volume is equal to n, the macroscopic scattering cross section for a monodisperse micelle population is given by multiplying the sum of eq (A4) (A5) (A10) (A11) (A13)(A19) (A23)(A26) by n/N_m:

$$\frac{d\Sigma}{d\Omega}(\vec{q};R;Rg;L) = \frac{n}{N_m} \Bigg[\Bigg[N_m^2 b_B^2 z_B^2 \frac{9}{(qR)^6} \Big[\sin(qR) - qR\cos(qR)\Big]^2$$

$$+ N_m b_C^2 z_C^2 \left[2\frac{\exp(-q^2 R_g^2) + q^2 R_g^2 - 1}{(q^2 R_g^2)^2} \right]$$

$$+ N_m b_A^2 z_A^2 \left[\frac{2}{qL} Si(qL) - \frac{\sin^2\left(\frac{qL}{2}\right)}{\left(\frac{qL}{2}\right)^2} \right]$$

$$+ 2N_m^2 b_B z_B\, b_C\, z_C \left\{ \frac{3\big[\sin(qR) - qR\cos(qR)\big]}{(qR)^3} \right\} \left\{ \frac{1 - \exp(-q^2 R_g^2)}{q^2 R_g^2} \right\} \left\{ \frac{\sin\big[q(R+R_g)\big]}{q(R+R_g)} \right\}$$

$$+ 2N_m^2 b_A z_A\, b_B z_B \left\{ \frac{3\big[\sin(qR) - qR\cos(qR)\big]}{(qR)^3} \right\} \left\{ \frac{Si\big[q(R+L)\big] - Si\big[qR\big]}{qL} \right\}$$

$$+ N_m(N_m-1) b_C^2\, z_C^2 \left\{ \frac{1 - \exp(-q^2 R_g^2)}{q^2 R_g^2} \right\}^2 \left\{ \frac{\sin\big[q(R+R_g)\big]}{q(R+R_g)} \right\}^2$$

$$+ N_m(N_m-1) b_A^2\, z_A^2 \left\{ \frac{Si\big[q(R+L)\big] - Si\big[qR\big]}{qL} \right\}^2 \tag{A27}$$

$$+ 2N_m^2 b_A\, z_A\, b_C\, z_C \left\{ \frac{\sin\big[q(R+R_g)\big]}{q(R+R_g)} \right\} \left\{ \frac{Si\big[q(R+L)\big] - Si\big[qR\big]}{qL} \right\} \left\{ \frac{1 - \exp(-q^2 R_g^2)}{q^2 R_g^2} \right\} \Bigg]\Bigg]$$

The scattering cross section at q=0 is equal to:

$$\frac{d\Sigma}{d\Omega}(\vec{q}=0;R;Rg;L) = \frac{n}{N_m} N_m^2 \big(z_A b_A + z_B b_B + z_C b_C\big)^2 \tag{A28}$$

$$= n\, N_m \big(z_A b_A + z_B b_B + z_C b_C\big)^2$$

References

1.Pedersen, J. S.; Gerstenberg, M. C., Scattering Form Factor of Block Copolymer Micelles. **1996**, 1363-1365.
2.Higgins, J. S.; Benoît, H., Polymers and neutron scattering. **1994**.

Appendix II

Supporting Information of chapter IV

Contribution of the aggregates

In chapter IV, we have shown that the macroscopic cross section may be expressed as the sum of the contributions of free chains (index ch), micelles (index m) and aggregates (index a).

$$\frac{d\Sigma}{d\Omega}(q) = \left[\frac{d\Sigma}{d\Omega}(q)\right]_{ch} + \left[\frac{d\Sigma}{d\Omega}(q)\right]_{m} + \left[\frac{d\Sigma}{d\Omega}(q)\right]_{a}$$

$$= \underbrace{I_{ch}(q=0)P_{ch}(q,R_{g,ch})}_{free\,chains} + \underbrace{I_{m}(q=0)\int_{0}^{+\infty} P_{m}(q,R)\,\Gamma_{m}(R)\,dR}_{micelles} \qquad \text{(B29)}$$

$$+ \underbrace{I_{a}(q=0)\int_{0}^{+\infty} P_{a}(q,R)\,\Gamma_{a}(R)\,dR}_{aggregates}$$

We shall focus in this section on the contribution of the aggregates. The intensity at q = 0, $I_a(q=0)$, depends on the number of aggregates per unit volume (N_s^{tot}/V), the number of chains, $N_{m,a}$ involved in the aggregates and the composition of the chains through the excess scattering lengths $\tilde{b}$ and the degree of polymerization *z*. If *f* is the fraction of chains involved in free chains or micelles, I_a (q=0) can be expressed as a function of the number of chains in the sample N^{copo}.

$$I_{a}\left(q=0\right) = \frac{N_s^{tot}}{V}N_{m,a}^2\left(z_A\tilde{b}_A + z_B\tilde{b}_B + z_C\tilde{b}_C\right)^2$$

$$= \frac{N^{copo}}{V}\left(1-f\right)N_{m,a}\left(z_A\tilde{b}_A + z_B\tilde{b}_B + z_C\tilde{b}_C\right)^2 \qquad \text{(B30)}$$

As the aggregates population display size polydispersity, we can introduce it through the expression of the size distribution:

$$\Gamma\left(R\right)dR = \Gamma(N_{m,a})dN_{m,a} \qquad \text{(B31)}$$

It is required to express $N_{m,a}$ as a function of R.

a) For a free chain, the size of the chain is usually expressed through $R = \sqrt{5/3}R_g$.

b) The expression of R_g, $R_g{}^2 = zlb/6$ (l is the length of the monomer unit and b is the length of the Kuhn) segment results from the hypothesis of the random walk.

c) If the aggregate is built from $N_{m,a}$ chains, we consider that the distance between the last monomer from a chain A and the first monomer of a neighbour chain B is in the same range than the length of the monomers. The radius of gyration of the aggregates, $R_{g,a}$ is therefore equal to the R_g of a longer chain made of $N_{m,a}$ chains joined end-to-end. We can then write:

$$R_{g,a}^2 = N_{m,a}\frac{zlb}{6}$$
$$R^2 = \frac{5}{3}R_{g,a}^2 \tag{B32}$$

Therefore

$$N_{m,a} = \beta R^2 \tag{B33}$$

where $\beta = \frac{3}{5}\frac{6}{zlb} = \frac{3}{5R_{g,ch}^2}$. The number of spherical aggregates N_S whose radius is in the range R and $R+dR$, is therefore equal to

$$N_s(R)dR = N_s^{tot}\Gamma(R)dR \tag{B34}$$

On the other hand:

$$(1-f)N^{copo} = \int_0^{+\infty} N_{m,a}(R)N_s(R)dR = \beta N_s^{tot}\int_0^{+\infty} R^2\Gamma(R)dR = \beta N_s^{tot}\langle R^2\rangle \tag{B35}$$

Therefore

$$N_s^{tot} = \frac{(1-f)N^{copo}}{\beta\langle R^2\rangle} \tag{B36}$$

$I_a(q=0)$ is therefore equal to

$$I_a(q=0) = (1-f)\frac{N^{copo}}{V}\left(z_A\tilde{b}_A + z_B\tilde{b}_B + z_C\tilde{b}_C\right)^2 \frac{\langle R^4 \rangle}{\frac{5}{3}R_{g,ch}\langle R^2 \rangle} \tag{B37}$$

If the aggregate is built from a unique chain, $\frac{\langle R^4 \rangle}{\frac{5}{3}R_{g,ch}^2\langle R^2 \rangle} = 1$
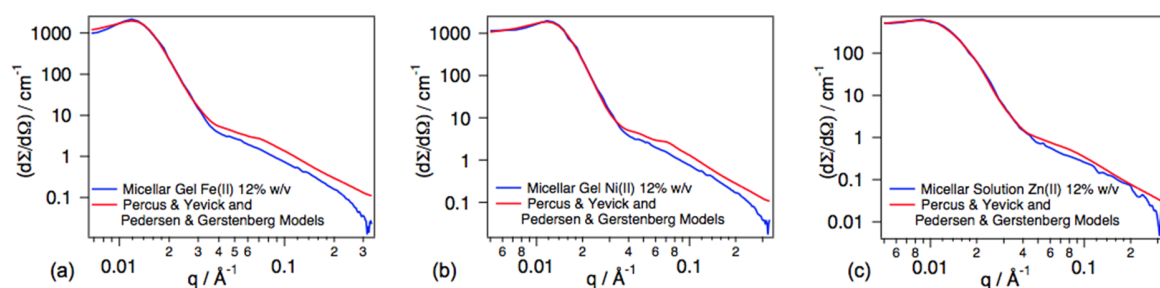
Appendix III

Supporting Information of chapter V

Structure of Metallo-Supramolecular Micellar Gels

C. Mugemana, A. Joset, P. Guillet, M.-S. Appavou, N. De Souza, C.-A. Fustin, B. Leyh, J.-F. Gohy, Macromolecular Chemistry and Physics 2013, 214, 1699.

Figure A1 *Experimental and calculated SANS intensities of the micellar solutions, from the PS$_{70}$-b-PtBA$_{180}$-tpy block copolymer at a concentration of 12% w/v in deuterated ethanol, in the presence of Fe(II) (a), Ni(II) (b) and Zn(II) (c) ions.*
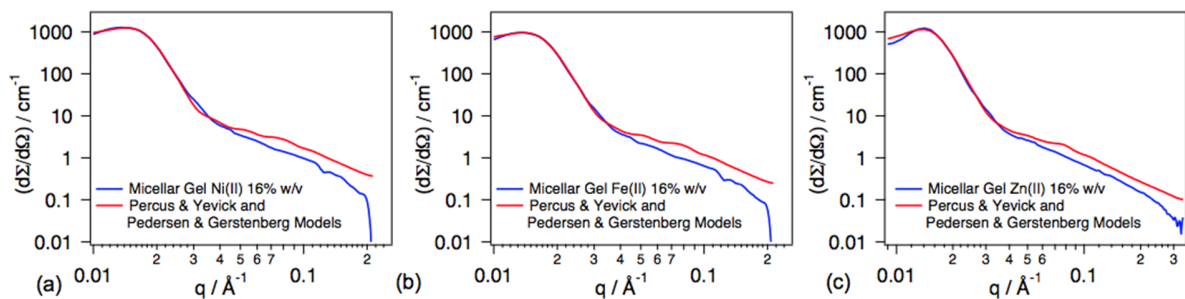
Figure A2 *Experimental and calculated SANS intensities of the micellar solutions, from the PS$_{70}$-b-PtBA$_{180}$-tpy block copolymer at a concentration of 16% w/v in deuterated ethanol, in the presence of Fe(II) (a), Ni(II) (b) and Zn(II) (c) ions.*

Table A1 *Results obtained from the fits of SANS data for the micellar networks prepared from different metal ions starting from the PS$_{70}$-b-PtBA$_{180}$-tpy block copolymer micelles at a concentration of 16% w/v in deuterated ethanol.*

Sample	$\overline{R}_i / \mathring{A}$ [a,b]	$\Delta R_i / \mathring{A}$ [a,c]	$R_g / \mathring{A}$ [a,d]	$R_t / \mathring{A}$ [e]	ϕ [a,,f]	$\sigma / \mathring{A}$ [a,g]
Fe (II)	84	5.9	41.0	166	0.24	365
Ni (II)	82	6.6	40.7	164	0.23	357
Zn (II)	89	9.5	41.2	171	0.27	389

(a) The confidence intervals, resulting from the numerical fitting procedure, are estimated to about 2 Å for the core radius, to 1 Å for the coronal chain radius of gyration, to 0.01 for the hard sphere volume fraction, and to 2 Å for the hard sphere interaction distance.
(b) Average radius of the PS core, deduced from the average aggregation number $\overline{N_m}$
(c) Standard deviation on the PS core radius
(d) Radius of gyration of PtBA coronal chains
(e) Micellar total radius ($2R_g + \overline{R}_i$)
(f) Hard sphere volume fraction
(g) Hard sphere interaction distance
(h) Data corresponding to 16 % *w/v* obtained by linear interpolation between 12 and 20 % *w/v*